Suspension High Velocity Oxy Fuel Thermal Spraying for Biomedical Coatings

By: **Saira Bano**

(MSc)

Thesis submitted to the University of Nottingham for the degree of
Doctor of Philosophy

Date: June 2021

Abstract

Thermal spraying of bioglasses offers the opportunity to produce coatings for different biomedical applications. The resorption of the coatings can be adjusted by tailoring the chemical composition of the glass and the coating microstructure.

This thesis describes the production of novel bioactive and bioresorbable glass coatings for biomedical applications via an emerging suspension high velocity-oxy fuel (SHVOF) thermal spray.

Bioglass® (45S5) was sprayed at the flame power of 90, 75, 50 and 25 kW by varying fuel (hydrogen) and oxygen flow rates. No coating was obtained at the flame power of 90 kW, and thin coating (< 10 μm) was obtained at 25 kW. Thick (25 ± 3 μm) and uniform coatings were obtained at the flame powers of 50 and 75 kW. The 50 kW coating was 16 ± 2 % porous, while the 75 kW coating was 10 ± 1 % porous. The bioactivity tests of the coatings showed that no hydroxyapatite (HA) was deposited on the surface of 25 kW coating even after seven days of immersion in simulated body fluid (SBF). Whilst, the coatings produced at 50 and 75 kW revealed HA deposition after three days. EDX analysis of the cross-section of the coated samples showed that the 50 kW initial coating thickness reduced from 25 μm to 6 μm after immersion in SBF for 7 days, which means that this microstructure was highly reactive towards SBF and hence behaved like a resorbable coating.

Coatings from two bioactive glasses, namely ICIE16 (48.0 % SiO_2, 33.0 % CaO, 6.6 % Na_2O, 2.4 % P_2O_5 and 10.0 % K_2O, in wt %.) and 13-93 (53.0 % SiO_2, 6.0 % Na_2O, 20.0 % CaO, 12.0 % K_2O, 5.0 % MgO and 4.0 % P_2O_5, in wt %) were successfully produced at the flame powers of 50 and 75 kW. For both formulations, thick, porous and less hard coatings were obtained at 50 kW, whilst harder, dense and less thick coatings were obtained at 75 kW. ICIE16 coatings showed more dissolution in SBF than the 13-93 coatings. Moreover, in-vitro cell tests, using MG63 cells, showed good cell attachment and proliferation on the surfaces of the coating, revealing good cytocompatibility.

Resorbable phosphate based glass (PBG), P-40 (40.0 % P_2O_5, 16.0 % CaO, 24.0 % MgO, 20.0 % Na_2O in mol %) was sprayed at 50 and 75 kW flame power. The 75 kW coating was thinner and rougher than the 50 kW coating; both coatings presented globules on the surface. The Raman analysis of the P-40 coatings suggested that the structure of the glass had changed as the concentration of Q^2 (2 bridging oxygen) species has been decreased. Whilst, Q^1 (1 bridging oxygen) concentration has been increased and Q^0 (0 bridging oxygen) species has been formed. Due to these structural alterations, these coatings showed less ion release and mass degradation than those reported in the literature for P-40 thin films and bulk glass.

Ga_2O_3 doped Bioglass® was manufactured for antimicrobial applications and deposited at 50 kW. Moreover, Ga_2O_3 and Bioglass® suspensions were co-deposited via a hybrid nozzle at 50 kW to mix them in the flame. Both coatings showed bioactivity as HA was deposited on the surfaces of these coatings after immersion in SBF for 3 days.

In summary, SHVOF thermal spraying has been proven to be an effective and versatile technique to deposit different bioglasses, maintaining their amorphous tetrahedral structure and composition.

Acknowledgement

I would like to acknowledge the University of Nottingham for funding my PhD and would like to express my appreciations to my supervisors, Dr. Tanvir Hussain, Dr. Ifty Ahmed and Prof. David Grant for putting up with me.

I would like to thank all the technical team of Wolfson, in particular Mr. Rory Screaton and John Kirk for thermal spray experiments and Julie Thompson, Louise Briggs in cell culture tests, and Scott Young in ion leaching tests. I really appreciate Dr. Colin Scotchford for his support for cell work.

I am also grateful to my colleagues and friends, who made my PhD journey a pleasant one. Further, thanks to my husband Muhammad Arshad and my daughter Maria Khan, who always been available there for me.

Declaration

I **Saira Bano** hereby declare that this thesis and the work reported herein has been composed entirely by myself. Information derived from the published and unpublished work of others has been acknowledged in the text and references are given in the list of sources.

Ms Saira Bano (June, 2021)

List of General Publications

1. **Bano, S.**, Ahmed, I., Grant, D.M., Nommeots-Nomm, A. and Hussain, T., 2019. Effect of processing on microstructure, mechanical properties and dissolution behaviour in SBF of Bioglass (45S5) coatings deposited by Suspension High Velocity Oxy Fuel (SHVOF) thermal spray. *Surface and Coatings Technology,* 372, pp.229 - 238. **(Chapter 4)**

2. **Bano, S**., Romero, A.R., Grant, D.M., Nommeots-Nomm, A., Scotchford, C., Ahmed, I. and Hussain, T., 2021. In-vitro cell interaction and apatite forming ability in simulated body fluid of ICIE16 and 13-93 bioactive glass coatings deposited by an emerging suspension high velocity oxy fuel (SHVOF) thermal spray. *Surface and Coatings Technology,* 407, pp.126764, **(Chapter 5)**

3. **Bano, S.,** Acacio, R., Islam, M.T., Grant, D.M., Ahmed, I., and Hussain, T., 2021. Development and Characterisation of Phosphate-Based Glass Coatings via Suspension High Velocity Oxy-Fuel (SHVOF) Thermal Spray Process. *Journal of Thermal Spray Technology.* **(Chapter 6)**

4. **Mrs. Saira Bano** and Dr. Tanvir Hussain; Conference Paper on "Effect of Processing on Microstructure, Mechanical Properties and Dissolution in Simulated Body Fluid of 45S5 Bioglass Coatings Deposited by Suspension High Velocity Oxy Fuel Thermal Spray" *In International thermal spray conference and exposition.* (Yokohama, Japan) 612–618, 2019.

Nomenclature

Air plasma spray	APS
Bioactivity index	Ib
Bridging oxygen	BO
Carbonated hydroxyapatite	HCA
Crystallisation Temperature	Tc
Collision cell technology with energy discrimination	CCTED
Dulbecco's Modified Eagle Medium	DMEM
Electrophoretic deposition	EPD
Ethylene diamine tetraacetic acid	EDTA
Energy dispersive X-ray spectroscopy	EDX
Extracochlear percutaneous implant	EPI
Food and drug administration	FDA
Glass Transition Temperature	Tg
Hydroxyapatite	HA
High velocity oxygen-fuel	HVOF
4-(2-hydroxyethyl)-1-piperazineethanesulfonic acid	HEPES
Hexamethyldisilazane	HMDS
Industrial methylated spirit	IMS
Inductively coupled plasma mass spectroscopy	ICPMS
Milli- Q	MQ
Middle ear prosthesis	MEP
Mixed alkali effect	MAE
Network connectivity	NC
Non-bridging oxygen	NBO
Nuclear magnetic resonance	NMR
Parts per billion	ppb
Parts per million	ppm
Perfluoroalkoxy	PFA
Phosphate buffered saline	PBS
Physical vapour deposition	PVD
Phosphate based glasses	PBGs
Simulated body fluid	SBF
Scanning Electron Microscopy	SEM
Suspension high velocity oxy fuel	SHOVF
Standard mode	SM
Thermal spray	TS
Thermal Expansion Coefficient	TEC
Tissue culture plastic	TCP
X-ray Diffraction	XRD

Contents

List of Figures

List of Tables

Chapter 1

Introduction

1.1 Overview

Biomedical implants intended for load bearing applications such as orthopaedic, and bone fixation; are made of metals and alloys such as titanium alloys (Ti-6Al-4V), stainless steel and Co-Cr alloys. This is due to their high yield strength and ability to perform under cyclic load applications [1]. However, these are susceptible to chemical and electrochemical degradation in the body as the body fluid is aqueous with dissolved oxygen and ions such Cl^{-1} and OH^{-1} [1]. Moreover, these metallic materials cannot form any biological or chemical bond at the interface between the implant surface and host tissue which leads to relative movements resulting in to inflammatory reactions [2].

The surface of an implant plays an important role in the body, since most chemical and biological reactions occur at the surface. Thanks to surface modification of materials, it is possible to combine the desired surface properties (bioactivity and ion release) of the surface with the ideal bulk properties such as tensile strength or stiffness of the implants [3]. So an effective approach to avoid unwanted reactions and achieve stronger bonding of the implant with the host tissue is to modify the surface of the implant with coating of desired properties [2]. Selecting the appropriate coating material and coating technique is a major challenge in the production of implants for biomedical purposes.

In the United Kingdom alone 708,311 hip procedures were carried out between 2003 and 2013 of which 93% were due to osteoarthrities [4]. Primary revisions were carried

out for 17,916 patients, while asceptic loosening occurred in 4,376 cases, and this was the biggest reason of implant failure. Moreover, 2,443 revisions were conducted due to infections [4].

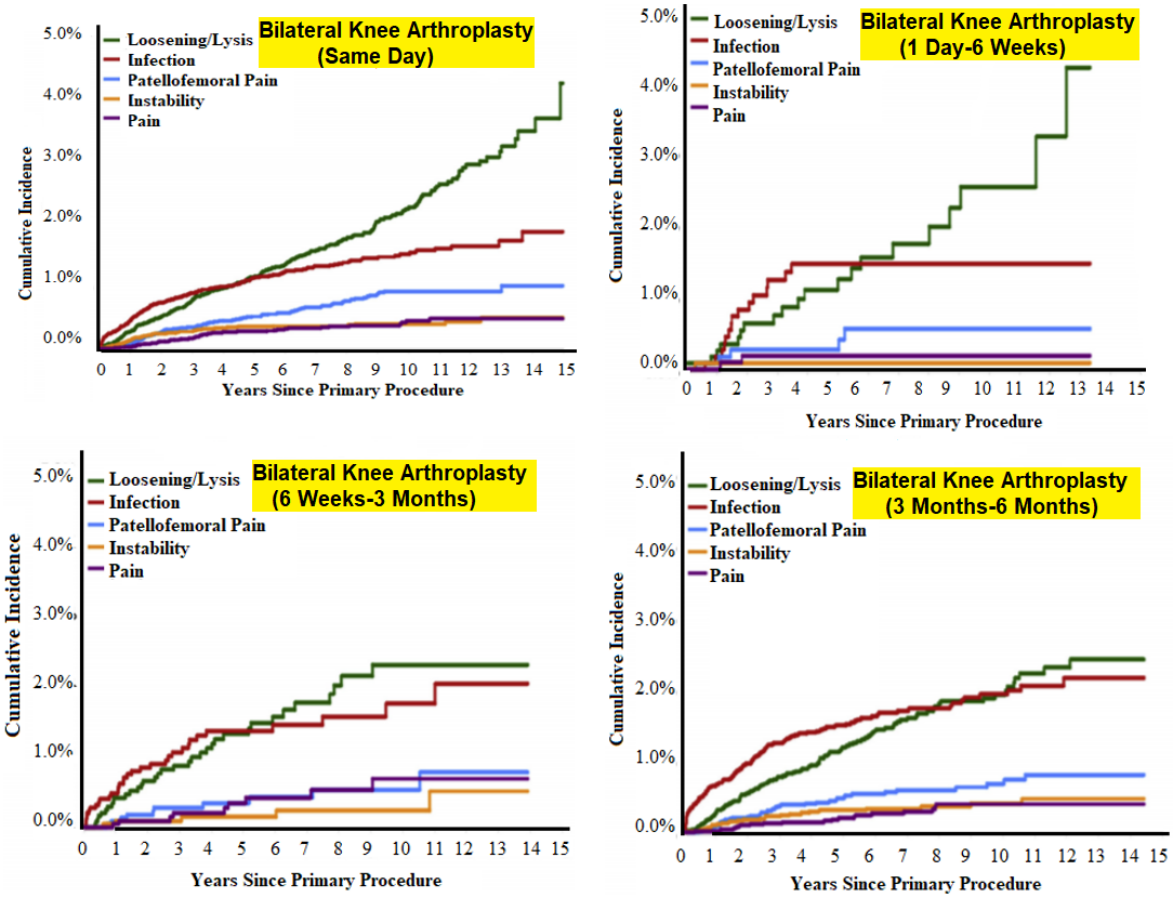

Figure 1.1: *Cumulative incidence revision diagnosis of primary total knee arthroplasty [5].*

Similarly in a study carried out using data from Australian Orthopaedic Association National Joint Replacement Registry for total knee arthoplast (TKO), data collected from September 1999 to December 2015, and it was found that the most common reasons for the revisions were loosening and infections. It can be seen in Figure 1.1) that the reason for the revisions in simultaneous as well as staged bilateral TKA groups were infections and loosening of implants [5]. Moreover no significant differences were found in the revision rates for loosening/lysis or infection when the 3 different staged interval groups were compared with the simultaneous bilateral TKA. Due to these reasons the development of innovative implants is necessary for more reliable applications [5]. Thermal sprayed, coatings presented here may be useful for a range of applications

from hard tissue fixation and soft tissue integration to the therapeutic ions delivery at the implant site for the promotion of osteogenesis, preventing infection or for the treatment of degenerative diseases. To anchor the load bearing implant with the host tissue, hydroxyapatite (HA) coating is usually applied for fixation. Particularly, hip replacement is fixated to the host tissue via the acetabular cup and the femoral stem and therefore the coatings are designed to be applied at these locations [6].

Bioactive and fully resorbable coatings have applications for a variety of orthopaedic implants and could be utilised to fix dental implants, bone fracture plates and cranial reconstructions. These coatings can stimulate cellular activity that results in enhanced human osteoblast cells attachment, proliferation and differentiation to regenerate bone [6].

Bioglass® (45S5) was the first bioactive glass developed by Hench et al. [7] containing 45 % SiO_2, 24.5 % Na_2O, 24.5 % CaO and 6.0 % P_2O_5 (wt %). Bioglass® makes a bond with the host tissue, undergoes specific surface reactions when incubated in simulated body fluid (SBF) [8] or implanted in human or animal body [9]. After implantation, a hydroxyapatite (HA) layer forms on the surface of the implant, which makes a strong bond with the host tissue [9]. In addition, bioactive glasses are osteoconductive (which means bone forms on the surface of the material), and release osteogenic ions (which stimulates bone formation cells) and therefore attracted much interest for bone tissue engineering [10]. These glasses can also be used for drugs delivery applications [11].

The network connectivity (NC) for 45S5 is 2.11 and is suitable for rapid bone regeneration. The NC is the mean number of bridging oxygen per silicon atom and is a predictor of the bioactivity and hence reactivity in the physiological fluid of the composition [12]. Although 45S5 is promising for coating, there are some limitations such as the higher bioactivity and biodegradability of 45S5, and coating deposited with this glass may degrade over time resulting in instability of the implant in the long term [13]. Later other silicate-based glasses were developed, which also had the ability to bond to bone tissue and enhance bone formation but with low solubility in

the physiological fluid in comparison to Bioglass®, such as ICIE16 (NC = 2.13) and 13-93 (NC = 2.58). The addition of more network modifiers such as K_2O and MgO is a way to adjust bioactive glasses' thermal, chemical and biological properties [14, 15].

Another family of biomaterials that is completely resorbable are Phosphate based glasses (PBGs); these glasses have attracted a lot of interest in the field of tissue engineering due to their controllable degradation profiles and chemical similarity with the inorganic component of bone [16, 17]. Fully resorbable coatings could potentially be advantageous for a variety of orthopaedic implants, such as bone fracture plates and dental implants. These coatings may promote cellular activity and can result in enhanced attachment, differentiation and proliferation of human osteoblast cells [6]. Implants have a potential risk of infection; thus, Bio-engineering researchers are developing solutions to avoid them. One of the possible strategies to prevent infections relies on doping of antibacterial agents such as Ag^+, Cu^{2+} and Zn^{2+} in the implant coatings [18–20]. The antibacterial effect of these materials could be explained by the electrical double layer theory [21]. The electrical double layer consists of a positive charge layer at the surface of the solid and a negative charge layer in the solution next to it (Figure 1.2).

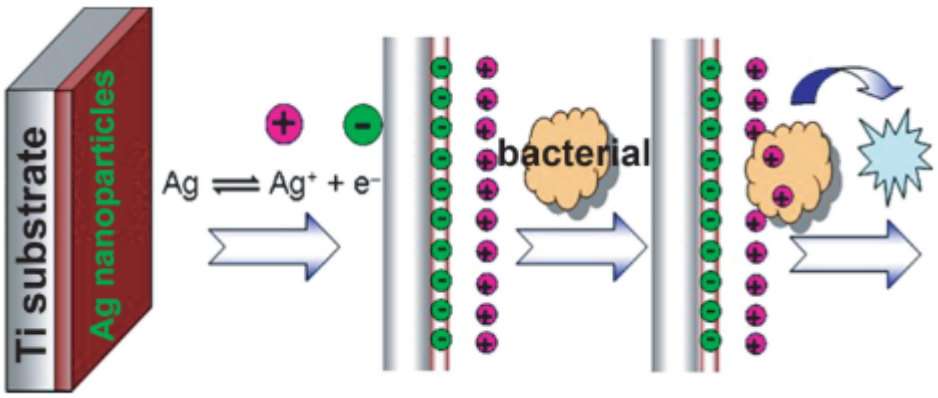

Figure 1.2: *Ti substrate coated with Ag nano particles showing the antibacterial mechanism of Ag ions [21].*

Due to the chemical similarity of Ga^{3+} (as bactericidal agent) to the Fe^{3+} ions (which is critical for the biological system), it can be used as Trojan horse, as the biological system cannot distinguish Ga^{3+} from Fe^{3+}. Ga^{3+} replaces Fe^{3+} in protein,

and that is the reason for its antibacterial properties [22]. Slow release of Ga^{3+} ions from a coating could be considered as the desired material for biomedical applications [20].

The thermal spray is a group of techniques that produce coated surfaces by melting and accelerating the particles onto a substrate. The thermal spray has existed for more than a hundred years; however, the research is still ongoing on how to control the properties of the coatings [23]. Air plasma spray (APS) and High velocity oxygen-fuel (HVOF) are the two techniques among the thermal spray processes which are widely used for powder processing [24]. APS utilises hot plasma to melt powder particles and carried on to a substrate via an inert carrier gas, while, for HVOF, the coatings are deposited utilising hot hypersonic gas. The jets produced due to the continuous fuel combustion, which melts and propels the particles to produce coating [25, 26]. Both these techniques are capable of producing coatings by processing nano sized particles; however, HVOF coatings appear to be superior to APS due to the defect contents of APS coatings [27].

The HVOF process is limited to use feedstock in the form of dry powder with a particle size of 5 μm, as with smaller particle size, the powder flow ability is affected [28, 29]. Nano or micro sized particles can be used as feedstock if these are agglomerated into granules of size > 5 μm [29–31]. However, coatings obtained from the thermal spray of large nanostructured granules consist of a non-uniform microstructure in which the outer layer has lost its nanostructure due to melting and re-solidification, while the non-molten core has some nano-sized particles remaining [32, 33]. To produce a homogeneous microstructure, each particle should be individually sprayed [33–35]. Using feedstock in the form of suspension is one of the approaches used to produce microstructured and nanostructured coatings using thermal spray [31, 32, 35, 36]. The emerging technology of Suspension high velocity oxy fuel (SHVOF) thermal spraying is a coating deposition technique with the key advantage of enabling processing of nano and micrometric particles in a suspension [28, 32, 37]. This process relies upon a modified HVOF torch to spray a stable suspension instead of powder feedstock [38]. It

has been shown that using a suspension as feedstock allows producing nano structured coatings with improved strength and durability [17, 18, 20, 21]. This process produces layers of flattened particles, resulting in a dense, thick microstructure coating with good cohesive and adhesive strength. This process has already been experimentally verified for bioactive coatings such as tri calcium phosphate, HA and Bioglass® [23–25].

1.2 Aims and Objectives

The primary aim of this study was to develop a comprehensive processing-microstructure-performance relationship for a range of biomedical coatings using the emerging suspension high velocity oxy-fuel (SHVOF) thermal spray. Coatings were deposited via SHVOF using bioactive glasses, Bioglass®, ICIE16 and 13-93 and PBG (P-40). Moreover, chemically mixed Ga_2O_3-Bioglass® was sprayed, and Ga_2O_3 and Bioglass® suspensions were co-sprayed via a hybrid nozzle to produce hybrid coatings with potential antibacterial properties.

The overall aim of the PhD was achieved using the following four interconnected objectives:

1. To manufacture Bioglass®, understand the effect of ball milling on powder size reduction and prepare a stable suspension. Produce Bioactive coatings onto metallic substrates with varying flame power (25, 50, 75 and 99 kW) and understand the effect of flame on the microstructure of the coatings. Characterise the coatings using advanced scanning electron microscopy (SEM), X-ray diffraction (XRD) and Raman spectroscopy. Study the response of these coatings in simulated body fluid (SBF) for potential end use applications.

2. Studying two more bioactive glass compositions namely ICIE16 and 13-93. Preparing their respective suspensions after size reduction and producing ICIE16 and 13-93 coatings at two flame powers of 50 and 75 kW. After basic characterisation of these coatings, comparing their behaviour in SBF i.e HA precipitation and

dissolution in SBF of these coatings after immersion in SBF. Moreover, testing biocompatibility of these coatings using MG63 cells.

3. Third objective was to study the resorbable PBG P-40, ball milling the glass and then making the suspension and coating at flame powers of 50 and 75 kW. Determining the microstructure of as-sprayed coatings and then the ion release study of P-40 coatings in milli-Q water via inductively coupled plasma mass spectroscopy, whilst, studying the mass degradation conducted in milli-Q water and phosphate buffered saline (PBS) solution.

4. The last objective was the production of two bioactive coatings (each at 50 kW) having Ga_2O_3 as antibacterial agent. Deposition of Ga_2O_3 doped Bioglass® suspension making one coating, while, making the other coating by co-spraying Ga_2O_3 and Bioglass® suspensions. Then determining the microstructure of the coatings, studying their bioactivity in SBF and determination of cytoxicity using MG63 cells.

1.3 Thesis Outline

This thesis has been divided into following chapters

- **Chapter 2**, reviews different generation of biomaterials, explaining bioactive and bioresorbable glasses, and different antibacterial ions incorporated in bioactive and bioresorbable glasses. Moreover, coatings for biomedical applications via SHVOF has been reviewed too. Summary of the literature has been made also reporting gaps in the literature.

- **Chapter 3**, presents the materials and methods used throughout this work.

- **Chapter 4**, discusses the deposition of Bioglass®, the optimisation of the spray parameters, the characterisation of the coatings, and their bioactivity through SBF and toxicity tests.

- **Chapter 5**, presents the deposition of ICIE16 and 13-93 bioactive glasses, the coating characterisation, the apatite forming ability and cell proliferation.
- **Chapter 6**, explains the deposition of P-40 glass, ion release and degradation profiles of the produced coatings.
- **Chapter 7**, presents the production of antimicrobial coatings (first coating produced by depositing Ga_2O_3 doped Bioglass® suspension and the second one was produced by depositing Ga_2O_3 and Bioglass® suspension via a hybrid nozzle) its characterisation, SBF tests, and toxicity tests.
- **Chapter 8**, concludes the findings of this work.
- **Chapter 9**, suggests the future work in this area.

Chapter 2

Literature Review

2.1 Introduction

This chapter focuses on the key concepts which illustrate the underpinning science of the work presented here, providing information behind the basis for the selection of the materials and the processes used in this work to produce coatings for biomedical applications.

Starting with different generations of Biomaterials, explaining bioactive glasses and PBGs and then their utilisation as coating for biomedical applications, this chapter also reviewed antibacterial species incorporating in bioactive or PBG, concluding with the Ga_2O_3 as antibacterial agent incorporating in bioactive glass for the purpose of an antibacterial and bioactive coating deposition on metallic implants.

2.2 Biomaterials

Materials which are employed in implants and medical devices are called biomaterials. These materials can perform predetermined functions when they interact with a biological system [2]. In particular, the main feature required for a biomaterial is biocompatibility. Biocompatible materials do not release ions in a concentration that is toxic for the human body, and must not trigger a foreign body response by the immune system which could lead to reactions such as inflammation and rejection of the implant

[39, 40]. Also allowing the material to perform the desired function and creating the appropriate favourable cellular response [40]. Biomaterials can be classified into three types based on their specific interaction with the human body. These are bioinert, bioactive and bioresorbable.

2.2.1 Bioinert Materials/Biotolerant

This first generation of biomaterials were designed to be as inert in the physiological environment as possible. These materials do not release toxic ions and the immune system does not cause a foreign body response after implantation. The main purpose of the bioinert materials was to avoid prosthesis rejection [41]. Ceramics such as alumina and zirconia, Ti and Cr-Co alloys in metals, polymers such as ultrahigh molecular weight polyethylene, are examples of bioinert materials. In the past, these materials have been frequently used and are still common in bone repair applications; however, these materials do not form any chemical or biological bond at the implant- host tissue interface which could lead to inflammatory reactions due to relative movements [42]. Due to these reasons, bioinert materials could be implanted successfully only if loaded under compression and with a close mechanical fitting [43]. The relative micro-movements can be overcome; some procedures such cementation have been developed which improves the adhesion between the host tissue and the implant by applying a polymeric or an inorganic cementing paste [44]. The interfacial adhesion between prosthesis and implant could be improved when the growing bone attaches to the surface irregularities of the implant. This can be further enhanced by increasing the surface area of the implant, this fixation of the implant with the host tissue is called 'morphological fixation'. When the bone grows in the pores of the implant, it also improves the adhesion of the implant with host bone and the method is called 'biological fixation' [43]; however, these methods of fixation do not generally improve survivability over cementation [43]. Also for biological fixation, the implant should be porous which may be mechanically inadequate.

2.2.2 Bioactive Materials

The second generation of biomaterials are those which facilitated bond formation at the interface between the host tissue and the implant by allowing hard tissue formation at the surface of the implant [45]. The first bioactive material was proposed by Professor Larry Hench for resolving the problem associated with implant rejection. The hypothesis for the development of bioactive materials was;

"The human body rejects metallic and synthetic polymeric materials by forming scar tissue because living tissues are not composed of such materials. Bone contains a hydrated calcium phosphate component, hydroxyapatite (HA) and therefore if a material is able to form a HA layer in vivo it may not be rejected by the body" [46].

When these materials are implanted in the body, they induce the formation of bond with the host tissue due to the development of dense carbonated hydroxyl apatite (HCA) layer on the surface and which is similar to the mineral component of the bone and therefore the implant is not perceived as foreign body [47]. Accordingly, the implant is not covered with a fibrous tissue as happens with bioinert materials and also the surface directly bonds to the new host tissue. The direct bonding of the surface to the host tissue, results in strong adhesion between the implant and host tissue which reduces the problems associated with the micro-movements [43]. After few (3-6) months of implantation, the bond between the host tissue and bioactive material reaches to the strength comparable to the of the host bone; this is called 'bioactive fixation' [43]. Moreover, some bioactive materials can make a bond with the collagen of soft tissue [46]. Bioactivity of these materials is measured in terms of 'index of bioactivity (Ib)', which relates bioactivity with the time required for 50% of bonded interface ($t_{0.5bb}$) [48], and is given as

$$Ib = \frac{100}{t_{0.5\mathrm{bb}}} \tag{2.1}$$

Bioactive glasses possess the highest bioactivity index (6-12), and glasses with bioactivity index greater than 8 make a bond with the soft tissue as well [49]. This bonding to bone behaviour was first demonstrated for a range of bioactive glasses that were

composed of SiO_2, NaO_2, CaO and P_2O_5 in specific proportions. The important compositional features of these glasses were that it had < 60 mol % SiO_2, high content of CaO and NaO_2 and high ratio of CaO to P_2O_5. These features make the glass highly reactive when in exposed to an aqoues medium, such as physiological fluid [49].

A compositional diagram SiO_2–Na_2O–CaO system is shown in Figure 2.1, the effect of composition on the bioactivity of these glasses can be seen and hence the bonding ability of different compositions. Composition in region A bonds to bone, region B are container and window glasses which are bioinert, and their implantation would result in a fibrous tissue formation around the implant. This behaviour is due to the very dense silica network of the glass, which makes it resistant to dissolution in the body fluid. While, region D composition is not feasible due to very low silica content and due which glass network cannot form or crystals form [42], whereas E is the composition of Bioglass® (45S5) [50].

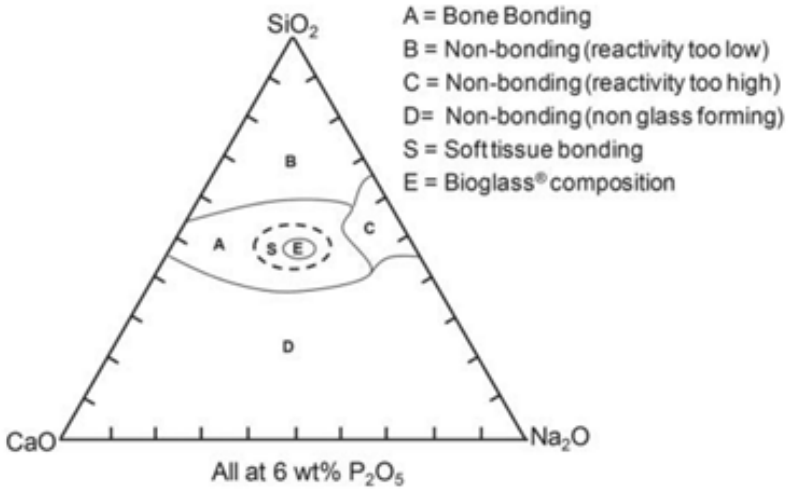

Figure 2.1: *Bioactive Glasses and Glass ceramics, bioactivity dependency on composition, where A/W is for apatite-wollastonite. In region A P_2O_5 is 6 wt % [42].*

2.2.2.1 Bioglass® (45S5)

Bioglass which is also known as 45S5, is a soda lime phospho silicate glass. This glass becomes reactive in a physiological environment and consists of SiO_2 network (Figure 2.2 A) with other components such as CaO, Na_2O and P_2O_5 as network modifier (2.2 B) [50]. In the formulation of 45S5 is 45 wt % SiO_2, 24.5 wt % Na_2O, 24.5 wt % CaO

and 6 wt % P_2O_5, and so the name is 45 % SiO_2 and Ca/P ratio 5 [49]. Bioglass is the first known bioactive glass discovered by professor L.L. Hench [42, 43] and that has the highest bioactivity index (12.5) in the family of bioactive materials [43]. This finding led to a revolution in the world of prosthetic materials.

Dissolution in the body fluid of different glass composition depends on the connectivity of the silicate network. A glass is more durable if it contains a large proportion of bridging oxygen bonds. Bridging oxygen bond is silica tetrahedra covalently bonded to other silica tetrahedra via –O-Si-O bonds. Network connectivity is directly proportional to silica content, due to this reason melt derived glasses with more than 60 mol % silica are not bioactive [50].

Bioactivity of a material can be assessed by using simulated body fluid (SBF). SBF is an acellular solution with an ionic concentration similar to blood plasma. Tests are carried out by immersing sample in SBF in a fixed volume for a specific time period in a controlled environment [8]. This test is based on Hench's hypothesis about the development of HA on the surface of the material while in a physiological environment, which led to the formation of bioactive glasses. The development of HA on the surface of biomaterial in SBF is the verification of its bioactivity [8]. The significance of SBF test is still under debate due to the limitation of their inability to verification of antibodies reactions; however, SBF tests are the preliminary way for the determination of potential bioactivity [51].

As supposed by Hench, a material is bioactive if it can form a surface layer of HA [46]. In total 11 steps are involved in the mechanism of HA layer formation and consequently bonding with the living tissue [43]. The first 5 steps consist of ionic reactions between the glass and the physiological fluid, while the subsequent steps are of the cellular level. This mechanism is described in Table 2.1. Theoretically bioactivity of these glasses can be predicted from their composition. In these glasses SiO_2 acts as a network former.

Table 2.1: *Reaction of Bioactive Glass with the surrounding tissue and bone formation with time [43].*

LogT (Hrs)	**Surface Reactions Stages**	
—	1 and 2	Na^+ exchange with H^+ leads to the formation of silanol group (Si-OH), Network Dissolution: Formation of SiOH groups and release of $Si(OH)_4$
1	3	Polycondensation of silanol groups
	4	Formation of amorphous $CaO\text{-}P_2O_5$
2	5	HCA Crystallisation
3	6	Biological moties adsorption in HCA layer
4	7	Macrophages Action
5	8	Stem cells attachment
6	9	Osteoblast differentiation and proliferation
7	10	Generation of matrix
8	11	Crystallisation of Matrix

Bioglass and other bioactive glasses can be made by two methods, melt quench and sol-gel. In the melt-quenched oxide are melted at high temperature (>1300 °C) in a platinum (95 wt % platinum and 5 wt % gold crucible [12], and platinum-rhodium crucible [52, 53]) and quenched in a mould of graphite or steel or quenched in water. The sol-gel is a comparatively low temperature processing method where the precursors in the form of solution (sol) convert to a gel after a polymeric reaction at room temperature [54]. Gel is three-dimensional skeleton network surrounded by a liquid phase. Both of the phases are continuing with nanometric dimension. Gelation of the solution is achieved by hydrolysis and condensation in 48 hrs. Gel is then converted to glass after drying and heating at high temperature fro 3-6 hrs, such as 600 °C [53, 55]. Via sol-gel technique, bioactive glasses can be made that are either mesoporous or nanoparticles simply applying different catalyst while making the sol [55]. With

sol-gel, bioactive glasses can be made with wider composition, which is not possible with the conventional melt-quenched. This is due to their structure which results from the condensation of Si–OH bonds in solution. This process spontaneously occurs in the physiological environment and sol-gel glasses assumes an appropriate structure for the promotion of HCA formation in biological environment [2]. However, the sol-gel glass may degrade too rapidly in some application where longer regeneration time is required [56].

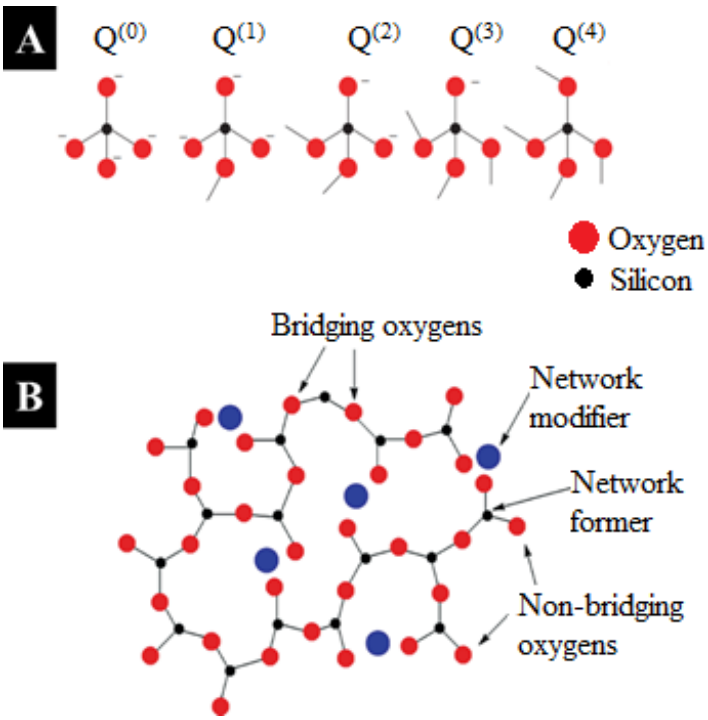

Figure 2.2: *(A) Silica tetrahedral of silicate glasses, (B) random glass network of network formers and modifiers [53].*

The bioactivity of Bioglass and other bioactive glasses can be predicated theoretically from the network connectivity, which is given as follows

$$NC = 2 + \frac{BO - NBO}{G} \tag{2.2}$$

Where BO represents the total mol % of oxides that can form bridging oxygen per network forming ions, NBO is the total mol % of oxides that form non-bridging oxygen and G is the mol % of glass forming units within the network [50]. NC of Bioglass is 1.90 if P is assumed to enter in the silicate network by forming P–O–Si bonds. However,

in the melt derived glass phosphate forms Q^0 $[PO_4]^{3-}$ units instead of becoming a part of silicate network. This phosphate complex requires three positive charges to balance its own charge [57]. Due to this reason, the modified NC of 45S5 is 2.11 [15]. Glasses with NC greater than 2.40 are not likely to be bioactive, as can be seen in Figure 2.3 that with NC greater than 2, the rate of deposition of HCA layer decreases quickly [50].

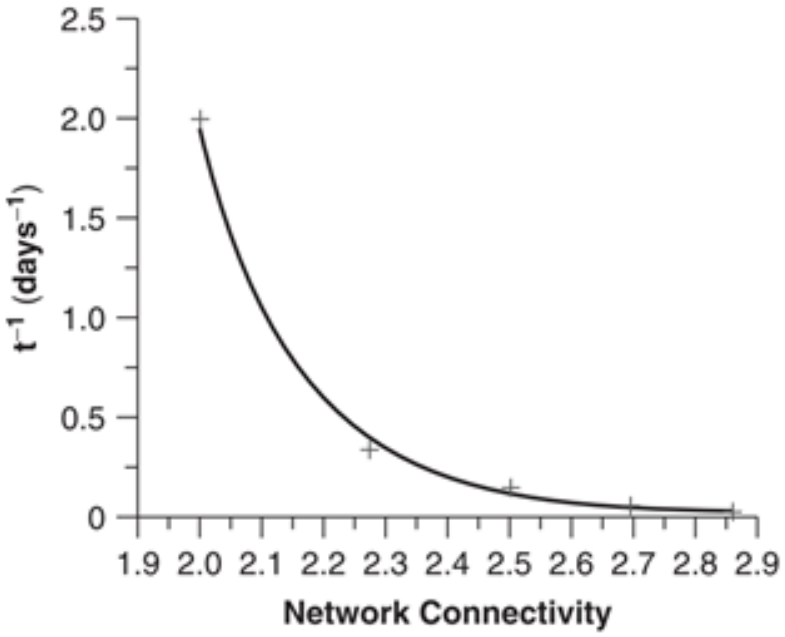

Figure 2.3: *NC affects HCA formation on SiO_2–CaO–Na_2O glass discs in simulated body fluid (SBF) [50, 58].*

Other properties such as crystallisation tendency can be predicated from NC of the glasses. Such as the glasses with NC > 2 generally have high energy barrier to overcome for crystallisation in comparison to the glasses with NC < 2 [50]. Crystallisation temperature (Tc) of Bioglass® (45S5) is 677 °C while its glass transition temperature is (Tg) is 538 °C. The thermal processing window (Tc-Tg) of this glass is 130 °C [50], which is narrow for sintering purposes [15, 56].

The first Bioglass based implant was used in the USA to replace the small bone in the middle ear for the treatment of conductive hearing losses [59]. This device was approved by FDA in 1985 with a commercial name of "Bioglass® Ossicular Reconstruction Prosthesis", also known as "Middle Ear Prosthesis" MEP®. This implant

consisted of a truncated nonporous cone made of 45S5 produced by the melt-quench method. Sound was conducted through this implant from the ear drum to cochlea. The implant was firmly bonded at both the ends to the living tissues due to the ability of Bioglass to bond with hard as well as soft tissue (eardrum) [60]. Better performance was observed for short term and midterm application of the MEP® than the inert implants made of alumina; however, long-term clinical study with a follow-up of 10 years showed that Bioglass was liable to progressive dissolution. Also, bioglass was fragmented in the biological environment of middle ear [45, 61]. Due to these reasons, MEP® were taken from the US market in the early 2000s. However, in some European countries, a modified version of MEP® (Douek-MEDTM) which 45S5 Bioglass® cones of three different sizes, is still commercially available [45]. Similarly, Bioglass®-EPI (extracochlear percutaneous implant) was commercialised; however, this was taken off the market in late 1990s due to the risks associated with the dissolution of 45S5 with time.

In powder form 45S5 has been used to repair bone defects in jaw and orthopaedics, called 'NovaBone®' (NovaBone Products LLC, Alachua, FL) with a particle size range of 90–710 μm [62]. While using Novabone®, surgeons mix it with the patient's blood or balanced salt solution to acquire mouldable consistency. The resultant putty can then be pressed into defects as its shape and size [45]. In a comparative study carried out by Brice Ilharreborde et al. while using NovaBone® putty and Iliac crest autograft revealed less infection (2 %) and mechanical failures (2 %) for NovaBone® in comparison to Iliac crest autograft (5% and 7.5 % respectively) over four years follow up [59]. Biogran® (Biomet 3i, Palm Beach Gardens, FL, USA) is another bioactive glass product with a particle size range of 300–360 μm. Biogran is mainly used in maxillofacial and dental applications to repair of defects in the jaw bone [63]. 45S5 has also been commercialised as a sintered porous block; however, the working window of Biogalss is small (130 °C) and devitrification occurs while sintering it which adversely affects its bioactivity [64]. Novamin® (Technology, FL, USA) is another 45S5 Bioglass based product in the form of very fine powder (average particle size 18 μm). This new prod-

uct has been owned by GlaxoSmithKline, Brentford, UK, and added to toothpaste for treating tooth hypersensitivity [65–67]. Dentinal tubules occlusion and tooth surface mineralisation are done by Novamin® and so eliminates the origin of disease [68].

2.2.2.2 Alternative Bioactive Glass Formulations

After the discovery of Bioglass (45S5) by Hench, a large number of silicate-based bioactive glasses have been developed which show excellent bone-bonding properties [69]. As glass is a random arrangement of units, so a large number of therapeutic ions can be incorporated in the chemistry without significantly changing its properties. As mentioned earlier, the processing window of 45S5 is low (130 °C), and thus crystallises when heated at higher temperature than Tg. Crystallisation presents a problem if sintering of the glass particles is required to make a scaffold or coating a metal implant with it [50]. Another drawback of the coating metals with Bioglass (45S5) is the mismatch between thermal expansion coefficients (TEC) of the substrate and 45S5. Ideally, the TEC of 45S5 should be similar to that of the substrate so that upon cooling after thermal processing, the glass would not pull away from the substrate [70]. Such as TEC of 45S5 is 15×10^{-6} °C^{-1} and that of Ti alloys about 9×10^{-6} °C^{-1} which are commonly used to fabricate orthopaedic and dental implants [13, 45]. So it was needed to develop new bioactive glass formulations with a TEC more suitable for coating purposes on metals. Bioactive glasses in the system of SiO_2-CaO-MgO-Na_2O-K_2O-P_2O_5 have been extensively explored to match TEC of Ti6Al4V alloy [70–72]. Partially replacing Na_2O and CaO with K_2O and MgO was the common strategy to design and adjust the TEC of the bioactive glass in a controlled way [72] [39]. Addition of B_2O_3 is also a way to decrease TEC; however borosilicate silicate glasses shows higher dissolution in aqueous media and physiological fluid than the silicate glasses [73].

2.2.2.2.1 ICIE16 Bioactive Glass: ICIE16 is a bioactive glass with a modified composition of 49.46 % SiO_2, 36.27 wt % CaO, 6.6 wt % Na_2O, 1.07 wt % P_2O_5 and 6.6 wt % K_2O, in mole %. Many of the physical properties such as Tg and solubility are related to the alkali metal content present in the glass. Incorporation of second alkali

metal oxide in oxide glass results in a marked deviation in its transport properties such as viscosity, ionic conductivity, diffusivity of network modifying ions. This phenomenon is known as 'mixed alkali effect (MAE)'. Due to the addition of second alkali oxide glass can be made at lower temperature [14]. Also, the problem associated with the high solubility of bioactive glasses can be overcome with this addition. MAE in bioactive glasses could be used to tailor their physical and biological properties [14].

Incorporation of K_2O into bioactive glasses has primarily been to manipulate the processing window. It acts as a network modifier, distorting the glass network reducing the melting temperature, and improving the durability of the glass with controlled dissolution characteristics. Salam et al. showed that substituting K_2O for Na_2O resulted in high Tc [74] by increasing of disorder within the system due to MAE [75]. The increment in the disorder of the glass system is due to the higher ionic radius of K^+ than Na^+ and less ionic field strength of K^+ than Na^+. Thus the addition of K_2O reduces the overall strength of the silicate network through the formation of Si-O-K^+ bonds resulting in reduced viscosity of the glass [76]. However, with the addition of K_2O, bioactivity was reduced in terms of delayed apatite layer formation [77]. Due to MAE the glass processing window of ICIE16 has increased to 180 °C, which was 130 °C for 45S5 composition [77]. Also, the TEC of this glass is 15.3 x 10^{-6} K^{-1} while for 45S5 TEC is 15.75 x 10^{-6} K^{-1} [77, 78]. However, ICIE16 composition is closer to 45S5 (as can be seen in Figure 1) and its NC is the same as of 45S5 (2.11) [15, 77], and is proved to be bioactive [15]. Also, the work done by Nomm et al. showed that this glass was non− toxic and the scaffold made of ICIE16 supported bone in−growth within a femoral head defect in a rabbit model [15].

2.2.2.2.2 13-93 Bioactive Glass: 13-93 is a bioactive silicate glass based on 45S5 composition; however, it has comparatively higher silica content and additional network modifiers such as K_2O and MgO (53.0 wt % SiO_2, 6.0 wt % Na_2O, 20.0 wt % CaO, 12.0 wt % K_2O, 5.0 wt % MgO and 4.0 wt % P_2O_5) [10, 79]. 13-93 has been approved for in vivo use in Europe [80], also approved for in vivo use by the US Food and Drug Administration [81]. Due to the better processing window (300 °C [82]) of 13-93, it can

be pulled in fibres more easily than 45S5 which is due to its better viscous flow [83, 84]. Also, 13-93 is the most common glass used for making dense 3D scaffolds without crystallisation [10, 15]. Another advantage of 13-93 bioactive glass is that it can be coated on metallic implants with better (than 45S5 coating) adhesion between coating the substrate as its TEC is lowest 12.4 x 10^{-6} K^{-1} in comparison to other bioactive glasses such as ICIE16 and 45S5 as investigated by F.Dohler et al. [78]. The reason for the lower TEC is the low concentration of network modifier, high silica content and high NC [78]; however, due to high silica content (53.0 wt. %), high network connectivity (2.6 [77]) and presence of a high amount of MgO glass is less vulnerable to dissolution and hence reduced bioactivity in terms of HA formation [85, 86]. In vitro tests showed proliferation and differentiated function of osteoblastic MC3T3- E1 or MLO-A5 cells on 13-93 dense disks similar to 45S5 [87]. Fu. Qaing et al. evaluated in vivo 13-93 bioactive glass scaffolds with trabecular and columnar microstructures seeded and unseeded with stem cells (MSCs) in a subcutaneous rat implantation model. They found that seeded scaffolds showed better integration with the surrounding tissue as the scaffolds were surrounded by a band of fibrovascular tissue (100–300 μm thick). Bone like tissue was also noticed in the seeded samples and the authors concluded that 13-93 scaffolds could be used for bone regeneration and integration [9].

Role of magnesium in the glass is under debate in the literature. As investigated by Watts et al. for particular glass compositions, of the total added Mg^{2+}, 86.0 % of Mg^{2+} acts as network modifier, while 16.0 % as a network former [86]. However, in the literature, mixed reports are present for the role of magnesium in glass that it can act as network former or modifier and this also depends on its content present in the glass composition [88]. Addition of MgO is also beneficial as its presence causes a decrease in the glass Tg and an increase in Tc, thus widening the processing window of the glass [10, 86]. On the other hand, the presence of Mg has detrimental effects on the bioactivity of bioactive glasses as it retards apatite formation during bioactivity tests (SBF) [88–90]. However, Vallet. Regi et al, demonstrated that the rate of apatite formation would be slow if the MgO content in a bioactive glass was more than 7 mole

% [90]. It suggests that magnesium can slow down apatite crystal growth; however, it is a cofactor in a number of enzymes necessary for the bone health [89], as indicated by Ferreira et al. that bioactive glasses incorporating MgO are suitable for osteoblast like cell proliferation [91]

2.2.3 Bioresorbable Materials

The third generation of bio-materials is the 'Bioresorbable materials', which gradually dissolve in the body whilst being replaced by the new living tissue that replace the implant material completely [92]. Resorbable materials could be the optimal solution for the bone implants as living tissues can repair and replace throughout life. Also the problem associated with the long term stability could be overcome as the implant itself is gradually replaced by the living tissue [92, 93]. Disadvantage of these materials is their mechanical performance required for the substitution time, when the living tissues are regenerating while the implant materials is already being dissolved. Moreover rate of tissue regeneration must match with the degradation rate of these materials. The resorption rate of the implant material can be tailored using several methods such as doping, or the adjustment of the geometry (interconnected pores) of the bioreorbable device [92]. Also, the dissolution product of these materials must be tolerable by the human metabolism. Due to this reason resorbable materials are doped with ions which can induce genetic stimulation and tissue can heal naturally [94, 95].

Resorbable polymers such as poly (lactic-acid) and poly (glycolic-acid) are used in clinical practice (are employed for the sutures). These materials metabolise to CO_2 and H_2O after withstanding an appropriate time [93]. Ceramics such as tricalcium phosphate could be used as resorbable material in particulate form or porous devices. However, these materials are not able to withstand mechanical stresses while resorbing [96].

2.2.3.1 Phosphate Based Glasses:

Phosphate based glasses (PBG) consists of phosphate as the glass network former. For example, calcium phosphate glasses can have a composition similar to the mineral part of the bone (HCA), that is biological calcium phosphate [97]. These glasses are fully resorbable in aqueous media whilst realising a custom array of ionic constituents which activate the cellular response in a controlled manner and thus could be desirable for potential biomedical applications [17, 98–100]. Backbone of PBG is the PO_4^{3-} tetrahedra [101], while CaO and Na_2O act as network modifier [99]. These glasses can be doped with other metal oxides such as Mg [99, 102], Ca [103, 104], Sr [101, 105] , F [106] which have been investigated for tissue regeneration, Ti [107, 108], Fe [109], for durability, Ag [110, 111], Cu [112] and Ga for their antibacterial properties [113].

PBGs are made by the conventional melt-quench method, e.g. mixing the glass precursors (phosphates, oxides and carbonates in powder form; also phosphoric acid could be used as a phosphate source) and then melting this mixture at high temperature in Pt crucible. Melting temperatures of PBG are comparatively lower than bioactive silicate glasses and usually are in the range of 800-1300 °C [97]. In order to reduce stresses in the glass, the melt is poured into preheated graphite or metal moulds and placed into a furnace preheated to Tg of the glass and annealed (slow cooling to room temperature) [97] . PBG can also be made by a sol-gel process too, however, the sol-gel phosphate glasses are more fragile than bioactive silicate glasses and are very soluble [97, 114].

Similar to silicate glasses, PBGs show short-range order and do not have significant symmetry of atomic arrangement [97]. The basic network former in PBG is the orthophosphate tetrahedron (PO_4^{3-}) (Figure 2.4) [101]. In the glass structure, phosphate tetrahedra bond the bridging oxygen to the phosphorus atom and the tetrahedron forms P-O-P bonds with the adjacent tetrahedron [115] . Hoppe et al. investigated by Neutron diffraction experiments that within the PO_4 unit two bonds of different lengths existed, i.e., one bond is of the phosphorus with the terminal oxygen atom and other with the bridging oxygen atom [116]. The presence of terminal oxygen in

phosphate anions reduces the NC of PBG in comparison to silicate glasses [117]. The structure of PBGs are usually defined by the number of BO, which is represented by Q^n (where 'n' represents the number of bridging oxygen per tetrahedron as can be seen in Figure 2.5). So, the structure of PBG can be produced in 3D cross-linked Q^3 tetrahedra (ultra-phosphate), chain-like Q^2 structure (meta-phosphate), invert Q^1 (pyro-phosphate) and Q^0 ortho-phosphate structure [118]. The 3D network of P_2O_5 is very unstable due to its hygroscopic nature. P-OH bonds can form due to the presence of moisture in glass composition (or moisture from the atmosphere) and which can cause de-polymerisation. Moisture can also affect chain lengths in meta-phosphate glasses which results in shorter phosphate chains. With the decrease of chain lengths these glasses are resistant to water attack and the subsequent scission, and that's why the glass becomes more stable when exposed to the humid environment [97].

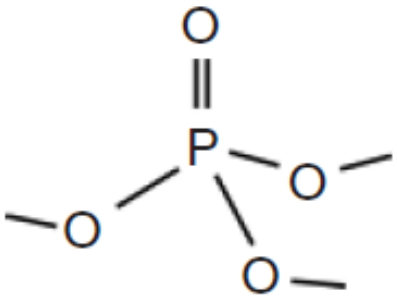

Figure 2.4: *Phosphate tetrahedron in PBG structure [97].*

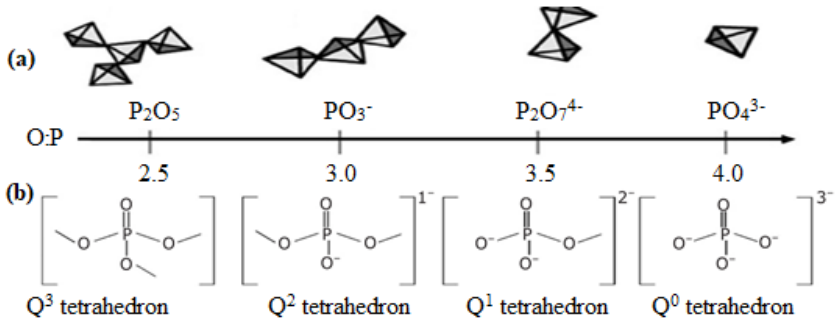

Figure 2.5: *In figure (a) shows phosphate tetrahedra with O:P ratios (b) shows the Q^n species [113].*

PBG network can also be depolymerised by the addition of alkali and alkaline metal ions (M), which breaks the bridging oxygen P-O-P bonds and creates more

terminal oxygen (P-O-M) and making the glass stable [115]. Chemical durability and other properties of PBG such as crystallisation tendency and mechanical characteristics depend on the P_2O_5 content as well as the charge to size ratio of the network modifiers [97]. Incorporation of metallic ions with small ionic radii with high electrical charges is known to form strong P-O-M bonds. The consequence of these bonds can be high resistance to hydration. Such as the addition of Fe_2O_3 and TiO_2 have been shown to significantly decrease the dissolution rate of PBG [109, 119]. These positive ions make the glass network strong via cross-linking between two NBOs. An increase in charge-to- size ratio results in stronger cross-linking. Due to this fact, the cross-linking would be expected to increase in the order of $Na^+ \rightarrow Ca^{2+} \rightarrow Fe^{3+} \rightarrow Ti^{4+}$ [97]. Similarly, for cations of the same charge but with decreasing ionic radii the cross-linking would be increased in the order of $Ba^{2+} \rightarrow Sr^{2+} \rightarrow Ca^{2+} \rightarrow Mg^{2+}$ [97].

2.2.3.2 Dissolution of PBG:

Deionised water (deiH_2O) and distilled water have been used to conduct the degradation studies of PBG [97, 107, 118, 120, 121]. To mimic conditions within the body, in vitro media such as SBF, Simulated Urine (SU), and Phosphate Buffered Saline (PBS) have also been used for dissolution [8, 111]. As said earlier, SBF mimics ionic concentration and chemical composition of human blood plasma [8]. Ionic concentration and chemical composition of SU is similar to human urine [111], whilst PBS buffers the solution to recreate the pH conditions within the body [122, 123]. Degradation of PBG is also highly dependent on the pH of the media, with increased degradation at lower pH as investigated by Bunker et al [122]. Similar to the physiological pH within the body, PBS buffers to a pH of 7.40 at 37 °C. That is why PBS has been the media of choice to observe the in vitro dissolution kinetics of degradable polymers and PBG [121, 124]. Melt quenched PBG degradation mechanism is well understood. The dissolution rates of PBG have been shown to vary by orders of magnitude as a consequence of changes in glass compositions. In aqueous solution, PBG degrades by reacting with H_2O molecules which de-polymerise the network by breaking P-O-P bonds [120, 122].

For the glasses containing monovalent ions such Na^+, the degradation process consists of three stages. Acid/base reaction is the first stage during which the glass surface becomes saturated with acid H^+ ions or base OH^- ions. This reaction increases linearly with time until no more uptake is possible (Figure 2.6) [120, 122]. H_2O molecules then diffuse in the network hydrating it, which results in the degradation profile of $t^{\frac{1}{2}}$ [122]. The third phase is the linear dissolution and is the hydrolysis reaction upon which the polymeric chains disentangle and separate completely as described by Bunker et al. [122].

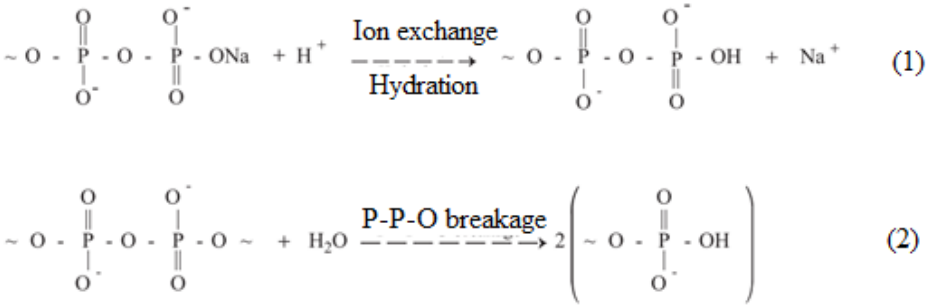

Figure 2.6: *Acid/base reaction leading to hydration and chain hydrolysis [120].*

In both dissolution phases ($t^{\frac{1}{2}}$ and linear) were uniform for the alkali ions present rather than the pre-selective leaching of certain elements and therefore throughout the degradation, the stoichiometry remained constant. Degradation is pH dependent, such that in various solutions degradation may be increased up to 100 times [122].

Post-degradation, the solution was saturated with Ca and P ions and no glass structure remained [122]. Haque et al. investigated the dissolution of 40-P_2O_5 24-MgO 16-CaO 16-Na_2O 4-Fe_2O_3 mol % fibres in dH_2O. Following 8 hrs degradation in water, they found that the glass fibres were peeling off and described this as a form of pitting corrosion [125]. Similar flaking around the boron-containing PBG fibres was found while degrading in PBS by Sharmin et al. [124]. Similar peeling effect of Fe containing PBG fibres was reported by Abou Neel et al. [109]. It was suggested that this peeling effect in fibres was due to the differential hydration at the surface and bulk layers, which led to the tensile forces and resulted in cracking [125, 126].

The effects of structural changes in controlling degradation rates have been explored by comparing various PBG compositions [127, 128]. Parsons et al. concluded that there was no significant correlation between the phosphate content and the glass degradation and thermal properties; however, the effects of di- and trivalent metals content on these properties were significant. Authors attributed the overriding cause of changes in glass properties to the cross-linking of the glass structure by di- and tri-valent metals than the state of the phosphate chain backbone. In addition, results presented suggested that with the increase of these metals content, density and Tg of glass increased while degradation rates decreased [127, 128]. Islam et al. reported that with varying MgO content in the glass composition $40P_2O_5$-(40-x)CaO-xMgO-(20-y)Na_2O-yTiO_2 (where $0 \leq x \leq 24$ and $y = 0$ or 1) the degradation rate also varied such that degradation rate decreased with an increase of MgO content [99]. Stuart et al. investigated the degradation of PBG, namely P40 ($40P_2O_5$-24MgO-16CaO-16Na_2O-4Fe_2O_3) in dH_2O and PBS and found that the glass exhibited a linear degradation profile over 83-days test period in both media. However, in dH_2O degradation occurred 1.38 times faster than in PBS which could be due to the pH of the two media, as during tests pH of dH_2O was in the range of 6.77 - 7.02 and for PBS was 7.27 - 7.40 [129].

2.2.4 Biomaterials Containing Antimicrobial Ions

Infections are the most serious and common cause of postoperative complications in patients surgically treated with implants. Implants related infections are generally difficult to cure and have a larger adverse impact on the quality of life [130–132]. Implants can become colonised by bacteria at the time of surgery or through haematogenous route from a distant source [133]. These infections are due to the highly adaptive ability of bacteria to colonise the surface of the implant or of adjacent damaged tissue cells [134]. Mostly implant surfaces are physiochemically active and control cellular adhesion, integration and inflammatory responses [135]. Moreover, the host extracellular matrix proteins such as fibronectin, fibrinogen, elastin and collagen adsorb by implant surfaces and hence provide receptor locations for bacterial adhesion [134–136]. Sev-

eral bacterial species have adhesins that facilitate cell anchorage and binding to host extracellular proteins [137]. Such as Staphylococcus aureus has distinct binding sites for extracellular matrix proteins (collagen and fibronectin). This family of adhesins facilitate adhesion to implants as well as bone matrix [136].

Mostly the isolates from the infected implant surfaces are Gram positive S. aureus and Staphylococcus epidermidis. Additional isolated microbes include Escherichia coli, Pseudomonas aeruginosa, Proteus mirabilis and beta haemolytic Streptococcus [134, 138]. However, a large proportion of these infections are due to S. aureus and S. epidermidis as infections occur due to other microbes represent small percentage of approximately 22.0 % [137]. The alarming level of antibiotic resistance of S. aureus is the reason of the most infections produced by this specie. As four out of five strains resist penicillin drugs, while four out of ten strains do not respond to methicillin/oxacillin [137]. Also S. aureus can form biofilms on implant surfaces where bacteria can continue in a low metabolic and stationary growth phase. In these biofilm, they resist the action of host immune system and antibiotics [139]. Antibiotics general toxicity (with associated liver and renal complications) and resistance, demonstrated antibiotics ineffectiveness in the prevention of implant-related infections [110].

Due to the onset of antibiotic resistance in many bacterial strains, innovative therapeutic strategies are being sought out [110]. Bioactive glasses could be the ideal material for implants as they not only promote regeneration of living tissue but they also have been shown to exhibit antibacterial activity. Furthermore, these glasses could be used for sustained delivery of antibacterial ions to the local microenvironment [140, 141]. The antibacterial effect of these glasses is due to the increase of the local pH because of the leaching of ions when these are implanted in the body. The elevated pH alters the pH gradient of the cytoplasmic membrane of bacterial cells (and the function of which is the movement nutrients in to the cells). As a result of this high pH cytoplasmic membrane is compromised, and eventually, cells die [142]. Second theory about the bactericidal effects of bioactive glasses is that the OH^- ions can react with the fatty acid present in the membrane and form free lipid radicals that weaken the

membrane and causing it to collapse [142]; however, these effects were found to kill certain oral bacteria [143] and skin pathogen [144]. Hu et al. investigated the effect of pH on killing bacteria. The media used by the author had a pH of 7.0 with a bactericidal percentage lower than 10. With the addition of 50 mg/ml of 45S5 particles, pH was increased to 9.8, and the bactericidal percentages for S. aureus, S. epidermidis and E. coli increased up to 98.0 % [144]. On the contrary, Bellantone et al. demonstrated that the bioactive glasses are not antibacterial as the authors did not find any significant difference between the mean cell viabilities of the control cultures and for the 45S5 containing cultures when tested against S. aureus, S. epidermidis and E. coli [145]. Stoor et al. reported that bioactive glasses are not antibacterial and could only be subject to bacterial adhesion [146]. Although, bioactive glasses have been found to have bactericidal effects on a range of pathogenic bacteria in vitro, adding antibacterial ions in the glass system have also demonstrated bactericidal effects. Research has been done by developing bioactive glass doped with Ag^{+} ions and have shown promising results [18, 145]. Cu^{2+} ions doped PBG have also been proved to be antibacterial [19, 112]. Similarly, Zn^{2+} has been shown to inhibit biofilm formation from several Gram-positive and negative bacteria when used in micromolar concentration [20]. However, recently bioactive glasses containing Ga^{3+} attracted more attention due its bactericidal and chemotherapeutic properties [20, 147].

Ga^{3+} ion chemical properties are similar to those of Fe^{3+} ion, such as ionic radius [20], and can be used as Trojan horse as many of the biological systems cannot distinguish Ga^{3+} from Fe^{3+}. The oxidation and reduction of Fe^{3+} is critical for of biological systems so supplementation of Ga^{3+} can disrupt these Fe^{3+} processes by incorporated into enzymes and as Ga^{3+} cannot be reduced under physiological conditions, this disrupts enzymatic action and leads to cell death [22]. The ability of Ga^{3+} to replace Fe^{3+} in proteins makes it antimicrobial. Chemically durable materials which can release gallium slowly would be considered the desired materials for medical applications. Ga^{3+} has been previously incorporated in phosphate-based glasses (PBG) for controlled antibacterial effect [148]. Wren et al. and Towler et al. doped bioactive

glasses with gallium for bone cementation and antibacterial functionality [124], and the results presented suggest that the glasses were bioactive [149, 150].

The toxic limit of Ga^{3+} in the blood is 14 ppm [151], and the amount of gallium incorporated in materials should be balanced to avoid cytotoxicity and have antimicrobial effects. Frachini et al. incorporated Ga_2O_3 in 45S5 in the range of 1.0 - 3.5 mol % and observed that the glass having Ga_2O_3 1.0 mol % and 1.6 mol % behaved in the same way as the 45S5 glass composition in SBF; however, the glass having 3.5 mol % was very stable in SBF and did not form HA even after 30 days of immersion in SBF [152]. Wren et al. added Ga_2O_3 in bioactive glass 42.0 mol % SiO_2-, 8.0 mol % CaO-, 10.0 mol % Na_2O_3-, (40-x) mol % ZnO-, x mol % Ga_2O_3, where x = 8 and 16. They observed that by adding 8 mol % of Ga_2O_3 increased network connectivity from 1.23 (glass with no Ga_2O_3) to 2.32 and for 16.0 mol % of Ga_2O_3 it increased to 3.0 [153]; however, glasses with network connectivity more than 2.4 are not bioactive [50]. Keenan et al. continued by performing cell viability tests with the same glasses as reported by Wren et al, and found that after 90 days larger amounts of Ga was released induced toxic effects on the L-929 fibroblast. However, these glasses did not negatively affect MC-3T3-E1 osteoblasts [150]. Valappil et al. studied the antibacterial effect of Ga doped phosphate-based glass (PBG) with different Ca content and having 3.0 mol % of Ga, and found that the PBG which had 14.0 mol % Ca with 3.0 mol % of Ga_2O_3 had an antibacterial effect on planktonic P. aeruginosa species [148]. Valappil et al. in another study tested Ga doped PBG which had 1.0, 3.0 and 5.0 mol % of Ga_2O_3 against S. aureus, E. coli, P. aeruginosa, MRSA and C. difficile, and found that the PBG containing 1 mol % of Ga_2O_3 had more bactericidal effect than the glasses containing 3.0 and 5.0 mol % of Ga_2O_3. Also, the ion leaching data showed that the 1.0 mol % Ga_2O_3 released the highest level of Ga_{3+} ions than the glasses with 3.0 and 5.0 mol % of Ga_2O_3, which is due to the network stability of glass by adding more Ga_2O_3 [22].

2.3 Coatings for Biomedical Applications

Bioactive coatings are important for metallic implants such as hip prosthesis and periodontal implants as due to the inert nature of metals these encapsulated with fibrous tissue after implantation. Bioactive coatings have the potential to bond with the host tissue and thus improve the stability of the implant [60].

Inorganic phase in bone tissue is mainly composed of carbonated- HA. Moreover, it is the reason that HA ceramics have always been a choice for deposition a coating on to bone implants. The calcium phosphate (CaP) coatings were shown to be bioactive and in numerous pre-clinical and clinical studies have shown to stimulate the formation of new bone tissue [154–158]. To optimise the performance of these ceramic coatings, chemical parameters such as Ca/P ratio, crystalline structure and phase composition have been evaluated and tested extensively. CaP coatings significantly improved the osteoconductivity of the metallic implants [159–161].

Recently and during the past two decades, research trends on CaP coatings focused on modification of its chemical structure and doping with other ions. Several CaP based coatings have been explored, such as HA [162–166]. HA incorporating Si [165], as it has been investigated that Si substituted HA can improve the rate of bone apposition significantly compared with the pure HA [167]. Sr^{-} doped HA [168], as the presence of Sr in coating enhanced osteoblast activity and differentiation, whilst inhibit osteoclast production and proliferation [168–170]. Fluorinated-HA is made by substituting the OH^{-} with the F^{-} ions to increase the thermal stability and chemical solubility of coatings [171]. Also, Ag^{+} ions substituted HA films have been shown to exhibit excellent antimicrobial properties as well as bioactive at the same time [172–174].

HA coated implants have been examined in clinical trials with contrasting results. Some studies show improvements in the oseointigration, while other show failure of the HA coating. Studies revealed that one mechanism of the failure involves the delamination and resorption of the HA coating due to worst attachment between coating and implant. Due to loosing HA coating debris particles form leading to micromotions of the implant [175]. Moreover, HA coating induces a layer of HCA in the body soon

after implantation as a result of ion exchange with the environment. The deposited HCA layer acts as a scaffold for osteoblast cells and further resorb by ostecoclast and replaced by new bone tissue. The amount of HCA that forms on HA coating is determined by the amount of soluble calcium phosphate in the coating [176]. Since HA is relatively less soluble due to the resemblance with the body environment, hence new bioactive materials were needed to be explored for coating purposes and are required for fast fixation applications [27, 177, 178].

Several researchers proposed bioactive glasses as a promising alternative to HA to produce coatings on metallic implants [179] due to their excellent bioactivity [180], and could be used to enhance the adhesion of the implant to the bone. Moreover, PBG could be potentially exploited as coatings for enhanced bonding to bone tissue due to the fact that these glasses mainly composed of calcium phosphate ions [129].

Commonly used coating techniques for the production of glass coated- implants are sol-gel, electropherotic deposition, enamelling, laser cladding and thermal spray [181]. Enamelling is relatively cheaper and simple, moreover thick (several tens of micron) and few microns thin coatings can be obtained with this technique [182]. In this process, a thin piece of glass or a suspension containing glass particles are deposited on to a metallic substrate and then glazing the glass by a proper heat treatment. Temperature of the process should be carefully select to avoid the crystallisation of the glass, degradation of the substrate and also to avoid the substrate- glass reaction, which could lead the formation of by products and subsequently may reduce coating- substrate adhesion [94]. The main disadvantage of the enamelling is possible the inter-facial stresses and poor adhesion which may be caused by the thermal expansion mismatch between glass and substrate [183].

Electrophoretic deposition (EPD) is an inexpensive technique and has a high deposition rate. Moreover this technique allows coating complex shaped objects. In this process a suspension of colloidal particles in a liquid medium is used. The substrate acts as an electrode and the glass particles are deposited on to it after an electrical field is applied to the suspension. After coating, a sintering step is done to fuse the

glass particles present in the deposited coating. With EPD suspensions which are stable and can be electrically charged can be processed. Currently, via EPD suspension of glasses, ceramics, polymers and metals are processed. The coating microstructure can be easily optimised by controlling deposition parameters [184]. Manrique et al. deposited bioactive glass on to Ti6Al4V substrate which were used as anode. Sintering of the coating was done in a hybrid microwave furnace, where SiC absorbers were used for the conventional heating. The benefit of the hybrid microwave was the very fast heating and cooling. The combination of EPD and microwave optimised the interface strength between the coating and substrate and also limited the reactions between these. Further improvement can be done in the process as some cracks propagated on the coating surface [185]. Similar EPD was employed by Balamurugan et al. for depositing composite HA-Bioglass coating on to Ti6Al4V substrate. This coating had controlled solubility due to the presence of 45S5 and the stability of HA. However, due to sintering of the coating β-Tricalcium phosphate was present with pure HA. Also, due to sintering small amounts of (Ca Mg)$_3$(PO$_4$)$_2$ and calcium silicate (CaSiO$_3$) were present in the coating [186]. Moreover, the main disadvantage of the EPD process is the requirement of the conductive substrate or it should be coated with a conductive material [184].

An alternative coating technique for the production of biomedical coated implants could be Laser cladding too. In this powder feedstock is melted for coating the substrate. The powder is normally injected on to the substrate through a nozzle. To melt the powder, the laser beam hits the powder flow. Currently HA coatings are produced via conventional laser cladding process [187]. This technique can also be used as a reactive deposition process for HA coating. The feed stock is a precursors paste for HA, and synthesis of HA occurs during the coating deposition [188]. Recently bioactive glass (S520) coatings produced has reported good results with dense microstructure and good interface with the substrate. This technique is promising as the deposition rate is good and also the substrate is not exposed to high temperature. However, despite of the good results obtained with this technique, crystallisation of the glass

coating was observed [189].

Thin film technology such as physical vapour deposition (PVD) which is currently used to produce thin film coatings on to implants via radio frequency magnetron sputtering [129]. In this process, ions or neutral particles are bombarded on to solid target, consequently material is removed from the target by its atomisation [115]. Stuart et al. deposited 2.5 μm thick coating of PBG on to Ti6Al4V substrates via radio-frequency magnetron sputtering. The author found that the coatings composition was similar to the bulk glass, however, the structure of these coatings was different from the bulk glass [129]. Stuart et al. investigated the structure of the PBG coatings and melt-quenched glass and found that the dissimilarity in the structure of the coatings and bulk glass is due to the polymerisation of the glass in coatings as suggested by NMR and XPS results [16]. Stuart et al. also studied the mechanical properties of 2.7 μm thick coatings of PBG and found that both, the as deposited and heat treated coatings displayed interfacial strength more than 73.6 MPa [190]. However, the disadvantage of magnetron sputtered PBG coatings is their variations compared to melt quenched glass. The coatings consisted of reduced phosphate content and hence lower sputtering rates; whilst the network modifying ions such as Ca, Na, and Mg were deposited more. It was shown that the order of sputtering was P <Fe <Ca <Mg <Na [191]. Moreover, due to higher sputtering powers ($>$ 100 W) the target could crack [114].

Among all above mentioned technique for coating of biomedical implants, the most popular is thermal spray [192], due to the high productivity, its ability to coat complex shapes and its flexibility concerning the choice of both coating material and substrate. Moreover, uncontrolled microstructural changes and distortion of substrate is prevented due to the low temperature of substrate [192]. With this family of processes, successfully controlled chemically and structurally coatings can be obtained [193].

2.3.1 Thermal Spray

In the field of surface engineering, the term thermal spray (TS) is generally used for a family of processes in which a feedstock metallic or non-metallic (but do not decompose

at high temperature at melting point) is melted and accelerated towards a substrate as distinct particles or liquid droplets. These materials are heated by using combustion or thermal energy. The molten or semi-molten feed particles are propelled to a surface by a compressed carrier gas, striking the surface, impingement and flattening forming splats, adhering to the surface . As these particles are sprayed, they cool and form splats in a lamellar arrangement, forming a coating. Thermal sprayed coatings are not uniform and contain porosity, and if the feedstock is metallic, the deposited coating material will contain oxide [194, 195]. Feedstock can be in the form of powder, wire and rod. Coating and substrate may be bonded through chemical, mechanical, and metallurgical or any combination of these. Properties and microstructure of these coating depends on the nature of feedstock, thermal spray process, process parameters and any treatment after application of coating [40, 196, 197]. Also thermal spray can yield coating thickness with few micrometres to millimetres (Figure 2.7) [24]. The history of TS dates back to late 19^{th} century when M.U Schoop yielded the first patent by spraying tin and lead on a metallic substrate using a technique which is almost the same as flame spray [24]. Staring from these early studies and passing through many evolutionary stages, resulting in innovative techniques such as Plasma Spraying (PS), Arc Spraying, Detonation-Gun Spraying, High-Velocity Oxy-Fuel (HVOF) Spraying and Cold-Gas Spraying [24].

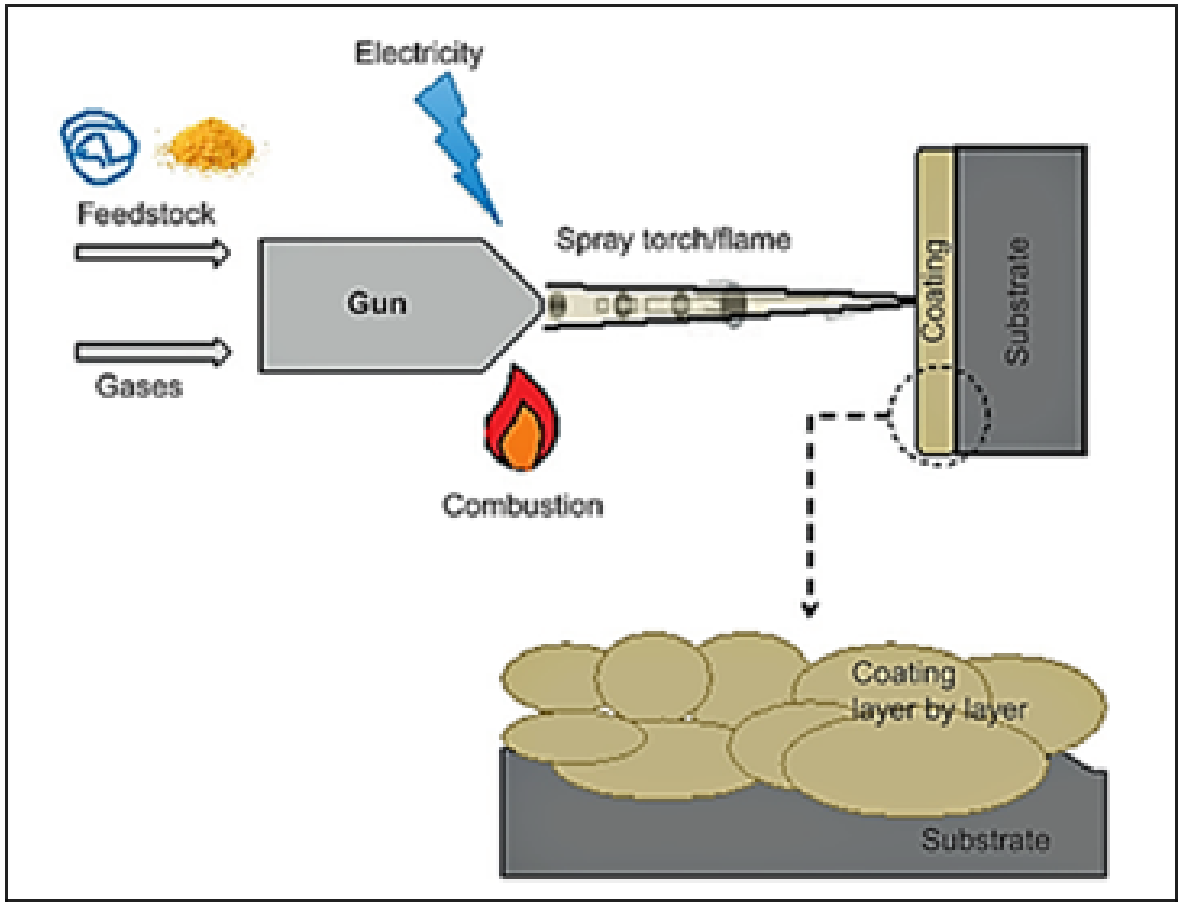

Figure 2.7: *Schematic representation of thermal spray process [24].*

2.3.2 Thermal Spray Techniques

Based on the energy source (which is used for melting of the material) there are two major classes of thermal spray, and these are further divided into sub-types. These are i) electric energy spraying ii) combustion spraying [23, 24]. In the first class of the spraying process, the energy for melting is produced by the electric arc of the direct or pulsating current [24]. In the second, class heat energy is produced by combustion of fuel such as hydrogen, methane, propane etc. The third class developed since 1980's, which is called "Cold Spray" and use no electric energy nor flame or uses low-temperature combustion. It sought to deposit materials with their original features intact. It does so at a low degree of oxidation (warm spray and air-fuel system) or without melting (solid-state spraying) [196]. Different spray techniques are shown diagrammatically in Figure 2.8.

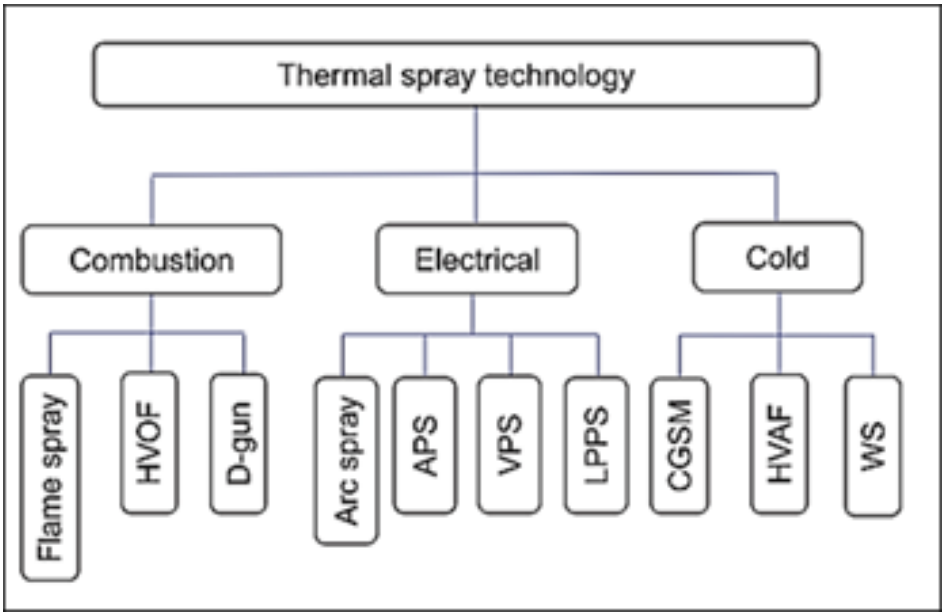

Figure 2.8: *Classification of thermal spray process based on energy source. Where the abbreviations meanings are HVOF (high-velocity oxygen fuel), D-gun (detonation gun), APS (atmospheric plasma spray), VPS (vacuum plasma spray), LPPS (low-pressure plasma spray), CGSM (cold gas spraying method), HVAF (high-velocity air fuel) and WS (warm spray) [24].*

Spray material, spray process and its parameters affect coating microstructure and its properties. To get desired microstructure with a pre-determined set of properties is a challenge which is existed since early 1900's and passed from several evolution stages [198]. Flame temperature and particle velocity are the two important variables for any thermal spray technique, which are known as "T-V relationship". T-V relationship illustrates the interaction of particles, the high energy temperature field, gas velocity field, and splat formation. T-V value is influenced by factors such as spray parameters [197]. Thermal energy of the particle is the function of flame temperature while kinetic energy is dependent on the carrier gas velocity. For material having high melting point such as ceramics plasma spray(PS) is suitable while for materials like tungsten carbide high velocity oxy-fuel (HVOF) is suitable because of its high kinetic energy [29]. Temperature and velocity of the particles play an important role for a coating microstructure and its properties (Table 2.2) [24].

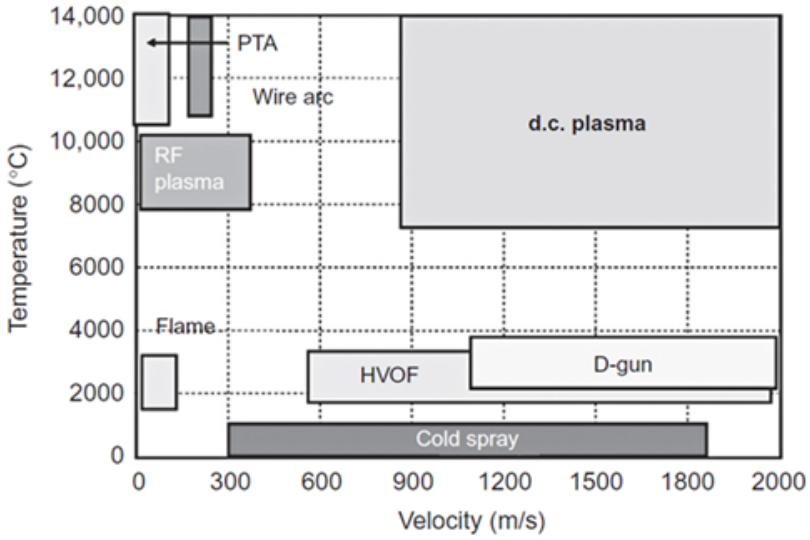

Figure 2.9: *Flame temperature and particle velocity relationship for different thermal spray techniques [199].*

2.3.3 High Velocity Oxy Fuel Spray (HVOF)

In the HVOF process, the fuel and oxygen mixture is introduced in the combustion chamber and ignition starts the combustion. The exhaust gas is formed, pass through nozzle to a barrel and emerges out in the atmosphere. The coating material can be introduced in radial position as well as in axial into the gas jet [199]. In this process, the particle velocity can be 450 m/s [200], with this much velocity particle when it strikes with the substrate surface it flattens resulting in a dense microstructure with good bond strength. Advanced HVOF guns with convergent-divergent nozzle design can increase particle velocity up to 1200 m/s [201]. In HVOF thermal spray, liquid fuel (kerosene) or gaseous fuel (hydrogen, methane, acetylene, propylene, propane and ethylene) can be used. Fuelling spray gun with kerosene requires extra controls, like liquid fuel pumps and a high volume of air to support combustion. Flame temperature can be tailored by adjusting fuel to oxygen ratio [194]. Challenging materials like WC–Co and ceramic-metallic coatings (cermet) can be sprayed with high bonding strength with HVOF thermal spray. With this process particles in the range 5-45 μm can be sprayed with a stand-off distance 150-300 mm [202].

Table 2.2: *Thickness, porosity and temperature-velocity for different spray techniques.*

	Flame Spray	**Arc Spray**	**Detonation Gun**	**HVOF**	**APS**	**Cold Spray**
	Flame/Jet					
Temp °C	3500	> 6000	> 4000	2500-3000	10,000-5,000	0-700
Velocity (m/sec)	80-100	50-100	> 2500	500-2000	300-1000	300-1200
Fuel Type Gases	Oxygen Acetylene Propane Hydrogen	Air Nitrogen Argon	Oxygen Acetylene Propane Hydrogen Butane	Oxygen Natural Gas, Propane Hydrogen Ethylene Propylene Kerosene	Argon Helium Nitrogen Hydrogen Mixture (N_2/H_2)	Nitrogen Helium Air
Power (kW)	20	5-10	—	150-300	40-200	—
Feed Stock						
In-Flight Max Temp C	2500	> 3800	—	3300	> 3800	250
In-flight Velocity (m/sec)	50-100	50-150	750-1000	200-1000	50-100	500
Coating						
Porosity (%)	10-15	10-20	<2	< 2	5-10	< 5
Thickness (μm)	100-2500	100-2000	100-400	50-2000	100-1500	250-600

2.3.4 Suspension High Velocity Oxy Fuel Spray (SHVOF)

SHVOF is the novel form of HVOF which uses feedstock in the form of suspension rather than powder as shown in Figure 2.10 [203]. Material is deposited by melting submicron or nanoscale particles by carrying in a liquid media and can be injected radially or axially [202]. Spray with sub micrometric and nanoscale particles give a coating with significantly improved wear resistance, fracture toughness and enhanced hardness [29]. All these benefits are since the nanoscale ceramic particles are more ductile than the bulky material which is brittle. Similarly, nanoscale metallic particles are stronger than the bulk as these are free from dislocation [204].

Nanostructured thick coating can be obtained by thermal spray; however, this faces two problems, i.e. poor flowability of the powder, which is due to the agglomeration and discontinuation in the powder feeding system and the injection of fine light particles in a flame. The low mass of these sub micrometric particles give them low thermal and kinetic inertia, as these particles tend to be outside of the main core of the flame, they deposit as lumps without flattening as compare to individual particle flattening on its impact [205, 206]. Powder flowability is extremely important to have a homogeneous microstructure, because if flow-ability is poor so there will be fluctuations in the powder feed rates resulting in a non-uniform coating microstructure [207].
Powder flowability can be increased by increasing the carrier gas flowrate but it will lower the flame temperature [32]. To overcome these problems the best approach is the use of feedstock in the form of suspension. The attraction in suspension spraying is the freedom in the particle size choice, chemical composition and solute and solvent percentages. The spray process and coating structure depend on the suspension characteristics as particle size, solid loading, solvent used and suspension viscosity. Various interaction occurs between the liquid suspension and the hot gas stream of a flame or plasma. The solvent and solute show different effects when those come in contact with the hot gas stream [208]. The enhanced properties of the coating are achieved via direct injection of the suspension into the combustion chamber. This favours significant heat transfer between particles and the flame. After the solvent evaporates, particles are heated by the gas in the combustion chamber and expansion nozzle. The combustion gas attains supersonic velocity upon expansion to ambient pressure outside of the torch, and the particles are ejected at high velocity towards the substrate. This results in layers of flattened particles, which results in a dense thick microstructure coating with high cohesive and adhesive strength [27].

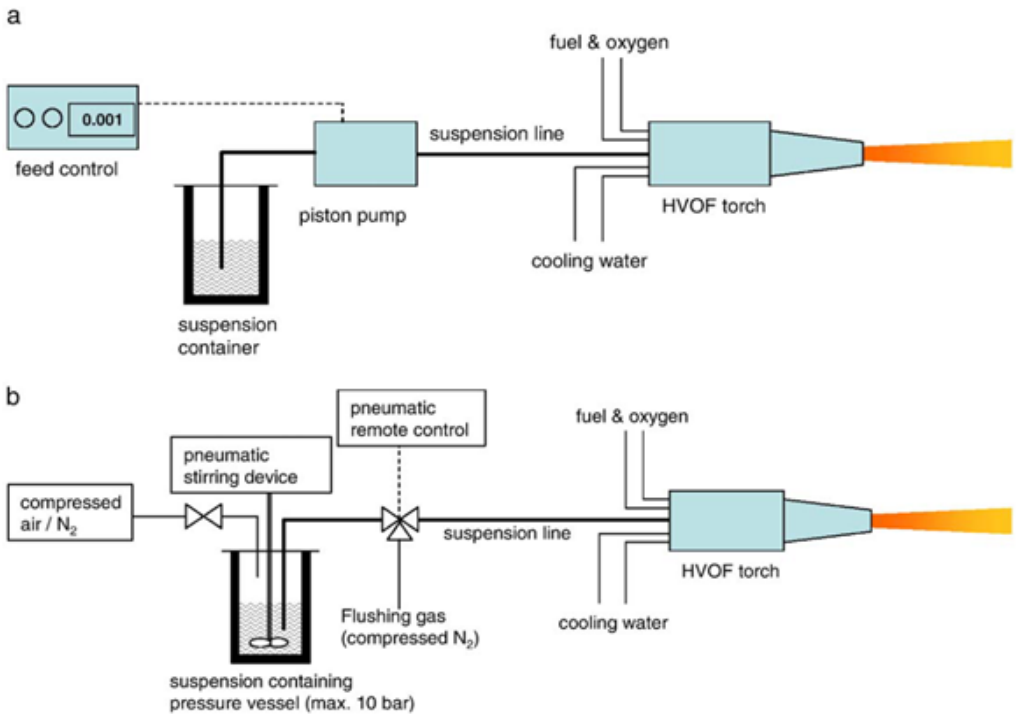

Figure 2.10: *Suspension High Velocity Oxy Fuel (SHVOF) set up for suspension feeding: (a) Piston-pump (b) Pressurised vessel [32].*

In SHVOF heat is generated in a pressurised chamber by the continuous combustion of the fuel-oxygen mixture. The combustion chamber geometry depends upon the melting point of the material to be deposited different combustion geometries given in Figure 2.11. For example, high melting point materials such as ceramics need a long chamber for enhancing heat transfer by encountering turbulence and giving high residence time to the particles in the chamber. For low melting point materials such as glass and hydroxyapatite (HA) small shorter length chamber is appropriate [208].

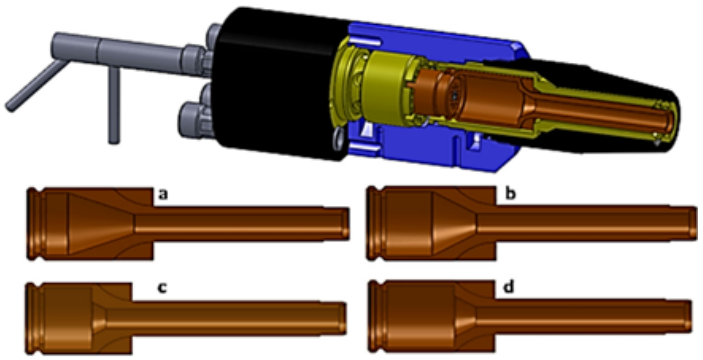

Figure 2.11: *GTV Top Gun SHVOF spraying system with exchangeable suspension injectors (a, b, c, and d of different injector geometries) [208].*

As the stand-off distance effect the substrate temperature and deposition pattern, SHVOF has a wide range of stand-off distance which is 90-300 mm, but it can be specified by feedstock, desired coating properties [209]. SHVOF is being used for a dense coating of high bond strength and better mechanical properties [32, 36, 208]. So, it can be said that SHVOF has the potential to be a standard for coating submicron and nanoscale materials.

This process has already been explained so starting with the process parameters.

2.3.5 Suspension Thermal Spray Feed Stock Preparation

Two sets of variables govern the process and affect the resulting microstructure. These are 1) Suspension parameters 2) Spray parameters. These are given below in Table 2.3:

Table 2.3: *Suspension and Spray parameters for SHVOF process.*

Suspension Parameters	**Spray Parameters**
Particle size	Feed flow rate
Type of solvent	Fuel and Oxygen flow rate, their ratios
Suspension stability	Spray distance
	Substrate Temperature + scanning speed,

2.3.5.1 Particle Size (Ball milling)

A uniform coating highly depends upon the particle size and their stable dispersion in the suspension throughout the whole process as stationary and aggregated particles would lead compositional gradient in coatings. At the same time, this cause sedimentation and may clog the gun. Reducing the particle size would result in small flattened splats instead of flowery ones, and nano-sized splats attract cells, enhancing bioactivity. However, if the particle size is small, which results in larger surface area, higher electrostatic attraction and ultimately flocs will form. For larger particles, gravitational forces are more, which will result in sedimentation of particles. So for a stable suspen-

sion, the particle size needs a compromise to avoid flocculation and sedimentation [36, 207, 208, 210].

Mechanical ball milling is a way to reduce the particle size, as the ball mill is the most energy-intensive, less expensive and also less time consuming [211, 212]. Planetary ball mill (PM) is the ball mill in which two forces act on balls and the materials to be ground, one gravitational and centrifugal force. Mills move on the disk like a planet that is why it is called a planetary ball mill [108]. Important parameters for ball milling are milling speed, milling time, process control agent (PCA), and ball diameter, the number of balls and weight ratio of balls to materials. In these parameters, the rotation speed offers the largest (84 %) contribution in materials milling, while, milling time and PCA offer second largest contribution (i.e., 16 %) [213]. By increasing mill speed and milling time, machine efficiency will increase, but after a specific time, there would be no change on particle size. There is a specific speed which is called critical speed, speeding the machine beyond this point would have no effect on grinding because the ball and material will be stuck with the shell of the mill. Similarly, after a specific particle size, there would be an equilibrium between grinding and agglomeration. So further grinding will increase the surface area, which will result in more attractive forces and ultimately, agglomerates will form [213, 214].

2.3.5.2 Type of the Suspending Media

The suspending media used for making bioactive glass suspension must not react with the glass. Water solely is not a suitable media for making bioactive glass suspension, as the water leach out alkaline earth and alkali metal oxide and then these react with atmospheric CO_2 resulting as layers of carbonates on the top surfaces [210, 215]. At the same time dielectric constant (78.5) for water is enough for making a stable suspension but its surface tension is high (72.75 erg/cm) which would be a hindrance for uniform dispersion. If organic solvent (mostly alcohols for safety and health) is used, because of its low dielectric constant (18.8 for Isopropyl alcohol), the suspension would be unstable, but its low surface tension (21.4 ergs/cm) is a good sign for particles

dispersion [216]. In the case of bioactive glass suspension, a mixture of solvents is suggested to have a good compromise in surface tension and dielectric constant for stable homogeneously dispersed suspension,[217–222].

2.3.5.3 Suspension Stability

Suspension stability is mainly related to the particle size, solvent used, and solid loading. Particle size is a factor for determination of the tendency of sedimentation and flocculation as discussed earlier. Similarly, solvent type has a major contribution in suspension stability. By increasing the amount of solids in suspension will increase the deposition efficiency, whilst, it would decrease the distance between particles, which would cause more electrostatic attractive forces resulting in flocculation. The best approach for suspension stability is to manipulate zeta potential [223]. Zeta potential is the difference between the double layer and diffused layer if its value is high so the particles would be covered by counter ions resulting in more electrostatic repulsion and higher suspension stability (Figure 2.12) [224].

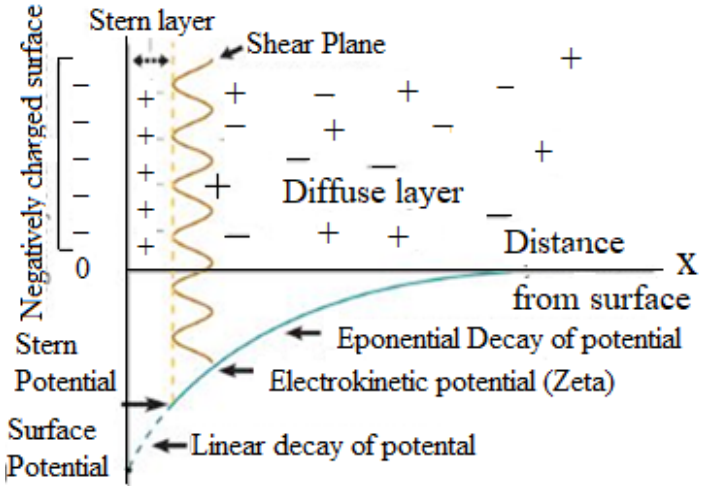

Figure 2.12: *Negatively charged particle surface and double layer model [225].*

Zeta potential can be increased by electrostatic stabilisation or steric stabilisation. Electrostatic stabilisation is achieved by adding a surfactant which may be 1) non-ionic 2) anionic 3) cationic 4) zwitterionic having both positive negative charges. Type of surfactant depends on the net charge of the particle. Since the net charge on bio-glass particle is positive, so anionic is used for stabilisation [216]. Dolapix -65 and Dolapix-

64 ($C_3H_4O_2.XH_3N$) is mostly used for bio-glass suspension and ceramic suspension [27, 218]. Sometime with higher zeta potential sedimentation occurs because of larger particle size [225]. Steric stabilisation is done by the addition of stabilizer, which must be copolymer. These copolymers may be random, graft, or block. One part of these polymer absorbed on the surface of the particle and the other keep away the other particle at a distance usually 10-20 nm as can be seen in Figure 2.13 [226].

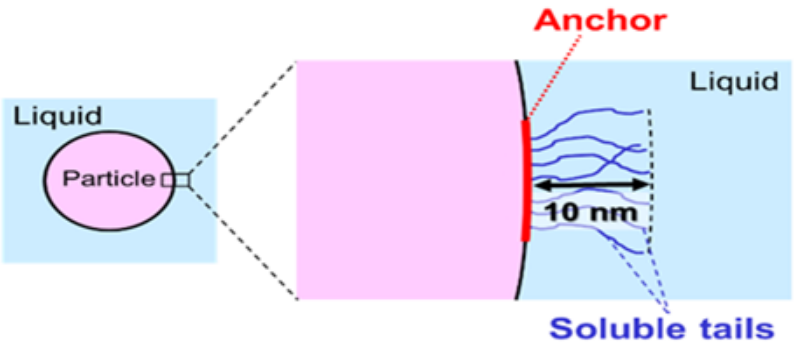

Figure 2.13: *Stearic stabilisation achieve by adding polymer [226].*

2.4 Novel Thermal Spray Techniques for Deposition of Biomedical Coatings

Several investigations have been conducted by using innovative techniques to produce glass coating and are summarised in Table 2.4. Reactive plasma spray (React PS) is one of the innovative techniques, in which the glass is made in the plasma to skip the conventional melt, and quenching or sol-gel method so have a uniform glass composition without any gradient in it. In the reactive plasma method the raw material required for glass production is used in aqueous suspension form, then homogenised and milled to have a particle size of 20 μm, then spray dried. Now this is the feedstock for PS instead of making glass and then milling, so it will save time and also energy [227, 228].

The innovative technique of suspension plasma spray was utilised to spray bioactive glass (4.7 Na_2O, 42.3 CaO, 6.1 P_2O_5, 46.9 SiO_2 in oxide wt %). The Coating was all amorphous with some development of crystalline wollastonite as can be seen in Figure

2.14, while the circled areas show splat and crystallised zone. However, the coatings were bioactive as the HA precipitated on the surface of the coatings after immersion in SBF [217].

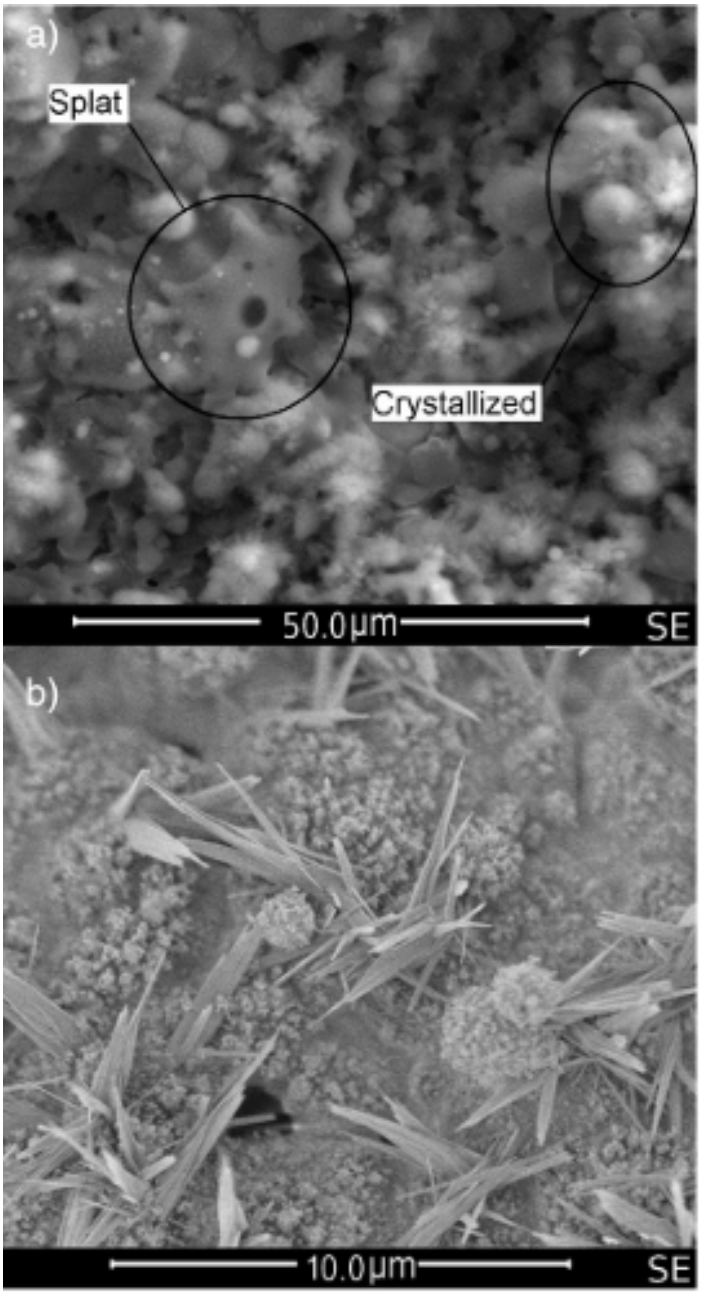

Figure 2.14: *(a) SE SEM image of the as sprayed SP sprayed wollastonite coating with outline molten splats and crystallised zone, (b) the high magnification image of the crystallised area with the acicular morphology of $CaSiO_3$ [217].*

The non-conventional thermal spray technique for bioactive glass coating SHVOF are given in Table 2.4 [192, 229, 230]. section 2.5 is on the studies reported about the SHVOF bioactive coating.

Table 2.4: *Bioactive glass thermal sprayed coating characteristics where values in the bracket indicate standard deviation ∗Scratch critical load. ∗∗ Shear test. Tensile test. # According to ASTM C-633.*

Year	Technology	Substrate	Glass Composition wt%	Thickness(μm)	Adhesion Strength	Ref
1995	PS	Ti6Al4V	Biovetro (50% SiO_2, 25% CaO, 15% Na_2O, 10% P_2O_5).	80	21-32 [N]*	[231]
1995	PS	Ti6Al4V	HA, Composite Glass (50% SiO_2, 25% CaO, 15% Na_2O, 10% P_2O_5)	13+50	—	[232]
1996	PS	Ti6Al4V	Ti bond coat + 45S5 (45.0% SiO_2, 6.0% P_2O_5, 24.5% CaO, 24.5% Na_2O)	150	—	[233]
1997	React. PS	Ti6Al4V	52% SiO_2, 30.5% CaO, 9.8% Na_2O, 6.2% P_2O_5, 1.5% CaF_2	150	>35**	[228]
1998	VPS	Ti6Al4V	AP40/TAP/RKKP, composite, Ti	80	21-22 (1.5)**	[234]
1998	PS	Ti	HA, composite 45S5 (45.0% SiO_2, 6.0 %P_2O_5, 24.5% CaO, 24.5% Na_2O)	160	—	[235]
1999	PS	Ti6Al4V	HA, composite 45S5(45.0 %SiO_2, 6.0% P_2O_5, 24.5% CaO, 24.5% Na_2O)	50	—	[177]
1999	React. PS	Ti6Al4V	52% SiO_2, 30.5% CaO, 9.8% Na_2O, 6.2% P_2O_5, 1.5% CaF_2.	50	40.1 (4.8)** 69.4 (9.4)ˆ	[236]

2000	React. PS	Ti6Al4V	52% SiO_2, 30.5% CaO, 9.8% Na_2O, 6.2% P_2O_5, 1.5% CaF_2.	50	48.6 (7.9)** 43.6 (1.1)** post invitro	[227]
2000	PS	Ti6Al4V	50% SiO_2, 25% CaO, 15% Na_2O, 10% P_2O_5, HA.	120	52-56# <20 after 30 days invitro #53.5#	[237]
2001	PS	Ti6Al4V	50% SiO_2, 20% Na_2O, 16% CaO, 6% P_2O_5, 2% Al_2O_3, 1% MgO.	50-100	—	[238]
2004	PS	Ti	Amdry 6250 bond coat + Bioglass 45S5 (45.0% SiO_2, 6.0% P_2O_5, 24.5% CaO, 24.5 %Na_2O).	20-80	—	[239]
2008	SHVOF	Stainless Steel	52% SiO_2, 31% CaO, 16.5% ZrO_2.	15	4.27 ± 0.56 (Vickers micro hardness (GPa)	—
2009	SHVOF	Ti gr2	AW-glass	100	(2.24)#	
2010	SHVOF	Ti gr2	BioK (39.8 % SiO_2, 21.8% CaO, 33.1% K_2O, 5.3% P_2O_5).	50-60	18.2-23.1GPa (Elastic modulus)	[229]
2012	SHVOF	Ti gr2	$Ca_3(PO_4)_2$, BioK, 39.5 % SiO_2, 21.8 % CaO,33.1 % K_2O, 5.3 % P_2O_5).	10-15	—	[192]
2013	SPS	316 L Stainless Steel	4.7 % Na_2O, 42.3 % CaO, 6.1 %P_2O_5, 46.9 % SiO_2	30-40	—	[217]

2014	SPS	AISI 304 Stainless Steel	45S5 (45.0 % SiO_2, 6.0% P_2O_5, 24.5 % CaO, 24.5 % Na_2O).	Ra 16 ± 4 (μm) (Surface roughness)	Water contact angle(o) 24	[240]
2015	SHVOF	Ti gr2	2.3% K_2O, 2.3 Na_2O, 45.6% CaO, 2.6% P_2O_5, 47.3% SiO_2 (mol %)	20-25	—	—
2016	SPS	AISI 304 Stainless Steel	47.6% SiO_2, 5.3 % P_2O_5, 23.1 % CaO, 24.0 % Ca_2O, + TiO bond coat.	60-20	77-82 GPa (Elastic modulus)	—
2020	APS	AISI 304 Stainless Steel	45S5	—	—	[230]

2.5 SHVOF Sprayed Glass Coatings for Biomedical Implants

SHVOF thermal spray has been shown to be a promising technique for the deposition of bioactive glass coatings. For instance, L. Altomare et al. produced 45S5 coatings using SHVOF thermal spray. The microstructure of these coatings exhibited a gradient, and that's why the process parameters need to be optimised to reduce the overall porosity. Moreover, the produced coatings were very reactive towards SBF, as the original glass coatings had been replaced by the interaction product with the SBF in one week as can be seen in Figure 2.15 a, that only a small layer of the glass was there whose chemical composition was lightly altered when compared with the original bulk glass (Figure 2.16 b EDX analysis, spectrum 1 is for layer 1(HA), spectrum 2 for SiO_2 gel layer (layer 2), spectrum 3 is for the residual glasses and spectrum 4 is for the bulk glasses . So, these coatings might be useful in those applications where short osseointegration and progressive dissolution of the bioactive layer is required. these coatings were cytocompatible towards MG63. As can be seen in Figure 2.16a that after 1 day of incubation cells spread on the 45S5 coating surface homogeneously. Figure 2.16 b, c shows the coating surface was uniformly covered with cell sheets [241]. Similarly, Bolelli et al. used SHVOF technique and deposited 45S5 and a newly developed bioactive glass labelled as Bio-K. The coatings' thickness and porosity were significantly affected by the process parameters. Both glass coatings were glassy; however, the structure of the Bio-K glass coatings was different from that of the bulk as revealed by Raman analysis as can be seen in Figure 2.17 b, the peaks at 862 cm^{-1}, 933 cm^{-1}, 965 cm^{-1} and 1052 cm^{-1} in the spectrum of bulk were assigned to the symmetric stretching of $SiO_4{}^{-4}$ monomers, symmetric stretching of $Si_2O_6{}^{-4}$ chain and ring structures, P-O-P network stretching and three dimensional network of SiO_2 asymmetric stretching [242]; however, the peaks in the spectrum of the Bio-K coating have appeared at 869 cm^{-1}, 948 cm^{-1}, 1000 cm^{-1} and 1081 cm^{-1} (Figure 17 b). The first two peaks although shifted, still can be assigned to the symmetric stretching of $SiO_4{}^{-4}$ monomers and $Si_2O_6{}^{-4}$ rings and

chain structures; however, the peak at 1000 cm^{-1} was due to the ^{0}O-P-O stretching in $P_2O_5^{-4}$ sheet.

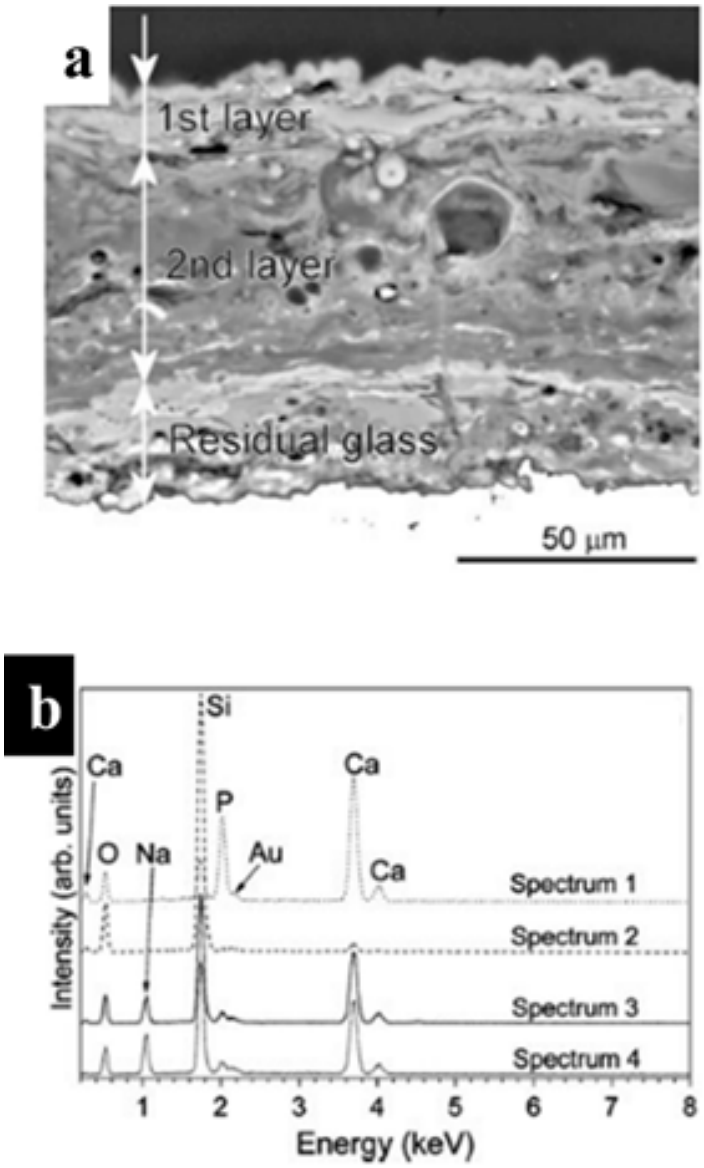

Figure 2.15: *(a) cross-section of the 45S5 coating after 7days of SBF test, (b) is the EDX analysis of the same cross-section, where spectrum 1 and 2 are for layer 1,2 3 is for the residual glass coating while spectrum 4 is for the original glass [237].*

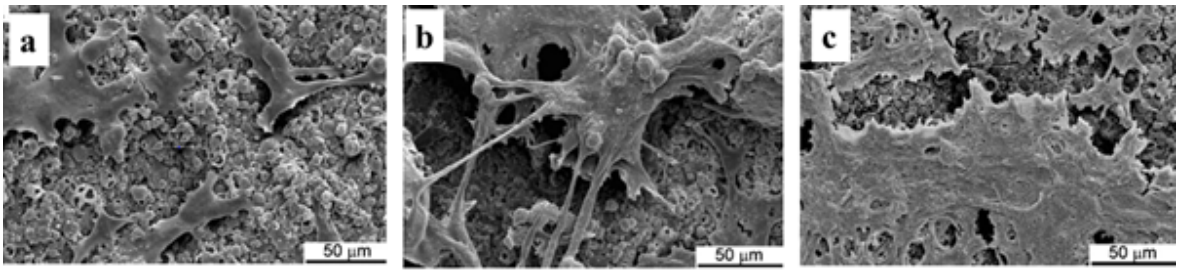

Figure 2.16: *SEM images of MG63 cells on SHVOF sprayed 45S5 coatings, (a) after 1 day, (b) 3 days and (c) 7 days, in SBF [241].*

Moreover, the peak at 1081 cm^{-1} belonged to the $Si_2 2O_5{}^{-2}$ planer structure [242]. It means that due to SHVOF spraying of Bio-K glass, the peaks belonging to the three-dimensional SiO_2 and P-O-P network, became so weak that these could not be recognised any more. These peaks were replaced by the planer structures of $Si_2O_5{}^{-2}$ and P_2O_5 sheets. This indicated that the three-dimensional network of the glass was degraded in the SHVOF deposited Bio-K coating [218]

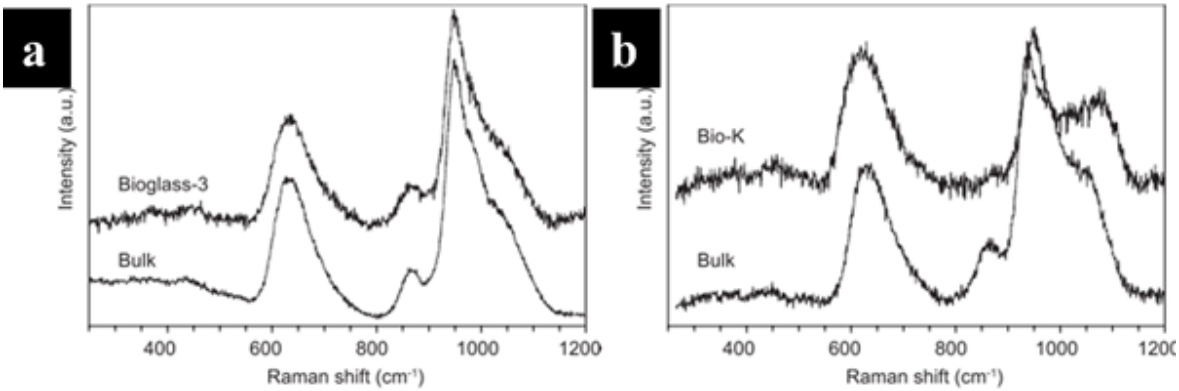

Figure 2.17: *(a) Raman spectra of 45S5 coating and (b) Bio-K glass coating and the corresponding bulk glasses [218].*

The Bio-K glass was also deposited utilising the same deposition technique (SHVOF thermal spray) by Bellucci et al. onto titanium substrates with and without a bond coat of TiO_2, and it was found that the microstructure of the coatings was independent of the bond coat but dependent on the process parameters, as can be seen in Figure 2.18, the difference in the coating thickness and porosity was due to the different feed, oxygen and fuel flow-rates. However, the bond coat contributed significantly to the adhesion strength of the coating with the substrate reaching a maximum value of 17 MPa. Also, all of the coatings were bioactive in terms of HA precipitation on the surface of the coatings in SBF [192].

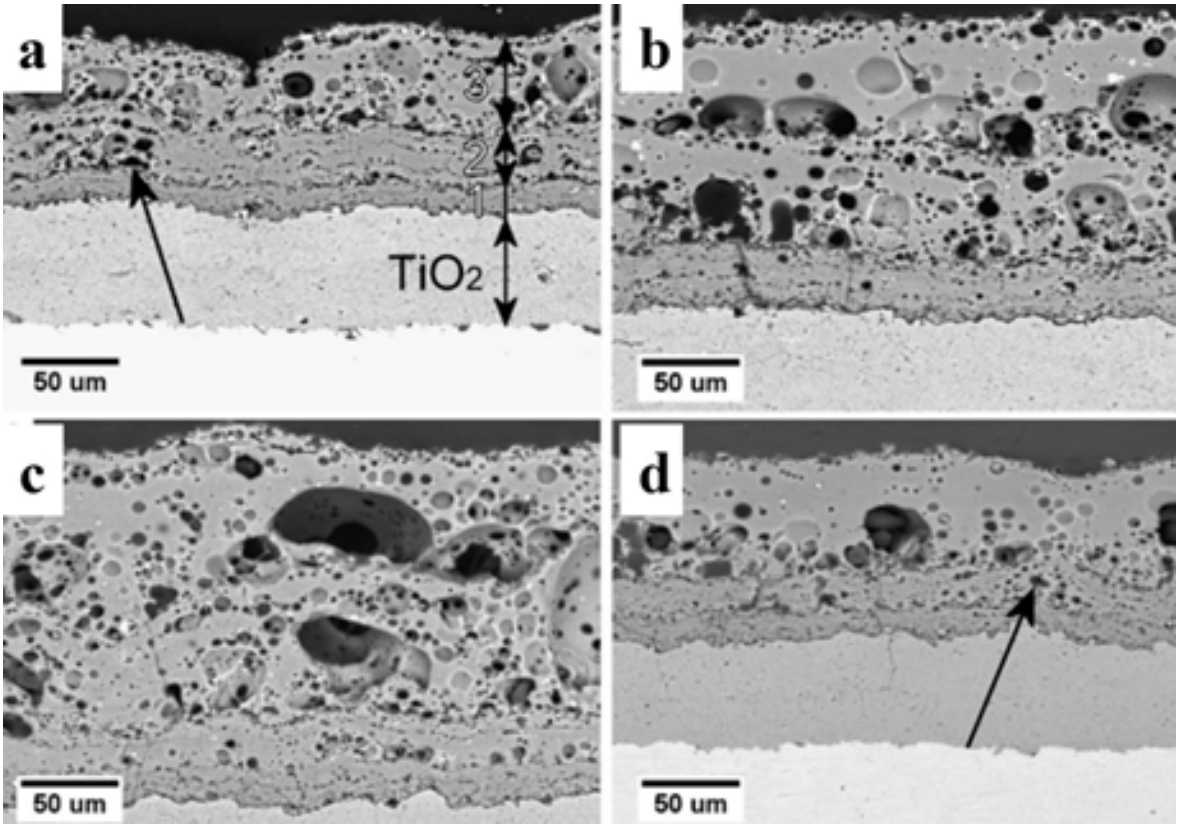

Figure 2.18: *BSE, SEM images of the cross-section of Bio-K glass deposited at different spray parameters (feed, oxygen and fuel flow rates), all coatings have TiO_2 bond coat [192].*

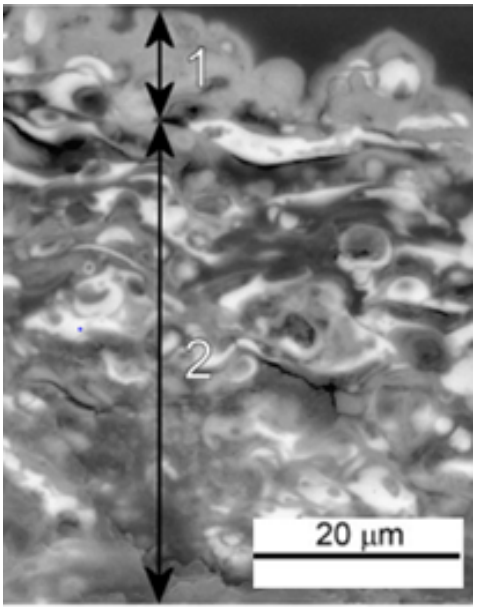

Figure 2.19: *BSE, SEM image of Bio-Ka glass coating after two weeks of immersion in SBF, where layer1 is the precipitated HA and layer 2 is the depleted glass coating.*

Bolelli et al. investigated Bio-K coatings that showed high reactivity towards SBF,

as the entire coating thickness ($\sim$ 50 μm) was affected by the interaction with the SBF in two weeks as can be seen in Figure 2.19, whereas layer1 is the precipitated HA and layer 2 is the depleted glass coating [229]. However, the Raman analysis of the coatings showed that alterations occurred in the glass structure during SHVOF thermal spraying which is also reported in the previous studies [218, 229, 234].

In another study by Bolelli et al. SHVOF thermal spray was used to deposit apatite–wollastonite bioactive glass–ceramic and good quality coatings consisted of lamellae and partially molten particles with spherical morphology that had central pores as shown in Figure 2.20. These coatings showed reactivity in SBF with the formation of HA crystals; however, unlike common bioactive glasses, HA did not precipitate as a layer on top of the coatings, but rather as regions dispersed inside each layer as shown in Figure 2.21. Moreover, at the top of the coating, 10 μm thick SiO_2 was observed which increased to 30 μm after two weeks and 70 μm after 5 weeks of immersion in SBF [243].

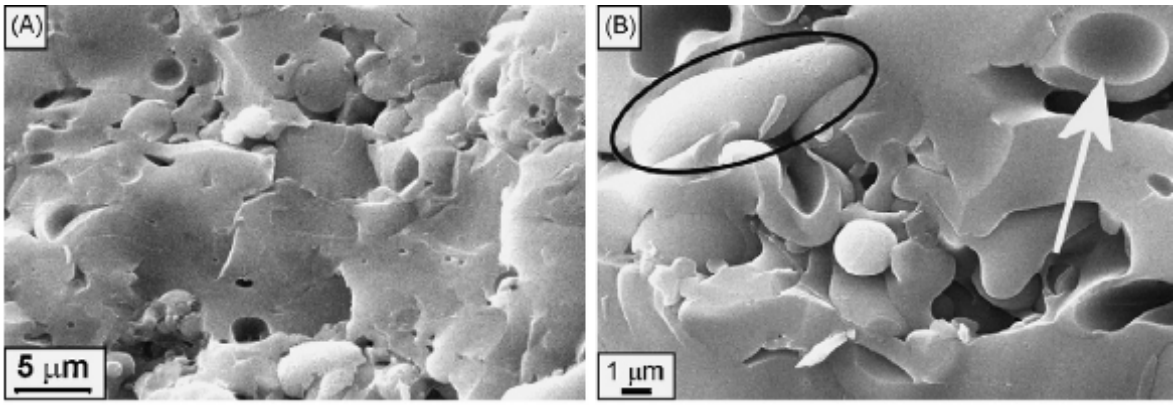

Figure 2.20: *Fractured sections of SHVOF deposited A-W coatings. (A) General view; (B) details (circle: flattened lamella; arrows: rounded particles with central pore[243].*

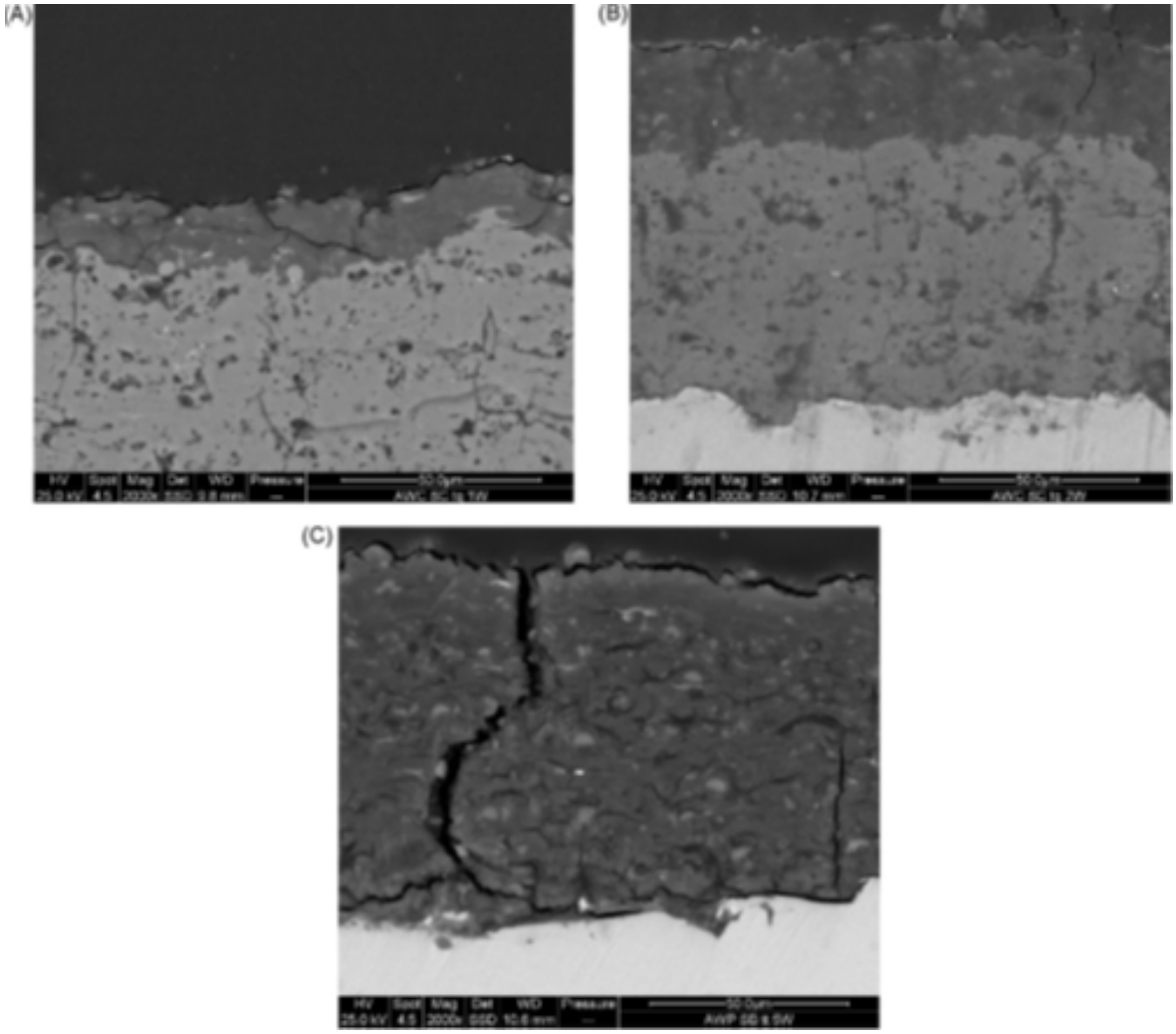

Figure 2.21: *SEM cross-sections of AW coating after soaking in SBF for 1 week (A), 2 weeks (B) and 5 weeks (C), while the bright inclusions are HA [243].*

According to the literature about the deposition of biomedical coatings, SHVOF thermal spray deposition has been proved to produce high quality dense bioactive glass coatings of approximately 50 μm thick [27, 244], these coatings proved to be very reactive towards SBF solution. ICIE16 and 13-93 are bioactive glasses and comparatively stable in SBF than 45S5. Therefore, coating production using these two compositions could result in less coating dissolution towards SBF. Moreover, bioactive coating with Ga_2O_3 as an antibacterial agent would be a worth try to address the post operative infections. Moreover, the structure of the melt-quenched and PVD thin film of PBG (P-40) is well documented in literature. However, the properties of thermal sprayed P-40 coatings will depend upon process parameters leading to structural and compositional changes. Whilst, the functionality of these coatings will depend upon their

dissolution and ion release properties to facilitate cellular activity.

2.6 Summary

Following summary can be made from this chapter:

- This review highlighted different generations of biomaterials and their utilisation for orthopaedic applications.
- Ga_2O_3 incorporated bioactive glasses and PBG have been explored for tissue generation and antimicrobial effects. In the literature it is reported that incorporating more than 1 mol % Ga_2O_3 in PBG, make the glass resistant to dissolution. Moreover, adding high mol % (3.5) of Ga_2O_3 made 45S5 resistant to SBF.
- HA was and still is the first choice for producing a bioactive coating for biomedical applications, however, HA is comparatively stable in body environment and thus more bioactive materials such as Bioglass® or other bioactive glasses needed to be explored for the said purpose.
- Similarly PBG mainly contain calcium phosphate and could be another choice for coating on metallic implants for enhanced osseointegration due to the high resorption rate in physiological fluid.
- Several competing deposition technologies such as plasma spray, sol-gel, enamelling, PVD for production of biomedical coatings have been assessed.
- Due to the high productivity, ability to coat complex shapes, flexibility about the choice of both coating material and substrate and no microstructural changes and distortion of substrate (due to the low temperature of substrate) of thermal spray technique, it could be a choice of deposition technique for biomedical applications.
- SHVOF thermal spraying is a coating deposition technique with the key advantage of enabling processing of nano and micrometric particles in a suspension.

This process allows the production of nano-structured coatings and has been shown be to be a potent technique for the deposition of bioactive glass coatings.

- However, these coatings microstructure needs to be optimised to meet the end applications. As these glasses are highly reactive in the physiological environment, so coatings made of these glasses may be resorbed before the integration of the implant with the host tissue.

2.7 Gaps in the Literature Review

- Currently no literature is available on thermal sprayed coatings of ICIE16 bioactive glass which is closer to 45S5 composition, and 13-93 bioactive glass which is not very reactive in SBF as 45S5. Meaning this will be the first work to produce ICIE16 coating with more dissolution in SBF and 13-93 coating which can survive longer in the media.

- For resorbable PBG, literature is reported only about the PVD coating technique and which changes the structure and composition of the glass coating than the bulk due to the preferential sputtering of the ions based on atomic weight of the elements. So thermal spraying of PBG (P-40) will be a novel work too.

- Addition of Ga^{3+} ion as antibacterial agent is an emerging research area. This work will add to the current knowledge by coating Bioglass® and Ga_2O_3 via SHVOF spraying by assuming that Ga_2O_3 will improve the base coating antibacterial and osteogenic properties whilst maintaining the desirable characteristics of the Bioglass® coating.

Chapter 3

Materials and Methods

In this chapter, an overview of the suspension high velocity oxy fuel (SHVOF) thermal spraying with the summary of the manufacturing process of the glasses used in the deposition of coatings is provided. Besides, bioactivity tests of the bioactive coatings using simulated body fluid (SBF), and cytotoxicity tests using MG63 cells (osteoblast like cells) has been explained here. Moreover, ion release and mass degradation study of P-40 coating is reported too. The characterisation techniques of the as-deposited coatings and after SBF and cell tests are also included in this chapter.

3.1 Glass Manufacturing

The glasses used in this project were made through the melt and quench method. High purity silica (SiO_2) (high purity, prince minerals, Stoke on Trent), phosphate (P_2O_5) and carbonates for the modifying oxides were purchased from Sigma Aldrich UK of 99.5% purity (Table 3.1). Except of Ga_2O_3, which was used in the fourth formulation (chemically mixed Ga_2O_3-Bioglass®) given in Table 3.1, was purchased from Changsha Rich Nonferrous Metals Co., Ltd China of 99 % purity.

Table 3.1: *Composition (mol %) of glasses used in this work.*

Oxides	**Bioglass® (45S5)**	**ICIE16**	**13-93**	**P-40**	**Chemically Mixed Ga_2O_3 Bioglass**
SiO_2	46.1	49.46	54.60	-	45.1
CaO	26.9	36.60	22.40	16	26.9
Na_2O	24.4	6.6	6.0	20	24.4
P_2O_5	2.6	1.0	1.7	40	2.6
K_2O	—	6.6	7.9	—	—
MgO	—	—	7.7	24	—
Ga_2O_3	—	—	—	—	1

The quantity of different precursors, used to make glass are given in Table 3.2.

Table 3.2: *Amounts of precursor used for glass.*

Precursor (g)	**45S5**	**ICIE16**	**13-93**	**P-40**	**Ga_2O_3 Incorporated 45S5**
SiO_2	27.7	72.0	32.0	—	27.0
Na_2CO_3	25.8	16.9	6.3	—	25.8
$CaHPO_4$	7.0	—	—	32.6	7.0
$CaCO_3$	21.7	87.9	22.1	—	21.7
K_2CO_3	—	22.1	10.9	—	—
P_2O_5	—	—	—	—	—
$NaHPO_4$	—	—	—	47.9	—
$MgHPO_4.3H_2O$	—	—	5.9	27.8	—
$MgCO_3$	—	—	3.6	—	—
Ga_2O_3	—	—	—	—	1.0
Total	**82.3**	**202.7**	**81.1**	**108.5**	**82.7**

When the precursors are heated, the following reactions occurs in a batch of the

molten glass.

$$CaCO_3 \longrightarrow CaO + CO_2 \tag{3.1}$$

$$Na_2CO_3 \longrightarrow Na_2O + CO_2 \tag{3.2}$$

$$K_2CO_3 \longrightarrow K_2O + CO_2 \tag{3.3}$$

$$2\,CaHPO_4 \longrightarrow 2\,CaO + P_2O_5 + H_2O \tag{3.4}$$

$$K_2CO_3 \longrightarrow K_2O + CO_2 \tag{3.5}$$

$$2\,NaHPO_4 \longrightarrow Na_2O + P_2O_5 + H_2O \tag{3.6}$$

$$2\,MgHPO_4 \cdot 3\,H_2O \longrightarrow 2\,MgO + P_2O_5 + 4\,H_2O \tag{3.7}$$

$$MgCO_3 \longrightarrow MgO + CO_2 \tag{3.8}$$

All the precursors were mixed in Wheaton mini roller (UK) and homogenised for 2 hours. This mixture was then transferred to a 95 wt % platinum and 5 wt % gold crucible and heated for 2 hours at 1400 °C. Glass melt was then quenched in deionised water and coarse frit was obtained. This frit was then dried at 100 °C. Melting temperatures of 45S5, 13-93 and chemically mixed Ga_2O_3-45S5 were also 1400 °C. However, the melting temperature for P-40 glass was 1150 °C, while the preparation time was 1.5 hours. Platinum-rhodium crucible was used to make this glass (Birmingham Metal Company, Birmingham, UK).

3.2 Grinding of Glass

PM-100 ball mill (Retsch1-5, Germany) was used for milling of all glasses. PM is the abbreviation for the planetary mill and it owes its name due to the planet- like movement of its jars. Jars are arranged on a rotating disk while these rotate around their own axis due to a special mechanism. The centrifugal forces produce by rotating vials and the rotating support disk act on the content present in the vials. This content consists of the material to be ground and the grinding balls. Since the disk and vials

rotate in opposite directions, hence the centrifugal forces act in the same and opposite directions. This causes the grinding balls to run down along the walls of the vials producing a friction effect, followed by the material being ground. Also, the lifting off and then travelling freely inside the chamber and colliding against the opposing inside walls produce an impact effect (Figure 3.1). In a single mill, there can be one, two or four vials. The grinding jars and balls are available in different types of materials, such as silicon nitride, agate, zirconia, tungsten carbide, chrome steel, Cr-Ni steel, sintered corundum and plastic polyamide.

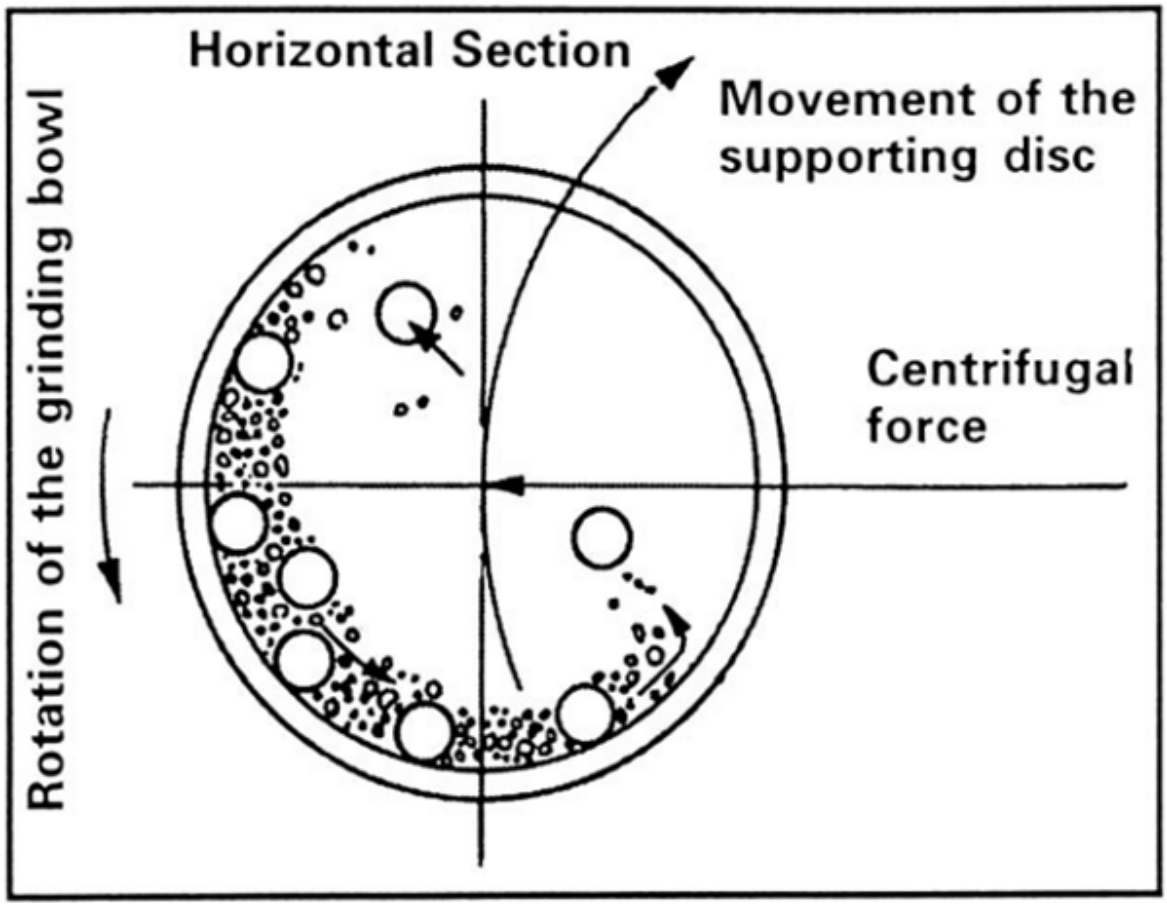

Figure 3.1: *A schematic diagram showing the movement of balls inside the mill [212].*

The 45S5, ICIE16, 13-93 and Ga_2O_3 incorporated 45S5 was milled in 150 ml zirconia jar with 5 mm diameter zirconia balls for 30 minutes at 550 rpm. A second ball milling step was performed with 2 mm diameter zirconia beads for 30 minutes at 500 rpm. For P-40 glass, the first step of ball milling was performed for 30 minutes at 450 rpm with 5 mm diameter balls, and the second step of milling was done again for 30 minutes

at 350 rpm with 2 mm diameter zirconia beads. In all case balls to materials weight ratio was kept at approximately 5. Results for the first step of ball milling for all of the materials are given in Table 3.3.

Table 3.3: *Particle size after 1st step of ball milling.*

Materials	$\mathbf{D_{10}}$**(**μ**m)**	$\mathbf{D_{50}}$ **(**μ**m)**	$\mathbf{D_{90}}$ **(**μ**m)**
45S5	2	21	55
ICIE16	1.8	8.3	24
13-93	1	4	20
Chemically mixed Ga_2O_3-Bioglass®	2	16	51
P-40	1.5	12	48

3.3 Particle Size Measurement

Particle size was analysed by using laser diffraction (Beckman Coulter, USA) having a 750 nm laser. Particles are dispersed in water and in a micro volume cell. The added particles should be 8- 10 % of the volume of the liquid in the chamber. The laser is scattered by particles when they move in the medium. The particles are continuously stirred during measurement. Small particles scatter light at a large angle and vice versa (Figure 3.2). The particle size distribution is measured by measuring the scattered laser pattern. The critical component of this instrument is the Fourier lens, which focuses the incident beam and prevents its interference with the scattered light. Also, this lens transforms the scattered light into a function of location in the detection plane. The scattered light's intensity and pattern are analysed to determine the particle size by using Mei theory [245]. This theory depends on the characteristics of suspending media and the particles. The analysis gives the particle size as the diameter of the equivalent sphere volume.

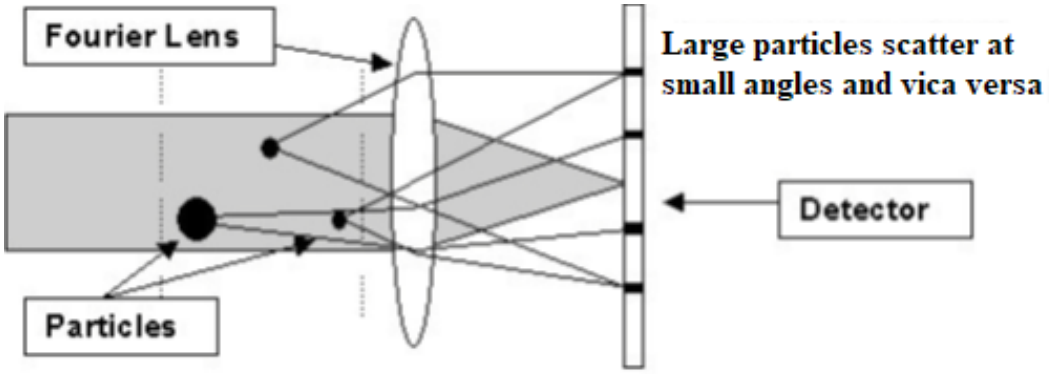

Figure 3.2: *Working principle of Coulter diffractometer, light scattering through different size of particles (μm) [245].*

3.4 Suspension Preparation

45S5, ICIE16, 13-93 and Ga_2O_3 doped 45S5 suspensions were made in mixed suspending media of water and isopropanol alcohol (IPA) with 85 wt % water and 15 wt % IPA [246]. water alone was not used as a suspending media for suspension preparation as water leaches out alkali and alkaline oxides from the glass [210, 219]. For 45S5 suspension, the solid loading was 8 wt %, while for ICIE16, 13-93 and Ga_2O_3 doped 45S5 the solid loading in the suspension was 10 wt %. For P-40 glass, water was used as suspending media with 10 wt % solid loading.With this solid loading, the suspension was for the time duration which was enough for spray. The suspensions were made by using electric stirrer (IKA® RW 20 digital dual-range mixer system, Cole-Parmer UK). The suspensions were stirred at 1000 rpm for 1 hour at room temperature.

3.5 Substrate Preparation

A good substrate is a pre-requisite for good quality coatings, as the adhesion of the coating is critical. 304 stainless substrates with a nominal composition of 9.25 Ni, 19.0 Cr, 1.0 Si, 2.0 Mn, 0.08 C, 0.04 P, 0.03 S and 68.6 Fe—all in wt % were used for coating deposition as it is less expensive in comparison to Ti and its alloys which are commonly used for the implant production. The thickness of the substrates was 2 mm, while these were 25 mm wide and 60 mm long. Substrates were first grit blasted using

Guyson blast cleaner, UK, with F100 brown alumina (0.125–0.149 mm) particles at 3 bar pressure. After this, substrates were cleaned with the industrial methylated spirit (IMS) in an ultrasonic bath for 10 minutes to remove any embedded alumina particles. These substrates were then mounted on twelve substrate holder carousel rotating at 73 rpm.

3.6 SHVOF Thermal Spraying

The SHVOF spray (Figure 3.4) consists of the following units:

3.6.1 Gas Supply and Flowmeter

The gas supply unit controls the pressure and flow of oxidant and fuel gas. Oxygen was used as an oxidant, while hydrogen was used as fuel. The pressure of these both gases may be adjusted using regulators attached to each of the gas cylinders. These cylinders are kept outside of the spray room for safety reasons. Gases are sent to the flowmeters given in Figure 3.3. The flowmeters here are actually rota metres, which consists of graduated tubes with a float in. These floats travel freely inside the tubes depending on the gas's flowrates. The gas flowing in the tube causes the float to the point of dynamic balance. With the increase of flow area, the float rises, while with the decrease, it goes down. Flowrates of these gases are adjusted according to the spray conditions and depending on the material to be sprayed.

Figure 3.3: *Gas flow meter control unit.*

3.6.2 Suspension Feeding Unit

The suspension feeding unit is a self-contained unit, which is designed to deliver suspension to the gun at specific flow rate. This unit consists of two vessels, one is for the cleaning liquid, and the second is for the suspension, which has of the capacity of 2l (Figure 3.5). There is a regulator with the assembly (Figure 3.5) with which sus-

pension flow rate may be adjusted by using an ultrasonic flow meter (ES – FLOWTM Bronkhorst, Nether Land) (Figure 3.5). This flowmeter can measure volume flow in the range of 4 - 1500 ml/min at operating pressures up to 10 bar. It has an ultrasonic flow sensor with a measuring probe which is protected with IP66/IP67 and equipped with LCD display. The touchscreen is there for adjustment of flow indication, alarm and control (if applicable). The feeding unit has a stirrer to continuously stir the suspension throughout the process to prevent sedimentation of the dispersed material while spraying.

3.6.3 UTP Top Gun

UTP top gun (UTP/Miller Appleton, WI, USA) is the main component of the SHVOF thermal spray (Figure 3.6). The gun consists of four parts; combustion chamber, mixing block, water circulation system and suspension injector. Fuel gas, oxygen and suspension enter the back end of the gun and pass through the combustion chamber and mixing block. In the water circulation system, cooling water circulates, which also enters at the back of the gun. The suspension injector has a diameter of 0.3 mm which injects suspension at the centre of the combustion chamber. The length of the combustion chamber is 22 mm with a 110 mm long barrel nozzle [247].

3.6.4 Substrate Holder

The substrate holder has a capacity of holding 12 samples for coating. This holder rotates at a speed of 75 mm/s.

3.6.5 Traverse Unit

A semi-automated system is used to control the spraying distance and number of passes of coating, which is called traverse unit (Trav 1200). This system can move up and down with a speed of 5 mm/s.

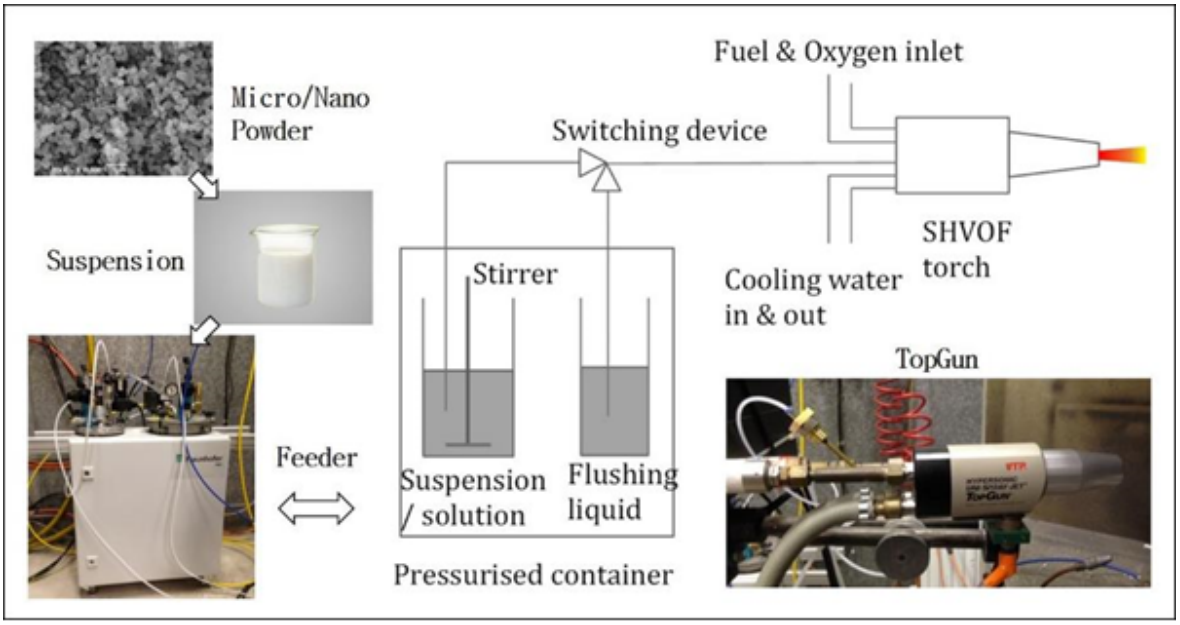

Figure 3.4: *Schematic diagram showing of SHVOF spraying set up [248].*

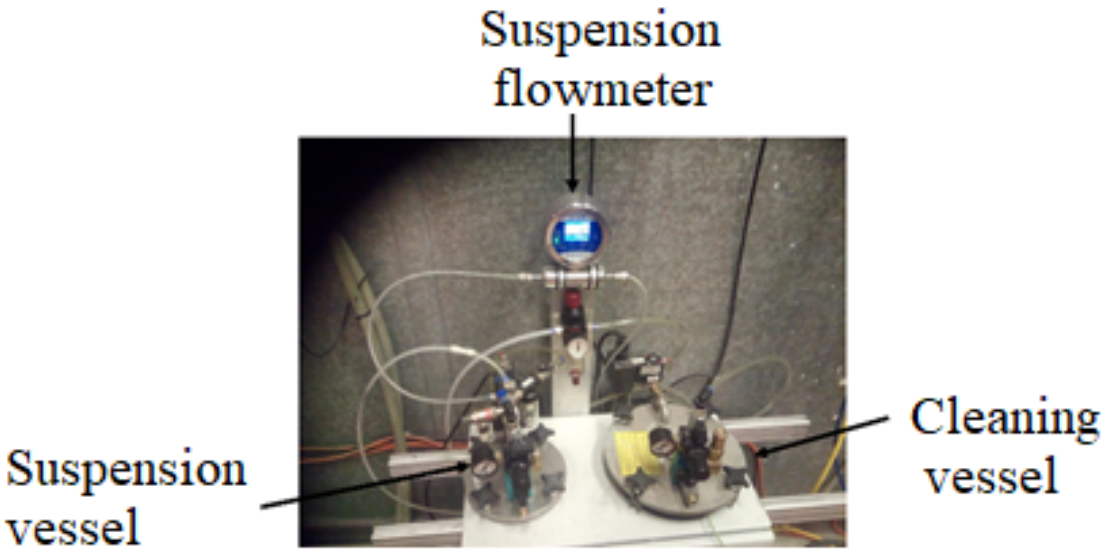

Figure 3.5: *Suspension feed unit.*

Figure 3.6: *Different parts of UTP top gun for SHVOF spraying.*

3.7 Coating Deposition

In this work, 5 different compositions were sprayed: 45S5, ICIE16, 13-93, P-40 and chemically mixed Ga_2O_3-Bioglass® (45S5). 45S5 was sprayed first as this is the common bio silicate glass. Different runs were made by changing oxygen and hydrogen flowrates, while spraying distance (85 mm), feed flow rate (50 ml/min) and the number of torch passes (20) were kept constant.

3.7.1 Bioglass® (45S5) Deposition

Four depositions of 45S5 were sprayed using the flow rates of hydrogen and oxygen given in Table 3.4. Theoretical flame power (kW) was calculated by using standard combustion formulae and each coating is labelled according to their theoretical flame energy.

Table 3.4: *Spray parameters for the deposition of 45S5.*

Run. Number	**H_2 flow rate (slpm)**	**O_2 flow rate (slpm)**	**Flame power (kW)**
1	182	77.9	25
2	355	152	50
3	527	226	75
4	695	249	90

3.7.2 ICIE16, 13-93, P-40 and Chemically mixed Ga_2O_3-Bioglass® coatings

After spraying 45S5 at four different parameters (flame power), 2 spray parameters were optimised:flame powers of 50 kW and 75 kW. ICIE16, 13-93, P-40 and Ga_2O_3 doped 45S5 were sprayed at the optimised 50 and 75 kW flame powers.

3.7.3 Coating Deposition via Hybrid Nozzle

1 wt % Ga_2O_3 suspension in water and 10 wt % Bioglass® suspension (85 wt % water and 15 wt % IPA as a suspending media) were co-sprayed via hybrid nozzle (Figure 3.7). Bioglass® suspension was axially injected at a flow rate of 50 ml/min,whilst, the Ga_2O_3 suspension was radially injected at 25 ml/min flow rate. The depositing flame power was 50 kW.

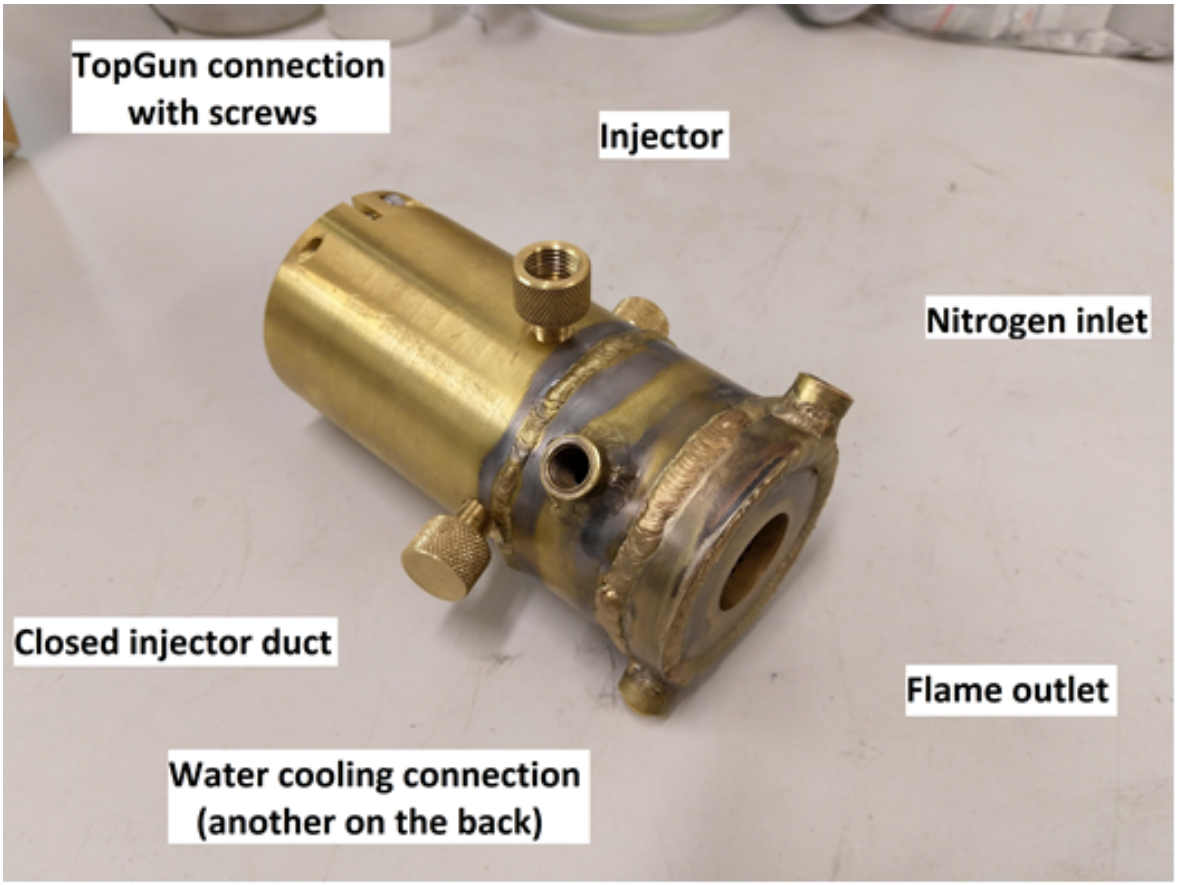

Figure 3.7: *The hybrid nozzle, a thermal spray attachment.*

3.8 Coatings and Powders Characterisation

3.8.1 Scanning Electron Microscopy SEM

A scanning electron microscope (SEM) focuses a beam of electrons on the area to be examined. After the interaction of the electrons with materials, different types of signals are produced, including secondary electrons, back-scattered electrons and characteristic x-rays. These signals are produced from specific emission volumes in the sample and may use to examine the surface topography and/or elemental composition of the material [249]. Typically in SEM the electron beam is produced by thermionic from the cathode, which is usually tungsten. Electron are accelerated by applying a voltage that usually ranges 0.2 keV to 40 keV, with the value depending on the sample being scanned. High-resolution images can be obtained by applying high voltage; however, if the samples are unstable or biological might be damaged if high voltage is

applied.

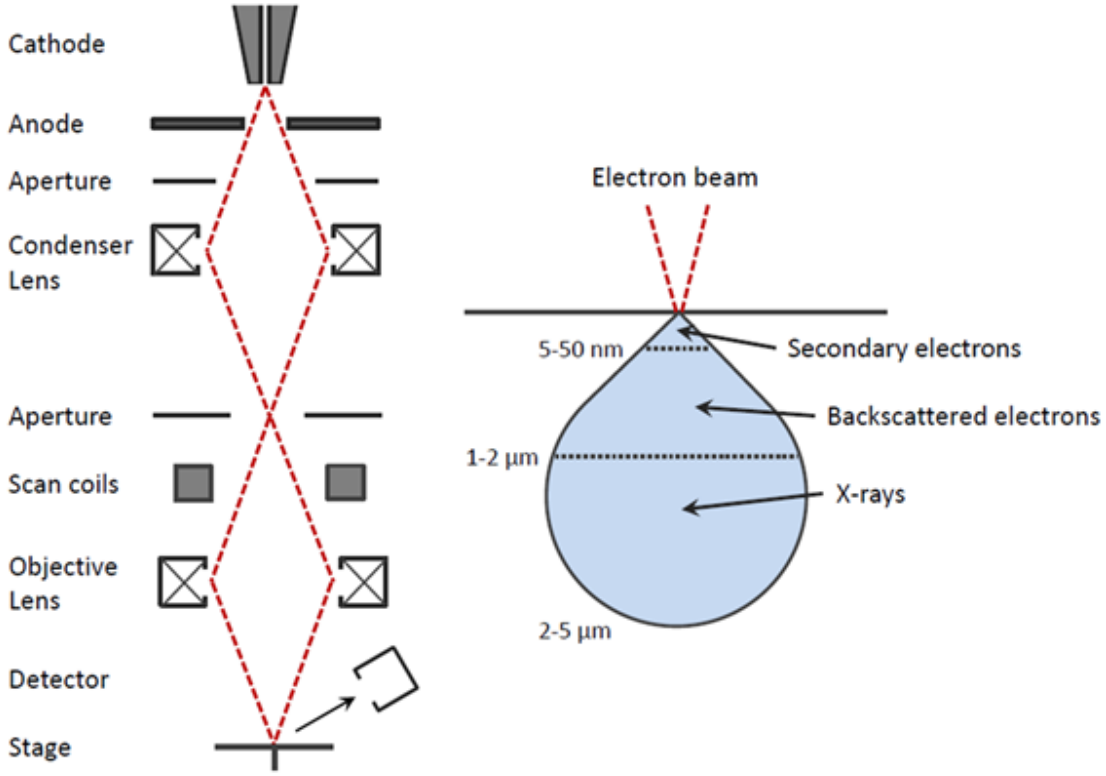

Figure 3.8: *Right image is the schematic of the electron microscope, the left image shows the interaction volume of and depth of penetration of electrons [250].*

Apertures, condenser and objective lenses are used to focus electron beam on to the sample to a spot of about 0.4 to 5 nm. For the scanning of the sample, the beam is deflected by the scan coils to interact with the sample. The size of the interaction volume depends on the applied voltage e.g. high voltage will result high volume of interaction. When the elements are of high atomic number, the large atoms will stop the electron from penetration. Secondary electrons are generated from the first few manometers of the sample (Figure 3.8) and thus make an image showing the sample's surface architecture. Whereas the backscattered electrons give information about the chemical composition of the sample as these are coming from much deeper within the sample, and also the signals depend on the atomic number. X-rays are detected using in-situ energy-dispersive X-ray spectroscopy (EDX). This gives information about the chemical composition of the sample where the beam is focused.

In this study, Quanta-600 and JEOL 6490 SEM were used to examine the coating

microstructure under secondary electron (SE) mode. EDX line scan along with the cross-section of coatings, area scan on the surface of the coatings, and point analysis for powder was done using SEM (JEOL 6490, Tokyo Japan, EDX: INCA 350, Oxford Instruments, Abingdon, UK). The accelerating voltage was 20 kV, spot size was 4 and the working distance was 10 mm.

3.8.2 Sample preparation for SEM

Sample preparation is required for the SEM characterisation of coatings as glasses are non-conductive. To observe the powder morphology a representative sample was placed on to carbon sticky tabs on steel mounts stub and carbon coated (using Edwards Coating System E306A) for 2 minutes. Also, the as-sprayed coatings were carbon-coated to observe the surface morphology. For the observation of the cross-sectional view of the coatings, these were cut transversely with SiC cutting disc using a precision cutting machine (Brilliant 220, ATM GmbH, Mammelzen, Germany). Then the cross-sectional samples were mounted in conductive resin of Bakelite . Then the cross-section samples were ground and polished to 1 μm using diamond paste. The cross-sectional samples were then carbon coated too for SEM observation.

3.8.3 X-ray Diffraction (XRD)

XRD is used to determine the crystalline phases within a material by using monochromatic X-rays. These X-rays are generated by the bombardment of electrons of the copper source to emit electrons from the inner shell and resulting in X-rays are directed towards the samples. After interacting with the material, these X-rays are diffracted depending on the long-range structure of the material (Figure 3.9). A detector determines the angle and scattering of diffracting X-rays for constructive interference, which satisfies Bragg's law (Equation 3.9). These diffractions are specific to the lattice parameters of material and results in a characteristic diffraction pattern. In Equation 3.9 'd' is the space between lattices, 'θ' is the incident angle of X-rays, whilst 'λ' is the X-rays wavelength and 'n' is any integer. From these information, crystal size and

structure may be determined.

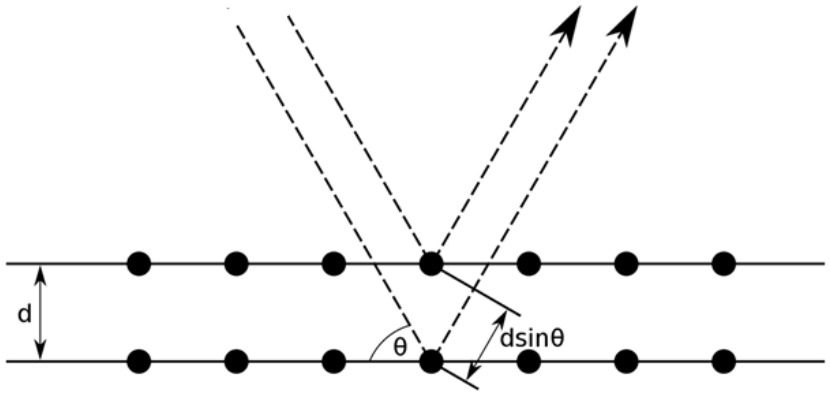

Figure 3.9: *Bragg diffraction from a cubic crystal lattice.*

$$2dSin\theta = n\lambda \tag{3.9}$$

In this study all the XRD analysis was carried out using Bruker D8 Advance, (Cu Kα source, λ = 1.5418 Å, 40 kV, 35 mA). Powder of the melt quenched glasses was flatly pressed into a sample holder, while the coated samples after thermal spray and the samples following SBF tests were centred and placed horizontally into the sample holder. For 45S5 glass and coatings after spray and SBF tests, the samples were scanned for 2θ range of 20° to 70° with a step size of 0.1° and dwell time of 3 s. for other glasses, the samples were scanned with a step size of 0.05° and dwell time of 7 s. Phase identification and peak matches were made using Eva software.

3.8.4 Raman Spectroscopy

Raman spectroscopy is a light scattering technique, a high-intensity laser light gets scattered when incident on a molecule. This technique provides information about chemical structure, phase and molecular interactions. The scattering of light depends on the interaction of light with the bonds in a molecule (Figure 3.10). After interaction with the molecule, most of the scattered light is of the same wavelength as the incident light and which is called Rayleigh Scatter- this does not provide any information about the sample. However, 0.0000001 % of the incident light scatters with a different

wave length than the original,which depends on the molecule under investigation - this scattering is called Raman Scattering [251].

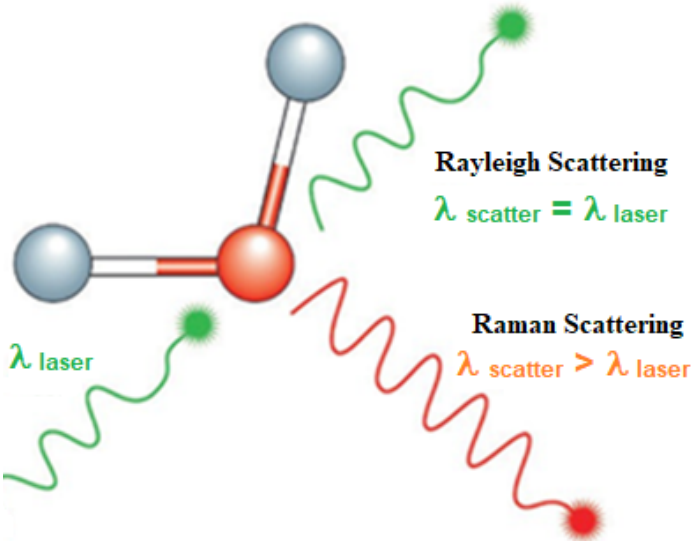

Figure 3.10: *Raman principle [252].*

Raman usually consists of the following four components

- Excitation source which is laser
- Illumination arrangement for the sample and optics for light collection
- Selector for the wavelength, which is a filter or a spectrophotometer
- Detector

A laser beam in the ultraviolet (UV), visible (Vis), or near-infrared (NIR) range is used to illuminate the sample. A sample is illuminated with a laser, and the scattered light is collected with a lens. Then this light is sent to an interference filter or spectrometer to get a spectrum. In this study, HORIBA Jobin Yvon LabRAM (Japan) HR spectrometer was used. 532 nm laser was used as the excitation source, while a 100× objective, 300 μm confocal pinhole and 600 diffracting gratings were used for the collection of spectra. Spectra were recorded for 15 s and 20 accumulations. Raman spectra were acquired for the powder, coatings and after SBF tests of the coatings. Also, commercial HA was analysed using Raman for a direct comparison with the HA deposited on the surface of the coatings [251].

3.8.5 Micro Hardness Measurements

Hardness of the coatings was measured using Vickers tester (BUEHLER, UK). All the tests were carried out on the polished cross-sectional surfaces of the coatings by applying a load of 25 gf for 30 sec in 5 different regions of the coatings.

3.8.6 Surface Profilometry

The surface roughness (Ra) following coating deposition was measured by using two techniques. For 45S5 coatings, Ra was measured by using Zygo NewView 8300. This coherent scanning interferometer (SCI) is 3D optical surface profiler and provides versatility in non-contact optical surface profiling. This technique is non-destructive and requires no sample preparation. The interferometer was used in a white light mode with 5.5× objective at 0.5× zoom (NA 0.15, a field of view (3.02 × 3.02) mm. Also, the LR- pixel was 2.95 μm, and LR-optical was 1.82 μm where LR is the lateral resolution. For each sample five fields of view were measured at various position across the sample by using Zygo proprietary software.

For coatings other than 45S5, the contact technique of form Talysurf Intra was used, which is a stylus profilometer. This instrument measures vertical displacement by using an inductive (LVDT) gauge over profile lengths of up to 50 mm. In this research, Talysurf Profilometer (Taylor Hobson Ltd, UK) was used which has a stylus radius of 2 μm. Also, the sampling distance was 0.5 μm in the scan direction, while the speed of the stylus was 0.25 mm/s.

3.8.7 Porosity and Thickness Measurement

The porosity of each coating was analysed from five SEM (SE) images (270 x 232 μm) using thresholding technique in image-J software (NIH, USA). Coating thickness was measured with the same software at five different locations by using SEM images (134 x 117 μm) of the polished cross-sectioned coatings.

3.9 Simulated Body Fluid SBF

A simulated body fluid (SBF) test is used to assess the acellular bioactivity of the bioactive materials (chapter 2). , The deposition of HA on the surface of the material is an indication of its bioactivity. SBF was prepared by using the standard method outlined in ISO 23317:2014 [253]. The reagents used in the preparation of SBF are shown in Table 3.5, these were added in the order as given in table. During preparation, the temperature was maintained at 37 ± 1 °C by using a heated water bath, while pH was adjusted at 7.40 ± 0.01 by adding 1 molar HCl through a drip- feeder. During preparation, the solution was magnetically stirred in a scratch-free polymer beaker. The SBF was filtered at room temperature using a 20 μm particle filter. The samples were placed in a specific volume (Vs in mm^3) of SBF in polyethylene vials, while Vs= Sa/10 such that Sa (mm) is the surface area of the sample. These samples were incubated at 37 °C and 5 % CO_2 for 1, 3 and 7 days. After soaking for one-time point, the samples were not soaked again. After removing the SBF samples, these were washed with distilled water and dried at room temperature. These samples were then analysed using SEM, XRD, and Raman for the assessment of HA.

Table 3.5: *Chemicals used for the preparation of 1 litre SBF [253].*

Number	Reagent	Amount
1	NaCl	8.035 g
2	$NaHCO_3$	0.355 g
3	KCl	0.225 g
4	$K_2HPO_4.3H_2O$	0.225 g
5	$MgCl_2H_2O$	0.311 g
6	1.0 Molar. HCl	39 ml
7	$CaCl_2.2H_2O$	0.292 g
8	Na_2SO_4	0.072 g
9	Tris ($(HOCH_2)_3CNH_2$)	6.118 g
10	1.0 Molar HCl	0 ml to 5 ml

3.10 Biological Characterisation of ICIE16 and 13-93 Bioactive Glass Coatings using MG63 Cells

Human osteoblast-like cells, MG63 were used for the cytotoxicity and cytocompatibility tests of the coatings. These cells are derived from osteosarcoma. Two time points of 3 and 7 days were used for cell tests.

3.10.1 Sample Cutting, Cleaning and Sterilisation

10 mm discs were cut from the coatings using an Ormond 5 axis waterjet cutting machine (Ormond LLC, Washington) with a 1 mm diameter nozzle. The pressure of the water was 3000 bar, while abrasive feed was 125 g/min, and cutting speed was 600 mm/min.

Before cell seeding, all the samples were cleaned and sterilised. Successive washes were done for the samples by using acetone, isopropanol and distilled water in an ultrasonic bath for 5 minutes each. Two more washes to remove any of the debris which might come from the sample cutting procedure. After this cleaning, the samples were washed with 70 % IMS for 5 to 10 minutes and then were placed in a hood for ultraviolet (UV) sterilisation. The sterilisation time was 30 minutes for each side.

3.10.2 Cell Seeding

MG63 cells (passage 6) in a confluent flask were washed with PBS. Then 1 ml of the enzyme solution (containing 100 ml sterile PBS, 1.5 ml of Trypsin (0.2 % Trypsin with Ethylene diamine tetra-acetic acid (EDTA)) was used to detach cells from the flask surface. Samples were placed in a 48 well plate. The cell suspension (µl) with density (40,000 cells/cm^2) (calculated from a cell count formula) was added to each of the sample. Also, cells were seeded to four empty wells for the tissue culture plastic control. 500 μl of the media (which consists of 500 ml of DMEM (Dulbecco's Modified Eagle Medium); Foetal Bovine Serum (50 ml); L-Glutamine (5 ml); antibiotics-antimycotics AA/AM (10 ml); HEPES buffer (10 ml); non-essential amino acids (5 ml) and ascorbic

acid (75 mg)) was added to each of the well. The well plates were then incubated at 37 °C in 5 % CO_2 atmosphere. After 1 day of seeding, the media was changed and then after every 2 days media was changed.

3.10.3 Alamar Blue Assay

Alamar blue assay which is a non-destructive technique to the cells and is used as cytotoxicity test. This test can quantify cell metabolic activity and thus evaluates cell growth and proliferation. Alamar blue is a dye and cells metabolic activity results in the reduction of the active component resazurin of the alamar blue to resorufin (Figure 3.11). Alamar blue spread into the cells reduced to a fluorescent dye. The concentration of the fluorescent dye is proportional to the number of viable cells. The rate of cell proliferation is analysed by the difference of cell relative fluorescence intensity at each time point.

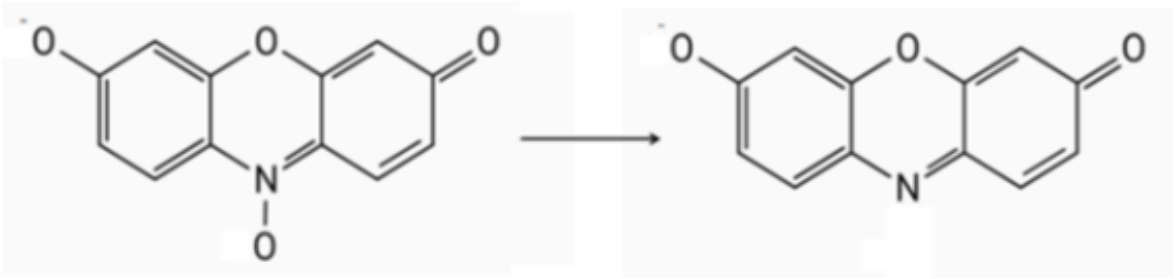

Figure 3.11: *Reduction of resazurin to resorufin.*

Before adding the alamar blue assay,, the samples were washed three times with PBS to remove any of the culture media. This was done for both time points. 1:10 ratio of the alamar blue with HBSS (Hanks Balanced Salt Solution) was used for the tests and of which 1 ml was added to every sample to submerge the samples. For the blank control, three empty well plates were filled with the solution. Samples were then placed in an incubator for 90 minutes. Then the samples were placed on the shaker to shake at 150 rpm for 10 minutes. Three aquilots of 0.1 ml of alamar blue were taken from each sample and placed in 96 well plates. The fluorescence of the sample was measured using FLx 800 microplate reader (BioTek Instruments Inc). 560 nm

excitation wavelength and 590 nm emission wavelength was used.

3.10.4 Sample Preparation for SEM after Cell Tests

For SEM examination, after each time point cells were fixed and dehydrated. For the removal of the media, samples were washed three times with PBS for 5 minutes for each of the wash. For fixation 3 % Glutaraldehyde in 0.1M Sodium cacodylate buffer (fixative) was added to the samples and kept in fume hood for 30 minutes. Then 0.3 ml of (7 %) sucrose was added to each of the sample and refrigerated overnight at 4°C. Samples were then washed three times with 0.1M cacodylate buffer for 5 minutes per wash. After washing, enough amount of (1 %) Osmium tetroxide was added to submerge samples. For fixation and staining, samples were left for 45 minutes. Then Osmium tetroxide was removed, and samples were dehydrated at steps with 20 %, 40 %, 60 %, 70 %, 80 %, 90 % and 100 % of ethanol. Hexa-methyldisilazane HMDS) was used for 5 minutes to dry samples. After all these steps, the samples were air-dried overnight by replacing the well plate lid with loose aluminium foil. Then samples were then gold-coated by sputtering and examined using JEOL JSM-6490LV SEM.

3.10.5 Statistical Analysis

Prism graph pad (2365 Northside Dr.Suite 560 San Diego, USA) was used for statistical analysis. To analyse data from cell experiments with Tukey post-test, one –way analysis of variance was used to determine the significant effect of the results. A smaller P-value than 0.05 would show significant differences, while a higher value would show no significant differences.

3.11 Degradation of P- 40 Phosphate Based Glass Coatings

9 mm diameter discs were cut from P-40 coatings using water jet cutting machine. These discs were then placed in polyethene vials with 15 ml of ultra-pure Milli Q water

or PBS and were incubated at 37 °C. The samples were kept for 1, 3, 7 and 14 days. At each time point the samples were removed from the solution and dried in an oven at 50 °C for the removal of surface water. The mass of the samples was measured using a Mettler Toledo precision scale accurate to 0.01 mg. The samples were then again immersed until the next measurement time point. The pH was measured before and after degradation when using PBS, while it was measured only after degradation in the case of ultra-pure milli Q water as degradation media. For PBS solution pre-prepared tablets of PBS (Sigma Aldrich) were dissolved in 200 ml of water. The mass was weighed after drying and loss was calculated using the following calculation (Eq: 3.10).

$$\frac{\%Mole \quad Loss}{Surface \quad Area} = \frac{M_o - M_t}{Surface \quad Area} \tag{3.10}$$

Where M_o is the initial mass, M_t is the mass and $Area_t$ is the area of the sample at test time point t.

3.12 Ion Release of P- 40 Phosphate Based Glass Coating

Ion release profiles of the P-40 coatings were determined by immersing 9 mm diameter discs in 15 ml of ultra-pure milli Q water. These tests were carried out for 1, 3, 7 and 14 days at 37 °C. The dissolution medium at each time point was analysed for phosphorus, calcium, magnesium and sodium ions. The dissolution medium was analysed for Ca, Mg, Na and P using Inductively coupled plasma mass spectroscopy (ICPMS).

ICPMS is a mass spectroscopy technique that detects very low metal ions concentration in a liquid sample. The sample is ionised via a high-temperature plasma, and then a mass spectrometer is used for the separation and quantification of those ions. A number of elements can be detected simultaneously with this technique or it can be set to detect the user required elements. The dissolution media was introduced to ICPMS (Thermo-Fisher ICAP-Q, Bermen, Germany) to determine the ion release profiles. This instrument runs employing three operational modes, which are,

- CCTED (collision cell technology with energy discrimination) is typically charged with helium gas and is upstream of the analytical quadrupole to reduce polyatomic interference.
- Standard mode (STD), where the collision cell is evacuated.
- The hydrogen mode cell (H_2-cell), which utilises H_2 gas as the cell gas.

An autosampler (Cetac ASX-520) was used to introduced the samples. The sampler was incorporated with an ASXpress™ rapid uptake module through a perfluoroalkoxy (PFA) Microflow PFA-ST nebuliser (Thermo Fisher Scientific, Bremen, Germany). Internal standards, which are Sc(50 μg l^{-1}), Ge (20 μg l^{-1}) Rh(10 μg l^{-1}) and Ir(5 μg l^{-1}) in the preferred matrix of 2 % HNO_3 were introduced to the sample stream on a separate line via the ASXpress. Instead of HNO_3, HCl can also be used with a similar concentration of 2 %. Calibration standards (external) are usually in the range of 0 – 100 μg l^{-1} (ppb). Sample analysis was done by using 'Qtegra software' (Thermo-Fisher Scientific). While the results were reported as mass weight concentrations (μg l^{-1} or mg l^{-1}) in Microsoft Excel spreadsheet format.

Chapter 4

Process Microstructure Properties Relationship of SHVOF Thermal Spraying of Bioglass®

4.1 Introduction

This chapter presents the processing, microstructure, and Bioglass® coating properties relationship by SHVOF thermal spraying. Process parameters were changed by changing the fuel (H_2) and oxygen flow rates, which ultimately change the flame power. Four spray runs were conducted by applying four different flame powers of 25 (low), 50 (medium), 75 (high) and 99 kW (very high). The as-sprayed coatings were characterised using different techniques such as SEM, XRD, Raman, and surface profilometry. The final section of this chapter reports the bioactivity tests results of the 45S5 coatings using SBF.

4.2 Feedstock Characterisation

4.2.1 Particle Size Distribution and Powder Morphology of the Bioglass® Powder for Suspension Preparation

The first step of ball milling resulted in D_{10} = 2 μm, D_{50} = 21 μm and D_{90} = 55 μm (where Ds is the particle diameter of S % particles). After second step of ball milling size distribution of the Bioglass® powder is given in Figure 4.1 a, and which characterises Bioglass® powder with D_{10} = 1.7 μm, D_{50} = 2 μm and D_{90} = 10 μm, which was used for suspension preparation.

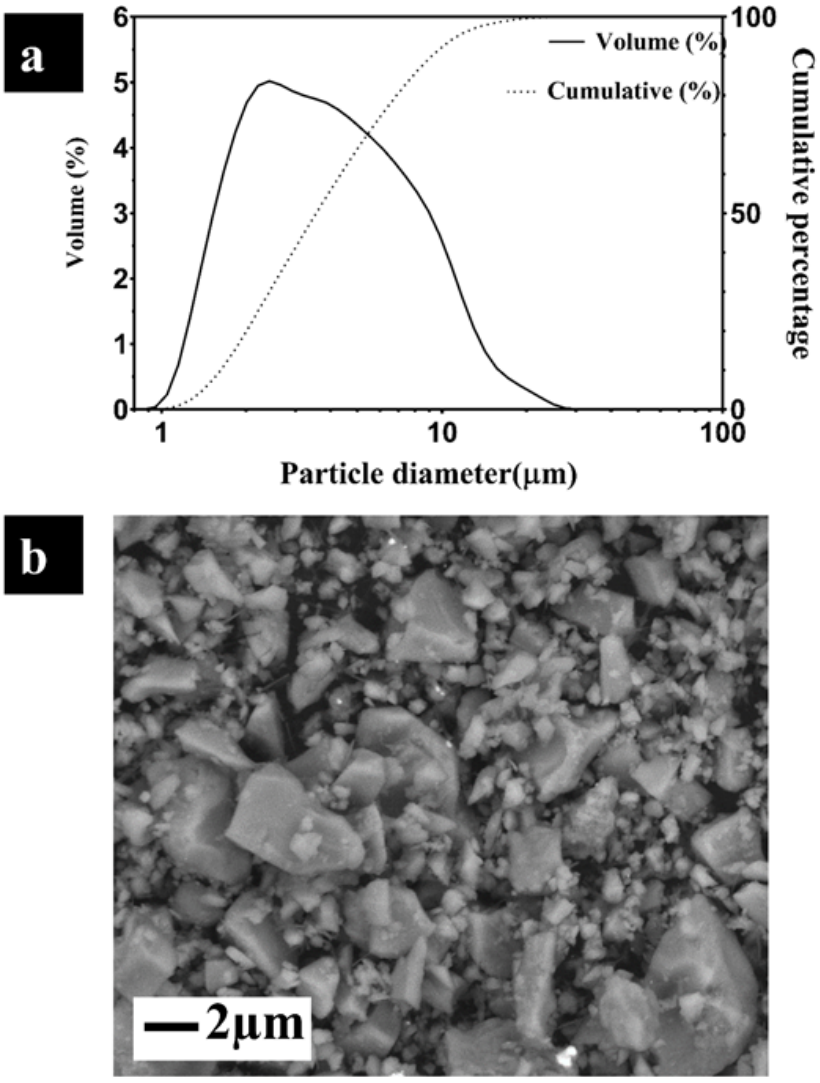

Figure 4.1: *(a) Bioglass® 45S5 particle size distribution and (b) SEM image of ball-milled Bioglass® powder before suspension preparation.*

The particles were distributed with a range of 0.8 μm -27 μm which suggests that the Bioglass® particles were agglomerated. The SEM image (Figure 4.1 b) shows that the Bioglass® powder was a mixture of fine and coarse particles before suspension preparation. Among the coarse particles the largest particle size was $\sim$ 5 μm, while the smallest was approximately 0.3 μm.

4.2.2 EDX of the Powders

EDX point analysis (Table 4.1) showed that the 45S5 powder used for suspension preparation was composed of 19.3 wt % Si, 17.7 wt % Ca, 16.4 wt % Na and 2.2 wt % of P. While for the 45S5 formulation, the wt % of the glass should have 21 wt % Si, 17.5 wt % Ca, 18.75 wt % Na, and 2.4 wt % P. The compositions were observed to vary by 1.7 wt % Si, 0.2 wt % Ca, 2.35 wt % Na and 0.2 wt % P from their intended composition.

Table 4.1: *EDX analysis of the final powder before suspension*

Number	**Elements**	**45S5 powder (wt %)**
1	Si	19.3
2	Ca	17.7
3	Na	16.5
4	P	2.2

4.2.3 XRD and Raman Analysis of Bioglass® Powder

XRD analysis (Figure 4.2 a) showed that the Bioglass® powder was amorphous. The amorphous hump present between 25°- 35° 2θ showed broad diffraction and the absence of any sharp peak, which is the characteristic of short-range order. The Raman spectrum of the 45S5 powder is given in Figure 4.2 b. The peaks observed at $\sim$ 610 cm^{-1} and 1079 cm^{-1} were due to the stretching of Si-O-Si, whilst the peak at 860 cm^{-1} was assigned due to the vibration of non- bridging oxygen i.e., Si-2NBO. The peak at 945 cm^{-1} was assigned to the stretching of PO_4^{-2} [254].

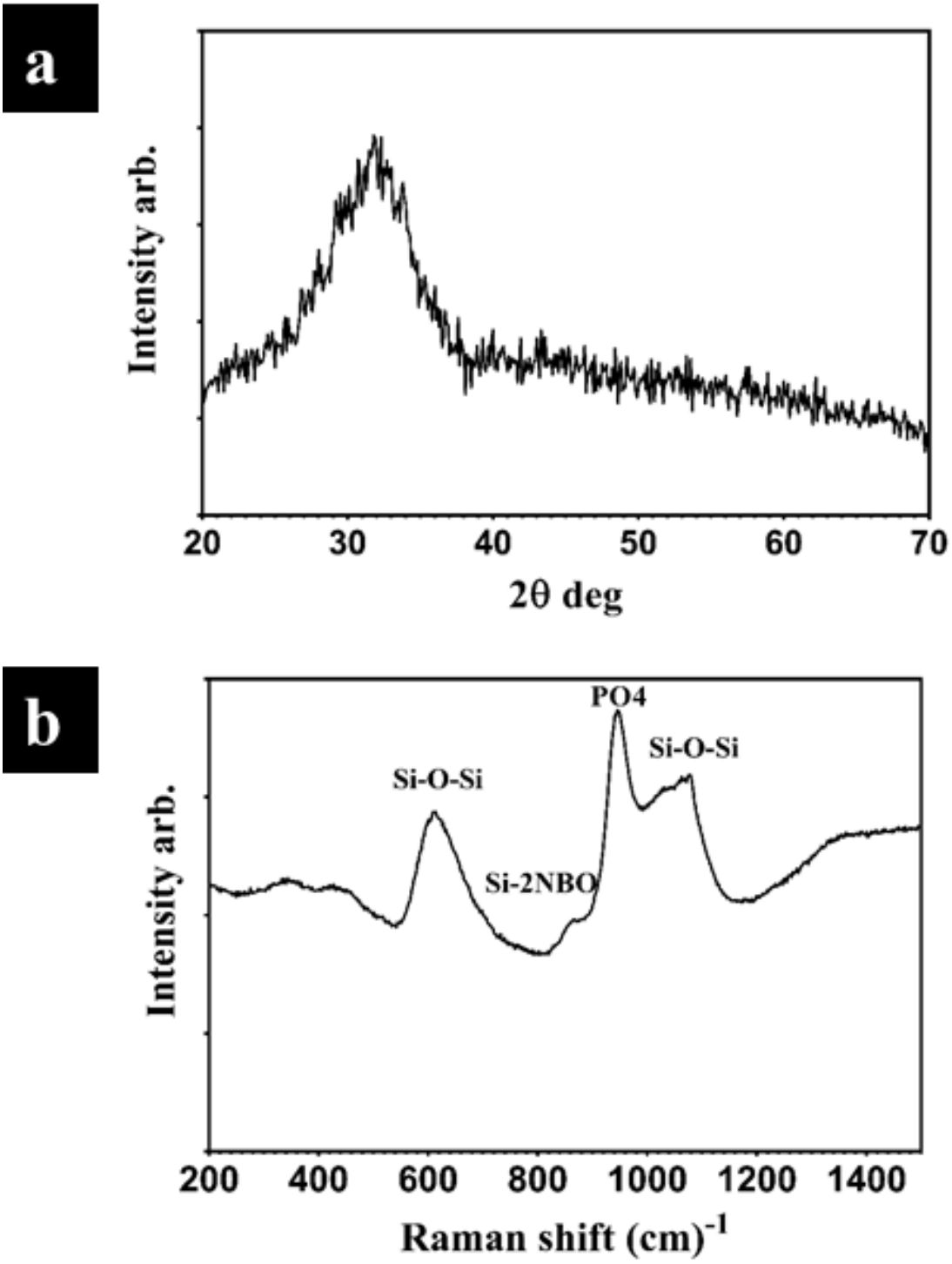

Figure 4.2: *(a) XRD and (b) Raman scan of Bioglass® powder showing its phase and structure*

4.3 As-Sprayed Coating Characterisation

4.3.1 Coating Surface Morphology and Cross-section

The surface morphology of the as-sprayed 45S5 coatings deposited at 25, 50 and 75 kW flame power was examined using SE imaging and is shown in Figure 4.3. Changing flame power from low (25 kW) to medium (50 kW) and then to high (75 kW) had a significant effect on the surface of the coatings. As shown in Figure 4.3, the low magnification image of the 45S5 coating deposited at 25 kW,this coating had a hollow porous sphere-like structures. Also, the higher magnification image of the 25 kW coating (Figure 4.3 d) shows that there were some smaller spheres on the surface of this coating. These spheres might be originated from the impact of slower and partially re-solidified Bioglass® (45S5) droplets. Also, the surface of this coating appeared to be porous due to the presence of these spheres and hollow sphere like structures. The surface morphology of the 45S5 coating deposited at 50 kW contained mostly well-flattened splats, as can be seen in Figure 4.3 b. The presence of these splats indicates that the 45S5 particles during the spray process under the conditions of 50 kW flame power were sufficiently heated and had experienced more significant deformation. The high magnification image of 50 kW coating (Figure 4.3 e) shows that the size of these splats was approximately 5 μm, and also their shape was irregular. Small spheres were also present on the coatings' surface like those present on the surface of 25 kW coating. Also, some large pores were observed on this surface. For the 45S5 coating deposited at 75 kW, large humps were observed on the surface which was evenly distributed over the surface. The size of these humps was approximately 10 μm. The origin of these humps might be the agglomeration of droplets at a higher flame (75 kW). Small round particles were also present on the surface of this coating similar to those present on the surface of 25 kW and 50 kW coatings (Figure 4.3). Figure 4.4 displays the BSE cross-section images of three 45S5 coatings deposited at 25 kW, 50 kW and 75 kW. All three images of the 45S5 coatings (Figure 4.4 a, b, and c.) showed a typical thermal sprayed microstructure. No delamination and cracks along the coating- substrate interface

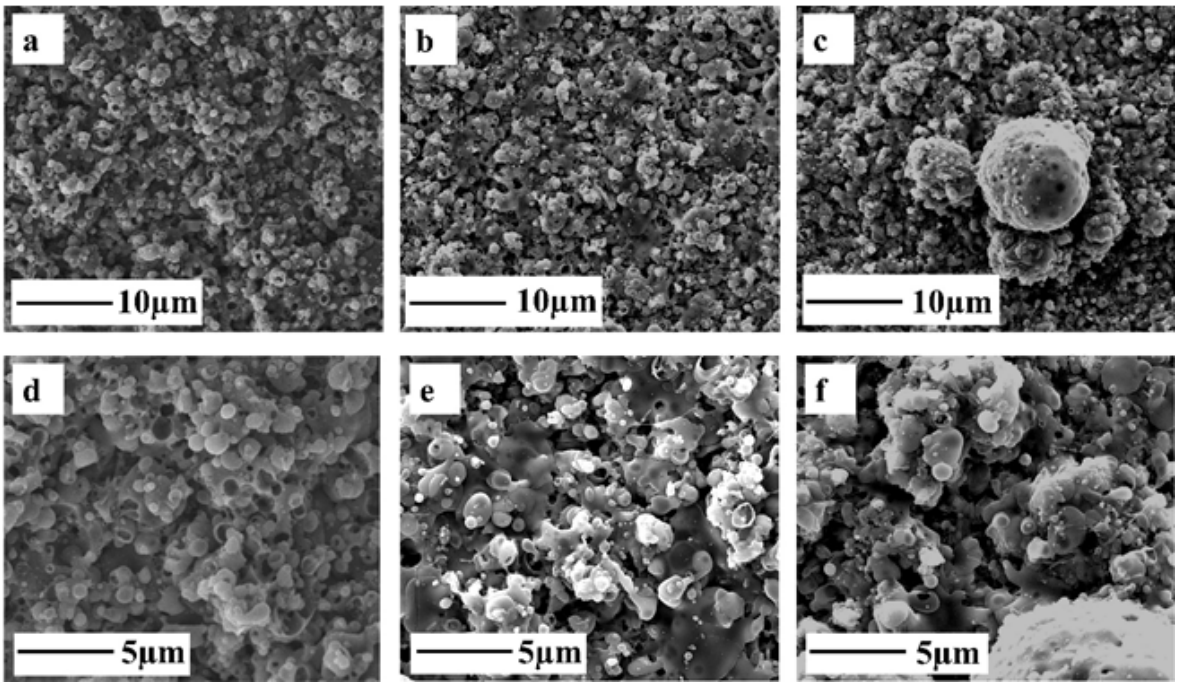

Figure 4.3: *SE, SEM images showing the surface morphology of the coatings deposited at different flame power: 25 kW (a and d), 50 kW (b and e), and 75 kW (c and f). The top row shows low magnification SE images and the bottom row shows high magnification images of the same area.*

were observed in any of the coatings. The coating deposited at low flame power of 25 kW was thin (<10 μm), and its thickness was also not uniform (Figure 4.4 a). The microstructure of this coating suggested that the 25 kW flame power did not transfer enough energy to particles for melting and accelerating them to deposit on to the substrate. That is why at 25 kW the deposition efficiency was impaired, and a thin coating (10 $\pm$ 1 μm) was obtained. Also, 25 kW flame power is the lower end of this HVOF gun's thermal spray, and it is a sub-sonic flame.

A thicker coating of uniform thickness was obtained at medium flame power of 50 kW (Figure 4.4 b). The thickness of this coating was 25 $\pm$ 1 μm; however, this coating revealed to be porous (16 $\pm$ 2 %). Some vertical cracks were observed in this coating which is probably introduced due to thermal stresses; however, there was no delamination along the interface between the coating and substrate. The coating obtained at high flame power of 75 kW was approximately of the same thickness as the coating deposited at 50 kW; however, this coating appeared to be less porous than the 50 kW coating (Figure 4.4 c). The porosity of this coating was 10 $\pm$ 1 %, and

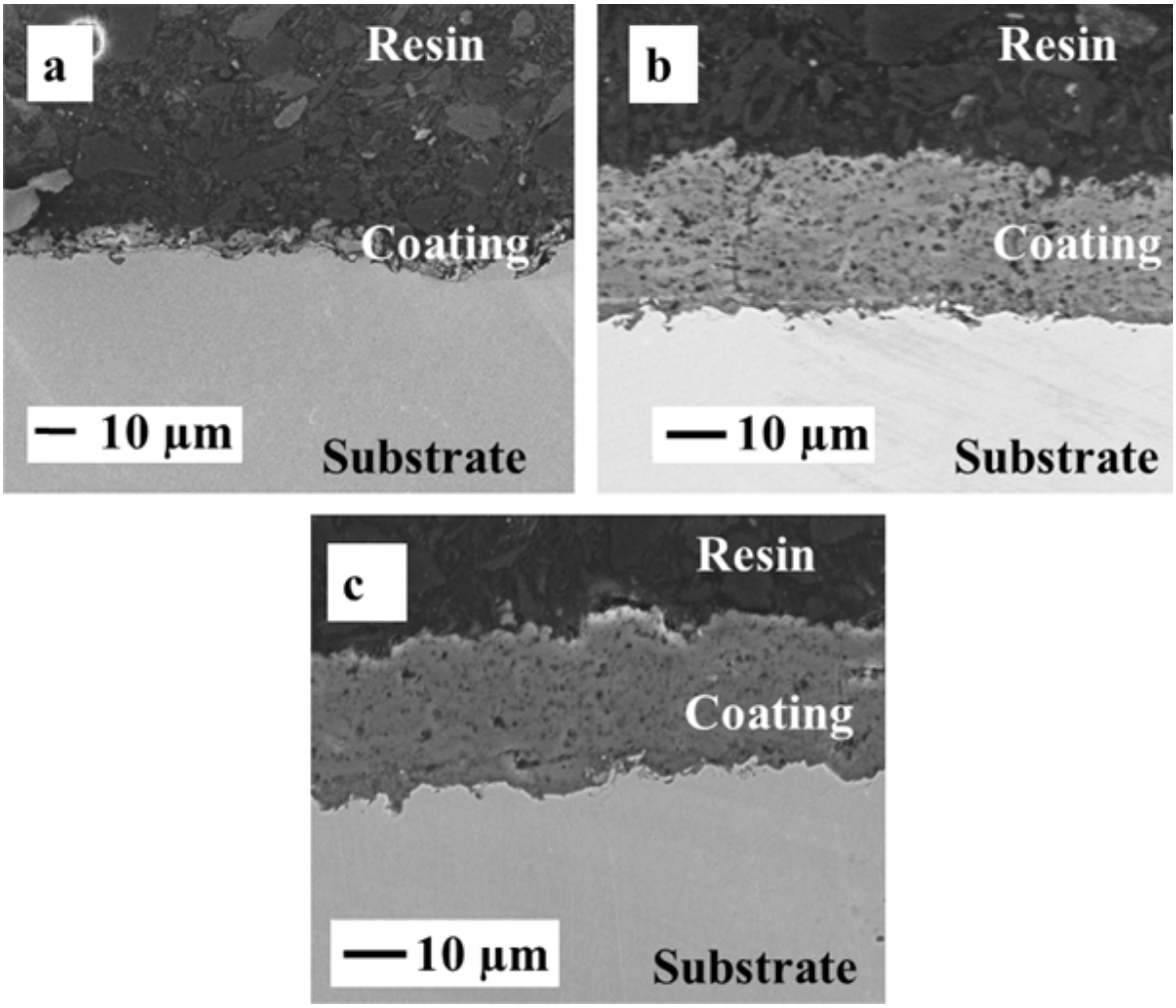

Figure 4.4: *BSE, SEM image of coating cross-section showing the microstructure of the coatings deposited at different flame power: 25 kW (a), 50 kW (b), and 75 kW (c).*

this might be due to the better melting of particles at high flame power. Also, there were no vertical cracks and cracks along the coating- substrate interface observed in the high flame power coating.

4.3.2 Mechanical Properties of 45S5 Coatings

Table 4.2 shows the physical and mechanical properties of 45S5 coatings. It can be seen that with increasing flame power from 50 to 75 kW, micro-hardness was increased from 253 ± 2 HV to 270 ± 1 HV. For the thin coating deposited at 25 kW, it was impossible to measure the micro-hardness as the indicative coating thickness was less than 10 μm. Also, as said earlier both of the coatings deposited at 50 kW and 75 kW flame powers were porous. However, the 75 kW coating was less porous, having a porosity of 10 ± 1

%, than the coating deposited at a medium flame power of 50 kW which had a porosity of 16 ± 2 % (Figure 4.4 b and c). Table 4.2 also shows that the surface roughness (Ra) of the low flame power coating was 2.0 ± 0.1 μm, similar to the Ra of 50 kW coating. However, Ra was 3.0 ± 0.2 μm for the coating deposited at 75 kW coating, which is probably due to humps present on the surface of this coating, making this coating rougher. This high roughness might be advantageous, as its surface roughness increases the surface area available for chemical reactions increase and it favours cell attachment as well [255].

Table 4.2: *Physical and mechanical properties of 45S5 coatings (mean value ± standard error) produced from SHVOF thermal spray (number of measurements=5)*

Run No	**Thickness** (μm)	**Porosity** (%)	**Microhardness** (HV)	**Surface Roughness** (μm)
R25	10 ± 1	-	-	2.0 ± 0.1
R50	25 ± 1	16 ± 2	253 ± 2	2.1 ± 0.1
R75	25 ± 1	10 ± 1	270 ± 1	3.0 ± 0.2

4.3.3 EDX Analysis

To determine the compositional gradient (wt %) as a function of the distance from the coating-substrate interface to the top surface of the coating, EDX analysis was carried out. Results are shown in Figure 4.5 with the corresponding SEM images, where points on the images show the position where the EDX analysis was carried out. The analysis showed that the composition of the Bioglass® (45S5) was varied along the cross-section of the coating after thermal spray while spraying at different flame powers. However, the compositional gradients for all three of the coatings were different. SEM image with the corresponding EDX line scan along the cross-section of the coating deposited at 25 kW is shown in Figure 4.5 (a and b). The Si content was expected to be 19.3 wt % (present in 45S5 powder Table 4.2); however, it was changed to 25 wt % at the coating-substrate interface of 25 kW coating. In the coating, Si content was decreased, and at the top surface of the coating, it reduced to 23.5 wt %,

16.4 wt % of Na was present in 45S5 powder before the spray which was reduced to 11 wt % closer to the coating- substrate interface. It increased toward the top surface, where Na content was 15 wt %. For Ca, the wt % was reduced from the expected 19 wt % to 18 wt %; however, in the coating and at the top surface, variations in Ca content were negligible. The P content was fluctuating around 2 wt % with negligible variations from the substrate- coating interface till the top surface of the coating. Also, some Fe was identified near the interface between coating and substrate, which originated from the substrate surface.

For the coating obtained at the flame power of 50 kW the compositional gradients with the corresponding SEM image are given in Figure 4.5 c and d,, and it can be seen that these gradients were more prominent than those observed for the coating deposited at 25 kW flame power. Si was increased to 25 wt % at the interface between coating and substrate and then started decreasing to 22 wt % at the top surface of the coating. At the same time, Na reduced to 8.5 wt % at the interface, and then increasing to 17 wt % at the top surface of the coating. Variations in the Ca content were again to be more stable as were observed for its content in the 25-kW coating. Variations in Ca content, which were observed during the analysis showed to be increased to 22 wt % at the interface and decreasing to 20 wt % on the top of the coating. A similar trend was observed for P content; it changed to 2 wt % at the interface to 2.5 wt % at the top surface.

Figure 4.5 f, represents the compositional gradients profiles along the cross-section of the coating deposited at high 75 kW flame power. These gradient profiles seem smoother and consistent compared to the gradient profiles of 25 kW and 50 kW coatings. Si variation observed was to increase to 28 wt % at the coating substrate interface and then reduced to 27 wt % till the top surface of the coating. Na wt % was approximately 2, and this 2 wt % remained constant till the top of the coating. Ca was increased to 22 wt % at the coating substrate interface and then started decreasing to 21 wt % at the top of the coating. For P, the wt % was remained constant in the whole thickness of the coating at 2. Though the compositional gradients showed the

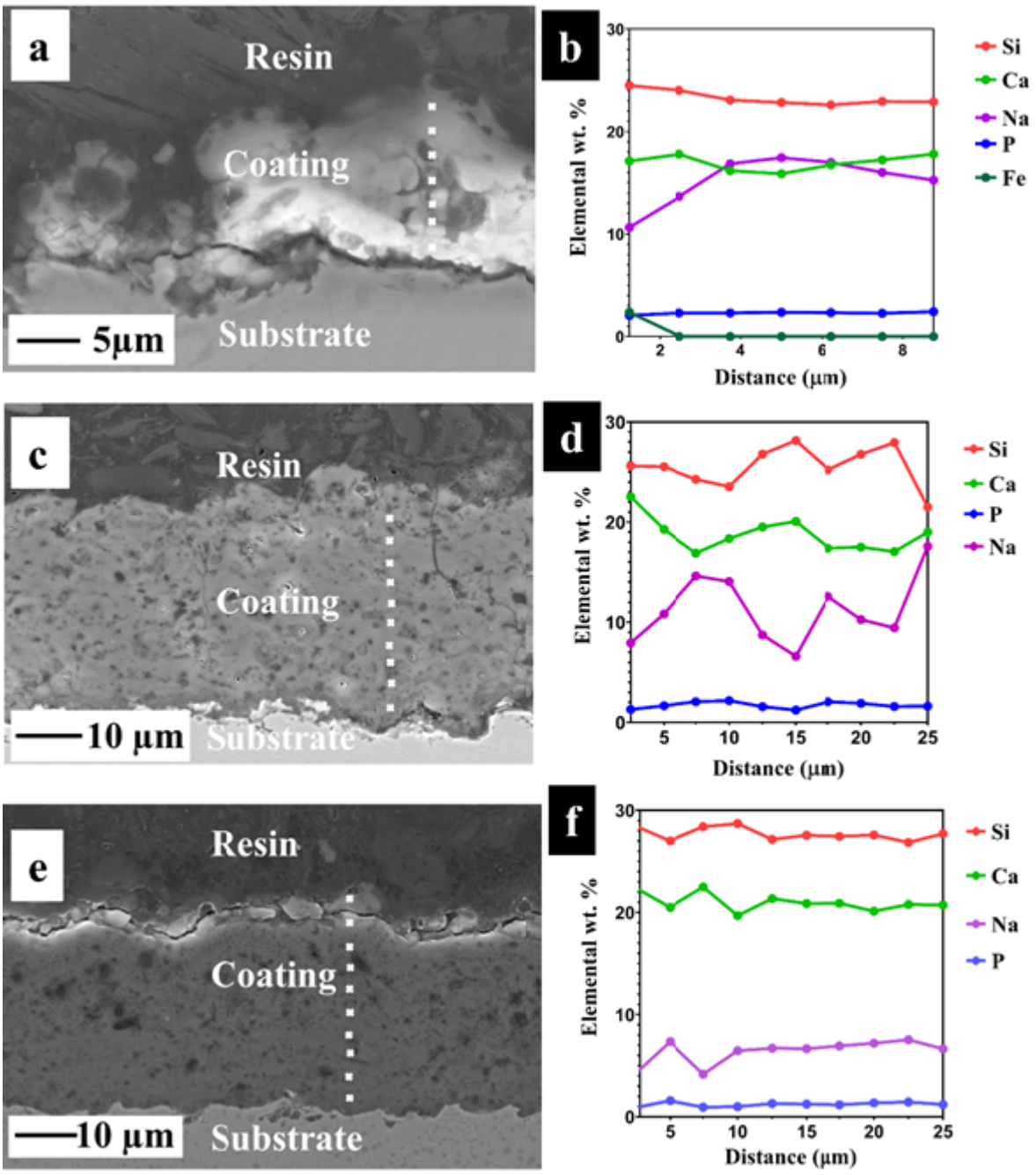

Figure 4.5: *SE, SEM images of the cross-section of coatings deposited at 25 kW (a), 50 kW (c), and 75 kW (e) and their respective EDX line scans through the coating cross-section in b, d and f. Points in the SEM images show the location of EDX data points in the graph (distance is from substrate-coating interface towards coating top surface*

).

least variations along the cross-section of the coating obtained at 75 kW flame power, however the observed composition was different in comparison to the starting original formulation of Bioglass®.

Table 4.3: *EDX area scan on the top surface s of the as- sprayed coatings.*

As-sprayed (wt %)			
Elements	**R25**	**R50**	**R75**
Si	23.5	25.3	27.4
Ca	19.4	20.8	22.5
Na	9.1	9.6	5.4
P	1.8	1.6	1.2
Fe	5.0	0.0	0.0
Cr	0.9	0.0	0.0

Table 4.3 shows the EDX area analysis on the top surface of all of the three coatings. It can be seen that increasing flame power from 25 kW to 50 kW and 75 kW had significantly changed the wt % of the contents of the Bioglass (45S5). Before spray 16.4 wt % of Na was present in the 45S5 powder which was reduced to 9.1 wt % in 25 kW coating, 9.6 wt % in 50 kW coating and 5.4 wt % in the coating obtained at 75 kW flame power. Similarly, the content of P was 2.2 wt % in 45S5 powder and which had reduced to 1.8, 1.6, and 1.2 wt % with increasing flame power from 25 to 50 and 75 kW. However, for Si and Ca the reverse trends were observed with the increase of flame power. Si content was 19.3 wt % in 45S5 powder which increased to 23.5 wt % in 25 kW coating, 25.3 wt % in 50 kW coating and 27.4 wt % in 75 kW coating % weight of Ca increased from 17.7 (present in 45S5 powder) to 19.4, 20.8 and 22.5 wt % with the increasing flame power from 25 to 50 and 75 kW.

4.3.4 XRD and Raman Analysis of the 45S5 Coatings

Figure 4.6 a, displays XRD spectra of 45S5 coatings deposited at 25, 50 and 75 kW. 45S5 experienced no devitrification while spraying at different flame conditions. Indeed,

the absence of any sharp peak and the broad band appearing in 25 - 35° 2θ range of the XRD patterns confirmed that the coatings were composed of glassy phase. The only recognisable peaks which can be attributed to the metal substrate (stainless steel) were austenite (PDF card no. 00-023-0298), and ferrite (PDF card no. 00-006-0696).

Raman spectra of 45S5 coatings and 45S5 powder (for comparison) are given in Figure 4.6 b. As can be seen the coatings' spectra were not different from that of the powder. Also, all of the spectra are consistent with spectra reported by D. Bellucci at.al [256]. The spectrum of coating deposited at 25 kW was similar to that of the 45S5 powder; however, the spectrum of 50 kW and 75 kW coatings were different after 1000 cm^{-1} and 1100 cm^{-1} from that of the 25 kW coating and 45S5 powder spectra. This is probably due to the difference of microstructure. In spectra of the three coatings and 45S5 powder, the peaks which were present at $\sim$ 610 cm^{-1} and 1079 cm^{-1} were associated to the stretching of Si-O-Si groups. These bands are commonly present for silicate glasses belonging to Na_2O-CaO-SiO_2 system [257], and also if silica is reduced in the glass composition, then this shifts to higher wave number [258]. Further, the peak at 860 cm^{-1} was associated with non-bridging oxygen–silica Si-2NBO, which was of the same intensity for all the coatings and glass powder. Also, the peak at 1030 cm^{-1}, which appeared as a shoulder on the right-hand side of the peak at 950 cm^{-1} was assigned to vibrations involving Si_2O_5 with 1 NBO and two-dimensional structures. Other than silica features, the intense peak was present at 950 cm^{-1}. It was associated with the symmetrical stretching of the PO_4^{-2} group [254, 259].

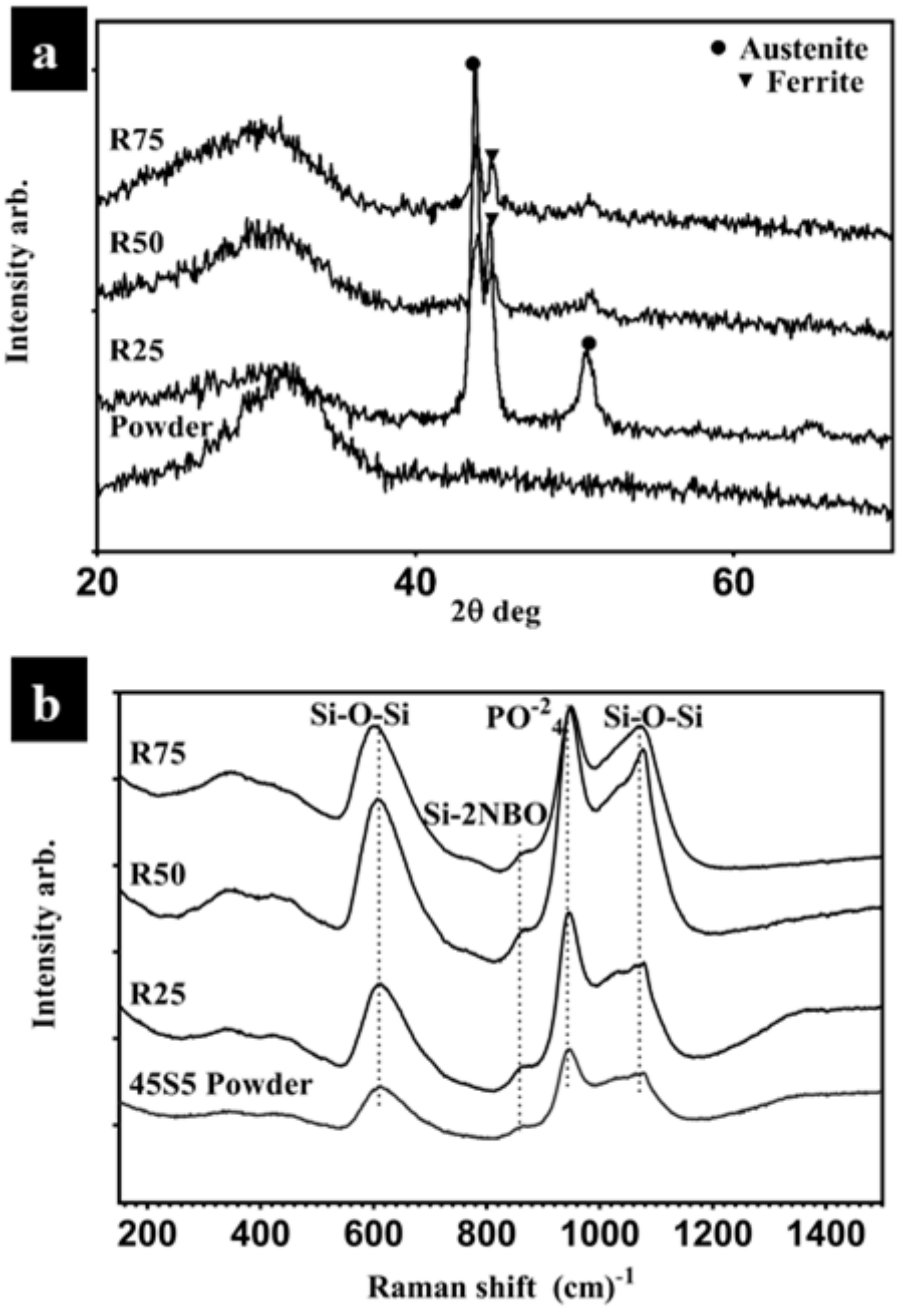

Figure 4.6: *XRD spectra (a) and Raman spectra (b) developed on the surfaces of the SHVOF deposited Bioglass coatings at different flame powers where R25 is 25kW, R50 is 50 kW and R75 is 75kW.*

4.4 SBF Tests of the 45S5 Coatings

4.4.1 SEM Analysis

Figure 4.7 shows the SEM images of the surface morphology of 45S5 coatings after immersing in SBF for 3 and 7 days. After 1 day of immersion of the coated samples in SBF no HA was precipitated on any sample. Also, it can be seen in Figure 4.7 a, that no HA deposition occurred after 3 days of immersion in SBF on the surface of the coating deposited at 25 kW. Also, no HA was precipitated on this coating even after 7 days of immersion in SBF (Figure 4.7 d). However, the samples containing coatings deposited at 50 kW and 75 kW were uniformly covered with a dome - like precipitates after 3 days of immersion in SBF and which is the characteristic for HCA grown in vitro [260] (Figure 4.7 b and e). With the increase of immersion time in SBF the dome- like morphology of the HA film was increased, as can be seen in Figure 4.7 c and f, which corresponds to the 50 kW and 75 kW coating surfaces after 7 days of immersion in SBF, respectively. This suggests that with the increase of immersion, further deposition of HA occurs. After taking out samples from SBF these were washed

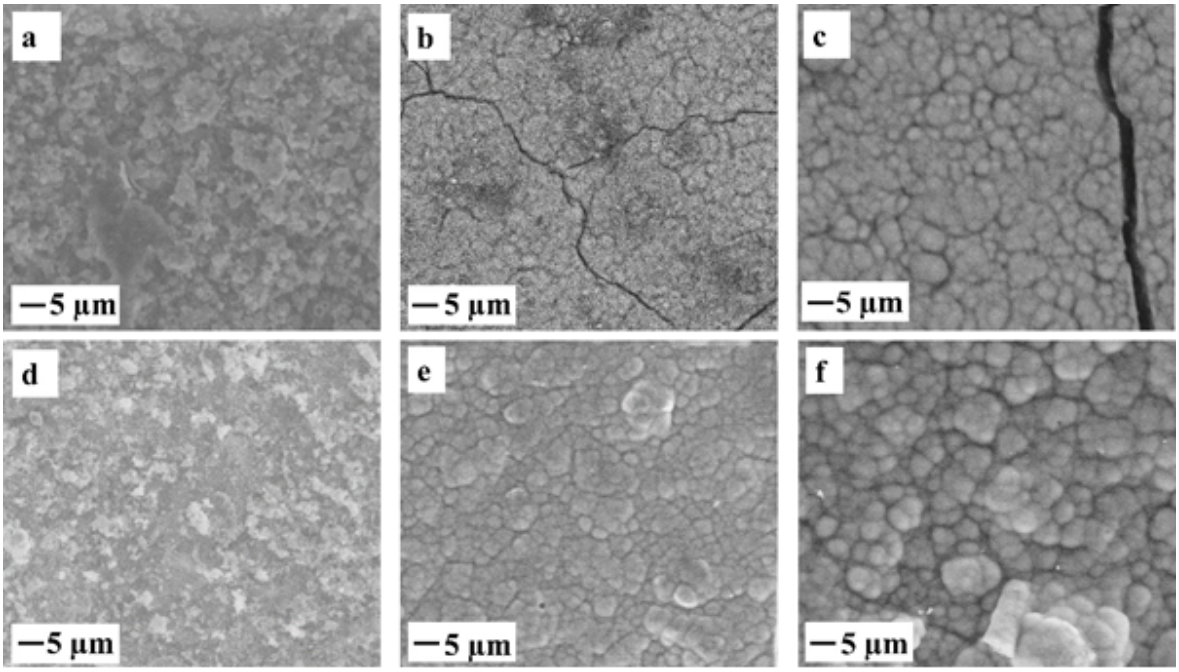

Figure 4.7: *SE, SEM images showing the surface morphology of the coatings after 3 days soaking in SBF solution (a), (b), (c) and after 7days soaking (d), (e), (f). Images (a) and (d) at 25kW, (b) and (e) at 50kW, and (c) and (f) at 75kW flame power.*

with deionised water and dried at room temperature; this caused shrinkage in HA film and resulted in cracks which can be seen in Figure 4.7 b, c, e and f [241].

4.4.2 XRD and Raman Spectroscopy

Figure 4.8 shows the XRD patterns of the 45S5 coatings after immersion in SBF for 3 and 7 days, and it can be seen that the diffraction patterns are consistent with the SEM observations (Figure 4.7), as these also showed the presence of HA. HA was identified from a broad peak at 32° 2θ, which corresponded to the prominent peak of HA. Also, a secondary peak at about 26° 2θ corresponded to HA. Figure 4.8 b, is the XRD patterns of the 45S5 after immersing in SBF for 7 days, and it can be seen that the intensity of HA peaks increased with immersion time. This is probably due to the more deposition of HA on the surface. It should be noted that HA was identified for coatings deposited at 50 and 75 kW; no HA peak was found in the XRD pattern of the coating deposited at 25 kW after immersion in SBF, even for longer time of 7 days.

In Figure 4.8 a and b, peaks other than that of the HA can be seen; these peaks corresponded to austenite and ferrite from the substrate. The substrate peaks were still recognisable in the XRD patterns after the precipitation of HA which might be due to the fact that HA film was cracked, as can be seen in SEM images Figure 4.7. Figure 4.9 shows the Raman spectra obtained on the surface of 45S5 coatings deposited at 50 and 75 kW after immersion in SBF for 7 days, and the synthetic HA powder. It can be seen that Raman spectra followed the same evolution for both of the coatings. The peak around 960 cm^{-1} is associated with the $\nu 1$ vibration mode of PO_4^{-3} for HA powder and for HA precipitated on the surfaces of the coatings; this is the main peak of HA. The peak at 1046 cm^{-1} in the spectrum of HA powder and the spectrum of HA precipitated on the coatings was associated with the PO_4^{-3} $\nu 3$ vibration. The peak at 1078 cm^{-1} in the spectrum of HA powder was associated with the PO_4^{-3} $\nu 3$ vibration too. Also, the peak at 432 cm^{-1} in all of the spectra was due to the $\nu 2$ domain of the PO_4^{-3}. Moreover, the peak at 1070 cm^{-1} for the precipitated HA on the surfaces of the coatings was assigned to the $\nu 1$ mode of the carbonate group, which confirmed the

carbonated nature of the precipitated HA [256, 261]. Moreover, the peaks at 579, 590, and 608 cm^{-1}, were due to the $\nu 4$ vibration of PO_4^{-3}. These peaks were present in the spectrum of synthetic HA powder and the spectra of precipitated HA on the surface of 50 kW and 75 kW coating [261, 262].

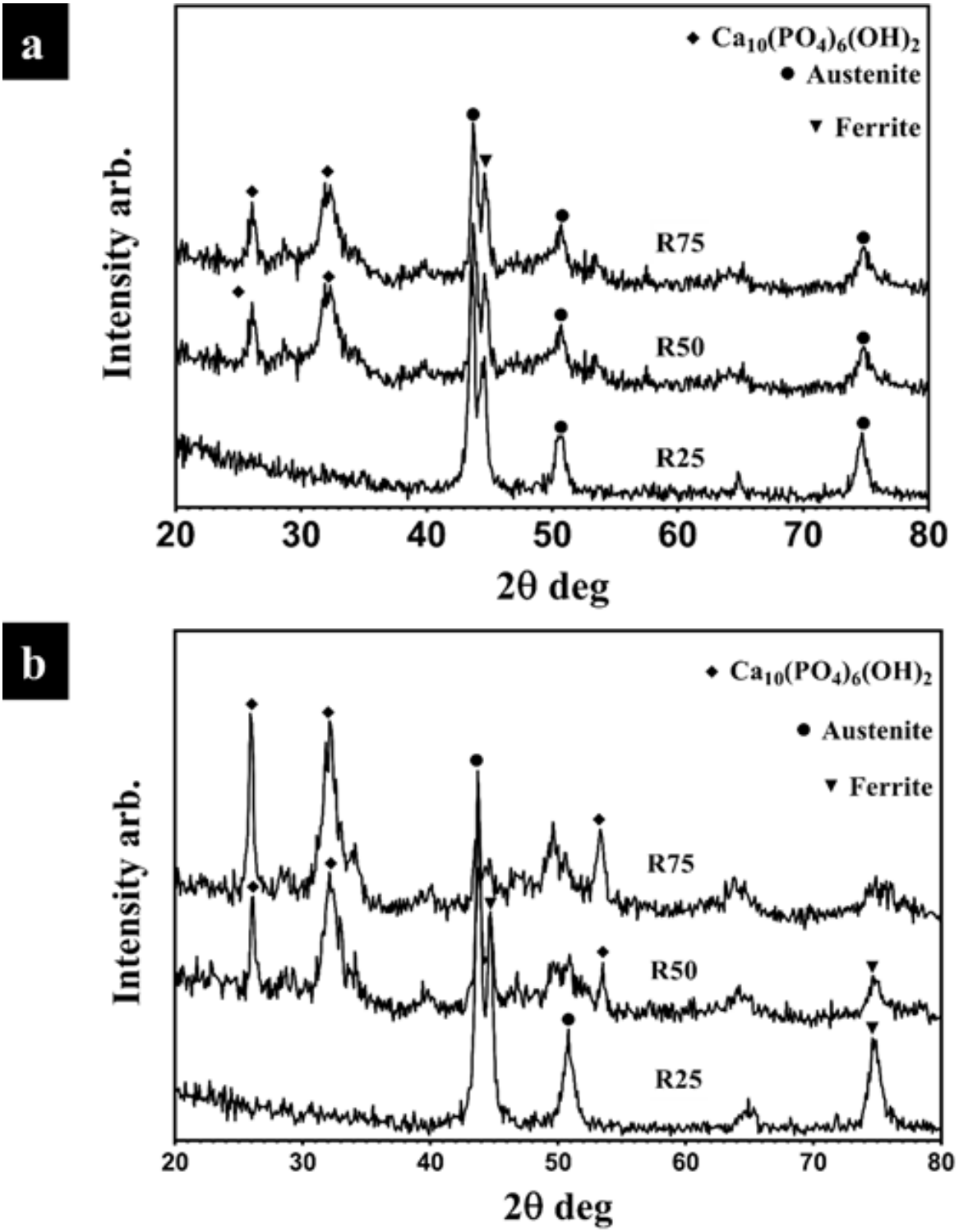

Figure 4.8: *XRD scan (a) 45S5 coatings after 3 days of soaking in SBF solution and XRD scan 45S5 coatings after 7 days of soaking in SBF solution (b).*

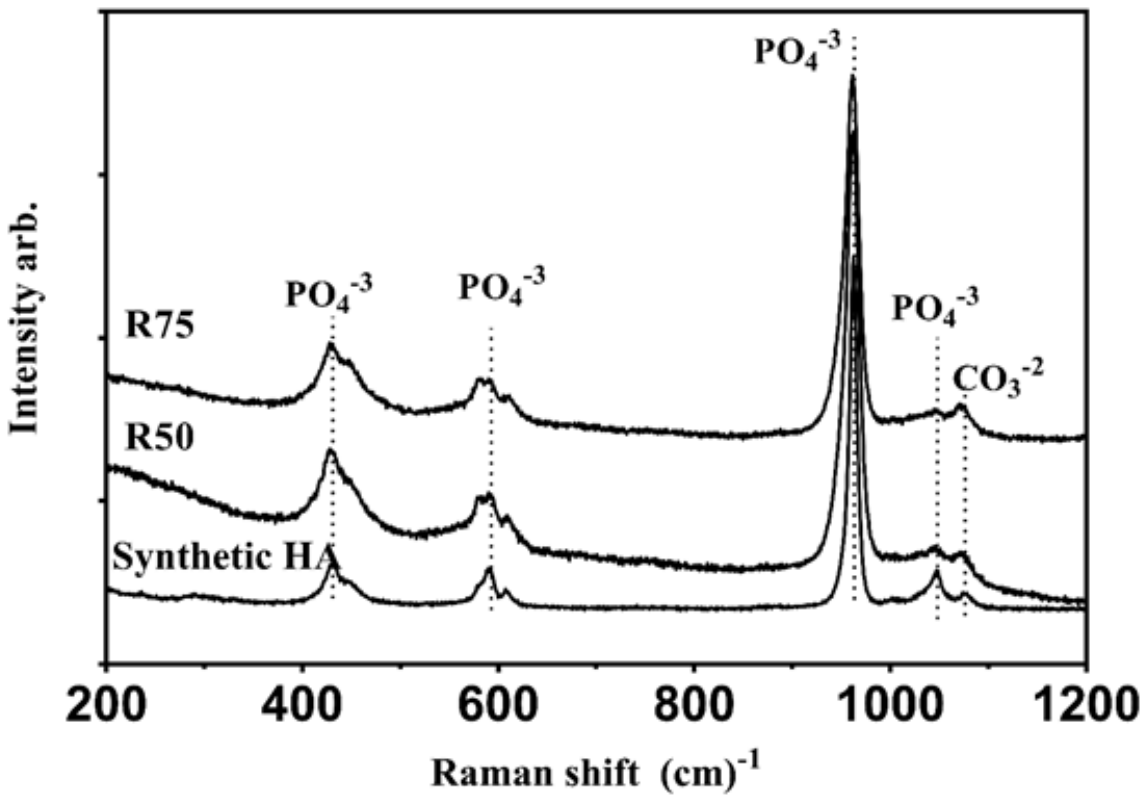

Figure 4.9: *Raman spectra acquired on the surfaces of the SHVOF thermal spray deposited bioglass coatings at flame powers of 50 kW and 75 kW after 7 days of soaking in SBF.*

4.4.3 EDX Analysis of the Coatings after SBF Test

EDX line scan along the cross-section of the coatings deposited at flame power 50 kW and 75 kW after immersion in SBF for 7 days was carried out and presented in Figure 4.10 b and d. While Figure 4.10 a and c are the corresponding BSE images of the cross-sections. As it can be seen from Figure 4.10 a, that the precipitated HA layer thickness on the coating, which was deposited at 50 kW and immersed in water for 7 days, was approximately 28 μm, while the residual glass underneath this precipitated HA layer was approximately 8 µm thick. The EDX line scan of the cross-section (Figure 4.10 b) showed that at the coating – substrate interface, Si content had reduced to 10 wt %, that further had reduced till the top of HA layer. Conversely, Ca content had increased to approximately 28 wt % at the coating – substrate interface, which further increased to 37 wt % in the top surface of the deposited HA layer. P content had increased to 17

wt % at the interface between coating and substrate. P content further increased to 20 wt % while going from the coating–substrate interface to the top of the HA layer.

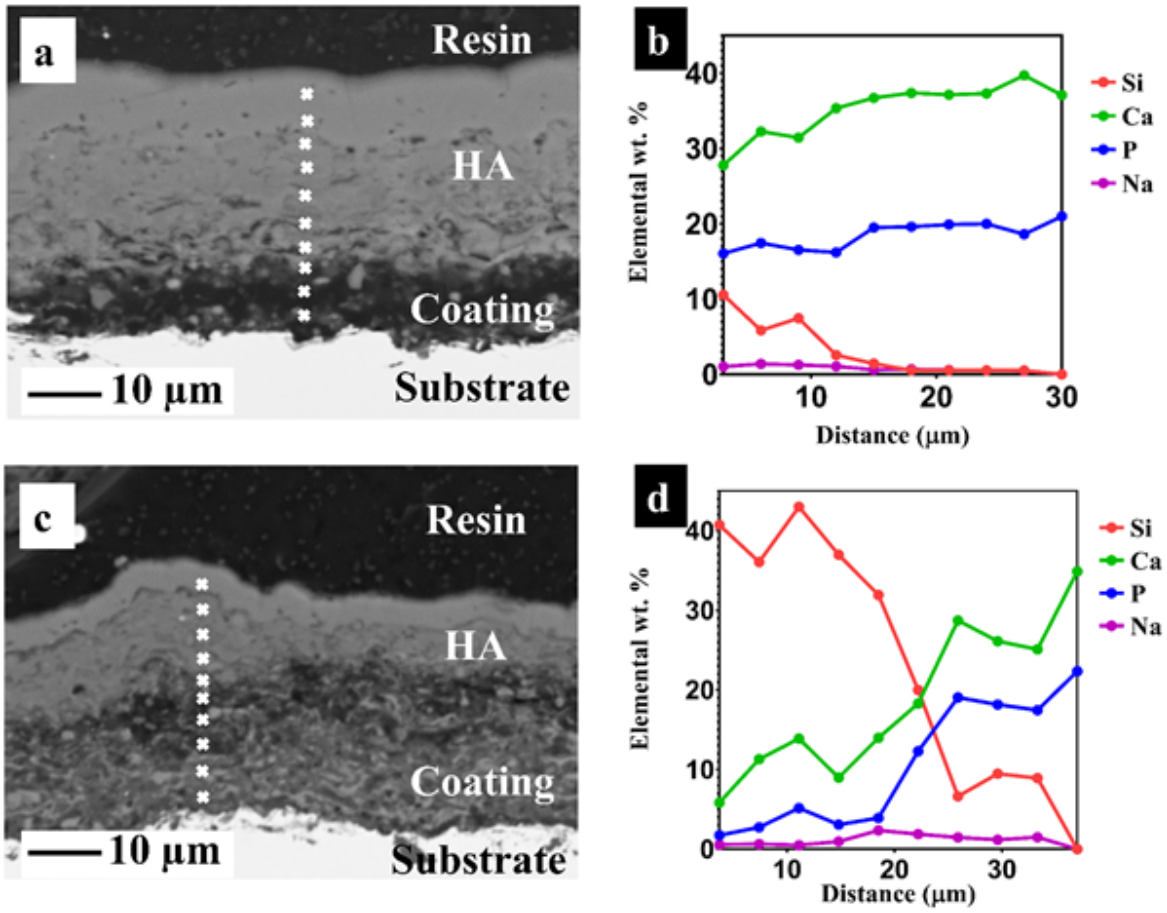

Figure 4.10: *BSE SEM images of the cross-section of coatings deposited at 50 kW (a), and 75 kW (c) after soaking for 7 days in SBF and their respective EDX line scans in b and d. Points in the images show the location of the EDX points. (distance is from substrate-coating interface towards coating top surface*
).

For the coating deposited at 75 kW flame power and immersed in SBF 7 days, the precipitated HA layer was approximately 10 µm thick. Also, it can be seen in Figure 4.10 c, that the residual glass coating was approximately 22 μm thick. Figure 4.10 d, shows the line scan of this cross-section, and as it can be seen that Si content was approximately 40 wt % at the interface between coating and substrate, then increased to approximately 43 wt % at the interface between coating and deposited HA layer. After which a significant decrease in Si content was observed. Ca content was 5 wt % at the coating- substrate interface and then increased to approximately 35 wt % on top surface of HA layer. The P content showed similar profile, initially at 2 wt % at

the interface between coating and substrate and the increased to 22 %.

Table 4.4 shows the EDX area scan conducted on the top surfaces of the 25 kW, 50 kW and 75 kW coatings immersed in SBF for 3 and 7 days. From this analysis, it can be seen that the coating deposited at 25 kW flame power the wt % of Si reduced to 3.7, Ca content was 12.4 wt %, Na was reduced to 1.8 wt %. While P content increased to 9 wt %. Also, this analysis suggested that Fe and Cr had been increased to 9.1 wt % and 7.4 wt % after immersing the 25 kW coating in SBF for 7 days. For the coating deposited at 50 kW, Si and Na had reduced approximately to 0.3 wt % and 0.9 wt %. However, Ca increased to 39.5 wt % and also, P increased to 18.7 wt % while those were immersed in SBF for 7 days. Similar trends were observed for 75 kW coating and immersed in SBF for 7 days. Its Si content had reduced to 2.5 wt %, while Na was reduced to 1.2 wt %. Ca was increased to 34.8 wt %, while P content was increased to 18.7 wt % after immersion in SBF for 7 days.

Table 4.4: *EDX area scan on top surfaces of the coatings soaking in SBF for 3 and 7 days, while R25, R50 and R75 are low, medium and high flame powers (number of measurements=3)*

Elements	**After Soaking for 3 Days in SBF (wt %)**			**After Soaking for 7 Days in SBF (wt %)**		
—	**R25**	**R50**	**R75**	**R25**	**R50**	**R75**
Si	28.6	1.2	5.4	3.7	0.3	2.5
Ca	10.1	37.0	32.9	12.4	39.5	34.8
Na	2.2	1.2	1.5	1.8	0.9	1.2
P	4.3	19.2	17.3	9.0	18.6	18.7
Fe	6.3	0.0	0.0	9.1	0.0	0.0
Cr	2.0	0.0	0.0	7.4	0.0	0.0

Table 4.5 shows the Ca/P ratio (atomic) for the three of the 45S5 coatings after thermal spray and immersed in SBF for 3 and 7 days. The results suggested that this ratio was 7.6, 11 and 10.4 for 25 kW, 50 and 75 kW coatings, respectively before SBF test. For 25 kW coating this ratio was decreased to 1.8 after 3 days of immersion in

SBF which further reduced to 1.04 with further immersion in SBF. For 50 kW coating, Ca/P ratio was 1.48 after 3 days of immersion in SBF, and this was increased to 1.5 with further precipitation of HA after 7 days of immersion in SBF. For 75 kW coating, after 3 days of immersion Ca/P ratio was 1.47, which increased to 1.63 with further immersion in SBF for 7 days.

Table 4.5: *Ca/P ratio (atomic %) of the as-sprayed and soaking in SBF after 3 and 7 days (number of measurements=3)*

Thermal Spray Coating at the Corresponding Flame Temperature	**Ca/P ratio Soaking for 0 days in SBF**	**Ca/P ratio Soaking for 3 days in SBF**	**Ca/P ratio Soaking for 7 days in SBF**
R25	7.6	1.8	1.04
R50	11	1.48	1.5
R75	10.4	1.47	1.63

4.5 Discussion

4.5.1 Coating Characterisation

It was observed that increasing the flame power from 25 kW to 50 kW and 75 kW had a significant effect on the 45S5 coatings microstructure. At lower flame power of 25 kW a thin coating of less than 10 μm thickness was obtained. While at flame powers of 50- and 75- kW thicker coatings of thickness 25 $\pm$ 1 μm were produced but of different microstructures. Formation of thin coating at 25 kW flame power and other literature studies based on SHVOF thermal spray proposes that the lower flame power of 25 kW does not provide enough energy to melt and accelerate the particles to deposit onto a substrate and produce a thick coating. When these unmelted large particles and agglomerates collide onto the substrate with low velocity, these bounce off, impairing the deposition of the material. The flame at 25 kW is regarded as being subsonic with a maximum temperature of 2,727 °C and velocity of 1,000 m/s, according to modelling work done in-house using a CFD software Fluent [263]. Low velocity particles result

in the formation of porous microstructure as some of the molten or partially molten particles (not well-flattened splats) adhere to the substrate. At 50 kW and 75 kW flame power, well-adhered to the substrate, thick and less porous coatings with rough surfaces were deposited. The 75 kW coating was less porous than the 50 kW, which may be due to the enough heat transfer from flame to the particles and melting them well, resulting in a denser microstructure [264, 265].

Increasing the flame power had a positive effect on the surface roughness (Ra) of the coatings. Ra of the coatings increased with increasing flame power. The coating deposited at 75 kW was 3.0 ± 0.2 μm rough, which was higher than for the coatings obtained at 25 and 50 kW flame power with 2.00 ± 0.01 μm rough surfaces. The high flame power of 75 kW resulted in fully molten splats with globules on the coating surface, which could be formed due to the agglomeration of molten particles in the flame leading to the formation of large humps on the surface resulted in a rougher surface [264]. Formation of humps in SHVOF sprayed coatings with alumina, titania, and zirconia has been reported in detail before [248]. Similarly, microhardness values of the 75kW coating 270 ± 0.9 HV were higher than that of the medium-power coating 253 ± 1.9 HV, which was also due to better melting of particles and agglomerates at this flame power—resulting in a harder coating. However, these values achieved were less than the microhardness of the bulk glass Bioglass® which is 586 HV hard [254], and approximately equal to that reported by Bolelli et al., who reported 296 HV hardness for the lowest thickness of the coating, which was 41 ± 3 for Bioglass (45S5) glass coatings deposited using SHVOF thermal spray [241].

EDX analysis of the coatings along the cross-section (Figure 4.5 b, d and f) showed that the Na_2O-CaO-SiO_2-P_2O_5 composition of the coating concerning the initial bulk glass formulation of 45S5 had been changed due to thermal spraying. However, these compositional changes were less noticeable in the coatings obtained at 25 kW and 50 kW flame power than for the coating obtained at the higher flame power of 75 kW. This was probably due to the higher heat transfer to the glass at high flame power and hence degradation of the feedstock powder [49]. Also, Table 4.3 showed a

decreasing trend in wt % of Na and P content in coatings when deposited at 25 kW, 50 kW and 75 kW flame power. However, wt % of Si and Ca showed increasing levels with the increase of flame power. Volatile components from the molten glass at high temperature of high flame power evaporate, which could reduce their wt %. Such as the direct evaporation of the volatile component, P_2O_5, from the glass might happen. Moreover, glass components such as Na_2O evaporates from the molten glass in the form of NaOH after reacting with water vapours in the combustion chamber. These vapours are present in the combustion chamber as a consequence of the combustion reaction [266].

45S5 coatings were amorphous as revealed by the XRD analysis and can be seen in Figure 4.6 a. The three crystalline peaks observed were related to the substrate due to the 40.8 μm penetration depth of the x-rays—the thickness of the coating was less than the penetration depth. This means that the glass did not undergo crystallisation during thermal spray. This is due to the rapid heating and cooling of the molten glass particles and insufficient time for crystallisation[9]. Moreover, the Raman spectra for the surface of 45S5 coatings are similar to that of the starting 45S5 powder as can be seen Figure 4.6 b. However, slight shifts were observed in the peaks of Si-O-Si from 1079 to 1075 cm^{-1} in the coatings obtained at 50- and 75-kW flame power; however, it can be still assigned to the stretching of Si-O-Si bond. Similarly, a peak had shifted from 610 cm^{-1} to 600 cm^{-1} for the coating deposited at 75 kW flame power which was also assigned to Si-O-Si. Since these peaks are quite strong, which is a clear indication that there is no alteration of the glass network of SHVOF deposited Bioglass® (45S5) coatings [218, 241].

4.5.2 SBF Studies of 45S5 Coatings

The steps involve in the reaction of 45S5 (Bioglass®) with SBF as reported in the literature [49, 267] are as follows: (i) exchange of alkali and alkaline earth ions with H^+ and H_3O^+ ions from the solution take place, (ii) loss of soluble silica occurs leaving behind -Si-OH bonds, (iii) condensation and res-polymerisation of a silica rich layer

depleted in cations, (iv) migration of Ca^{2+} and PO^{+4} to the surface from inside the glass and from the body fluid and formation of an amorphous CaO–P_2O_5 rich film on the silica-rich layer. This amorphous layer which also incorporates other ions such as OH^-, $(CO_3)^{2-}$ and F^- from the solution, crystallises into carbonated hydroxyapatite (HCA). HCA first nucleates and then grows, causing a dome-like morphology of the precipitated layer. Based on the reaction mechanism between Bioglass® (45S5) and SBF, all three SHVOF thermal sprayed 45S5 coatings showed different behaviour towards SBF. Such as no HA precipitated on 25 kW coating, thick HA layer ($\sim 24\mu$m) was observed on the surface of 50 kW coating, and comparatively a thin HA layer ($\sim$ 17 μm) precipitated on the surface of 75 kW coating.

For the coating deposited at lower flame power of 25 kW, no HA had precipitated even after three and seven days of immersion in SBF solution as can be seen in Figure 4.8 no peak was observed for HA, which could be due to the thickness of the coating. From Table 4.4, it can be suggested that the microstructure of the 25 kW coating was not stable enough in SBF for the precipitation of HA to occur on its surface [268]. As, the increasing wt % of Fe and Cr (from the substrate) observed from this sample after immersion in SBF for 3 and 7 days suggest that the low flame power coating may have degraded while in SBF, resulting in a reduction in the thickness of the coating [268].

The XRD patterns for the coatings deposited at 50 and 75 kW after immersion in SBF revealed peaks for HA as can be seen Figure 4.8. The broad diffraction peak at $\sim$ 32° 2θ may be due to crystalline structural defects such as the presence of HCA. The presence of a carbonated group is common for Bioglasses® while reacting with SBF for longer duration, and this group can be a cause in the broadening of XRD peak [241].

The Ca/P atomic ratios of the HA deposited on the surface of the coatings were equal to 1.5 for coating deposited at 50 kW flame power, while it was 1.63 for higher (75 kW) flame power coating after immersion in SBF for 7 days. Tri calcium phosphate (TCP), which is a precursor for HA has a Ca/P ratio of 1.55 [269]. However, the Ca/P ratio equal to 1.63 (for HA precipitated on the surface of 75 kW coating) is slightly different from the Ca/P ratio for synthetic HA which is 1.67 [99]. The different Ca/P

ratios obtained for the deposited HA layer on the surface of the coating were probably because the HA layer deposited after immersion in SBF was HCA rather than HA.

Similarly, the EDX line scans along the cross-section of the 50 kW and 75 kW coatings after immersion in SBF for 7 days showed that the interaction of these two coatings with SBF was different (Figure 4.10). The differences observed in the precipitated HA layers on the surfaces of these coatings were, i) the HA layer thickness on their surfaces, ii) reduction in the coatings thickness due to dissolution in SBF and iii) changes in the contents of coatings after immersion in SBF for 7 days. After immersion in SBF for 7 days, a thick precipitated HA layer approximately 24 μm thick was observed on the surface of the 50 kW coating, and which showed a reduction in coating thickness from 25 μm to 6 μm (Figure 4.10 a). This reduction in thickness is suggested to be due to the dissolution of the glass coating while in SBF. This happened most likely due to the high porosity observed in that coating that resulted in a larger active surface area for the ion leaching process [27]. The more porous microstructure may have also enabled infiltration of Ca and P ions from the SBF solution into the coating, as increasing levels of Ca and P were observed in this coating, as can be seen in Figure 4.10 b.

However, from the EDX analysis of 75 kW coating after immersion in SBF for 7 days (Figure 4.10 d), it was observed that the Si wt % was high in the residual glass coating and was increasing till the coating-HA layer interface. Then the wt % of Si decreased going from the coating-HA interface to the top of the HA layer. Moreover, Ca and P contents were observed to be increased from the coating-HA interface to the top of the HA layer. This suggests that no Ca, and P penetrated in the coating, which is probably due to the dense microstructure of this coating. Furthermore, only a small reduction in coating thickness from 25 μm to approximately 23 μm was observed for the 75 kW coating after 7 days of immersion in SBF with the formation of a thinner $\sim$ 17 μm thick precipitated HA layer on its surface. These results suggested that the coating deposited at higher 75 kW flame power followed the same reaction steps suggested in the literature for the formation of HCA precipitated on top of the residual

glass coating while immersed in SBF [27, 241, 268].

The above observations suggest that the 75 kW coating provided a comparatively stable and durable coating in SBF, which could provide prolonged interaction with bone tissue. Furthermore, if tailored layers of porous and dense micro-structures were desired, then a combination of the 50 kW and 75 kW could be considered to be applied.

4.6 Summary

The Bioglass® suspension was prepared by dispersing powder into water + IPA mixed media. This suspension was successfully deposited using SHVOF thermal spray on stainless steel substrates. The as-sprayed coatings have been studied for microstructure characterisation, phase identification and structural alterations. The SBF tests were carried out to study the reactivity of these coatings. From these observations following conclusion can be drawn:

- The results suggest that SHVOF thermal spray is a viable processing technique to produce Bioglass® coatings. However, the process parameters require careful optimisation and control to obtain a coating with the desired thickness and porosity on the substrate and showed desired reactivity in SBF. Well-adherent to the substrate, thick and uniform coatings were obtained at 50 and 75 kW flame power with varying microstructures

- The coating obtained at 50 kW had a porous microstructure, while the coating obtained at 75 kW had a higher surface roughness.

- No crystallisation of the feedstock occurred during the thermal spray as showed by the amorphous XRD spectra.

- The Raman spectra of the Bioglass® coatings were analogous to the spectrum of Bioglass® feedstock powder before spray, which showed no alteration of the glass network due to the production technique.

- The SBF results showed that HA was not deposited on the coating deposited at 25 kW.
- HA had precipitated on coatings deposited at 50 and 75 kW after 3 days of immersion in SBF. However, the coating's porous microstructure obtained at 50 kW led to resorption of the coating.
- The dense, thin and rougher coating deposited at high flame power of 75 kW developed HA layer on the surface, and the coating showed comparatively little degradation during immersion in SBF.
- These results show that by controlling spray parameters different microstructures coatings can be obtained that result in different dissolution behaviour in SBF solution.

Chapter 5

ICIE16 and 1393 Bioactive Glass Coatings and In-vitro Behaviour

5.1 Introduction

This chapter presents the set of results obtained by the deposition of ICIE16 and 13-93 bioactive glasses at flame power of 50 and 75 kW. The powder before spray and the as-sprayed coatings were characterised using SEM, XRD, Raman spectroscopy. The apatite forming ability of the coatings was assessed using SBF, while the cytotoxicity of the coatings was determined using MG63 cells.

5.2 ICIE16 and 13-93 Powder Characterisation

5.2.1 Particle Size Distribution and Powder Morphology of ICIE16 and 13-93 Bioactive Glass Before Spray

Frits of ICIE16 and 13-93 were ground separately in a zirconia jar with zirconia balls of 5 mm diameter for 30 min and 550 rpm using ball mill, which resulted in D_{10} = 1.8 μm, D_{50} = 8.3 μm and D_{90} = 24 μm for the ICIE16 powders and for 13-93 powders of D_{10}= 1 μm, D_{50} = 4 μm and D_{90} = 20 μm. After 2nd step of milling (for 30 min at 500 RPM), the ICIE16 bioactive glass had a particle size distribution of D_{10} = 1 μm,

D_{50} = 4.5 μm and D_{90} = 11.4 μm (Figure 5.1 a) and had a range of 0.4 μm - 28 μm. 13-93 powder had a distribution of D_{10} = 0.8 μm, D_{50} = 2.7 μm and D_{90} = 11 μm (Figure 5.1 c) with a range of 0.3 μm - 23 μm.

SEM (SE) imaging of ICIE16 powder after 2nd step of ball milling (Figure 5.1 b) showed angular shaped particles; also some larger than 10 μm particles were present. While, for 13-93 bioactive glass (Figure 5.1 d) it showed that most of the particles were finer; however particles larger than 10 μm were also observed.

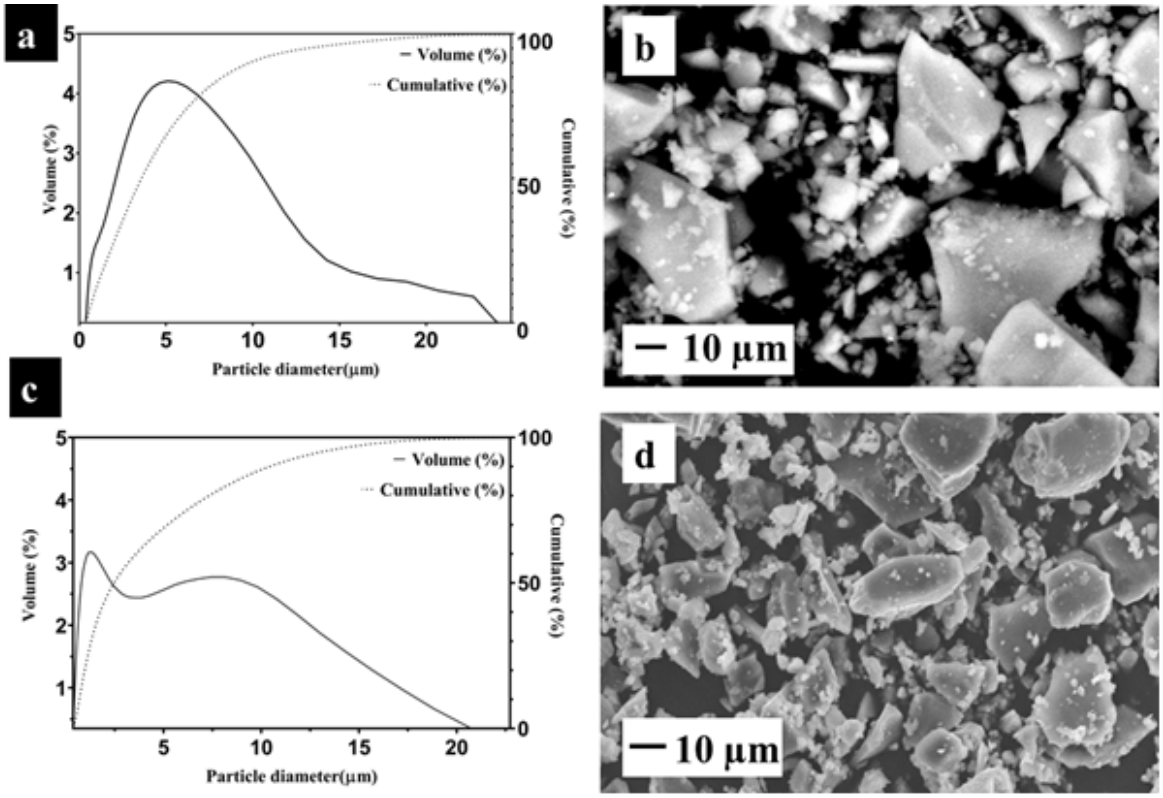

Figure 5.1: *(a) Particle size distribution and (b) SEM (SE) image of ICIE16, (c) particle size distribution and (d) SEM (SE) image of 13-93 bioactive glass.*

5.2.2 EDX of the ICIE16 and 13-93 Powder

EDX analysis (point) of ICIE16 and 13-93 powder is given in Table 5.1. For ICIE16, the composition was slightly different from that of the regular composition (48 % SiO_2, 33 % CaO, 6.6 % Na_2O, 2.4 % P_2O_5 and 10 % K_2O, in wt %) and had 3 wt % more Si, 5 wt % less Ca than the expected values. However, wt % of Na, K, and P in the prepared glass was approximately the same as expected values.

Composition of 13-93 powder was approximately the same as the expected values (Table 5.1). Negligible variations were observed for the elements, such as O.7 wt % for Na and Si and 0.2 wt % for P, whilst, wt % of K, Ca and Mg was the same as the intended values.

Table 5.1: *EDX analysis of the final powder before the suspension preparation (number of measurements=3*

).

Element (wt %)		Na	Si	P	K	Ca	Mg
ICIE16	Nominal composition	4.8	22.3	1.1	8.3	23	-
	Powder	5.0 ± 0.1	25.0 ± 0.6	1.1 ± 0.1	8.9 ±0.2	18.0 ± 2.0	-
13-93	Nominal composition	4.3	24.3	1.8	9.8	14	2.9
	Powder	5.0 ± 0.1	25.0±0.05	1.6 ± 0.1	10.0 ± 1	14.0 ± 0.3	3.0 ± 0.3

5.2.3 XRD and Raman Analysis of the Powder

Figure 5.2 presents the XRD spectra of ICIE16 and 13-93 powder. Both glass spectra were amorphous except the amorphous hump at 25° - 35°, which is the characteristic of glass.

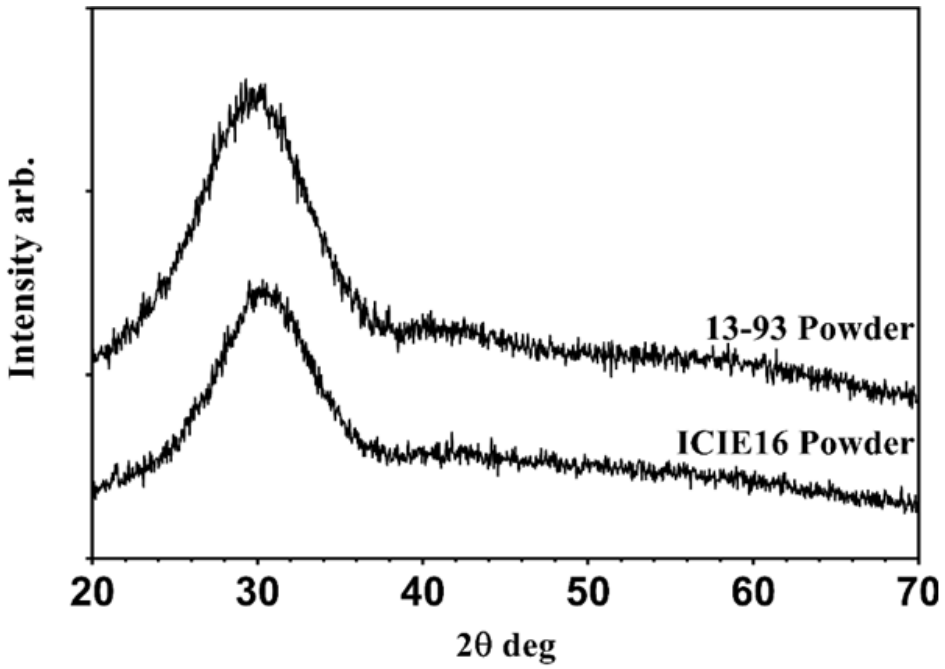

Figure 5.2: *XRD spectra of ICIE16 and 13-93 powder.*

The Raman spectra for both glass powder is given in Figure 5.3. For both spectra the peak at 621 cm^{-1} and 1057 cm^{-1} were assigned to the stretching of Si-O-Si [256] [1]. The peak at 950 cm^{-1} was associated with the stretching of PO_4^{-2} [256, 270]. However, the spectra of ICIE16 powder revealed a peak at 886 cm^{-1} which was associated to the non-bridging oxygen silica [256]; this band was not present in the Raman analysis of 13-93 powder. Moreover, a shoulder was observed in the Raman spectrum of 13-93 powder at 786 cm^{-1} which was related to MgO [271].

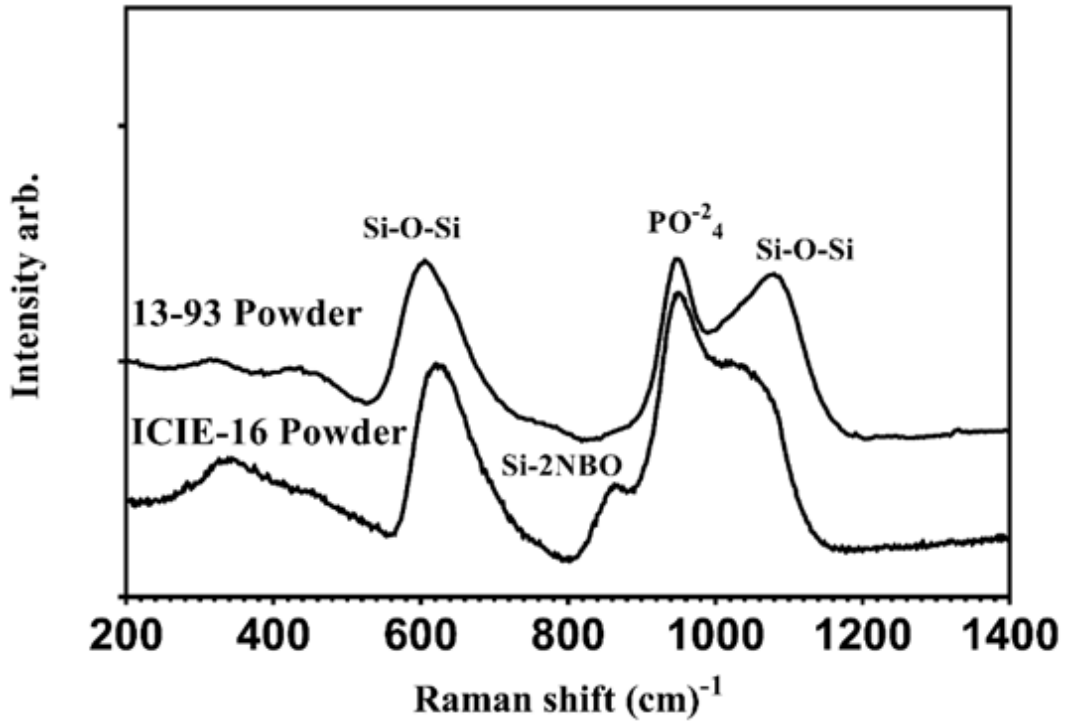

Figure 5.3: *Raman spectra of ICIE16 and 13-93 powder.*

5.3 As-Sprayed Coating Characterisation

5.3.1 Surface Morphology and Cross-Section of the Coatings

The surface morphology of the as-sprayed 45S5 coatings deposited at 50 kW flame power was examined using SE imaging and is given in Figure 5.4. Figure 5.4 a shows the surface of the ICIE16 coating deposited at 50 kW, and it can be seen that no globules appeared on the surface of this coating. The high magnification image (Figure 5.4 a) of the surface shows that this coating surface consisted of molten splats with

small round unmelted particles embedded in it. Moreover, well-flattened splats of size larger than 20 μm, as can be seen in Figure 5.4 c, were also observed.

The surface of 50 kW coating of 13-93 bioactive glass is given in Figure 5.4 d, which shows the absence of globules. The high magnification image of this coating (Figure 5.4 e) shows that the surface contained a higher amount of round unmelted splats and flattened splats. The size of these splats was around 10 μm in diameter (Figure 5.4 f). The surface roughness of the 50 kW ICIE16 coating was of Ra = 1.8 ± 0.1 μm, whilst the surface 13-93 coating was slightly rougher than ICIE16 coating with Ra = 2.4 ± 0.4 μm, which could be associated with the greater presence of the partially molten splats on the surface of 13-93 coating (Figure 5.4 c).

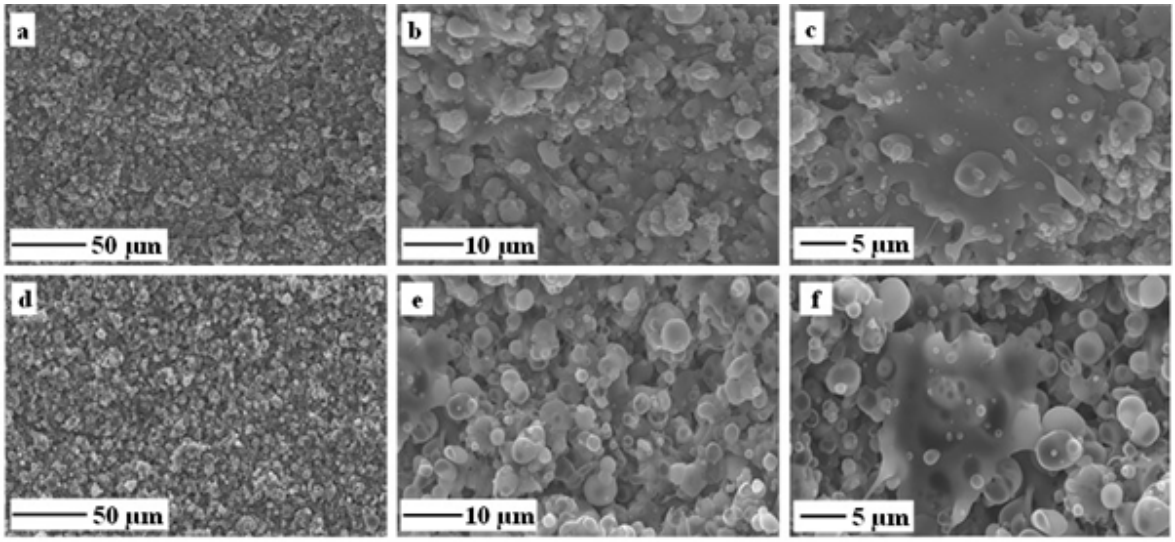

Figure 5.4: *SE, SEM images showing the surface morphology of the coatings deposited at 50 kW: (a), (b) and (c) ICIE16, and (d), (e) and (f) 13-93 coatings.*

Figure 5.5 presents the surface morphology of ICIE16 and 13-93 coatings deposited at 75 kW, as can be seen in Figure 5.5a that the surface of ICIE16 coating contained globules. A high magnification image (Figure 5.5 b) of this surface shows that those globules were spherical deposits with a porous structure, and the size of these structures was around 20 μm. Other than these globules, the surface had flattened lamellae and fine partially melted splats (see Figure 5.5 c).

The surface of the 75 kW coating of 13-93 bioactive glass showed similar features to the ICIE16 75 kW coating, presenting globules on the entire surface of the coating

(Figure 5.5 d). However, these semi-spherical structures were not as porous as those observed on the surface of the ICIE16 coatings deposited at the same power (i.e. 75 kW), and were also greater in size with a diameter around 40 μm, with fine particles adhered to the surface as can be seen in Figure 5.5 e. Moreover, the surface of this coating also contained well-flattened lamellae with some spherical particles as can be seen in Figure 5.5 f.

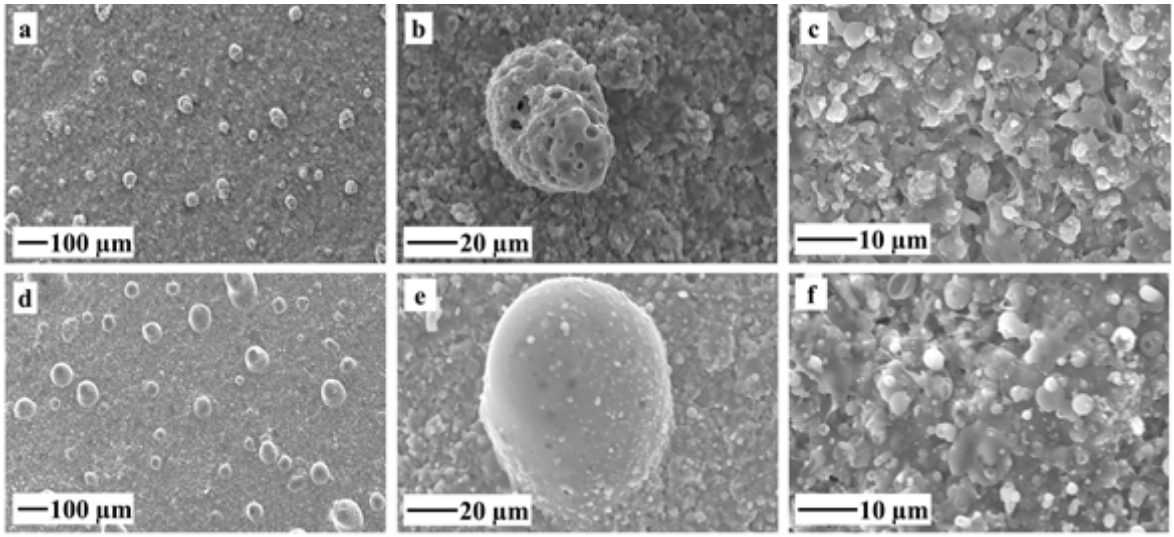

Figure 5.5: *SE, SEM images showing the surface morphology of the coatings deposited at 75 kW flame power: (a), (b) and (c) show ICIE- 16 coating and (d), (e), (f) show 13-93 coating.*

The surface of the 75 kW coatings of ICIE16 and 13-93 glasses were rougher than their coatings deposited at 50 kW. The 75 kW coating of ICIE16 had a roughness of 3.7 ± 0.3 μm, whereas the surface of 13-93 coating deposited at 75 kW coating had a surface roughness of 6.5 ± 0.6 μm.

All the coatings produced did not reveal any delamination at the coating-substrate interface, as seen from the cross-sectional images (Figure 5.6). In addition, they presented a uniform coating thickness where some remnant porosity was detected for coatings. Moreover, the globular features in the ICIE16 and 13-93 coatings deposited at 75 kW which were observed on the surface of the coatings, can be seen in Figure 5.6 b and d.

The physical and mechanical properties of the ICIE16 and 13-93 coatings are presented in Table 5.2. Vicker micro-hardness testing revealed very similar values for both

bioactive glass coatings deposited at 50 kW flame power (i.e. 250 ± 8 HV for ICIE16 246 ± 4 HV for 13-93). However, both of the glass coatings deposited at 75 kW revealed higher micro-hardness values (i.e. 301 ± 10 HV for CIE16 and 318 ± 12 HV for the 13-93 coating) than 50 kW coatings.

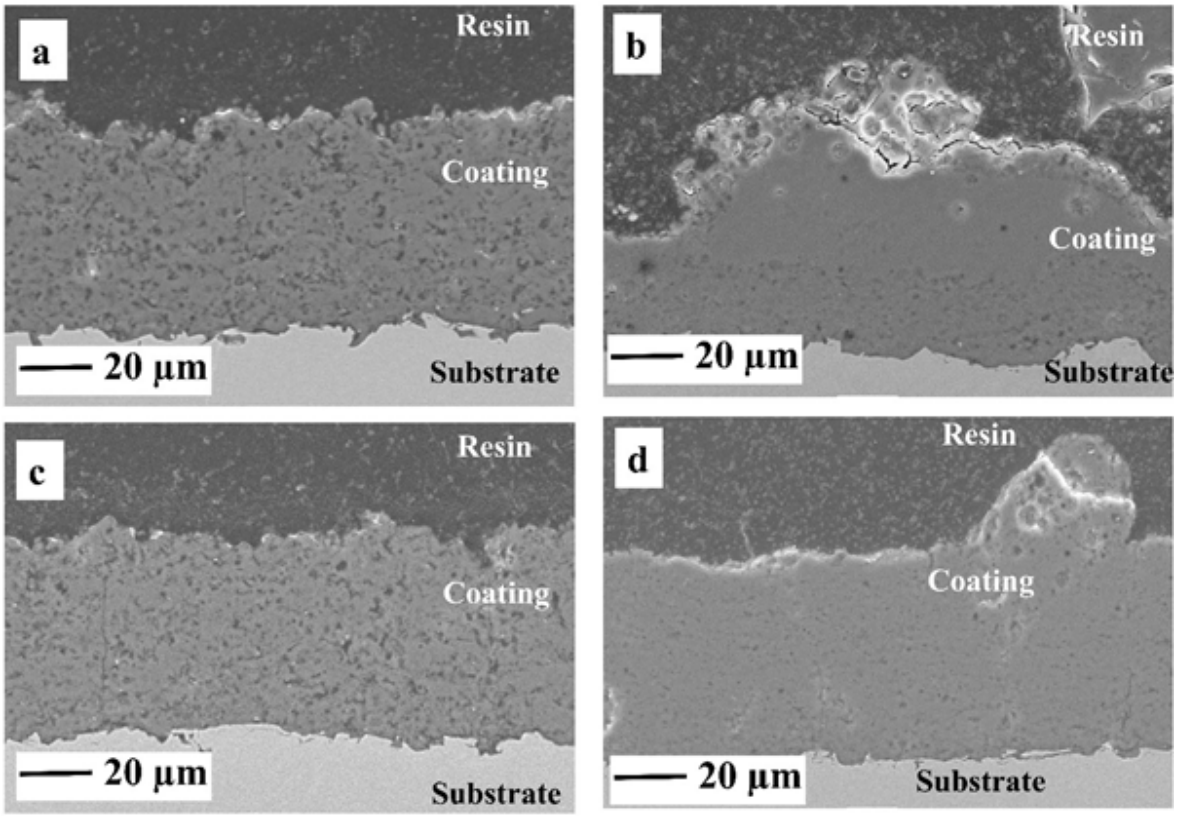

Figure 5.6: *Cross-sectional SEM images of the coatings deposited: ICIE16 coatings (a) deposited at 50 kW, (b) deposited at 75 kW, 13-93 coatings (c) deposited at 50 kW, and (d) at 75 kW.*

Table 5.2: *Physical and mechanical properties of ICIE16 and 13-93 coatings deposited at 50 and 75 kW flame power (mean value ± standard error) (number of measurements=5*

)

Flame Power (kW)	**Thickness (μm)**		**Porosity (%)**		**Microhardness (HV)**		**Surface Roughness (μm)**	
	ICIE16	13-93	ICIE16	13-93	ICIE16	13-93	ICIE16	13-93
50	68 ± 1	67 ± 1	5 ±1	6 ± 0.3	250 ± 8	246 ± 4	1.8 ± 0.1	2.4 ± 0.4
75	59 ± 10	62 ± 14	4 ± 0.5	3.5 ± 0.2	301 ± 10	318 ± 12	3.7 ± 0.3	6.5 ± 0.6

5.3.2 EDX Analysis along the Cross-Section and on the Top of the Coatings

In order to explore if any compositional variations had occurred during the thermal spray process, EDX line scans across the coating thicknesses were carried out. The results are presented in Figure 5.7, where elemental wt % is presented as a function of distance from the coating-substrate interface to the top surface of the coatings obtained with corresponding BSE images (points on the images show where the EDX analysis was conducted).

The composition of the ICIE16 coating deposited at 50 kW (Figure 5.7 a) was approximately uniform (see Figure 5.7 b). No changes were observed in Si wt % from the expected 25 ± 0.6 (present in glass powder) and remained at this value to the top surface of the coating. Ca wt % was 24 wt % in the coating, which was an increase from the original powder prior to spraying (18 wt % (Table 5.1). However, in the coating, variations in Ca content were small and were in the range of 24-25 wt %. In the starting powder P content was 1 wt % and had reduced at the coating- substrate interface to 0.7 wt %, and remained approximately the same to the top surface of the coating. K wt % changed from 8.9 wt % to 4 wt % at the coating-substrate interface and remained at approximately 3 wt % to the top surface of the coating. Na changed from 5 to 3 wt % at the interface between coating and substrate and remained at approximately 1 wt % to the top surface of the coating.

For ICIE16 coating deposited at 75 kW, composition showed slight variations when going from the coating-substrate interface to the top of the coating (Figure 5.7 d), also the concentration of the elements (wt %) changed from the starting powder. Variations in Si wt % was between 25 - 31 wt % from the interface between coating and substrate to the top of coating. Ca content changed to 23 wt % at the interface and to 18 wt % at the top of the coating. K was approximately 5 wt % at the interface, then decreased to 0.68 wt % at the top of the coating. P was 1 wt % at the coating- substrate interface and then decreased to 0 wt % at the top surface of the coating. Wt % of Na was reduced from 3 wt % at the interface to 0 wt % in the coating.

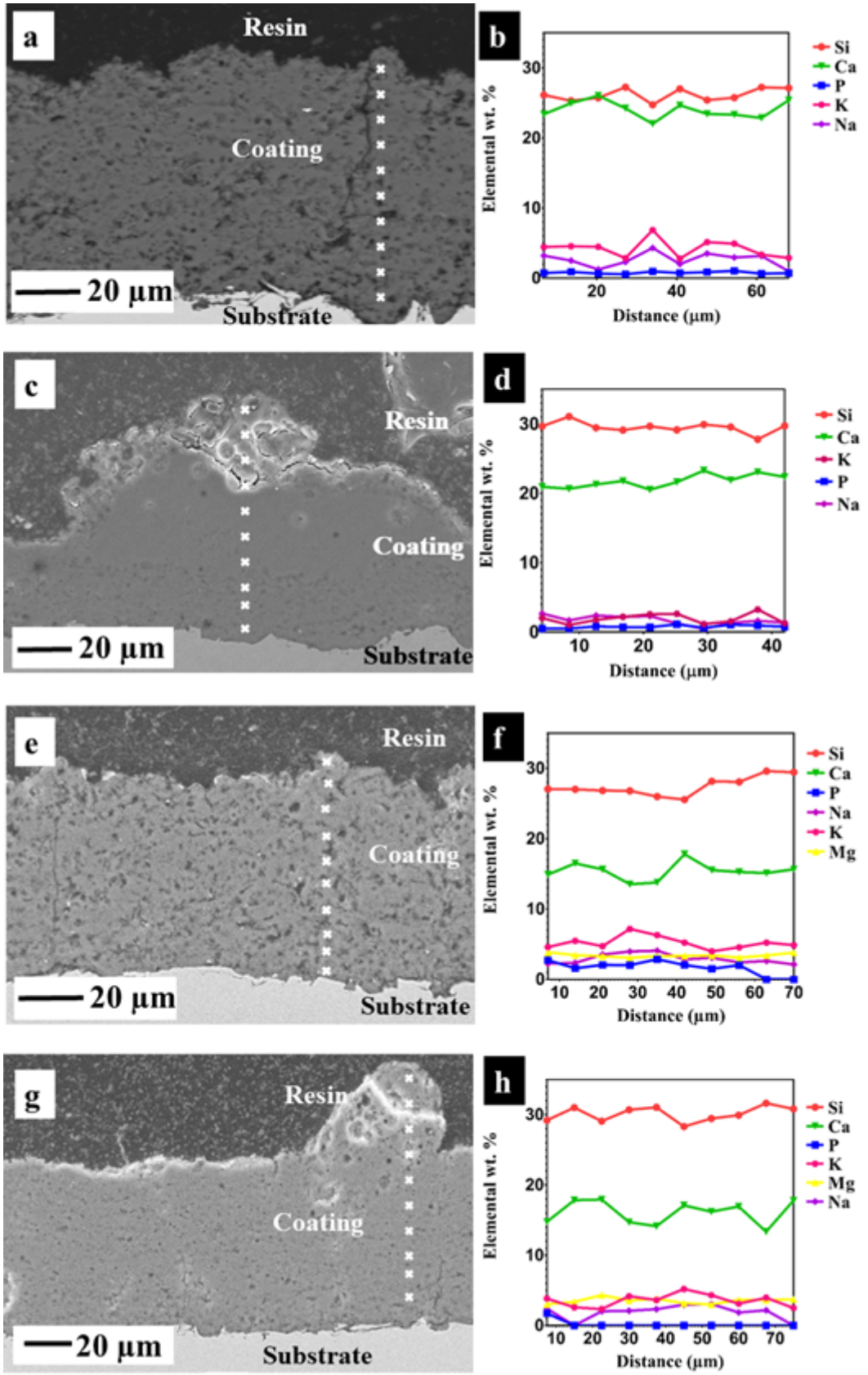

Figure 5.7: *In figure a and c are BSE images while b and d are the respective EDX line scan of ICIE16 coatings deposited at 50 and 75 kW, e and g are BSE images while f and h are the respective EDX scans of 13-93 coatings deposited at 50 and 75 kW (distance is from substrate-coating interface towards coating top surface*

).

Variations were also observed from the starting powder composition of 13-93 bioactive glass when deposited at 50 kW; however, the across the coating composition was uniform, as can be seen from the EDX line scan across the coating (Figure 5.7 f). 25 wt % of Si was present in 13-93 powder before spray, and the observed deviations were in the range of 27 to 29 wt % from the coating- substrate interface to the top surface of the coating. Ca content remained constant at approximately 14 wt % in the coating and which was similar to the starting powder composition. Wt % of P remained constant at 1 wt % in the coating and also did not vary from the original content; however, near to and at the top surface of the coating wt % of P was decreased to 0 %. Na was 5 wt % in the starting powder, which was then decreased to approximately 2 wt % at the interface between the substrate and coating, and remained constant to the top surface of the coating. Before the thermal spray process, K was approximately 10 wt % in 13-93 bioactive glass, and after deposition at 50 kW, it decreased to 4 wt % at the coating- substrate interface. The Mg levels also approximately remained constant after spraying at 50 kW in coating similar to the starting 3 wt % in powder.

For the 13-93 coating deposited at 75 kW, 25 wt % of Si (present in the starting powder) was increased to 29 wt %, and no variation was observed in its content across the coating. Ca was observed to have increased to 16 wt % and remained at this level across the coating. The wt % of Na content had reduced to approximately 1 wt % at the coating–substrate interface; however, it remained same in the coating. P did not change from the original wt % present in the powder which was 1 wt % and also remained at this level across the coating. 2 wt % K was observed (originally 10 wt % in powder) at the substrate-coating interface and with a small variation in coating layer till top of coating. Mg content remained constant at approximately 3 wt % at the interface between coating and substrate and in the coating after spraying at 75 kW.

EDX surface analysis of ICIE16 coatings can be seen in Table 5.3 3, which shows that increasing flame power affected the glass composition. The Si (wt %) was seen to vary slightly between 25 – 26 wt % for powder to the 50 kW samples and up to 28 % was seen for the 75 kW samples. Na wt % was seen to vary from 5 to 3 and

2 wt % when sprayed at 50 and 75 kW flame power Wt % of Ca was increased from 18 wt % to 24 and 26 wt % with the increase of flame powers from 50 to 75 kW. P remained approximately constant and similar in wt % to the starting powder wt % for both flame power samples. K, however, revealed a higher variability in comparison to the starting powder from between (8.9 wt %) to 4 wt % and 3 wt % when deposited at 50 and 75 kW.

EDX area analysis of the top surface of the 13-93 coatings is provided in Table 5.3, which shows that after spraying Na content had reduced from 5 wt % to 2 wt % and 1 wt % after spraying at 50 and 75 kW. Mg and P remained constant at 3 wt % and 1 wt % after spraying at both the different flame powers employed; however, K showed the same trend as Na, with reductions observed with increasing flame power from 6 wt % at 50 kW to 4 wt % at 75 kW flame power.

Table 5.3: *EDX analysis on the top of as sprayed surfaces of ICIE16 and 13-93 coatings, where R50 is the coating deposited at 50 kW and R75 at 75 kW flame power.*

Element wt(%)		**Na**	**Si**	**P**	**K**	**Ca**	**Mg**
ICIE16	Nominal Composition	4.8	22.3	1.1	8.3	23	—
	Powder	5.0 ± 0.1	25.0 ± 0.6	1.1 ± 0.1	8.9 ±0.2	18.0 ± 2.0	—
	R50	3.0 ± 0.4	26.0 ± 0.3	1.0 ± 0.1	4.0 ± 0.1	24.0 ± 0.2	—
	R75	2.0 ± 0.2	28.0 ± 0.1	0.7 ± 0.01	3.0 ± 0.1	26.0 ± 0.3	—
13-93	Nominal Composition	4.3	24.3	1.8	9.8	14	2.9
	Powder	5.0 ± 0.1	25.0±0.05	1.6 ± 0.1	10.0 ± 1	14.0 ± 0.3	3.0 ± 0.3
	R50	2.3 ± 0.3	28.0 ± 0.4	1.0 ± 0.1	6.0 ± 0.6	16.0 ± 1.0	3.0 ± 0.1
	R75	1.0 ± 0.5	29.4 ± 0.1	1.0 ± 0.0	4.0 ± 0.1	19.0 ± 0.7	3.6 ± 0.1

5.3.3 Raman and XRD of the Coating

The ICIE16 and 13-93 bioactive glass coatings were analysed post-deposition via XRD analysis to explore if any phase changes had occurred and the spectra are given in Figure 5.8. No crystalline peaks were observed in any of the spectrum (except signal from the stainless-steel substrate in the case of ICIE16 75 kW coating). This confirmed

that the amorphous nature of the starting materials had been preserved. The large hump observed at 25° - 35° is fairly typical of amorphous glass structures [272, 273].

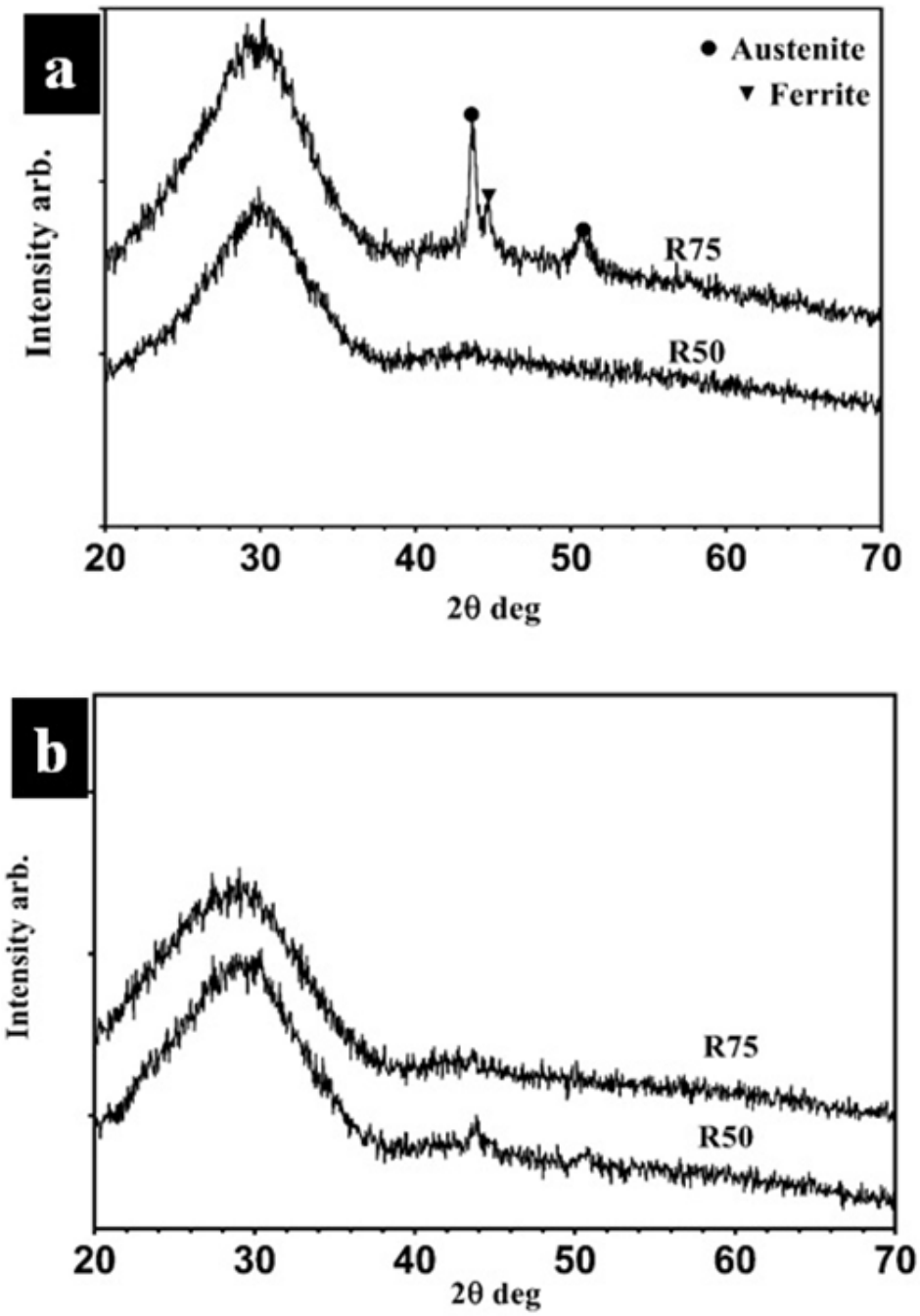

Figure 5.8: *XRD spectra of ICIE16 (a) and 13-93 (b) bioactive glass coatings deposited at 50 and 75 kW flame power. Where as R50 is the coating deposited at 50 kW and R75 coating deposited at 75 KW.*

The Raman analysis of the ICIE16 and 13-93 coatings and powder (for comparison) are given in Figure 5.9. As can be seen that the coating spectra were very similar to the respective glass powder, which proves that structure of both glasses did not disrupt

during thermal spray.

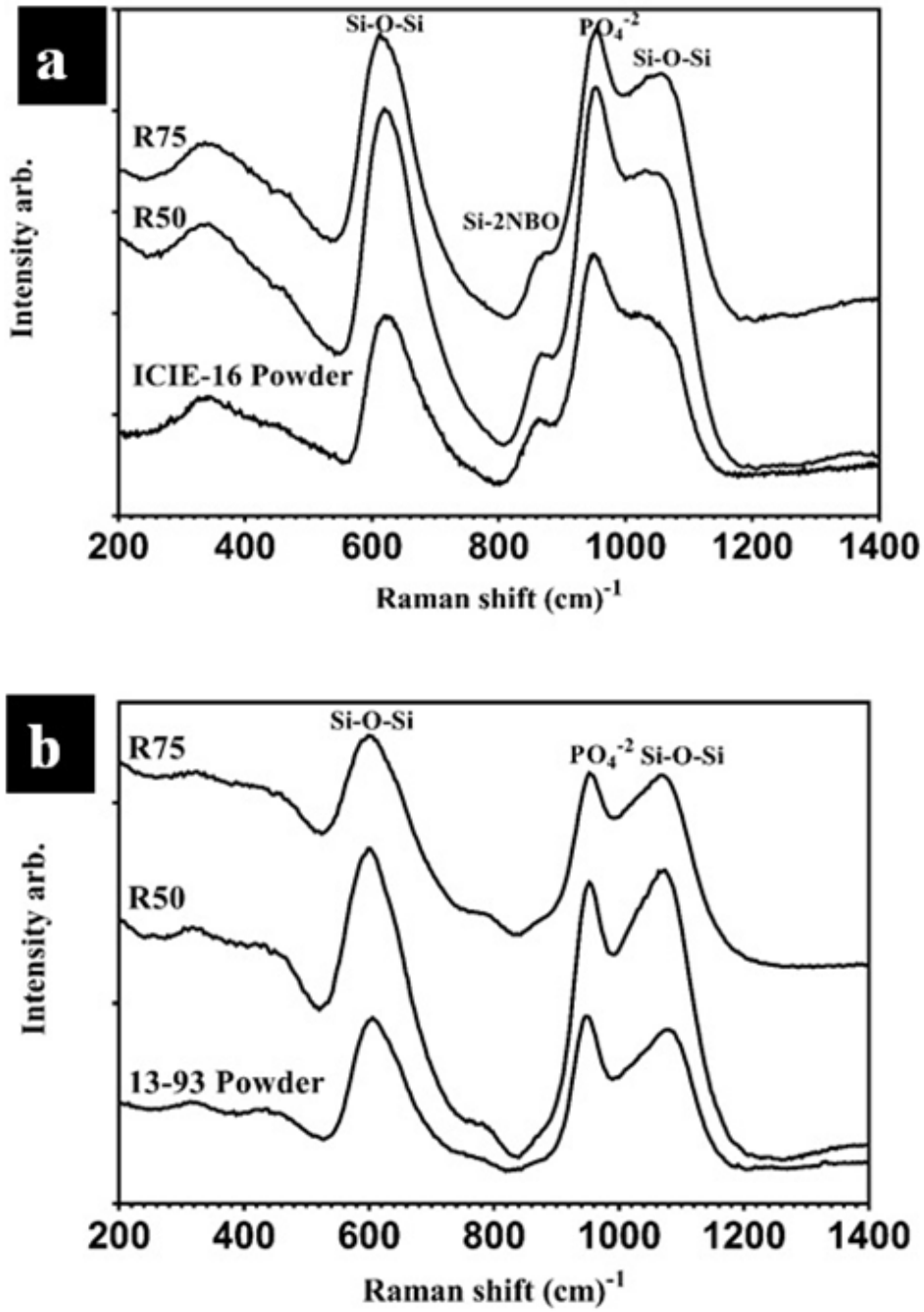

Figure 5.9: *Raman analysis (a) of ICIE16 (b) 13-93 bioactive glass coatings deposited at 50 kW and 75 kW.*

5.4 Apatite Formation on the Surfaces of the Coatings in SBF

5.4.1 SEM Analysis

The SBF tests and following SEM analysis showed that HA had formed on both (50 and 75 kW) ICIE16 coatings after three days of immersion in SBF (Figure 5.10 a and c, whereas Figure 5.10 b and d depict surface deposition after 7 days of immersion in SBF). The surface morphology of the coatings resembled "cauliflower" like features characteristic of HA deposits on the surface post immersion in SBF. The 13-93 coating samples deposited at 50 kW followed a similar pattern (see Figure 5.10 e for deposition after 3 days and Figure 5.10 f for deposition after 7 days of immersion in SBF). However, the 13-93 coatings deposited at 75 kW did not reveal any HA deposition on their surfaces after 3 days of immersion in SBF (see Figure 5.10 g). However, after immersion in SBF for 7 days, HA was detected on this coating surface, which was not fully covered (see Figure 5.10 h).

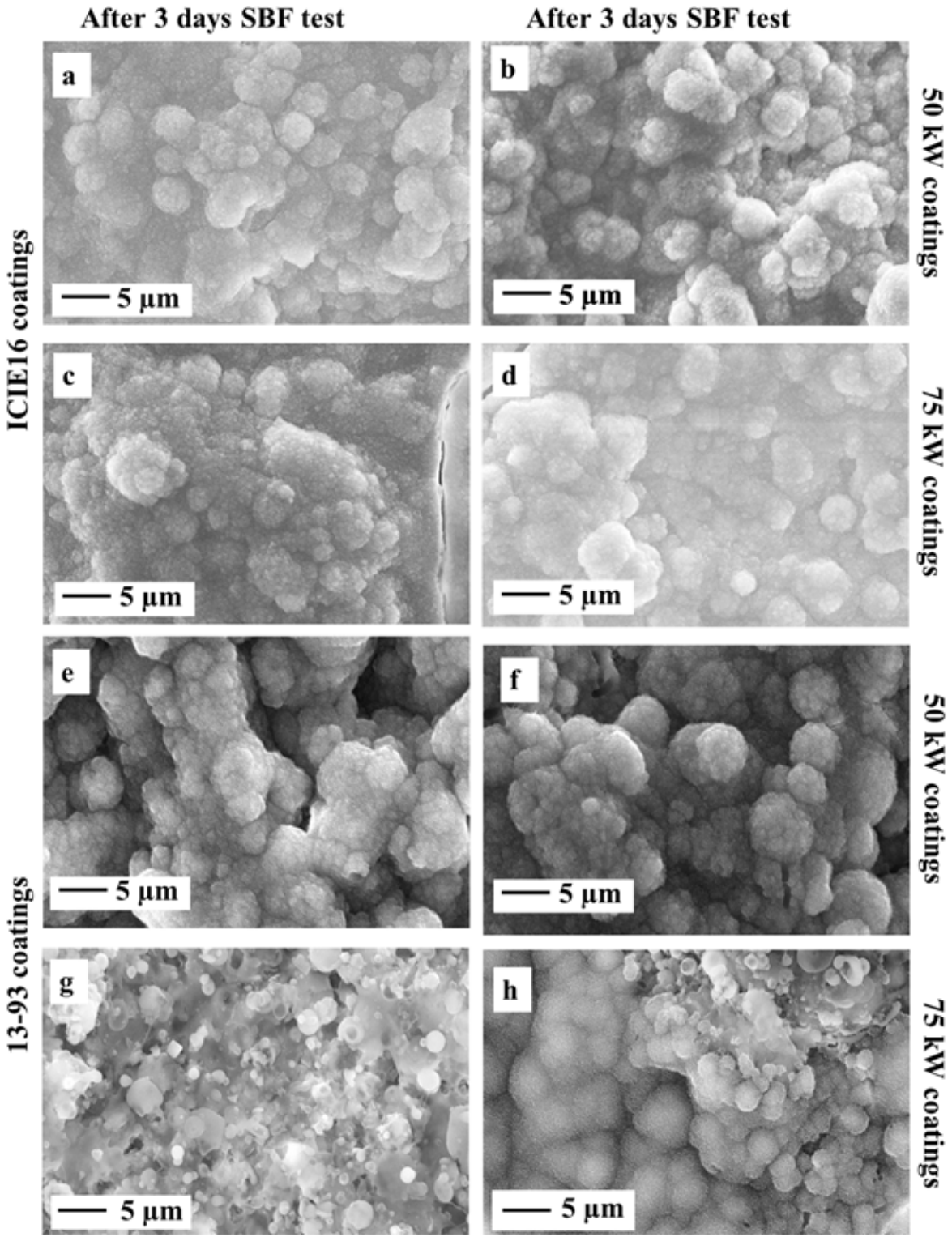

Figure 5.10: *Raman analysis (a) of ICIE16 (b) 13-93 bioactive glass coatings deposited at 50 kW and 75 kW.*

5.4.2 XRD and Raman Spectroscopy

Figure 5.11 shows the XRD analysis acquired at the surfaces of the ICIE16 and 13-93 coatings after SBF tests. The spectra revealed the presence of HA from peaks at 26° and 32° 2θ which matched with PDF no 00-001-1008; however, it can be seen (Figure 5.11) for ICIE16 coatings deposited at 50 and 75 kW revealed HA peaks after 3 days of immersion in SBF (Figure 5.11 a, b). The intensity of these peaks increased with increasing immersion time to 7 days. The same trend was seen for 13-93 coating deposited at 50 kW, and immersed in SBF for 3 and 7 days (Figure 5.11 c).

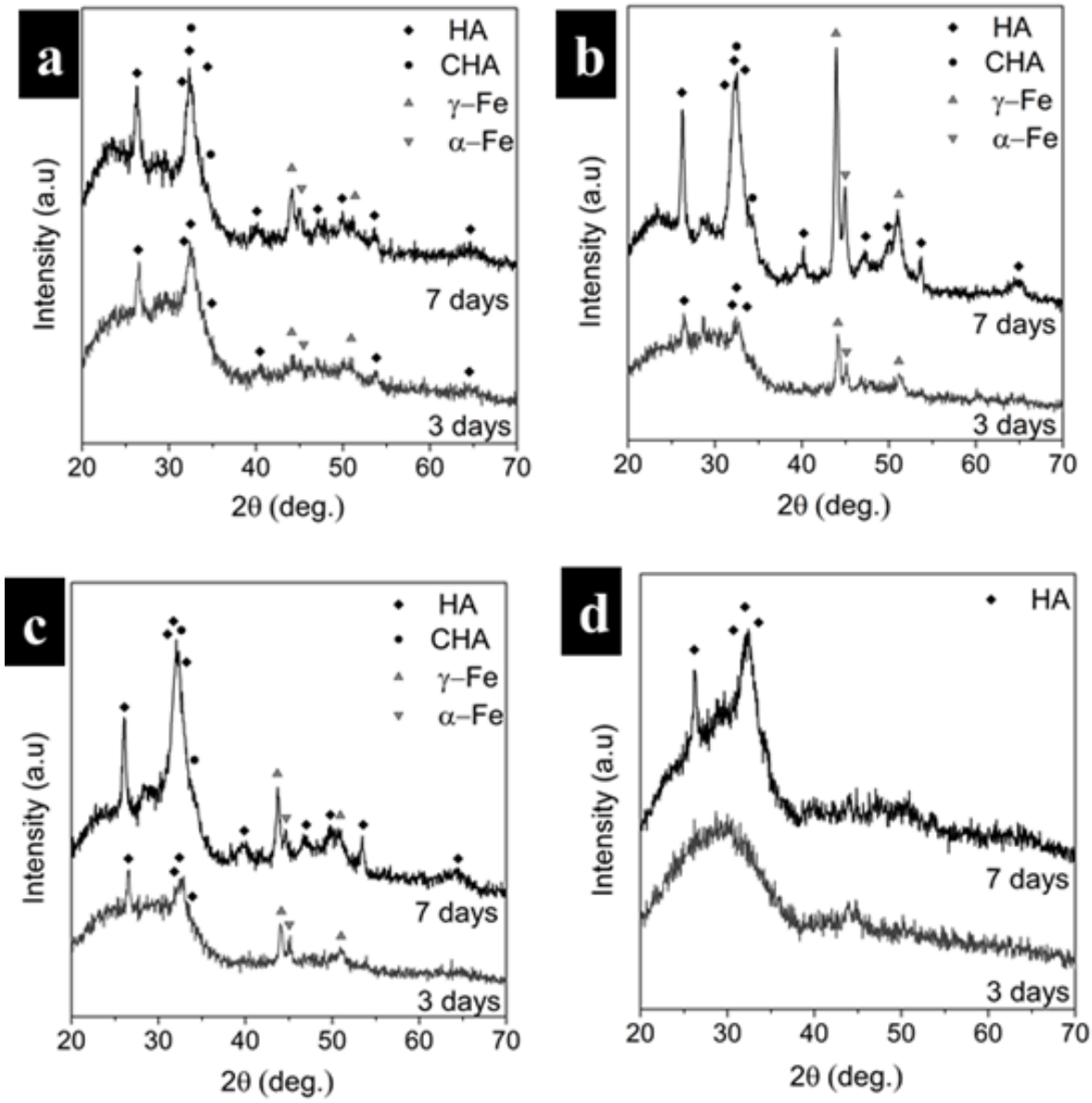

Figure 5.11: *XRD spectra (a), (b) of ICIE16 coatings and (c), (d) 13-93 coatings after SBF tests. While (a) and (c) are 50 kW coatings, (b) and (d) after 7 coatings deposited at 75 kW coatings.*

However, XRD analysis of 13-93 coating deposited at 75 kW showed no peak after 3 days of immersion in SBF, as shown in Figure 5.11 d. Also, this coating showed peaks that were associated with HA deposition after immersion in SBF for 7 days, though the intensity of these peaks was not high in comparison with the HA peaks developed on the other three coatings. The peak at 32° was broader (31° - 32°) in all spectra due to the carbonated nature of HA (HCA).

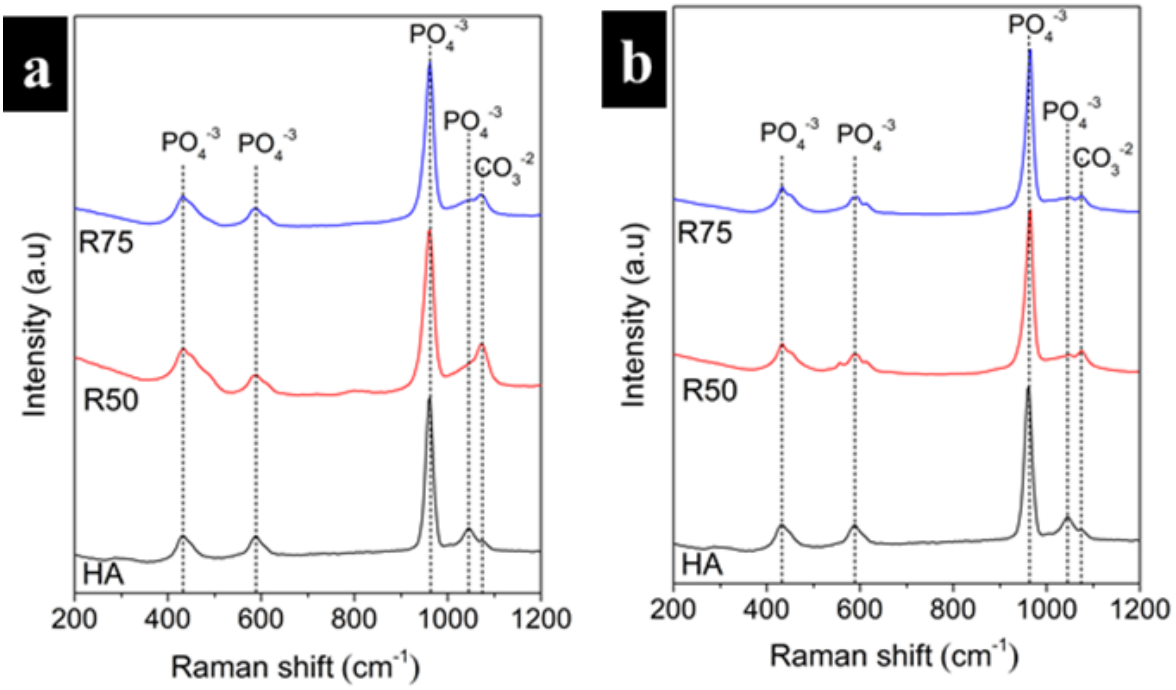

Figure 5.12: *Raman spectra acquired on the surfaces of the S-HVOF thermal sprayed bioactive glass coatings deposited at flame powers of 50 kW and 75 kW after 7 days of immersion in SBF, where (a) ICIE16 coatings and (b) 13-93 coating.*

Consistent with the XRD and SEM results, the Raman spectra measured at the top surface of all coatings immersed in SBF for 7 days resembled the spectrum of synthetic HA powder, as shown in Figure 5.12. The peak at 960 cm^{-1} in the spectra was assigned to symmetric stretching v1 of PO_4^{-3}. The broad peak at 432 cm^{-1} was assigned to v1 bending of PO_4^{-3}. In contrast, the broad peak at 585 cm^{-1} was due to the anti-symmetric bending v4 of PO_4^{-3} [274]. The peaks at 1045 cm^{-1} for the HA powder were assigned to vibration of the PO_4^{-3} v3. The peak at 1070 cm^{-1} was assigned to the stretching v1 mode of carbonate CO_3^{-2} groups, which was probably due to the precipitated HA, as it was not present in the spectrum of synthetic HA. This also

confirmed the carbonated nature of the precipitated HA of the coating surfaces [261]. Figure 5.10 b, which was the Raman spectra of 13-93 coatings deposited at 50 and 75 kW flame power immersed in SBF for 7 days, showed a small peak in the Raman analysis of 50 kW coating at 556 cm^{-1}. Moreover, Raman spectra of both 13-93 coatings after immersed in SBF for 7 days showed a band at 584-596 cm^{-1} and a shoulder at 614 cm^{-1}. These peaks and shoulders were due to the v4 bending of PO_4^{-3} [275].

5.4.3 EDX Analysis after Immersion in SBF

EDX line scans of the cross-sections of all the coatings after immersion in SBF for 7 days are shown in Figure 5.13. Figure 5.13 a is the cross-section of ICIE16 coating deposited at 50 kW, whilst Figure 5.13 b is its corresponding EDX analysis. The coating thickness was initially 68 ± 1 μm before immersion in SBF, and after immersion for 7 days the thickness had reduced to approximately 57 ± 1.5 μm whilst the deposited HA layer on this residual coating was approximately 9 ± 1 μm (Figure 5.13 a). Figure 5.13 b showed that Si content increased to 40 wt % at the coating – substrate interface and remained approximately constant through the coating. However, Si started to reduce at the coating- HA interface and reached 0 wt % at the top of the HA layer. The ICIE16 coating deposited at 75 kW was 59 ± 10 μm, and also reduced to 45 ± 13 μm, while the precipitated HA layer (after 7 days of immersion in SBF) on the surface of this coating was approximately 13 ± 3.5 μm (see Figure 5.13 c). EDX analysis of this coating (Figure 5.13 d) showed that Si had increased to 42 wt % at the coating- substrate interface, and then decreased by almost 5 wt % at the coating-HA interface. Ca was 5 wt % at the interface between coating and substrate whilst increasing to almost 32 wt % at the top surface of HA layer. P also reduced to 1 wt % at the coating- substrate interface and increased to almost 18 wt % in the deposited HA layer. The 13-93 coating deposited at 50 kW was initially 67 ± 1 μm, and after soaking in SBF for 7 days reduced to 58 ± 2 μm (Figure 5.13 e) whilst the precipitated HA layer was 8.5 ± 4.3 μm thick. Figure 5.13 f shows that the Si content was 30 wt %, almost the same as before the SBF test.

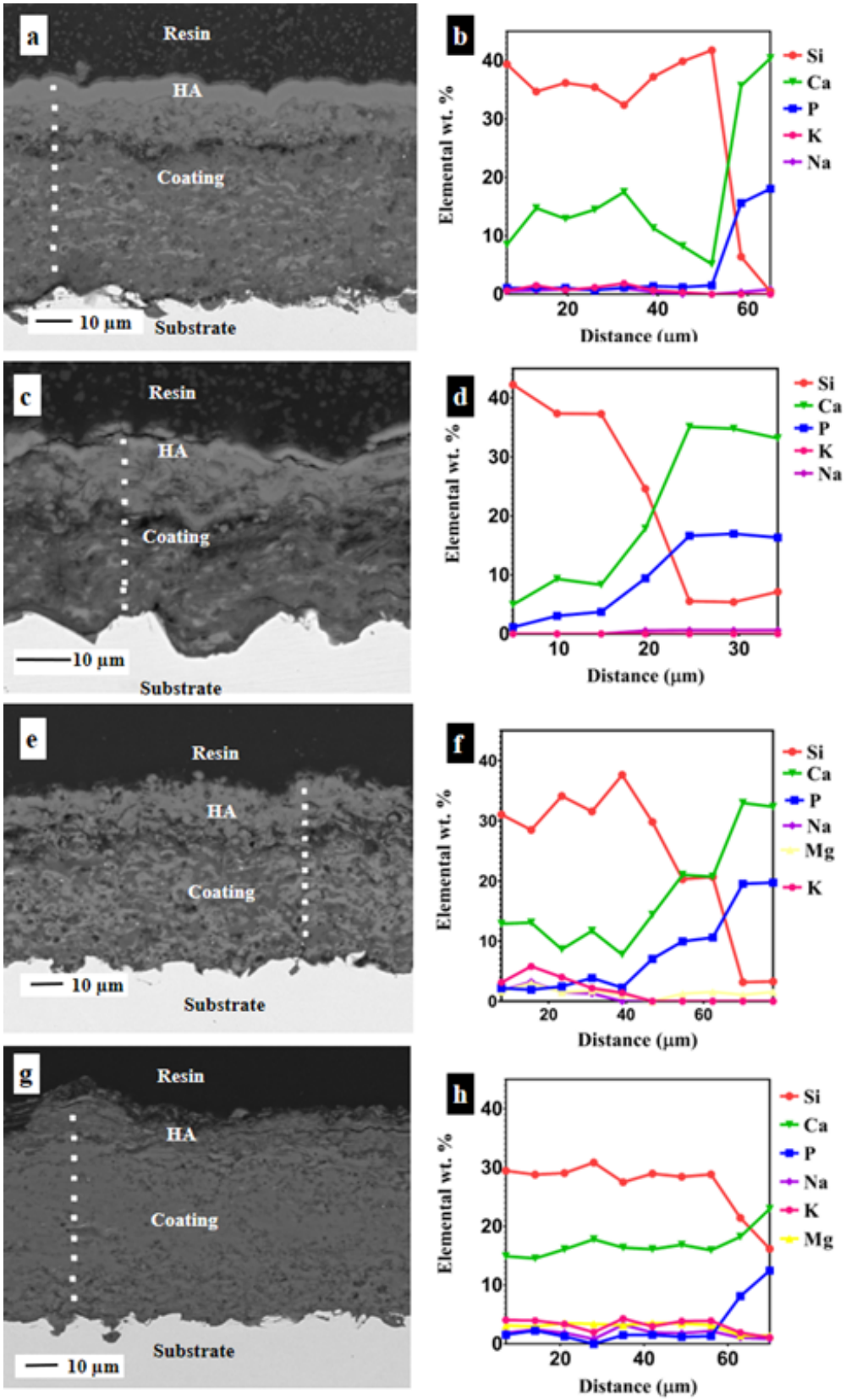

Figure 5.13: *In figure a, c are BSE images while b, d are the respective EDX line scan of ICIE16 coatings deposited at 50 and 75 kW after immersion in SBF 7 days, where e,g are BSE images while f,h are the respective EDX line scan of 13-93 coatings deposited at 50 and 75 kW after immersion in SBF 7 days (distance is from substrate-coating interface towards coating top surface).*

However, this also decreased at the coating- HA layer to 3 wt % in the HA layer. Ca content started at 13 wt % at the coating – substrate interface, and then increased at the coating- HA layer interface to almost 32 wt % in the precipitated HA layer. The 75 kW 13-93 bioactive glass coating was 62 ± 14 μm prior to immersion in SBF but was not uniformly distributed across the surface even after 7 days, as noted above. The thickness of this residual coating was 60 ± 5 μm, and the precipitated HA thickness was approximately 6 ± 1 μm (Figure 5.13 g). Figure 5.13 h showed that Si content remained constant at 30 wt % throughout the coating, and then started decreasing at the coating- HA interface to almost 15 wt % at the top of the HA layer. The Ca content also did not change in the coating and remained at around 15 wt %, which then started increasing at the coating- HA layer to almost 25 wt % in the deposited HA layer. The P content showed the same trend as Ca, and remained constant at 2 wt % in the coating and started to increase at the interface between coating and HA layer, increasing to almost 15 wt % at the top of HA layer.

Ca/P atomic ratio of the ICIE16 coatings before SBF and after immersion in SBF for 3 and 7 days can be seen in Table 5.4. It was observed that the Ca/P ratio decreased after the SBF tests. Before SBF tests, it was 27.0 ± 2.01 for 50 kW coating and 28.5 ± 1.61 for 75 kW coating. After immersion in SBF for 3 days, this had decreased to 1.78 ± 0.03 and 2.23 ± 0.08 for 50 and 75 kW coatings. These values further decreased to 1.71 ± 0.05 for the 50 kW coating and 1.55 ± 0.01 for the 75 kW coating after immersion in SBF for 7 days.

Table 5.4: *Ca/P ratio (atomic %) of the ICIE16 as-sprayed coatings and soaking in SBF after 3 and 7 days, where R50 is the coating deposited at 50 kW and R75 is the coating deposited at 75 kW flame power.*

Thermal Spray Coating at the Corresponding Flame Power	**Ca/P Ratio Soaking for 0 days in SBF**	**Ca/P Ratio Soaking for 3 days in SBF**	**Ca/P Ratio Soaking for 7 days in SBF**
R 50	27.0 ± 2.0	1.78 ± 0	1.71 ± 0
R 75	28.5 ± 1.6	2.23 ± 0	1.55 ± 0

5.5 In-vitro Cell Interaction

5.5.1 Cytotoxicity Tests using Alamar Blue Assay

Cell viability and proliferation tests were performed on ICIE16 and 13-93 bioactive glass coatings at two different time points of 3 and 7 days. Results from Alamar blue assay are summarised in Figure 5.14.

Two repeats of experiments were performed, and both of these were comparable in terms of cell viability. Moreover, significant differences were ($P < 0.05$) present between control and any of the coatings at time point of 3 days, and intensity was higher for the control than the coatings. However, no significant differences ($P > 0.05$) were present between control and any coating when 7 days were elapsed. After 7 days, it can be seen that the intensity was elevated for all of coatings than that of after 3 days, which indicates that cells proliferated on coating surfaces. From Figure 5.14, it should be noted that 13-93 coating, which was deposited at 75 kW showed highest intensity (more than the control) at time point 7, which means that cell response was better towards this coating in comparison to the other three coatings. Also, these tests demonstrated that all these coatings were cytocompatible.

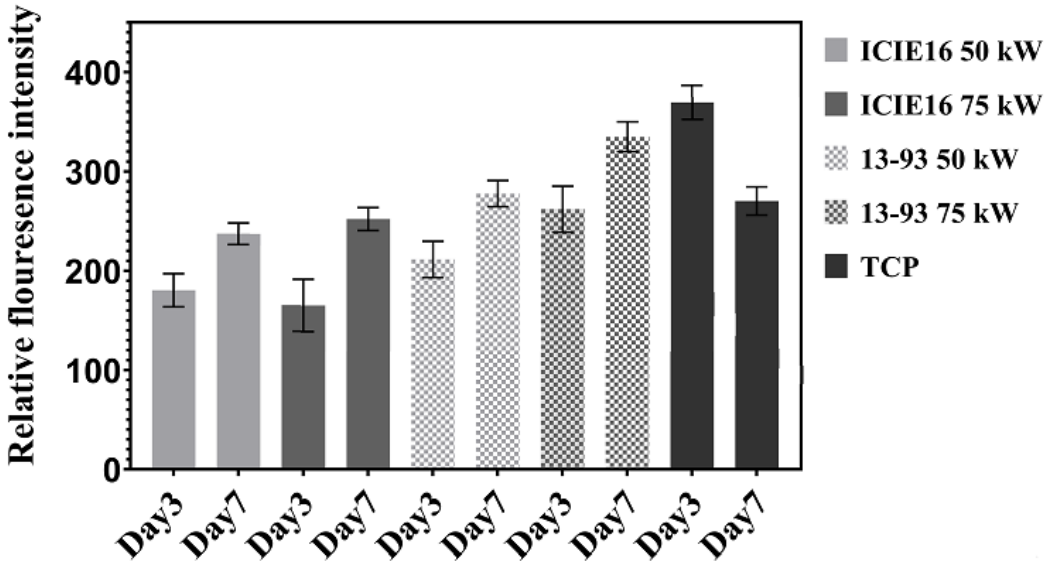

Figure 5.14: *Alamar blue assays results of the coatings using MG63 cells after 3 and 7 days of incubation, where TCP (Tissue culture plastic) is the control sample.*

5.5.2 SEM Observation

Figure 5.15 shows the morphology of MG63 cells adhered on to ICIE-16 and 13-93 bioactive glass coatings.

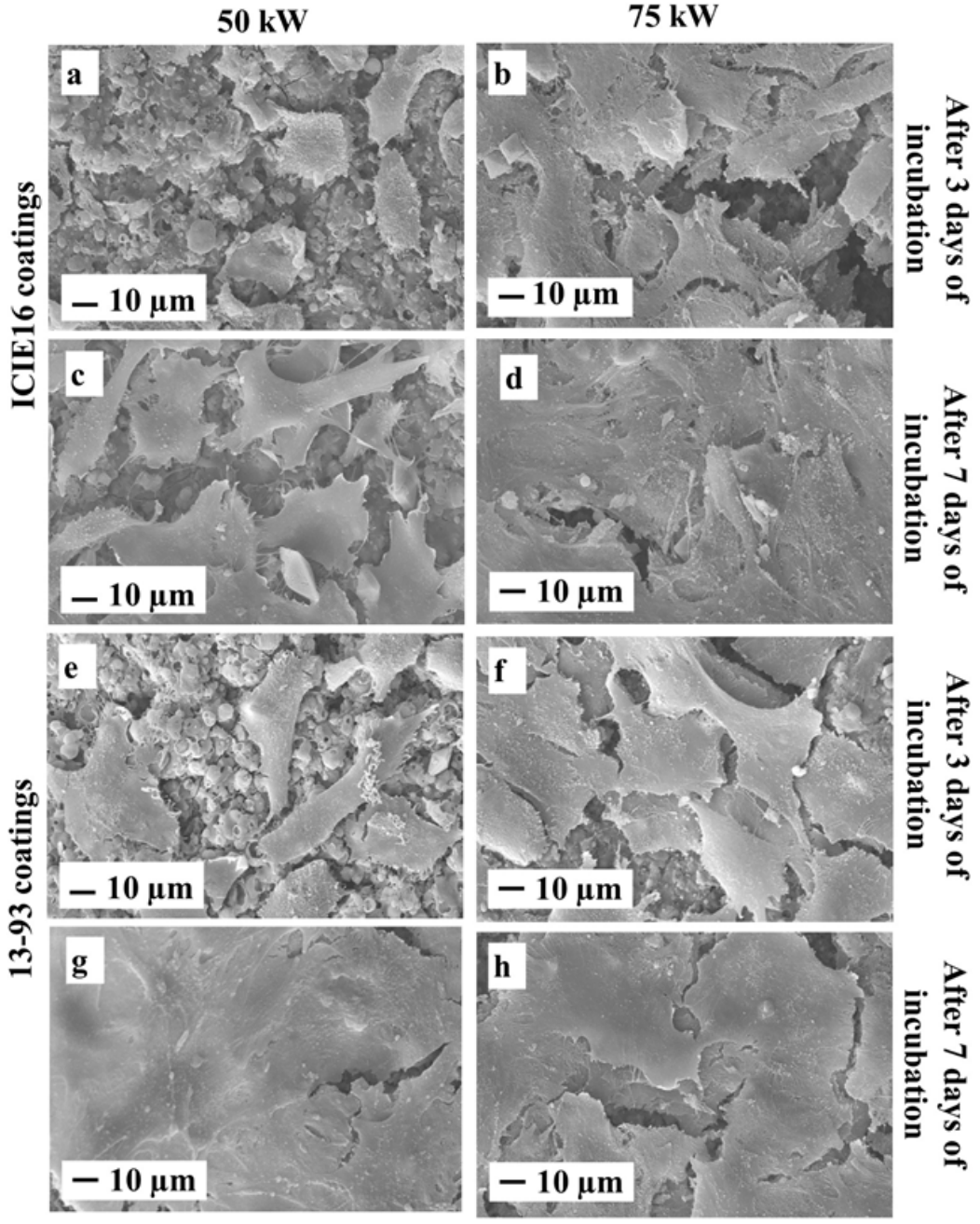

Figure 5.15: *SEM images of MG63 cells grown on ICIE16 (a-d) and 13-93 (e-h) bioactive glass coatings, a, b, e and f after 3 days of seeding and c, d, g and h after 7 days of seeding. a, c, e, and g are the coatings deposited at 50 kW and b, d, f and h are deposited at 75 kW of flame power.*

After 3 days of incubation, it can be seen from Figure 5.15 a, b, e and f that cells were growing on the surfaces of the coatings and demonstrated extended lamellopodia

and filopodia; however, as can be seen from Figure 5.15 b and f (which are SEM images of the ICIE16 and 13-93 coatings deposited at 75 kW of flame power after 3 days of incubation) multilayer cells were present on these surfaces. By increasing incubation time (Figure 5.15 c, d, g and f), surfaces of all of the coatings appeared to be covered with sheets of cells. Also, the cracks in sheets were due to dehydration of the samples for SEM observation.

5.5.3 Cytotoxiciy Tests using Alamar Blue Assay after Gold Coating of the Bioactive Glass Coated Surfaces

ICIE16 coating deposited at 75 kW and 13-93 at 50 and 75 kW coatings were gold coated (ICIE16 50 kW coated samples were run out, so couldn't include in this test) and the cell test was performed for 7 days' time point. The purpose of this test was to observe the effect of the surface topography on cell viability, as after gold coating, the composition of the glass coatings wouldn't affect cell grow. It can be seen in Figure 5.16,that no significant differences ($P > 0.05$) were present among the coatings and control after incubation for 7 days. However, 13-93 coating deposited at 75 kW showed high intensity in comparison to other coating (but like the control), suggesting that the rougher surface of this coating had a positive impact on the proliferation of the cells.

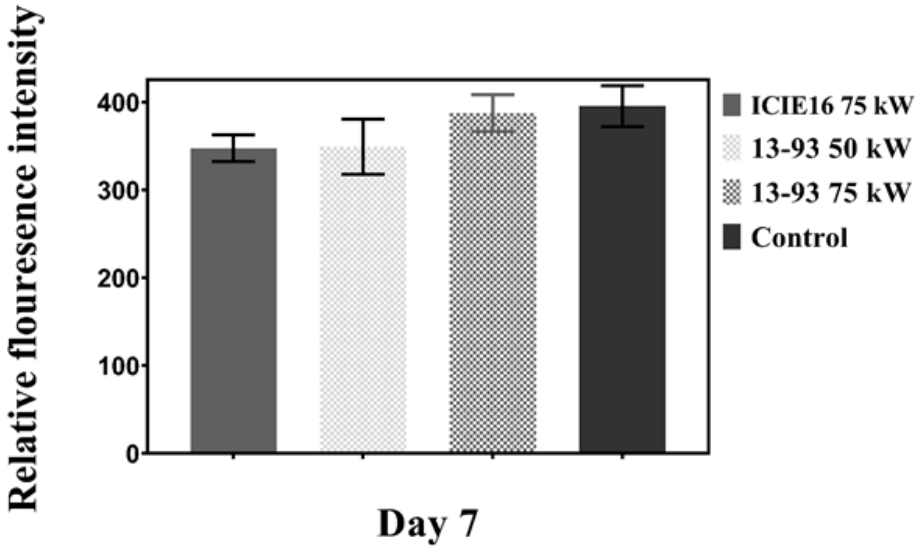

Figure 5.16: *Alamar blue assay results of the ICIE16 and 13-93 bioactive coatings using MG63 cells after 7 days of incubation.*

5.6 Discussion

5.6.1 Coating Characterisation

Regardless of the glass formulations tested or the flame power applied, all the coatings were observed to be adhered to the substrates as no crack was present along the coating-substrate interface. The 50 kW coatings of ICIE16 and 13-93 bioactive glasses had approximately similar microstructure; however, comparing the roughness of the as-sprayed samples, the 50 kW ICIE16 coating surfaces were smoother (1.8 ± 0 μm) than the 13-93 bioactive glass coating deposited at the same flame power (2.4 ± 0 μm). This could be due to the different particle size distribution of the two glasses used for spraying. As the particle size distribution of 13-93 (Figure 5.1 c) showed more fine particles present in this powder than present in the ICIE-16 powder samples (Figure 5.1). For fine particles, it has been reported that due to their low inertia, they do not deform upon hitting the substrate; instead, they retain their spherical morphology due to surface tension [37]. The presence of more globular particles on the surface of the 13-93 glass 50 kW coating (Figure 5.4 c, d) also contributed to its roughness, in comparison to the ICIE16 bioactive glass coatings deposited at the same power (Figure

5.4 a, b).

The surfaces of the ICIE16 and 13-93 bioactive glass coatings deposited at high flame power (75 kW) had semi-spherical features (Figure 5.5). This could have been caused by large agglomerates forming inside the combustion chamber during spray and adhering to the chamber walls. At high flame power, these agglomerates can melt due to more heat transfer, leading to detachment from the combustion chamber walls and sprayed onto the substrate [37]. These globules were also mainly responsible for the high surface roughness of the higher flame power coatings [276] compared to the lower 50 kW coatings [277]. However, the globules present on the 13-93 coating surface were not as porous (Figure 5.5 e) as were those present on the surface of ICIE16 coating deposited at 75 kW (Figure 5.5 b) which could be due to the particle size difference of the suspensions of two glasses.

The cross-sectional view of ICIE16 75 kW coatings (Figure 5.6 b) showed that in the globules, after the porous structure at the base, a dense region was present in the middle of these formations. From studying the morphology of these globular shapes, it can be argued that there was small surface disruption at the start. Subsequently, the incoming melted particles interact with these deviations, which results in larger porous regions due to localised splat disorder. With each torch pass, splat interaction repeats, creating more porosity [78, 276]. The 75 kW coatings of ICIE16 and 13-93 were thinner, harder and less porous in comparison with the 50 kW coatings (Figure 5.6), which was due to the enhanced melting of these materials at high flame power leading to less porous and more dense coatings than the 50 kW flame power coatings [264, 278].

5.6.2 SBF Studies of the ICIE16 and 13-93 Coatings

Investigation of the coatings after immersion in SBF revealed the development of cauliflower- like precipitates on their surfaces which are characteristic of HA deposition and growth in SBF [217, 279]. The broad crystalline peak at $\sim 26^{\circ}$ and 32° was associated with the nanocrystalline nature of the precipitated HA [280]. HA formed

just after 3 days of immersion in SBF on both glass composition coating deposited at 50 kW as confirmed via XRD (Figure 5.11 a, c). The HA precipitation continued with longer immersion times as the intensity of the HA peaks increased at 7 days. No HA was observed on the 13-93 coating deposited at 75 kW after 3 days of immersion in SBF (Figure 5.11 d). This coating revealed HA deposition only after 7 days of immersion in SBF (Figure 5.8 d). Due to more SiO_2 content, 13-93 glass is comparatively resistant to dissolution and hence apatite formation [37]. Where presence of MgO makes this glass less vulnerable to dissolution [281]. The 13-93 coating deposited at 75 kW has more SiO2 and MgO relative to the starting powder (Table 5.3) which could also have contributed to delayed apatite formation [281]. MgO in glass formulations has been reported to decrease HA formation in vitro [217]. However, in-vivo it has been shown to support early-stage mineralisation [217, 282]. MgO acts as network intermediate, [217] thus inhibiting the dissolution process, which is low for 13-93 compared to 45S5 and ICIE16, due to the higher silica content [276].

Both ICIE16 coatings showed more dissolution in SBF than 13-93 coatings as suggested by EDX analysis along the cross-section of the coatings after immersion in SBF for 7 days (Figure 5.13). This difference in reactivity of the ICIE16 and 13-93 coatings deposited at 50 kW was probably due to the higher content of silica in 13-93 than ICIE16 (Table 5.1), as previously discussed, which caused less dissolution of 13-93 in SBF [15]. Also, ICIE16 composition is closer to Bioglass (45S5) (which is the most bioactive material known), as can be seen in the ternary phase diagram described by Hench et.al [49], and this could be a reason for the more dissolution of ICIE16 coating in comparison to 13-93 coating. However, comparing the 50 kW coating and 75 kW of ICIE16, the 75 kW coating showed more reactivity than the 50 kW coating in terms of dissolution in SBF, which may be due to the higher surface roughness of the 75 kW coating than the 50 kW coating. It has been shown that higher surface roughness increases the contact area with SBF [283], which increases ion leaching from bioactive coatings [27]. On the other hand, the 75 kW coating of 13-93 showed less reactivity than its 50 kW coating during the SBF test. The reason for the lower reactivity of

13-93 coating deposited at 75 kW is the same as for its coating deposited at 50 kW, i.e. high silica content and low bioactivity in comparison to ICIE16 coating, which is the composition closer to Bioglass (45S5).

The Ca/P ratio for ICIE16 coatings deposited at 50 kW after 7 days in SBF given in Table 5.4, was 1.71 ± 0.05, which is approximately equal to the 1.67 Ca/P ratio of synthetic HA [99]. For the ICIE16 coating deposited at 75 kW, after immersion for 7 days, the Ca/P ratio obtained was 1.55 ± 0.01, much closer to that of synthetic tricalcium phosphate (TCP) for which Ca/P ratio is 1.5 and is also regarded as a precursor for HA [269]. However, the Ca/P ratio reported for physiologic HA has also been suggested to be around 1.5 [71].

After immersion in SBF for 7 days, the Ca/P ratio for 13-93 coating deposited at 50 kW was 1.24 ± 0.06 and for the coating deposited at 75 kW was 2.05 ± 0.74 (see Table 5.4). The Ca/P ratio of the deposition on the surface of the 50 kW coating of 13-93 glass suggests that it could be similar to either octocalcium phosphate (OCP) or dicalcium phosphate (DCP), with Ca/P ratios of 1.33 and 1 [284]. Ca/P ratio less than 1.67 (which was observed for the HA deposited on 75 kW coating of ICIE16 and 50 kW coating of 13-93 after 7 days of immersion in SBF) shows that the HA precipitated at the surfaces of the coating were calcium deficient and had carbonated nature [284, 285]. For the 75 kW coating of 13-93, Ca/P ratio was 2.0 ± 0.74, which is closer to the Ca/P ratio of tetra calcium phosphate (TTP). TTCP is a metastable compound that converts to HA in a continuous dissolution- precipitation process [286].

5.6.3 In-vitro Cell Interaction of ICIE16 and 13-93 Coatings Towards MG 63 Cells

In this work, through the study of MG63 cells, it was shown that ICIE16 and 13-93 coatings deposited via SHVOF thermal spray on to stainless steel substrate were cytocompatible, as the coatings showed no cytotoxicity and displayed good proliferation. From proliferation results, both coatings supported increased viability across the length of the study. However, it should be noted that the 13-93 coating, which was deposited

at 75 kW showed the highest intensity after 7 days of incubation in comparison to the other coatings (Figure 5.14). This may have been due to the rougher surface of this coating (6.5 ± 0.6 μm), and it has been shown in the literature that rough surfaces can significantly enhance the attachment of osteoblast-like MG 63 cells [287]; however, this effect was noted only during the first 24 hrs of incubation and did not affect their proliferation rate. The same effect of surface roughness on cells was also reported by Boyan et. al [288]. Also, from the proliferation results, intensity for the 75 kW coating of 13-93 bioactive glass was more than that of the control, this may have been due to the enhanced cell proliferation owing to the presence of MgO in the glass composition as Mg can directly enhance osteoblast proliferation [282]. From these results, it can be concluded that both ICIE16 and 13-93 coatings deposited at 50 and 75 kW were nontoxic and bioactive.

5.7 Summary

Bioactive coatings of ICIE16 and 13-93 compositions with varied apatite forming ability were successfully produced by an emerging SHVOF thermal spraying technique. Change of flame powers for the same glass resulted in different microstructure of the coatings, and hence their reactivity in SBF. Spraying at same flame power but with different compositions also resulted in different microstructure and apatite forming ability when tested using SBF. In-vitro cell culture tests showed that the surfaces of these coatings were biocompatible with human osteoblast-like (MG-63) cells. From the microstructure, SBF and cell tests of these coatings the following conclusions can be drawn:

- Coatings of ICIE16 and 13-93 sprayed at high flame power (75 kW) were harder, thinner and less porous than their 50 kW coatings due to better melting of feedstock materials at high flame power.
- ICIE16 coatings sprayed at both flame powers, and 13-93 coating sprayed at low flame power (50 kW) revealed HA deposition after 3 days of immersion in

SBF; however, 13-93 coating sprayed at high flame power (75 kW) showed HA precipitation immersed in SBF for 7 days.

- In SBF, both of ICIE16 coatings showed more resorption than the 13-93 coatings, which is due to the high Si content of 13-93 that makes this glass comparatively stable in SBF.

- In vitro cell tests showed that all of these coatings were biocompatible; however, the 13-93 coating deposited at high flame power (75 kW) showed the highest proliferation, which is likely be due to the high surface roughness of the coating (Ra = 6.5 ± 0.6 μm) and presence of MgO in the glass composition.

Chapter 6

P-40 Phosphate Based Glass Coatings

6.1 Introduction

In this chapter, Phosphate based glass (PBG) P-40 (40 mol % P_2O_5, 16 mol % CaO, 24 mol % MgO, 20 mol % Na_2O) coatings deposited via SHVOF thermal spray at flame power of 50 and 75 kW has been characterised. Ion leaching study of the coatings carried out in milli-Q water, whilst mass degradation study was carried out using PBS and milli-Q water.

6.2 Powder Characterisation

6.2.1 Particle size distribution

The final powder after ball milling had a distribution shown Figure 6.1. This distribution had the particle size with D_{10} = 1.1 μm, D_{50} = 3.6 μm, D_{90} = 14 μm. However, the distribution was wider (as shown in Figure 6.1) with a range of 2 μm -27 μm.

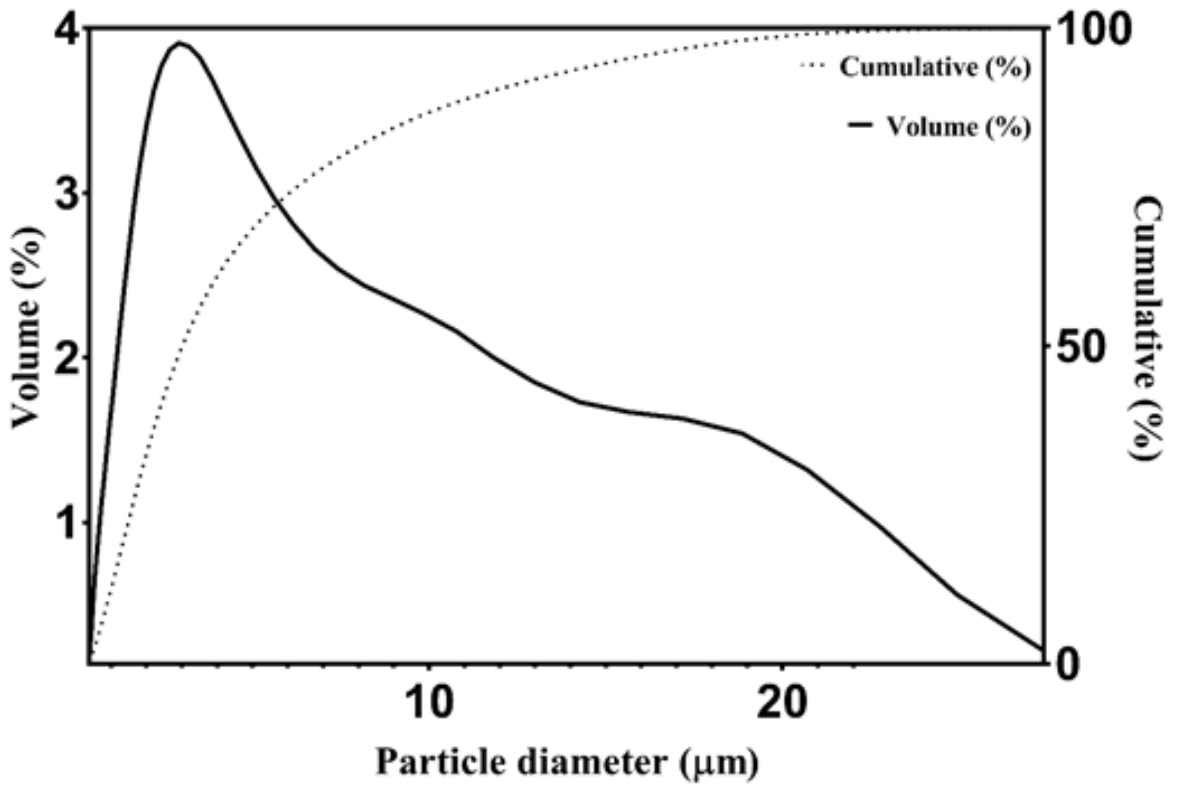

Figure 6.1: *Particle size distribution of P-40 powder used for suspension preparation.*

6.2.2 SEM Image and EDX Analysis of the Powder

Figure 6.2 shows the SEM image of the P-40 powder used for suspension preparation, and the powder contained both fine and coarse particles. The largest particle observed was approximately 10 μm.

EDX point analysis was carried out on the powder, and the results are presented in Table 6.1, which shows that the powder had contained 26.4 ± 0.2 wt % P, 12.5 ± 0.2 wt % Ca, 6.2 ± 0.1 wt % Na and 8.2 ± 0.2 wt % Mg, while the elemental wt % based on the formula of P-40 glass is 28.0 wt % P, 10.3 wt % Ca, 7.3 wt % Na and 5.0 wt % Mg, so it means that in the prepared powder P was present 2 wt % less than the theoretical wt %. Similarly, the contents of Na and Ca were present less than the theoretical values; however, Mg amount was more in actual than the theoretical value.

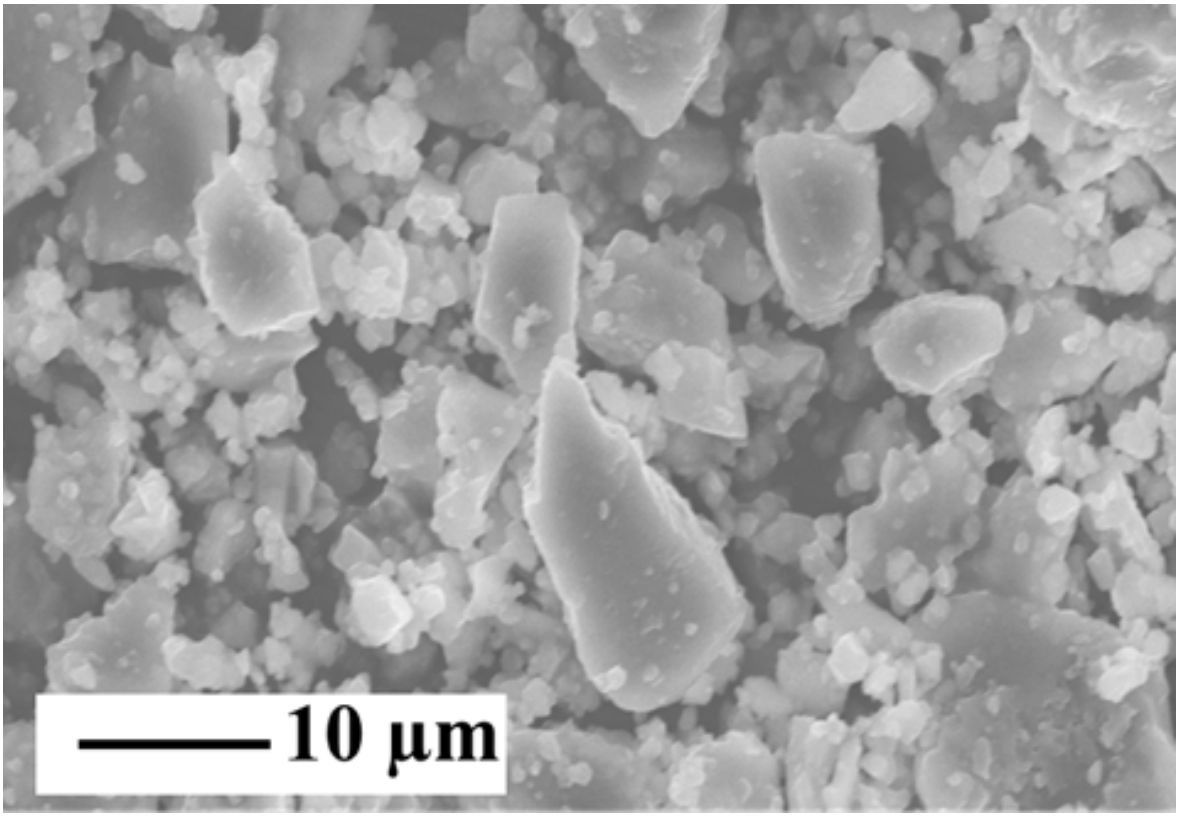

Figure 6.2: *SE, SEM image of the feed stock powder showing powder morphology.*

Table 6.1: *Elemental wt % of the starting powder from EDX scan.*

Elements	**Wt %** **Based on Formula**	**Powder (wt %)**
P	28.00	26.4 ± 0.2
Ca	10.36	12.5 ± 0.2
Na	7.30	6.2 ± 0.1
Mg	5.00	8.2 ± 0.2

6.2.3 XRD and Raman of the Powder

XRD profile of the P-40 powder is presented in Figure 6.3 a. A single broad peak at 25-30 ° 2θ ° was observed for the glass. The absence of any sharp crystalline peak confirmed the amorphous nature of the glass.

Figure 6.3 b shows the Raman spectra of the P-40 glass powder. For the Raman spectrum of P-40 powder, the band at 351 cm^{-1} was related to bending vibrations of the O–P–O bonds of Q^o tetrahedral units [29,30]. The low-intensity bands in the range of 470-620 cm^{-1} are due to the bending vibrations of the P-O bonds and in-chain P-O-P stretching vibrations [113]. The Raman bands at 670-790 cm^{-1} are associated with the P-O-P symmetric stretching of bridging oxygen in Q^2 units [289]. The bands at 1160 cm^{-1} are related to the symmetric stretching modes of P-O-P bridging oxygen and O-P-O non-bridging oxygen in Q^2 phosphate units [28]. Also, in Q^1 tetrahedra, the bending vibrations of O–P–O bonds peaked at 1046 cm^{-1} [113], and the shoulder at 1267 cm^{-1} was associated with the symmetric stretching of terminal oxygen bonds [113].

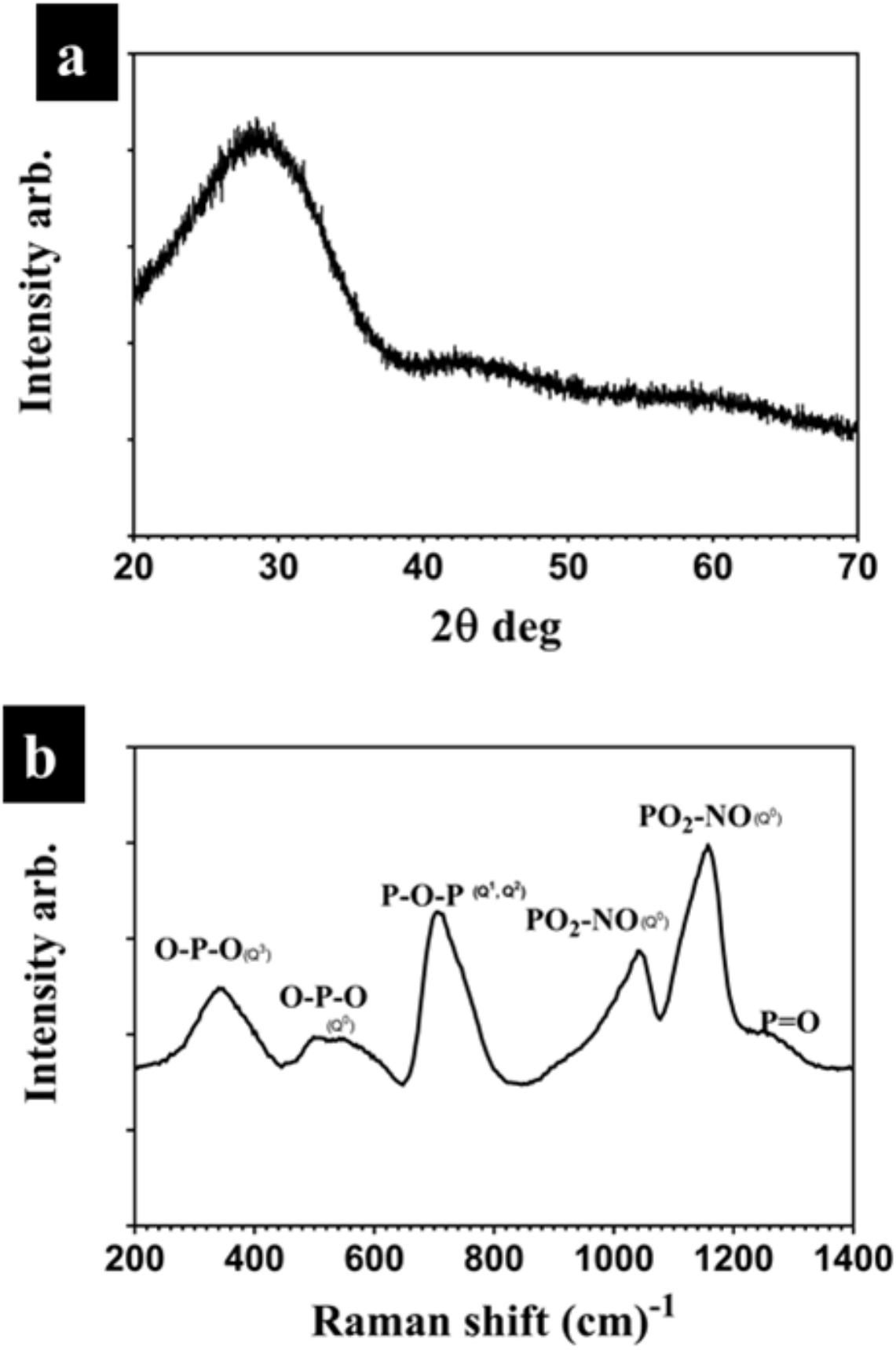

Figure 6.3: *(a)XRD amorphous phase and (b) Raman spectrum of P-40 powder showing structure of P-40 glass.*

6.3 Coating Characterisation

6.3.1 Surface Morphology and Microstructure of the Coatings

Two coatings of P-40 glass were deposited: 50 and 75 kW flame power. The surface morphology of these coatings can be seen in Figure 6.4, where a, b, c are the surface images at different magnifications of the P-40 coating deposited at 50 kW, and d, e, f are the images of coating deposited at 75 kW. Large humps were uniformly distributed on the surface of both coatings, as can be seen in a, d. However, the globules on the surface of 50 kW coating (Figure 6.4 seemed to be rough as finer particles were adhering to the humps. In contrast, the humps present on the surface of the 75 kW coating (Figure 6.4 e) looked smoother. In addition, humps present on the surface of both coatings were approximate the the same size and seemed to be larger than 10 μm in diameter. In the humps-free area, there were -molten splats in both cases, as seen in Figure 6.4 c and f. In both cases, the material was well molten so that the size of individual splats could not be estimated.

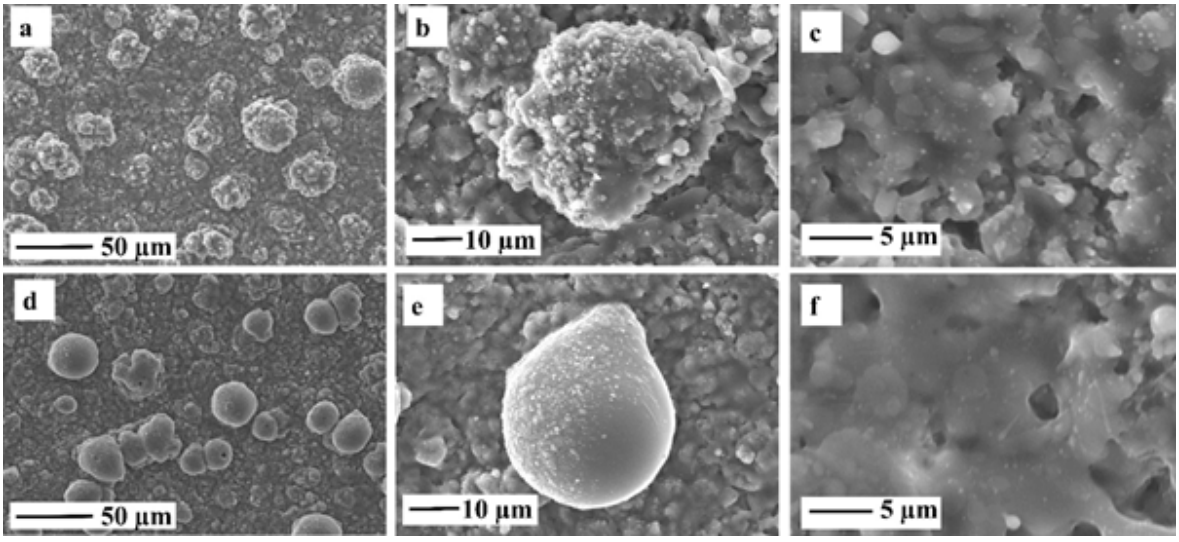

Figure 6.4: *SE, SEM images of the surface of the P-40 coatings, a, b, c coating deposited at 50 kW, while d, e, f of the 75 kW coating showing morphology of the coatings.*

Cross-section images of the SHVOF sprayed P-40 are shown in Figure 6.5. It can be seen that both coatings were well-adhered with the substrate, and no crack or delamination was observed at the interface between the coatings and substrate. The

microstructure of these coatings was dense, with 50 kW coating 2.9 ± 0.2 % porous and 75 kW coating 1.5 ± 0.4 % porous, respectively. The globular features on the top of the coatings made their thickness non-uniform (Figure 6.5 b, d). The observed thickness for the coating deposited at 50 kW was 24.6 ± 2.3 μm, and for the coating deposited at 75 kW, it was 16.0 ± 3.4 μm, respectively. These globules made the surface of the coating rough too, with 50 kW coating 2.7 ± 0.1 μm and the 75 kW coating 3.6 ± 0.1 μm.

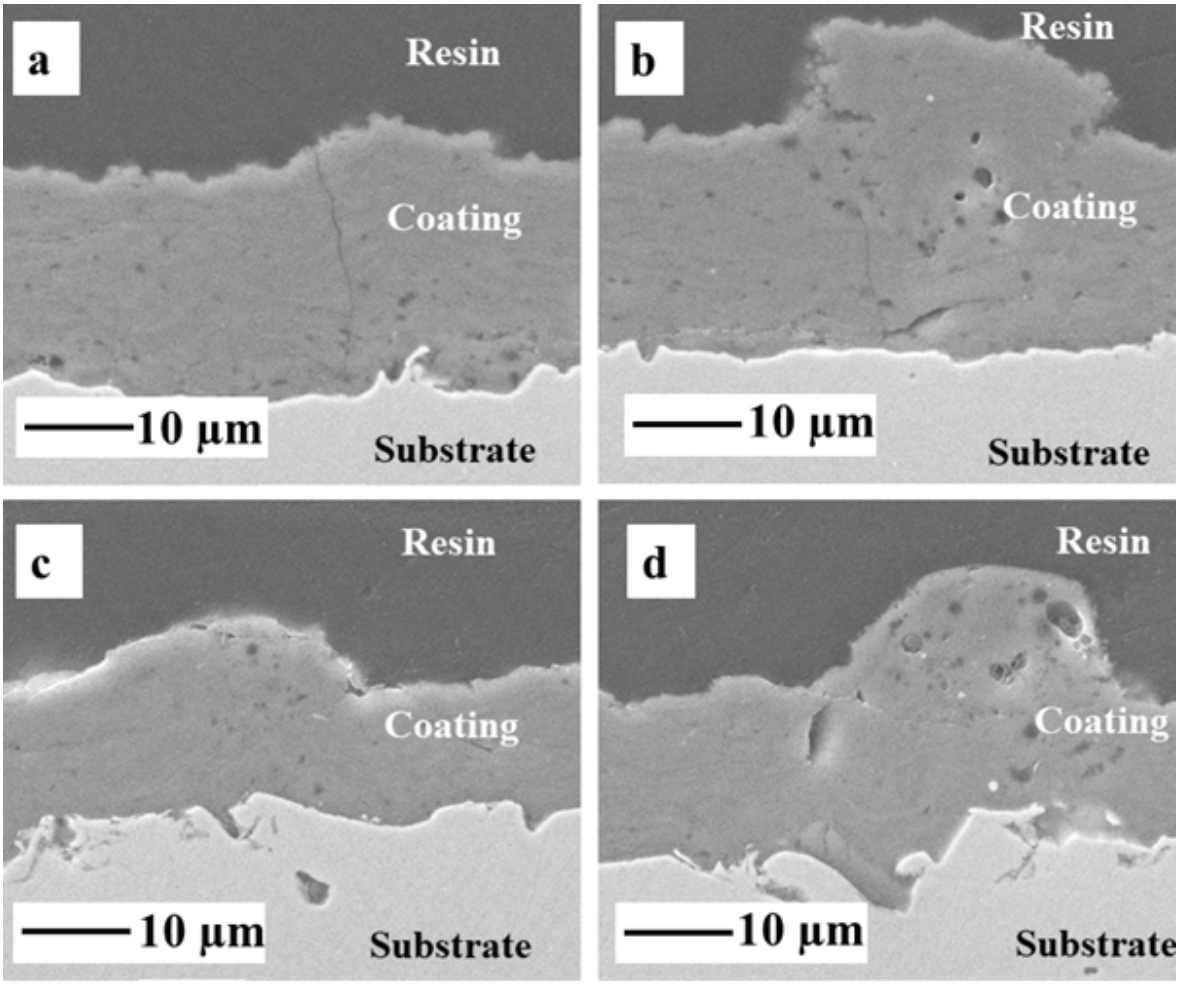

Figure 6.5: *SE, SEM images of the cross-section of P-40 coatings, a, b coating deposited at 50 kW and c, d deposited at 75 kW. While a and c are the globules-free regions, and b and d are with globules.*

6.3.2 EDX Analysis of Coatings

To determine any compositional changes in P-40 glass after thermal spray, EDX scans were carried out along the cross-section of the coatings and can be seen in Figure 6.6, where elemental wt % is presented as function of distance from the coating-substrate with corresponding BSE images. The points on the images show the location where the analysis was carried out.

In the P-40 coating produced at 50 kW, slight variation was observed in comparison to the starting powder composition (Table 6.2); however, the elemental wt % was approximately constant along the cross-section, while going from the coating-substrate interface to the top of coating. As can be seen in Table 6.2, P content was 26.4 wt % in the starting powder, and that was reduced to 24.5 wt % at the coating-substrate interface; however, it was observed that wt % of P was 26.4 wt % at the top of the coating. Before spraying, 12.5 wt % Na was present in the powder; however, Na wt % was reduced to approximately 5.5 wt % at the coating-substrate interface, and approximately no further variations were observed in this value up to the top of the coating. Ca of 9.2 wt % of was observed at the coating-substrate interface and remained at this value till the top of the coating. This means that the amount of Ca was increased from that present in the starting powder, which was 6.2 wt %. In Mg content, the increment was observed from that present in the starting powder, which was 8.2 wt % to approximately 10 wt % at the coating-substrate interface, and remained at this value to the top of the coating. Fe of 5 wt % and approximately 2 wt % of Cr were observed near the coating-substrate interface originating from the substrate.

For the coating of P-40 glass deposited at 75 kW, the same trends were observed as for the 50 kW coating. The elements wt % was approximately the same along the cross-section of the coating; however, relative to the starting material, the composition was slightly changed. Content of P was observed to be 22.6 wt % at the coating-substrate interface; however, this amount was increased to approximately 25 wt % at the top of the coating. For this coating, reduction in Na content was slightly more

than that observed for the 50 kW coating, as its content reduced to 3.53 wt % at the interface from that of 12.5 wt % (in powder) and did not change from this value till the top of the coating. Similar to the 50 kW coating, wt % of Ca and Mg were increased in the 75 kW coating. Ca content was less in the starting powder (6.2 wt %) before spray and increased to approximately 11.62 wt % along the cross-section of the coating. Similarly, 11.74 wt % of Mg observed along the coating cross-section till the top of the coating, while in the powder 8.2 wt % of Mg was present before spraying.

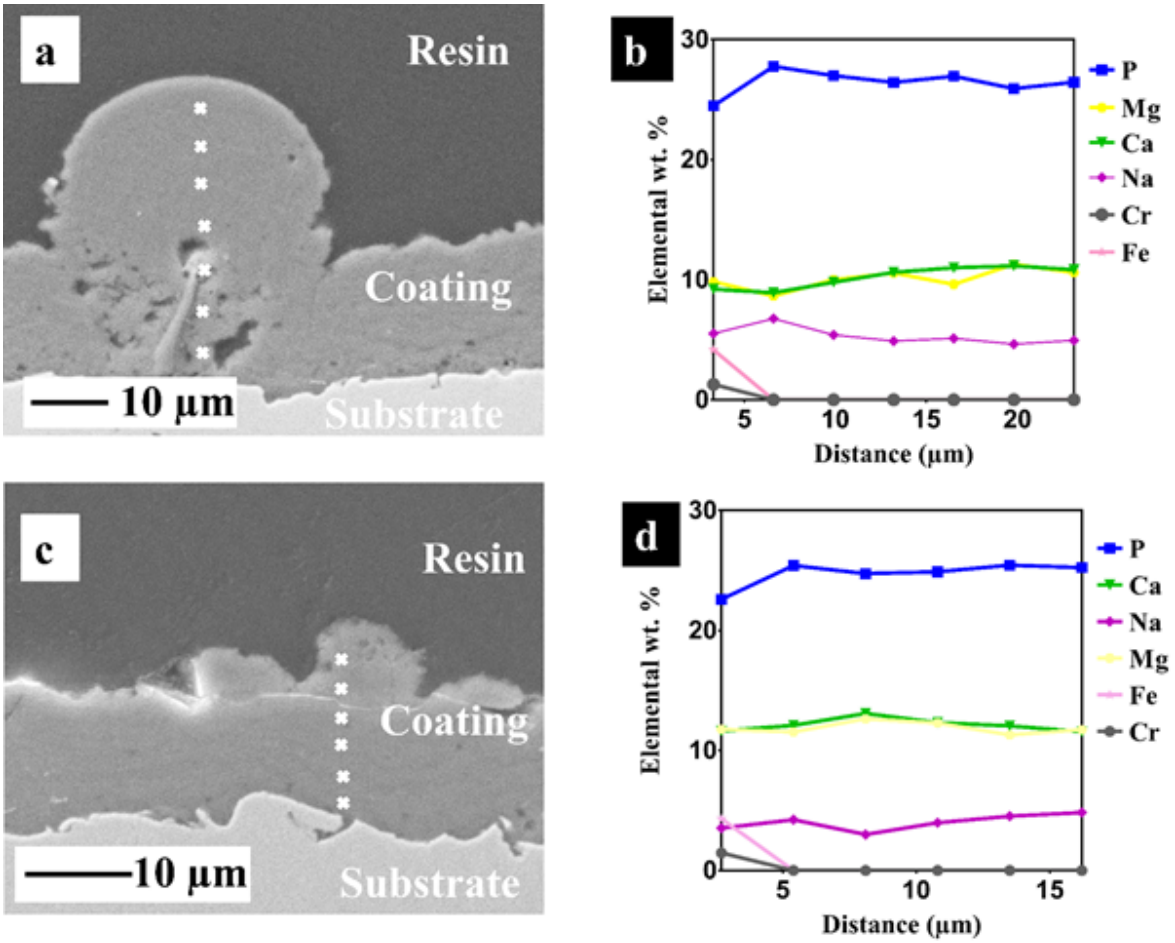

Figure 6.6: *a and c are the BSE images of the cross-section of P-40 coatings deposited at 50 and 75 kW, while, b and d are the respective EDX line scan across the cross-section (distance is from substrate-coating interface towards coating top surface).*

EDX area analysis carried on the top surfaces of the coatings are shown in Table 6.2. This analysis showed that changing the flame power had a significant effect on the composition of P-40 glass. 26.4 wt % of P was present in the powder, and this amount was reduced to 24.0 wt % while spraying at 50 kW flame power. This amount was

further reduced to 22.8 % while depositing at 75 kW flame power. Similar reductions were observed for the wt % of Na, as it was 12.5 wt % in the powder and reduced to 7.1 wt % at 50 kW and 5.5 wt % in the 75 kW coating. However, the inverse effect was observed for Ca and Mg content. As Ca wt % was increased from 6.2 (present in the powder) to 11.6 spraying at 50 kW flame power, and to 13.4 wt % while depositing at 75 kW. Similarly, Mg content was observed to be 11.4 wt % in the 50 kW coating and 12.8 in the 75 kW coating, while in the powder, it was observed to be 8.2 wt %.

Table 6.2: *EDX analysis on the top surface of the P-40 coatings in terms of elemental wt%/ oxide mol%, also the powder analysis is provided (number of measurements=3)*

Element/ Oxide	**Elemental Wt%/ Oxide (mol%) Based on P-40 Formula**	**P-40 Powder Elemental wt%/ Oxide (mol%)**	**P-40 Coating Deposited at 50 kW Elemental wt%/ Oxide (mol%)**	**P-40 Coating Deposited at 75 kW Elemental wt%/ Oxide (mol%)**
P/P_2O_5	28.0/40.0	26.0 ± 00.0/ 36.0 ± 1.0	24 ± 00.0/ 29.0 ± 1.0	22.0 ± 00.0/ 27.0 ± 00.0
Na_2O	10.3/20.00	12.5 ± 00.0/ 22.0 ± 00.0	7.0 ± 0.0/ 11 ± 00.0	5.0 ± 1.0/ 8.0 ± 1.0
Ca/CaO	7.3/16.0	6.2 ± 00.0/ 13.0 ± 00.0	11.0 ± 00.0/ 22.0 ± 1.0	13.0 ± 1.0/ 24.0 ± 2.
Mg/MgO	5.0/24.0	8.2 ± 00.0/ 28.0 ± 1.0	11.0 ± 00.0/ 36.0 ± 1.0	12.0 ± 1.0/ 39.0 ± 1.0

6.3.3 XRD and Raman Analysis of the Coatings

No crystallisation of the P-40 glass occurred due to thermal spraying, and the amorphous phase of glass was maintained while depositing at two different flame powers, as showed by the XRD analysis given in Figure 6.7. The broad diffraction halos centred at $2\theta \approx 30^\circ$ were identified in the powder and both coatings. The only crystalline peaks recognised were originated from the substrate and were identified as ferrite (PDF card no. 00-006-0696) and austenite (PDF card no. 00-023-0298).

Raman analysis was carried out to identify any structural changes in P-40 coatings,

which is shown in Figure 6.8. For the P-40 powder, the peak at 351 cm^{-1} was related to bending vibrations of the O–P–O bonds associated with Q^2 tetrahedral units (Q specie having two BO) [115]. The low-intensity peaks in the range of 470-620 cm^{-1} were suggested to be due to in-chain O-P-O stretching vibrations [290]. The Raman peaks at 670-790 cm^{-1} were associated with the P-O-P symmetric stretching of the bridging oxygen in Q^2 and Q^1 units (Q specie with 1 BO), respectively [290]. In the previous study, it has been shown that P-40 formulation contained 50 % Q^2 and Q^1 units [115]. The peak at 1040 cm^{-1} was related to symmetric stretching of PO_2 non-bridging oxygen in Q^1 unit. The peak at 1160 cm^{-1} was associated with the symmetric stretching modes O-P-O non-bridging oxygen in Q^2 phosphate units [290].

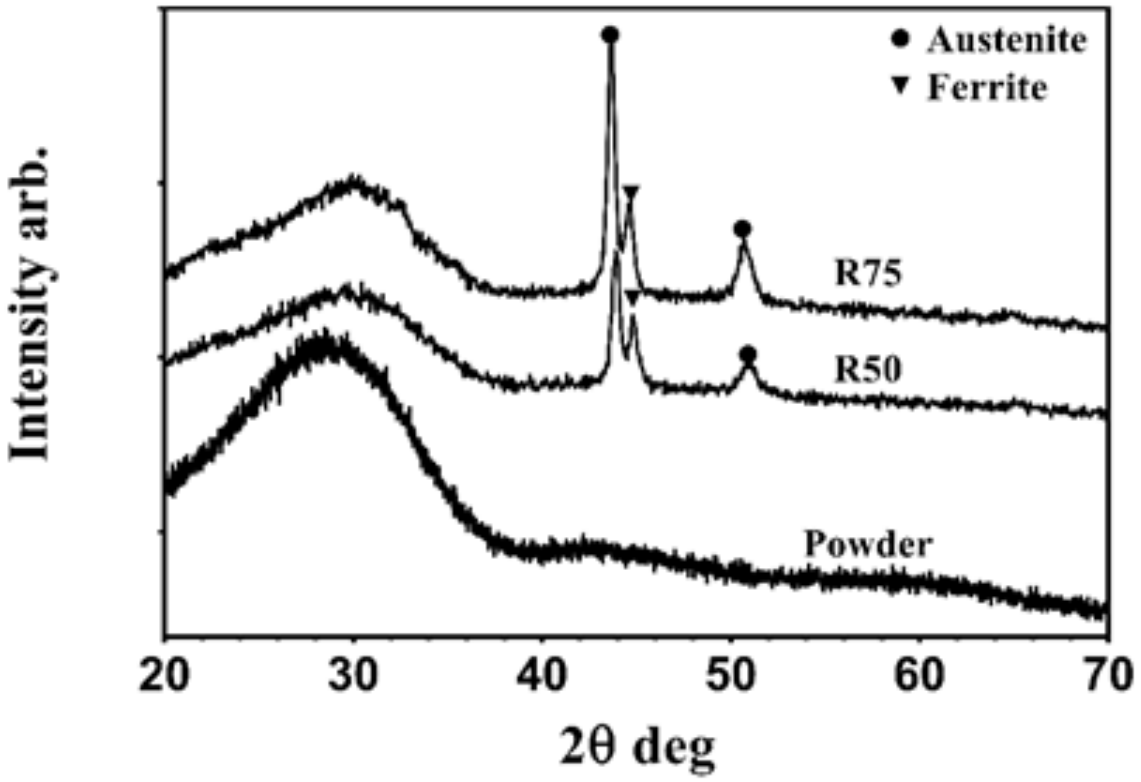

Figure 6.7: *XRD patterns of the P-40 coatings, where R50 is the coating deposited at 50 KW and R75 is the coating deposited at 75 kW flame power.*

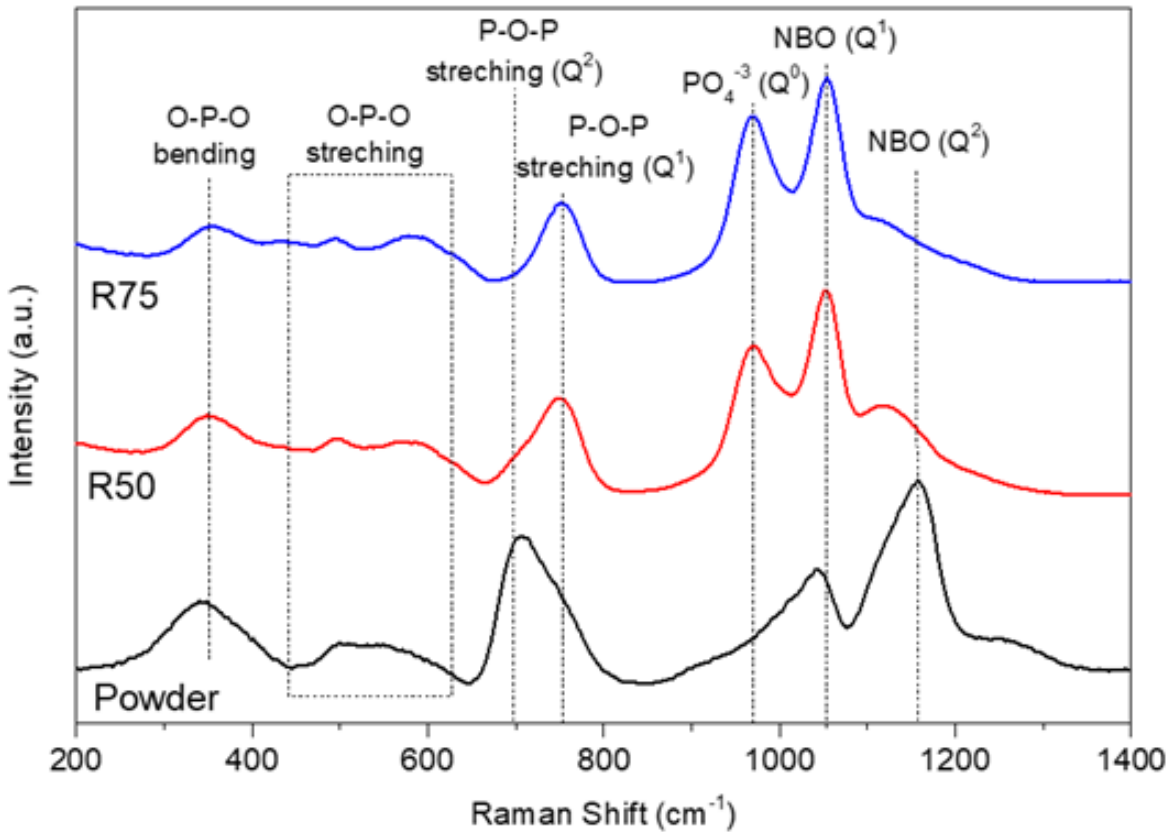

Figure 6.8: *Raman spectra of P-40 coatings showing peaks of P-40 coatings.*

Post thermal spraying, analysis of the P-40 glass coating at flame power 50 and 75 kW revealed that the peak at 670 cm^{-1} (which had been assigned to P-O-P symmetric stretching of the bridging oxygen in Q^2 units) had disappeared, whilst the peak at 790 cm^{-1} had appeared for both coatings. A new peak was also observed at 960 cm^{-1} for both the 50 and 75 kW coatings which was associated with the symmetric stretching of orthophosphate group (PO_4^{-3}) in Q^0 unit (Q specie with no BO) [289]. The intensity of the band at 1046 cm^{-1} (associated with Q1 unit) also increased for both coatings, whilst the peak intensity at 1160 cm^{-1} (associated with Q^2 unit) decreased for the 50 kW coating and appeared as a shoulder in the Raman spectrum of the 75 kW coating (Figure 6.8).

6.4 Ion Release Profiles of the P-40 Coatings

Cation release profiles Na^{+}, Mg^{2+}, Ca^{2+} and P^{5+} for the P-40 coatings were investigated via ICP-MS while recording the ions release in ultra-pure water. The cumulative ion release profiles of the glass coatings investigated appeared to follow a linear relationship with time as shown in Figure 6.9 a and b. In addition, Table 6.3 shows the ion release rates. The ion release rates were calculated as the slope from the linear interpolation of the values and are given in Figure 6.9.

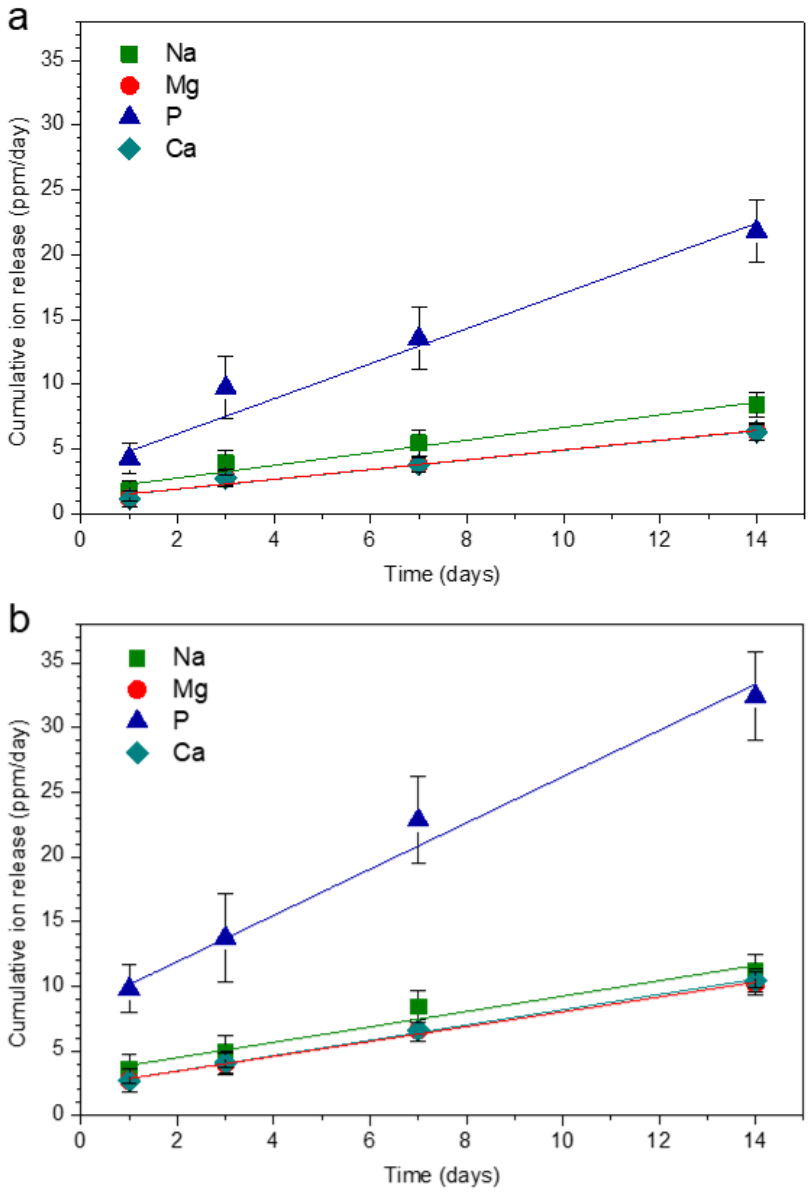

Figure 6.9: *Mg^{2+}, P^{5+}, Na^{+}, and Ca^{2+} ion release profile for P-40 coatings (a) deposited at 50 kW and (b) 75 kW flame power.*

For the 50 kW coating, the highest ion release was that of total P ions with the release rate of 1.4 ± 0.1 ppm/day, whilst the other ions such as Na^+, Ca^{2+} and Mg^{2+} were released in similar amounts with the release rate of 0.38 ± 0.04 ppm/day for Na^+ and a rate of 0.49 ± 0.06 ppm/day for Ca^{2+} and Mg^{2+} (while R^2 values for ions of P, Ca, Na and Mg were 0.95, 0.98, 0.99 and 0.97). Similar to the 50 kW, the 75 kW coating also revealed total P ion released at the highest rate (1.7 ± 0.1 ppm/day) in comparison to other ions analysed (Na^+, Ca^{2+} and Mg^{2+}) which were released at 0.57 ± 0.02 ppm/day for Mg^{2+} and the same rate of 0.59 ± 0.08 ppm/day and 0.59 ± 0.02 ppm/day for Na^+ and Ca^{2+} respectively (while R^2 values for ions of P, Ca, Na and Mg were 0.982, 0.996, 0.950 and 0.995). It can also be seen that the overall ion release rates were higher for 75 kW coating than for the 50 kW coating.

Table 6.3: *Ion release rates (ppm/day) of P-40 coatings deposited at 50 and 75 kW in ultra-pure water.*

P-40 Coatings	**Na Release Rate (ppm/day)**	**Mg Release Rate (ppm/day)**	**P Release Rate (ppm/day)**	**Ca Release Rate (ppm/day)**
50 kW	0.49 ± 0.06	0.38 ± 0.04	1.4 ± 0.1	0.38 ± 0.04
75 kW	0.59 ± 0.08	0.57 ± 0.02	1.7 ± 0.1	0.59 ± 0.02

6.5 Mass Degradation Studies of the P-40 Coatings

Degradation profiles of the coatings degraded in PBS and ultra-pure water at 37 °C for 14 days are presented in Figure 6.10. Degradation rates were calculated by assuming linear profiles and are given in Table 6.4. As can be seen that these rates were higher in MQ water than in PBS for the coatings. The highest rate of 1 x 10^{-4} mg/mm^2·day was observed for 75 kW coating in MQ water. The lowest degradation rate was observed for 50 kW coating in PBS, which was 1 x 10^{-5} mg/mm^2·day. While 50 kW coating degraded in MQ water at a rate of 5 x 10^{-5} mg/mm^2·day, that is 5 times its degradation rate in PBS.

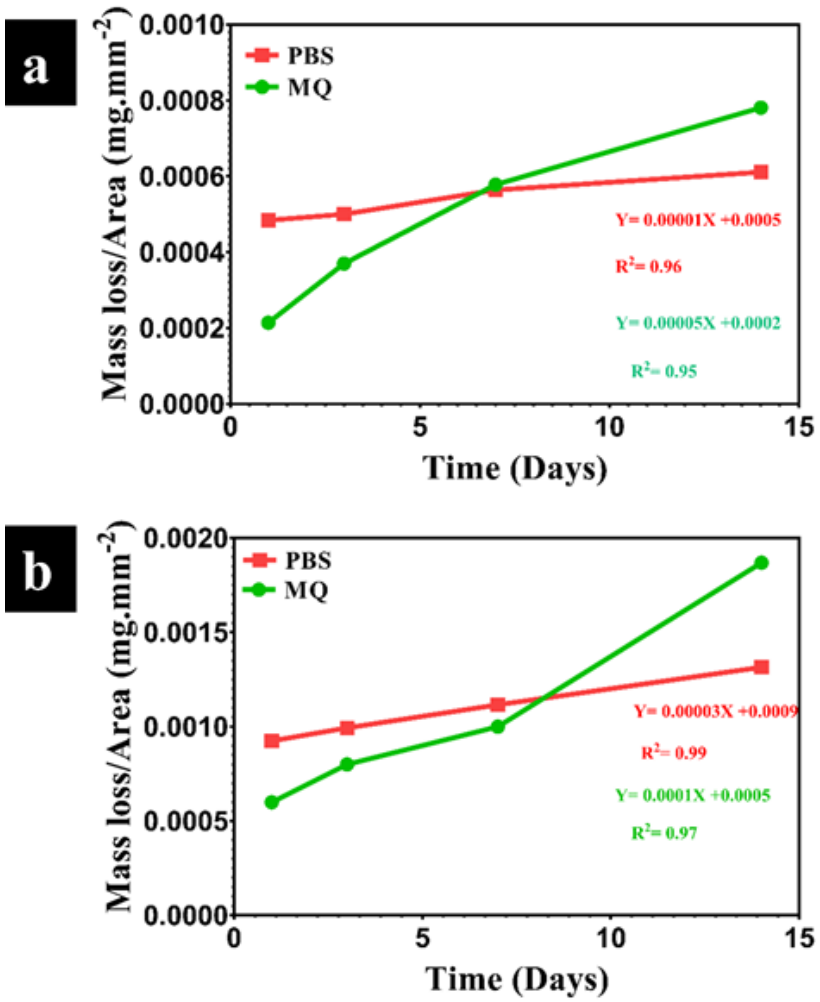

Figure 6.10: *Mass degradation profiles of P-40 coatings (a) deposited at 50 kW and (b) deposited at 75 kW flame power*

.

Table 6.4: *Mass degradation rates of 50 and 75 kW coatings of P-40 glass.*

P-40 Coatings	Degradation Rate in PBS ($x10^{-5}$ $mg/mm^2.day$)	Degradation Rate in MQ water ($x10^{-5}$ $mg/mm^2.day$)
50 kW	1	5
75 kW	3	10

6.6 Discussion

6.6.1 Coating Characterisation

It was observed that increasing the flame power from 50 kW to 75 kW had no considerable effect on the microstructure of the P-40 coatings. Spraying at 50 kW and at 75 kW flame power resulted in approximately similar surface topography, e.g. formation of globules on the surface of the coatings (Figure 6.4). In chapter 5 as well as chapter 4, it was observed that spraying of Bioglass® (45S5) at high flame power of 75 kW resulted in globules on the surface of the coating, but not with the 50 kW flame power [291]. The reason for this could be due the formation of large agglomerates inside the combustion chamber during spray and adhesion of these agglomerates to the combustion chamber and expansion nozzle walls. The high flame power of 75 kW had enough energy to melt these large agglomerates. Consequently, these agglomerates detached and resulted in the deposition onto the substrate [37]. However, in the case of P-40 glass, coating deposited at 50 kW had the same globules features on the surface of the coating. This means that the 50 kW flame power had enough heat energy for this P-40 glass to produce a similar surface morphology to the 45S5 coating deposited at 75 kW coating. The reason for this could be that the P-40 glass transition temperature (448 ± 1 °C) and melting temperature (764 ± 1 °C) is lower [99] in comparison to 45S5 bioactive glass for which glass transition temperature is 520 °C [77] and melting temperature is 1217 °C [82]. In globules-free areas, individual splats cannot be seen in both coatings s due to the better melting of the material at both flame powers of 50 kW and 75 kW.

The microstructure of both P-40 glass coatings was dense (Figure 6.5). The dense microstructure of 50 and 75 kW is the better melting of the glass at both flame powers due to more energy transfer, causing better melting of the P-40 particles and resulting in less porosity [264]. However, both coatings were of different thickness, as the 75 kW coating was approximately two-third in thickness of the 50 kW coating. This might be due to the fact that at a high flame of 75 kW the heat transfer was too high that

caused the material to get evaporated, resulting in thin coating [266, 291]. Another reason for the thin coating formation at 75 kW flame power could be comparatively more melting at 75 kW than at 50 kW, resulting in the less porous and thin coating as reported by Ming et al. while depositing TiO_2 suspension via SHVOF [264].

Thermal spraying of P-40 glass at both flame powers of 50 kW and 75 kW caused altering the composition of the glass with respect to the initial starting powder. Figure 6.6 shows EDX analysis along the cross-section of the coatings to determine these compositional changes while going from the coating-substrate interface to the top of the coating. These variations in composition were observed while carrying out EDX area scan at the top surface of the coatings too. As in Table 6.2, it can be seen that thermal spray caused reductions in contents of P and Na while spraying at 50 and 75 kW. This might be due to the direct evaporation of P_2O_5 at high temperature from the glass melt [266]. The volatile nature of Na_2O could be a cause that resulted in a reduction in its wt % [292]. Evaporation of Na_2O from the glass melt is due to the heterogeneous chemical reaction between Na_2O at the surface of the melt and water vapours present in the combustion chamber resulting in gaseous NaOH [293]. A decrease in the content of Na_2O is followed by an increase in wt % of CaO in the glass [293].

The structure of the P-40 glass was affected due to thermal spraying and it was found to be different in the coating than the original powder. Figure 6.8 shows the Raman spectra of the P-40 powder and coatings, as the Raman spectra of the coatings were different from the Raman spectrum of the powder. A new peak was found at 960 cm^{-1} in the Raman spectra of coatings which was not present in the starting powder spectrum. In the literature, this band was associated with the symmetric stretching of orthophosphate groups (PO_4^{-3}) [289, 290, 294] which suggested that the P-40 glass had depolymerised forming Q^0 units [113]. Higher intensity of the peak at 1046 cm^{-1} in coatings spectra compared to P40 powder indicated a higher concentration of Q^1 units [113]. Moreover, the intensity of the peak at 1160 cm_{-1} decreased in the spectra of the coatings, the decreased intensity of this peak in the coating spectra could be

due to the reduction in the concentration of Q^2 units [113, 289]. Finally, the evolution of the peak at 670-790 cm^{-1} as at 750 cm^{-1} indicated a reduction in the chain length. It can be concluded from the Raman spectra that the P-40 glass structure changed as a reduction in the concentration of Q^2 units, increased in Q^1 units and the potential formation of Q^0 units. In Raman analysis, the observation of orthophosphate (PO_4^{-3}) peak/ Q^0 species in both coatings could be attributed to the reduction of P_2O_5 content (from 36 mol % for glass powder to 27-29 mol % for coatings) post thermal spray, which was confirmed via EDX. In literature, it has been reported that the Q^0 species was observed for the phosphate glasses, which contained P_2O_5 below 35 mol % [295].

This structural analysis warrants further investigation via NMR characterisation. However, the challenge here is to ensure that sufficient powder samples can be obtained from the coatings deposited for accurate analysis.

6.6.2 Ion Release and Degradation Profile of P-40 Coatings

From the ion release studies conducted (Table 6.3), it can be seen that, for both P-40 coatings, cations release rates ranked P > Na > Mg > Ca. P-40 coatings suffered a structural change during spraying and presented a higher ratio of Q^1 and Q^0 species than the initial glass, as observed from Raman analysis, and these changes in the glass structure had an effect on the glass solubility. In PBGs, Q^2 species are more soluble than species with a lower degree of polymerization, so the P-40 coatings with a higher ratio of depolymerized species (Q^1 and Q^0 species) will present reduced ion release profiles than the initial glass. Ion release study of P-40 bulk glass has been conducted by Islam et al. [266], who reported ion release rates of 0.8 ppm/day for Mg, 0.9 ppm/day for Ca and 1.55 ppm/day Na ions, and these values are significantly higher than the ones obtained for the thermal sprayed P-40 coatings, indicating that the produced coatings were more resistant to hydrolytic attack, due to the structural changes induced in the glass during spraying, as proved by Raman analysis (Figure 6.8).

The ion release rates are also influenced by the spray conditions, and the intensity of

the bands associated with Q^1 and Q^0 species are very similar for both spray conditions. However, a higher ratio of depolymerized species was present in the coatings deposited at 75 kW, whereas a band associated with Q^2 units (1160 cm^{-1}) was absent in the 75 kW coating while it was present in the 50 kW coating (see Figure 6.6). Therefore, according to the glass chemistry, higher dissolution rates should be expected on the 50 kW coating. However, the coating deposited at 75 kW presented higher release rates than the coating deposited at 50 kW. This could be due to the rougher surface of the 75 kW coating, which involves a larger surface area in contact with the liquid, contributing to an increased ion leaching compared to the 50 kW coating. This could indicate that small changes in the glass structure of the coating had a limited effect on the ion release rates.

The degradation rates of the coating followed the same behaviour as the ion release profiles. In MQ water and PBS, both coatings were more stable and presented lower degradation rates than the PBGs thin films reported in the literature and produced via magnetron sputtering, probably due to the presence of a higher rate of depolymerized species. Also, the enrichment of MgO in the coating composition from the initial glass, which is due to the volatilization of labile elements during spraying, has an important role because PBGs with higher MgO content tend to present lower degradation rates [266]. The P-40 coating deposited at 75 kW showed higher degradation than the coating deposited at 50 kW (Figure 6.10 and Table 6.4),and this could be attributed to the higher surface roughness of the 75 kW coating.

Overall, thermal sprayed coatings of PBG showed less degradation in PBS and MQ water and released ions at lower rates in MQ water in comparison to bulk PBG and thin films. This behaviour of the PBG thermal sprayed coatings could be due to the change in the structure of the glass in coatings (as revealed via Raman analysis), i.e., thermal spray caused the structural changes in P-40, converting it into a less resorbable glass.

6.7 Summary

PBG P-40 was deposited onto the stainless substrate by SHVOF thermal spray, producing two coatings at the flame power of 50 and 75 kW. The surface topography and microstructure of both coatings were very similar, showing globules on the top surface of the coatings with dense cross-sections. However, ion release profiles and degradation rates of both coatings were different. This could be due to the difference in thickness and surface roughness of the coatings. From the above results following conclusion can be made.

1. The SHVOF thermal spray technique was used to deposit P-40 PBG on to stainless steel substrate at two flame powers of 50 and 75 kW. Surface topography of both coatings was very similar, showing globules on the top surface of the coatings. However, ion release profiles and degradation rates of both coatings were different, which might be due to the difference surface roughness of the coatings.

2. Both coatings were amorphous as shown by XRD analysis; however, the structure of the coatings was different from that of the starting powder as revealed by Raman analysis with the reduction in the concentration of Q^2 specie, increased of Q^1 specie and the formation of Q^0 specie in coatings.

3. 75 kW coating showed more mass loss and ion leaching in comparison to 50 kW coating, which could be due to the rougher surface of the 75 kW coating. However, comparing these results with those reported in the literature for thin films of P-40 glass and bulk P-40 glass, both coatings showed lower degradation and ions release rates. Therefore, if less vulnerable to resorption PBG coatings are required, then the technique of SHVOF is an optimal option to utilise.

Chapter 7

Antimicrobial Bioactive Coatings

7.1 Introduction

Strict operative procedures are followed to minimise the bacterial contamination; however, implants associated infections significantly raise postoperative complications. Adjusting and controlling the antimicrobial properties of the implant surface is one of the promising approaches to minimise these infections. Two antimicrobial coatings, containing Ga_2O_3 as an antibacterial agent (chapter 2, section 2.2.4) are reported in this chapter. The first coating was deposited with the Ga_2O_3 doped Bioglass® suspension. The second coating was deposited by co-spraying Ga_2O_3 suspension and Bioglass® suspension via a hybrid nozzle using axial and radial injection. Both coatings were deposited at 50 kW flame power. The second coating which was deposited via hybrid nozzle and named as co-sprayed coating in this chapter. Whilst the coating made with the Ga_2O_3 addition to Bioglass®, named as Ga_2O_3 doped Bioglass® coating. The characterisation results of the coatings are presented here. The SBF study of the coatings and cells tests are discussed, and then conclusions are drawn.

7.2 Feedstock Characterisation

7.2.1 Particle Size Distribution and Powder Morphology of the Ga_2O_3 powder, 45S5 Bioglass® and Ga_2O_3 doped Bioglass® powder

Figure 7.1 a represents the particle size distribution of Ga_2O_3 powder used in glass preparation and suspension preparation, and as can be seen that the powder had a multimodal distribution with D_{10} = 1.9 μm, D_{50} = 4.5 μm and D_{90} = 18.9 μm. The SEM image of the Ga_2O_3 powder (Figure 7.1 b) shows that the as-received powder had fine and coarse particles. As can be seen that the observed size of the largest particle was approximately equal to 5 μm, and the particles were angular in shape.

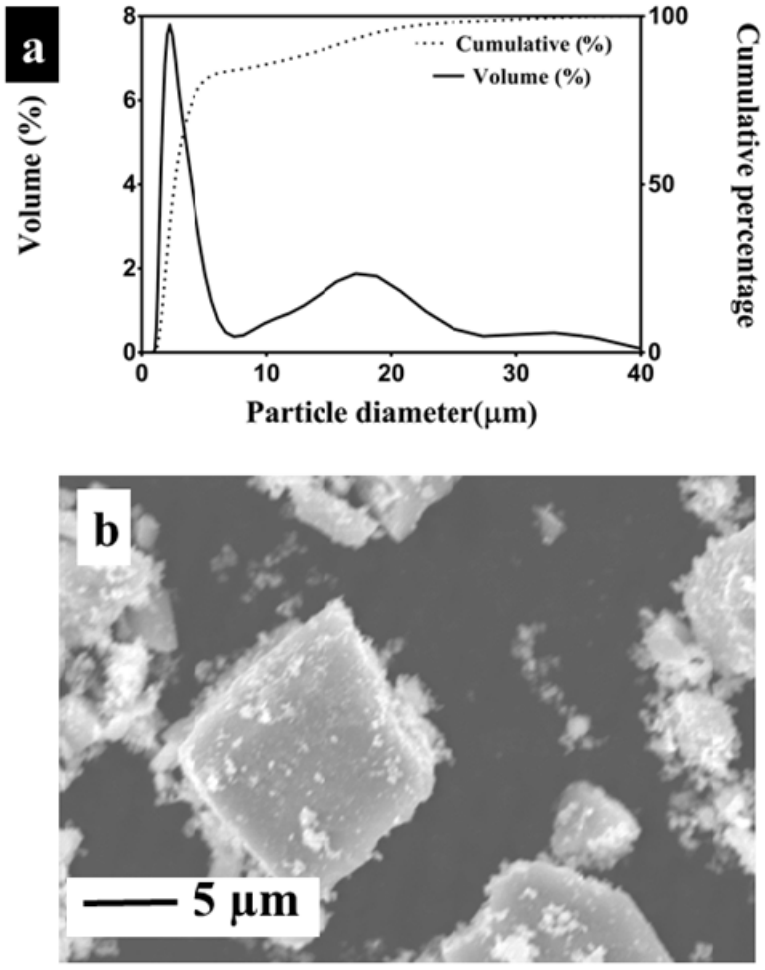

Figure 7.1: *(a) Particle size distribution and (b) SE image of the as received Ga_2O_3 powder.*

Figure 7.2 a, represents the particle size distribution of Ga_2O_3 doped bioglass®, and as can be seen that this distribution had a particle size range of 0.37 to 36.24 μm. Also, the distribution was characterised by D_{10} = 1 μm, D_{50} = 5 μm and D_{90} = 18 μm. The final powder of the glass was a mixture of fine and coarse particles, as can be seen in the SEM image of the powder (Figure 7.2 b). The particle of the largest size observed was larger than 5 μm. Also, particles were of irregular shape.

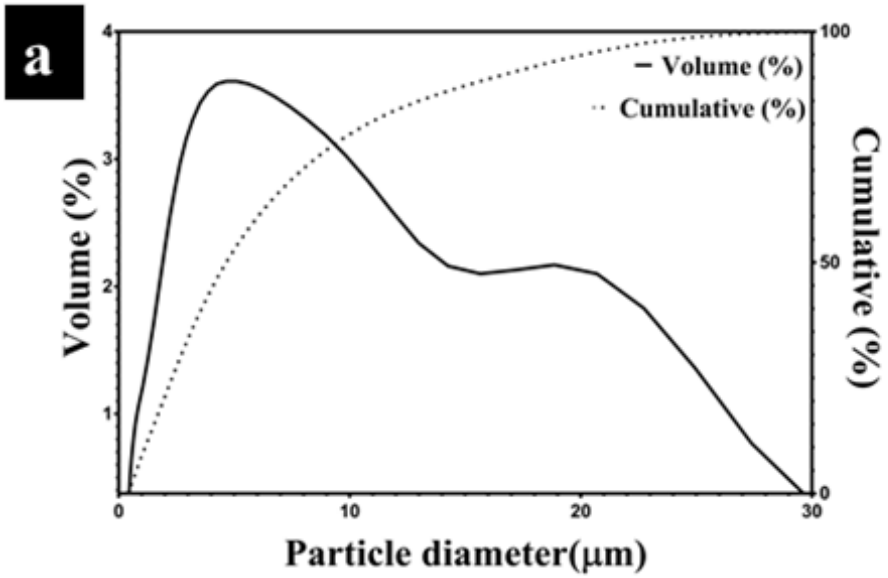

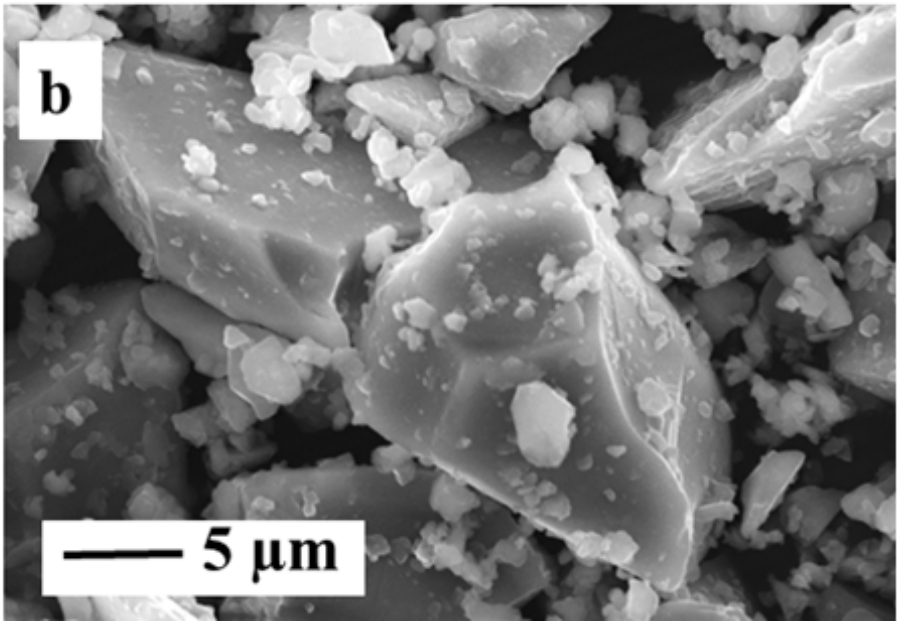

Figure 7.2: *(a) particle size distribution and (b) SE image of Ga_2O_3 doped Bioglass®.*

7.2.2 EDX Analysis of Ga_2O_3 doped Bioglass®

EDX point analysis were performed on the Ga_2O_3 doped Bioglass®, and the results showed that the Ga_2O_3 doped Bioglass® had approximately 1 % less Si and 1 % less Ca than the Si and Ca content present in Bioglass®. Na and P content were approximately were equal in both glasses, with 1.7 wt % Ga present in the new formulation.

Ga_2O_3 doped Bioglass® powder had 18.3 ± 1.2 wt % Si, 15.3 ± 0.3 wt % Ca, 14.3 ± 0.2 wt % Na, 2.1 ± 0.2 wt % P and 1.7 ± 0.1 wt % Ga (Bioglass® composition is given in chapter 4 section 4.2.2)

7.2.3 XRD and Raman Analysis

The XRD patterns of Bioglass® powder and Ga_2O_3 doped Bioglass® powder are shown in Figure 7.3 a, as can be seen, that both powders were amorphous. The amorphous humps present between 15 to 38 2θ ° showed broad diffraction with no sharp peak which is the characteristic of short-range order for the glasses. Figure 7.3 b shows the XRD pattern of the as-received Ga_2O_3 powder, where all peaks were identified as Ga_2O_3 (PDF card no. 00-041-1103).

Figure 7.4 shows the Raman spectra of Ga_2O_3, 45S5 (Bioglass®) and Ga_2O_3 doped Bioglass® powder. In the Ga_2O_3 spectrum, peaks at 650, 655 and 760 cm^{-1} were due to the bending and stretching of GaO_4. Peaks at 320, 343, 416 and 470 cm^{-1} were associated with the symmetric bending and stretching vibrations of GaO_6 octahedra. The intense peak at 199 and the peak at 168 cm^{-1} was due to O–Ga–O bending modes [296, 297].

In the Raman spectrum of Bioglass®, the peaks observed at 610 cm^{-1} and 1079 cm^{-1} were assigned to the stretching of Si-O-Si. The peak at 860 cm^{-1} was assigned due to the vibration of non-bridging oxygen, i.e. Si-4NBO and the peak at 945 cm^{-1} was assigned to the stretching of PO_4^{-2} [254].

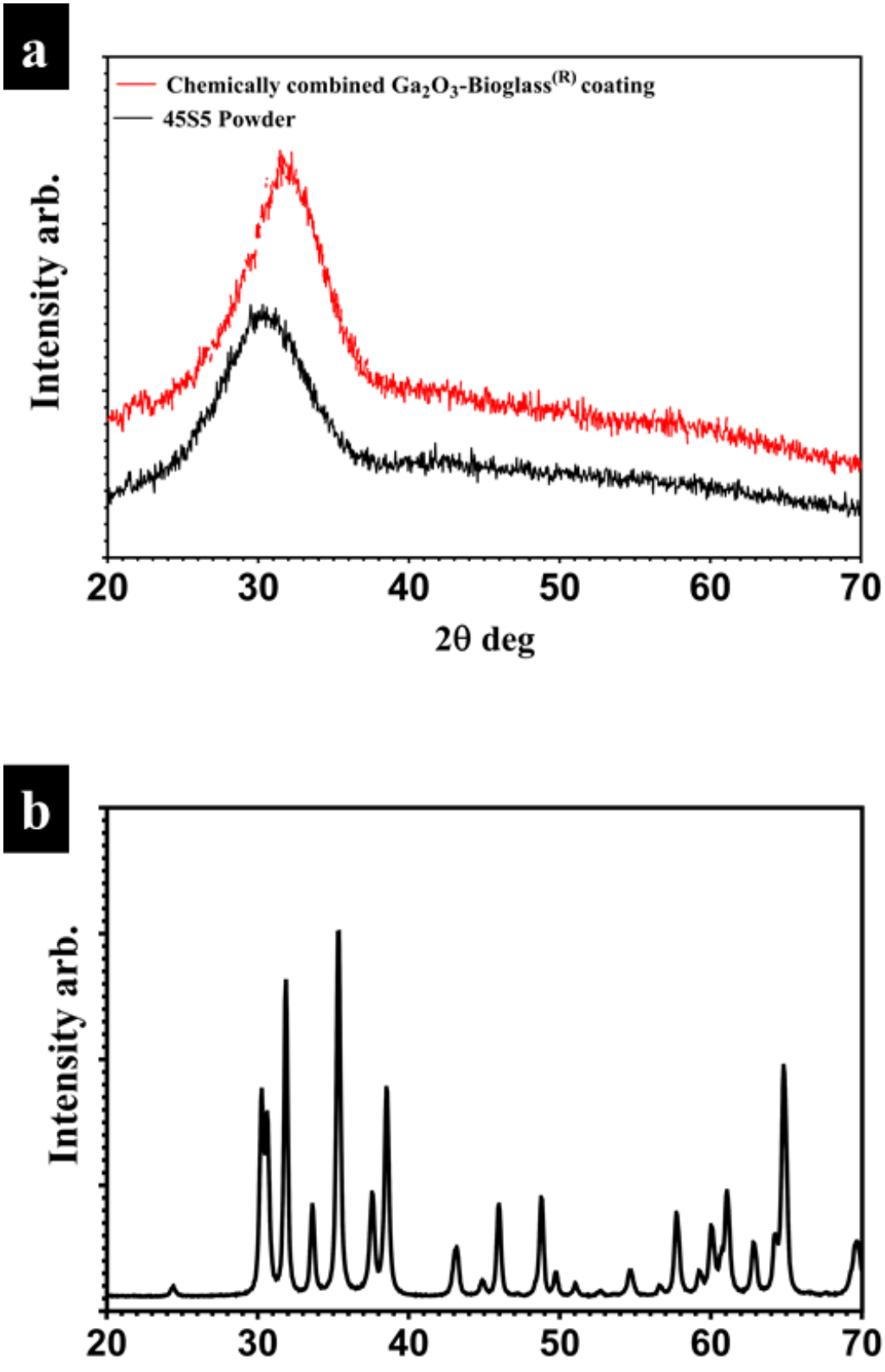

Figure 7.3: *XRD spectra (a) of Bioglass® and Ga_2O_3 doped Bioglass® powder (b)as received Ga_2O_3 powder.*

In the spectrum of Ga_2O_3 doped Bioglass®, peaks at 199 cm^{-1}, belonged to Ga_2O_3

can still be seen (Figure 7.4) while other Ga_2O_3 peaks were not anymore recognised. Peaks that belonged to Bioglass® can easily be seen in this glass spectrum. The band in the Bioglass® spectrum at 610 cm^{-1} had been moved to 625 cm^{-1}, indicative of reduction in bond length [113]. Also, the peak at 1075 cm^{-1} shifted to a lower wave number of 1066 cm^{-1} in Ga_2O_3 incorporated bioactive glass. The peak at 945 cm^{-1} appeared at the same wave number for the new glass.

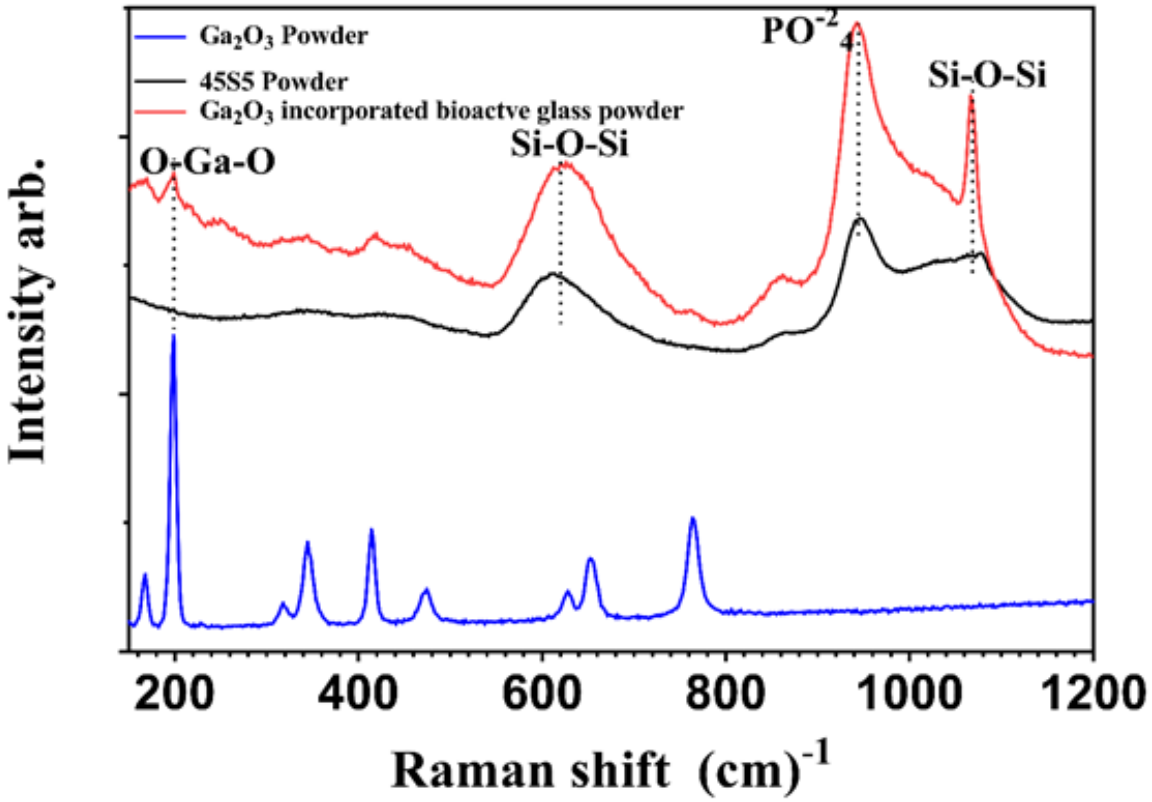

Figure 7.4: *Raman spectra of Ga_2O_3, Ga_2O_3 doped bioactive glass* and 45S5 (Bioglass®) powder.

7.3 As-Deposited Coatings Characterisation

7.3.1 Surface Morphology and Cross-section of the Coatings

The galium oxide doped bioglass was sprayed at 50 kW and 75 kW. Coating deposited at 50 kW flame power however no coating deposited at 75 kW. The morphology of the Ga_2O_3 doped Bioglass® deposited at 50 kW flame power is shown in Figure 7.5.

Figure 7.5 a shows that the surface of the coating had globules, the size of which was approximately more than 20 μm (Figure 7.5 b). In the globules-free area of the coating, well-flatten splats with glass drops were present, as shown in Figure 7.5 c.

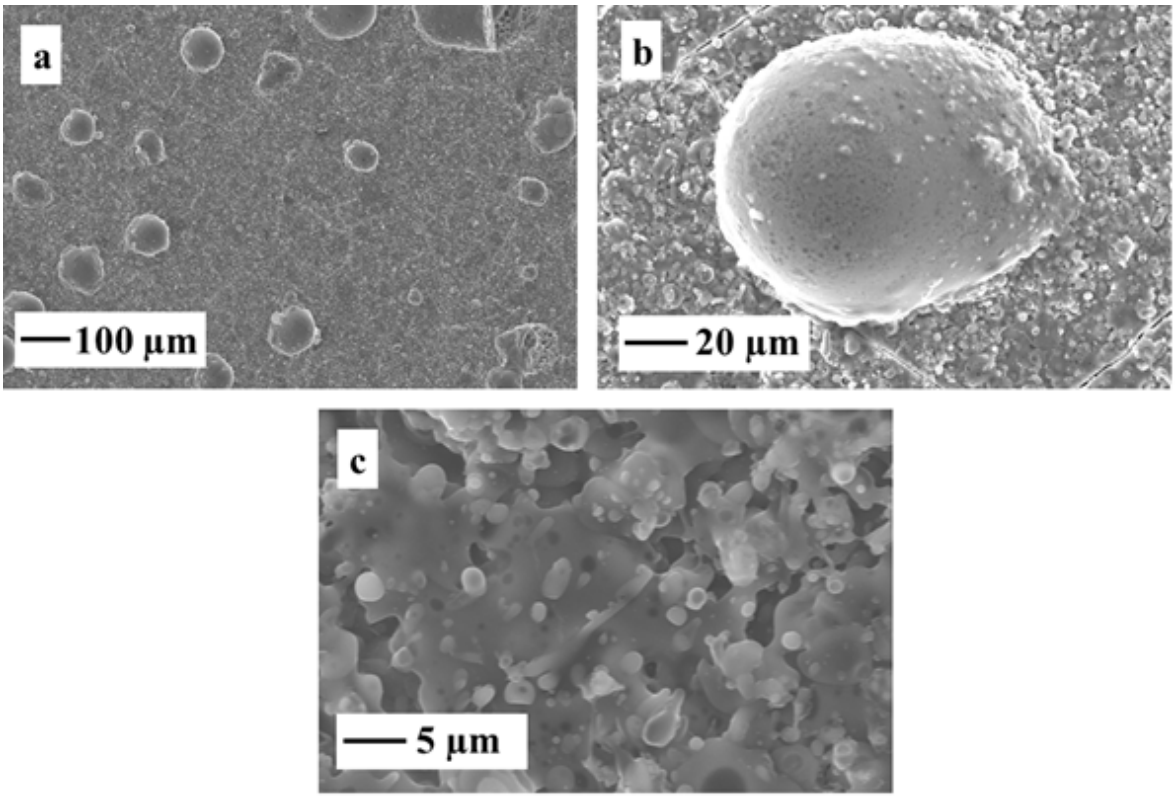

Figure 7.5: *SE, SEM surface morphology of Ga_2O_3 doped Bioglass® coating deposited at 50 kW.*

Ga_2O_3 doped Bioglass® glass was a thick coating of approximately 73 $\pm$ 2 μm as shown in Figure 7.6 a; however, this did not adhere to the substrate, as a long crack was present at the interface between substrate and coating (Figure 7.6 b). Also, from Figure 7.7, it can be seen that in some regions, there was coating; however, from some regions it was flaked- off.

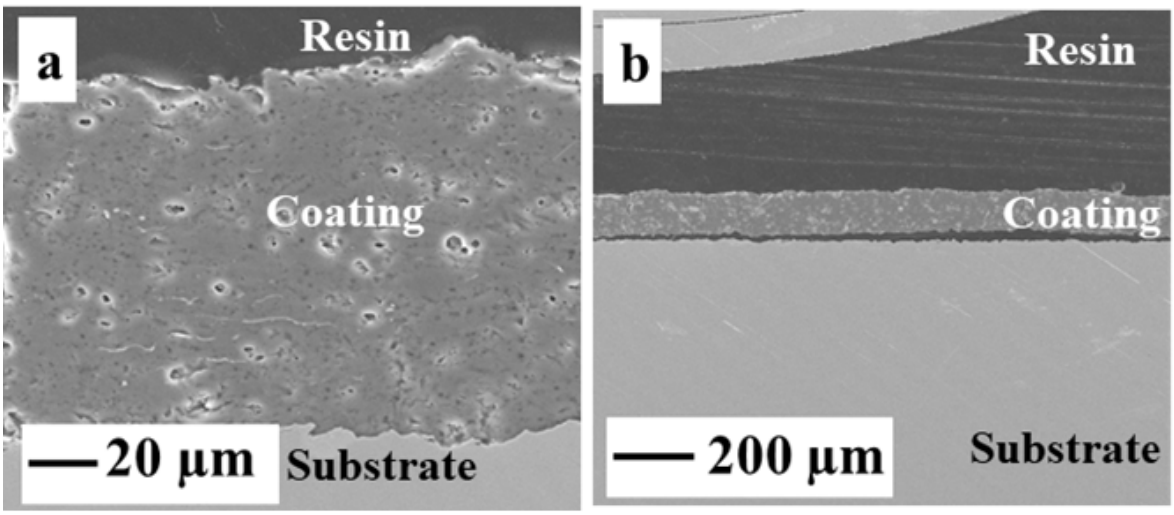

Figure 7.6: *SE, SEM image of the cross-section of Ga_2O_3 doped Bioglass® coating deposited at 50 kW.*

The co-sprayed coating was produced by depositing Ga_2O_3 suspension and 45S5 (Bioglass®) suspension at 50 kW flame power, and the surface morphology of the coating is displayed in Figure 7.8. The substrate was uniformly covered with the glass coating as can be seen in Figure 7.9. Re-solidified glass droplets were present on the surface (Figure 7.8 b), however, no flat glass splat was seen in the coating.

Figure 7.7: *Ga_2O_3 doped Bioglass® coating deposited at 50 kW.*

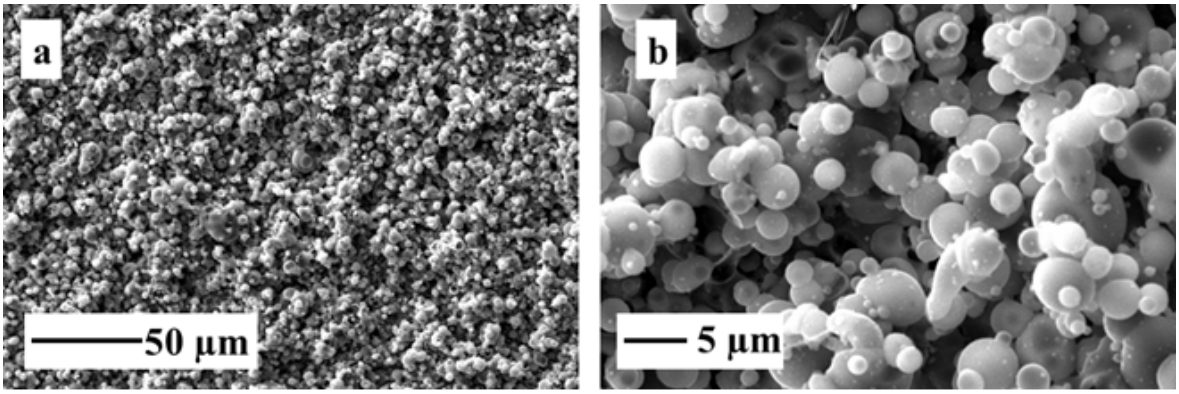

Figure 7.8: *SE, SEM surface morphology of Ga_2O_3 and 45S5 co-sprayed coating deposited at 50 kW.*

Figure 7.10 shows the cross-section of the coating prepared from hybrid spray, and as can be seen that the coating adhered to the substrate as no crack was visible at the coating-substrate interface. The coating thickness was approximately 16 ± 3 μm, as shown in Figure 7.10 b the coating thickness was not uniform.

Figure 7.9: *Ga_2O_3 and 45S5 co-sprayed coating deposited at 50 kW.*

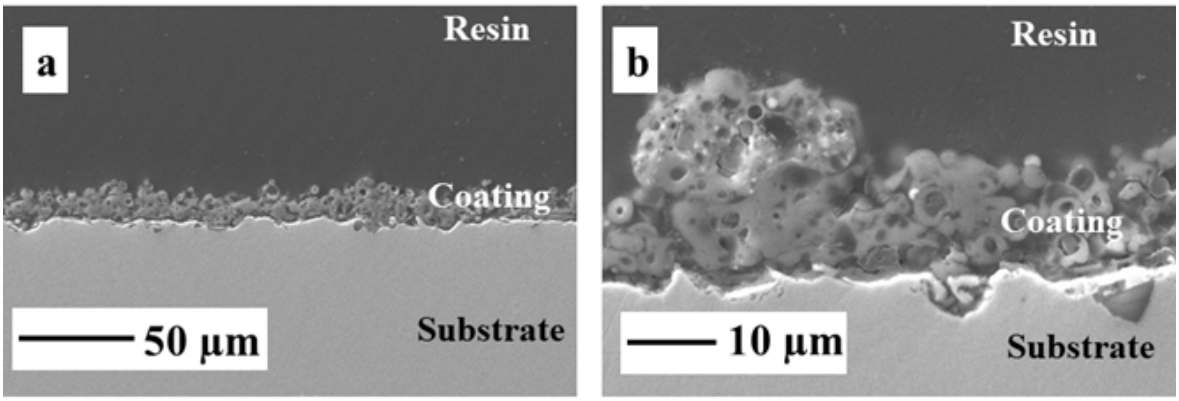

Figure 7.10: *SE, SEM image of the cross-section of Ga_2O_3 and 45S5 co-sprayed coating deposited at 50 kW.*

7.3.2 EDX analysis of the Coatings along the Cross- Section and Area Scan on the Top Surfaces

EDX line scan was carried along the cross-section of the coatings to explore any compositional changes in glass composition after thermal spray. Results are displayed in Figure 7.11, where a and c are the SEM images of the coatings and b and d are the corresponding EDX analysis. The EDX analysis showed that the composition of the Ga_2O_3 doped Bioglass® altered after thermal spray compared with the original glass powder (7.2.2).

The content of Si (18.3 ± 1.2 wt % present in the powder) was observed to be 23.3 wt % at the coating- substrate interface and then decreased till the top of the coating to wt % of 21.1 wt %. However, there was slight variation in Si content in the cross-section of the coating as it was observed to be 24 wt % at 49 μm. Ca content was 18.6 wt % at the interface between coating and substrate, while at the top of the coating, it was measured to be 17.7 wt %. Similar to Si content, fluctuations in Ca content also noted along the cross-section of the coating. Na wt % was approximately 12 at the interface between coating and substrate, and at the top, it was 12 wt % too. However, Na wt % reduced from that was present in the starting powder (14.3 ± 0.2 wt %). P wt % was observed to be 2.5 at the coating- substrate interface till the top of the coating. Also, P wt % was not reduced from that present in the powder, which was 2.1 ± 0.2 wt %. Ga wt % was 1.3 at the interface and approximately 1.4 wt % at the top of the coating, while in the starting powder, it was 1.7 ± 0.1 wt %. By comparing EDX line scan along the cross-section, the compositional changes of Ga_2O_3 doped Bioglass® coating with that of the Bioglass® coating deposited at 50 kW (4.3.3), it can be seen that Si wt % was first increased at the coating-substrate interface and then decreased at the top of the coating in both coatings. Similar to Si wt %, wt % of Ca and P showed similar trend in coatings. Moreover, the content of Na was decreased in both coatings than the starting powder, Bioglass® (50 kW coating chapter 4) and Ga_2O_3 doped -Bioglass® coating. It means that presence of Ga_2O_3 in the composition of Bioglass® did not affect the behaviour of other elements to thermal

spray.

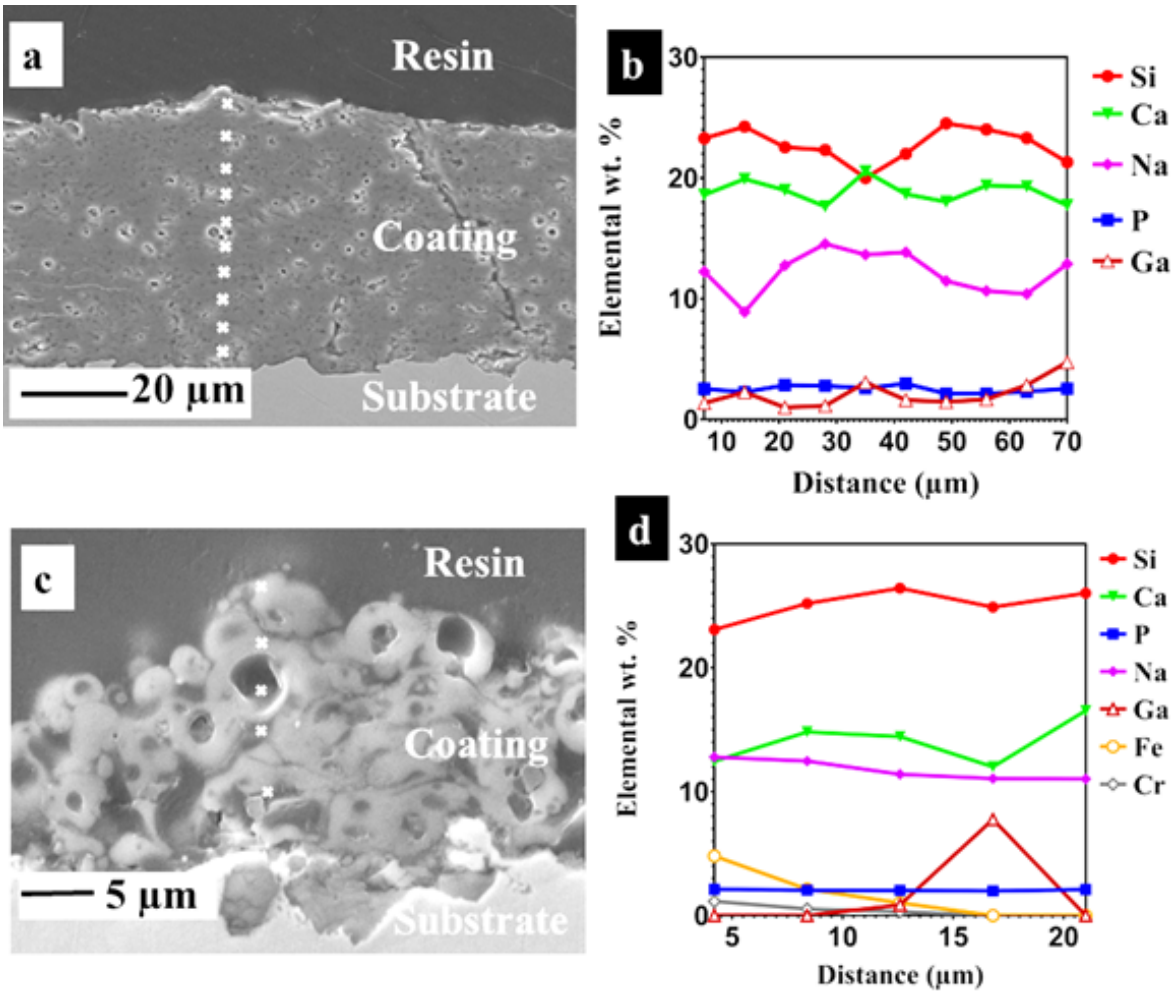

Figure 7.11: *SE SEM images of the cross-section of coatings (a) Ga_2O_3 doped Bioglass® (c) Co-sprayed Ga_2O_3 and 45S5 suspensions, and their respective EDX line scans through the coating cross-section in b, d. Points in the SEM images show the location of EDX data points in the graph (distance is from substrate-coating interface towards coating top surface).*

For the co-sprayed depositing Ga_2O_3 and 45S5 suspensions at 50 kW flame power, 45S5 composition changed due to thermal spray; however, variations in the coating composition along the cross-section were approximately similar to the chemically mixed glass coating (except for Ga) (Figure 7.11 d). Such as wt % of Si at the interface was 23 and at the top of the coating was approximately 26. Ca was observed to be 12 wt % at the coating- substrate interface and then started to increase to approximately 16 wt % at the top of the coating. Na wt % was 12 at the interface and 11 at the top of the coating. P content was observed to approximately 2 wt % along the cross-section

of the coating. Ga was not uniformly distributed along the cross-section. Its content was observed at two points, at one point, it was observed to be 0.9 wt % and 7.8 wt % near the top of the coating.

EDX area scan was done on the top surfaces of the coatings and displayed in Table 1. In the Ga_2O_3 doped Bioglass® coating, Si (23.3 ± 0.1 wt %) and Ca (19.7 ± 0.3 wt %) content had increased from the intended composition (7.2.2). Na content decreased to 10.8 ± 0.6, while in the powder, it was 14.3 ± 0.2. P wt % did not change in the coating, as 2.3 ± 0.1 wt % of P was present in the coating as well as in the powder before spraying. Moreover, the thermal spray did not affect the content of Ga much, as before spray, it was observed to be 1.7 ± 0.1 wt % and after thermal spray,1.5 ± 0.1 wt %.

Table 7.1: *EDX area analysis on the top surfaces of the as sprayed coatings.*

As Sprayed (wt %)		
Elements	**Ga_2O_3 dope Bioglass®**	**Co-sprayed Ga_2O_3 and Bioglass® Coating**
Ga	1.5 ± 0.1	2.0 ± 0.1
Si	23.3 ± 0.1	24.0 ± 0.0
Ca	19.7 ± 0.3	17.3 ± 0.2
Na	10.8 ± 0.6	11.2 ± 0.1
P	2.3 ± 0.1	1.9 ± 0.0

For the co-sprayed coating of Ga_2O_3 and 45S5 suspensions, the expected wt % of Ga was 1 and, in the coating, it was observed to be 2.0 ±0.1 wt %. Si content increased from 19.8 ± 1.7 wt % to 24.0 ± 0.0 wt %, whilst other elemental wt % were approximately the same as those that were present in the powder.

7.3.3 XRD and Raman of the Coatings

The XRD patterns of Ga_2O_3 doped Bioglass® coating and co-sprayed coating of Ga_2O_3 and Bioglass® (45S5) are plotted in Figure 7.12. As can be seen in Figure 7.12 a, no

crystallisation was experienced in Ga_2O_3 doped Bioglass® in the thermal spray process. The co-sprayed coating, composed of Ga_2O_3 and Bioglass® was amorphous too and characterised by broad diffraction peak appearing in 25° - 35° 2θ range. The identified phases (Figure 7.12 b) corresponded to either crystalline Ga_2O_3 (PDF card no. 00-041-1103) or metal substrate (stainless steel) were as austenite with PDF card no. 00-023-0298, and ferrite (PDF card no. 00-006-06 t96). The crystalline peaks due to the substrate in the spectrum were present as the thickness of the coating was less than penetration depth of X-rays (40.8 μm penetration depth of the x-rays).

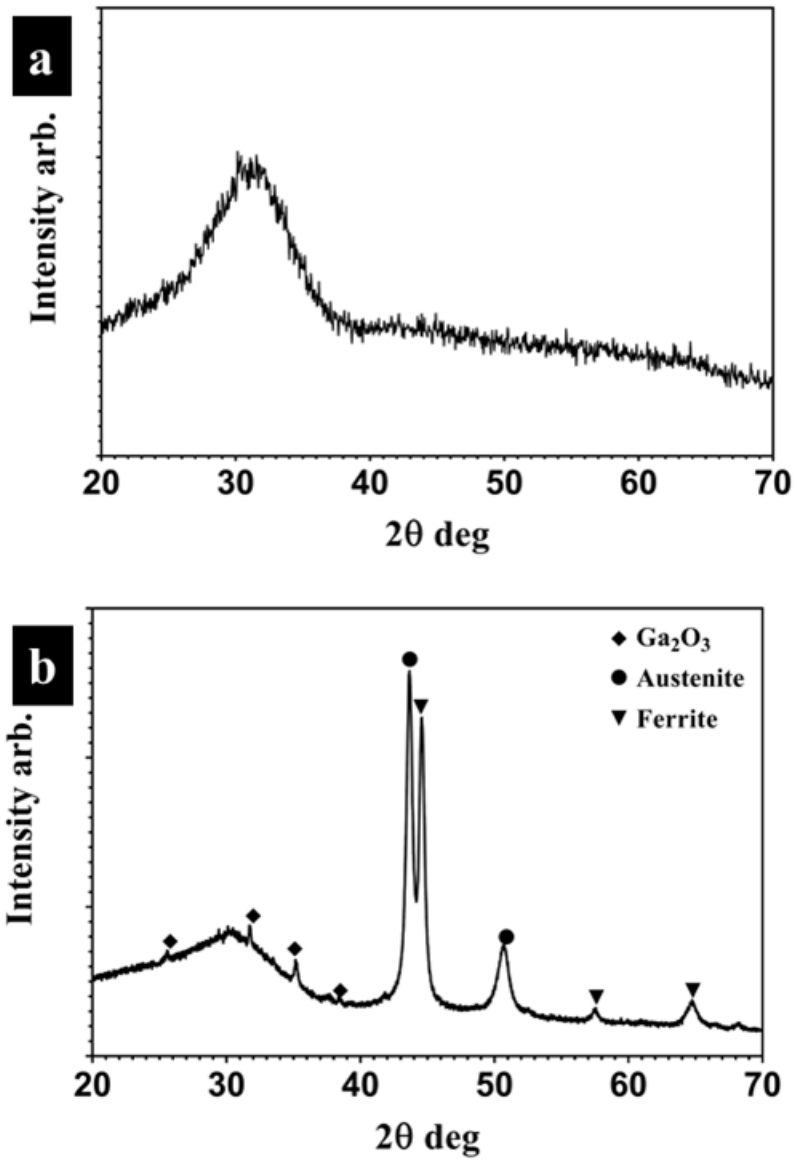

Figure 7.12: *XRD spectra of (a) Ga_2O_3 doped Bioglass® coating and (b) co-sprayed coating of Ga_2O_3 and Bioglass®.*

Figure 7.13 a represents the Raman spectrum of the Ga_2O_3 doped Bioglass® coating. The shoulder identified at 860 cm^{-1} was assigned due to the vibration of non-bridging oxygen (which represents 4 non-bridging oxygen/silica tetrahedra (Q^0) [153]) in the Raman spectra of Ga_2O_3 doped Bioglass® glass and Bioglass® powder (Figure 7.4), was no more identified in the coating spectrum (Figure 7.13). The peak that appeared at 430 cm^{-1} could be attributed to the symmetric stretching mode of GaO_6 octahedra [297]. Figure 7.11 b represents the Raman spectrum of the co-sprayed coating deposited by spraying Ga_2O_3 and Bioglass® suspensions. Peaks for Si-O-Si, PO_4^{-2} were identified; however, for Ga_2O_3, no peak was seen in the coating spectrum.

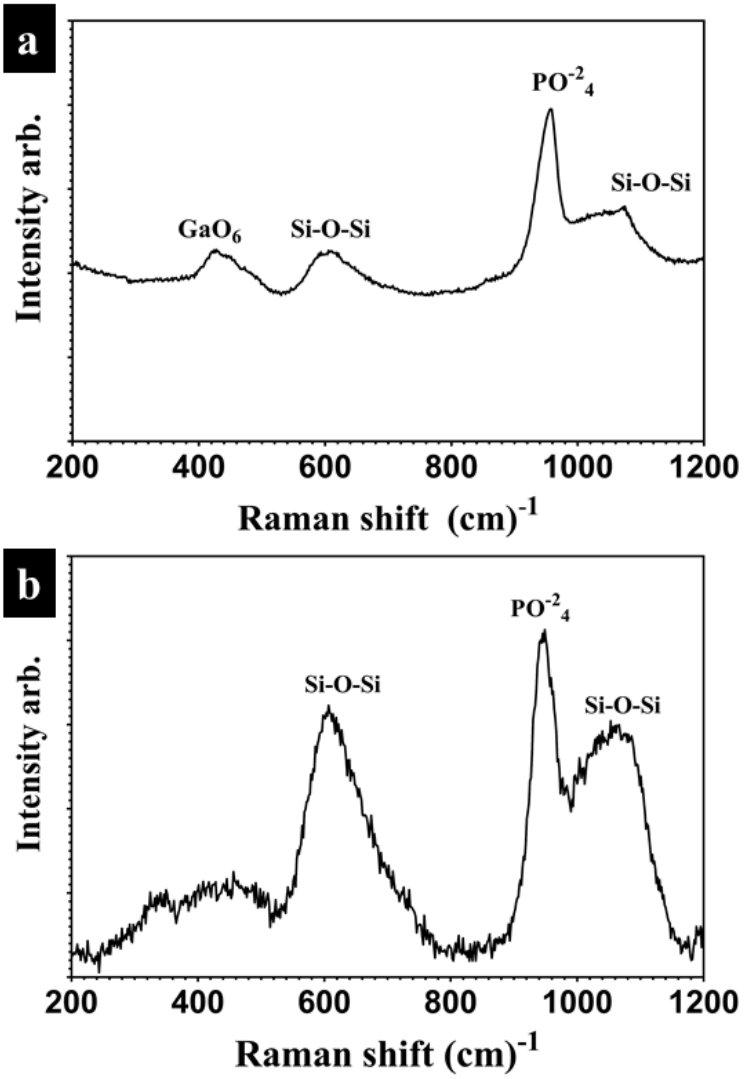

Figure 7.13: *Raman spectrum of the (a) Ga_2O_3 doped Bioglass® coating and (b) co-sprayed Ga_2O_3 and Bioglass® coating deposited at 50 kW flame power.*

7.4 SBF Tests

7.4.1 SEM Observations

Figure 7.14 represents the surface morphology of the coatings after SBF tests. After 3 days of immersion in SBF HA was deposited on the surface of the coatings (Figure 7.14 a, c), which can be identified from the dome- like morphology of the precipitate. However, this was not clearly visible on the surface of the Ga_2O_3 doped Bioglass® coating (Figure 7.14 a), but was visible on the surface after 7 days of immersion in SBF (Figure 7.14 b).

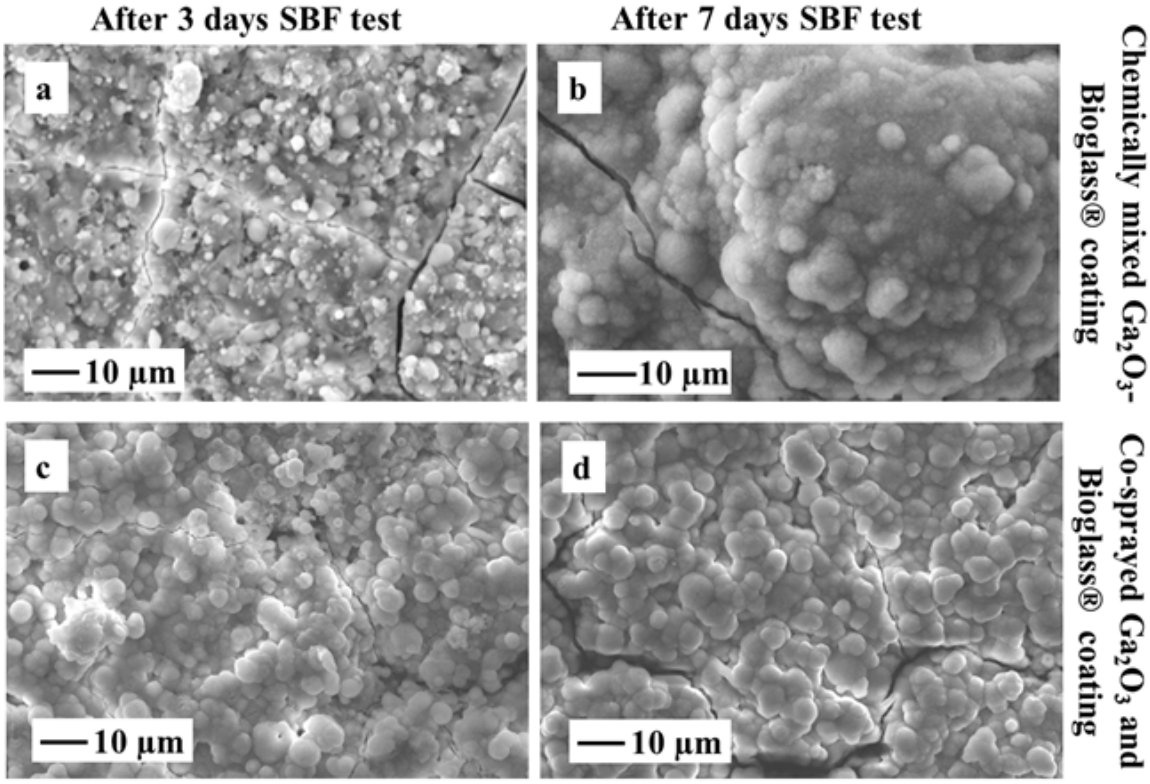

Figure 7.14: *SE, SEM images of the surface of the coatings (a) and (c) after 3 days and (b), (d) after 7 days of immersion in SBF. While, a,b are the images of the Ga_2O_3 doped Bioglass® and c, d are images of co-sprayed Ga_2O_3 and Bioglass® coating.*

7.4.2 XRD and Raman Analysis

Figure 7.15 represents XRD spectra acquired at the surface of the coatings after immersing in SBF for 3 and 7 days. HA was identified from the peaks at 32° and 26° 2θ (PDF no 00-001-1008). In Figure 7.15 a, Ga_2O_3 peaks were identified at 35° and 38° 2θ (PDF card no. 00-041-1103). However, no peak was identified in 7.15a for the XRD spectra of Ga_2O_3 doped Bioglass® coating after SBF test (Figure 7.15 a), which could be due to the precipitation of thicker HA layer than that precipitated on the other coating.

Figure 7.16 shows the Raman spectra obtained on the surface of Ga_2O_3 doped Bioglass® coating and the co-sprayed coatings, immersed in SBF for 7 days. The spectrum obtained for synthetic HA powder is also shown. As can be seen that Raman spectra followed the same evolution for both of the coatings. The peak around 960 cm^{-1} is associated with the $\nu 1$ vibration mode of PO_4^{-3} for HA powder and HA precipitated on the surfaces of the coatings; this is the main peak of HA. The peak at 1046 cm^{-1} in the spectra of HA powder and HA precipitated on the coatings was associated with the PO_4^{-3} $\nu 3$ vibration. Moreover the peak the peak at 1078 cm^{-1} in the spectrum of HA powder was associated with the PO_4^{-3} $\nu 3$ vibration too. Also, peak at 432 cm^{-1} in all of the spectra was due to the $\nu 2$ domain of the PO_4^{-3}. Moreover, the peak at 1070 cm^{-1} for the precipitated HA on the surfaces of the coatings was assigned to the $\nu 1$ mode of the carbonate group which confirmed the carbonated nature of the precipitated HA [256, 261]. The three peaks at 579, 590, and 608 cm^{-1}, and in which 590 cm^{-1} is the strongest among these was due to the $\nu 4$ vibration of PO_4^{-3}. These peaks were present in the spectrum of synthetic HA powder as well as in the spectra of precipitated HA on the surface of coatings [261, 262].

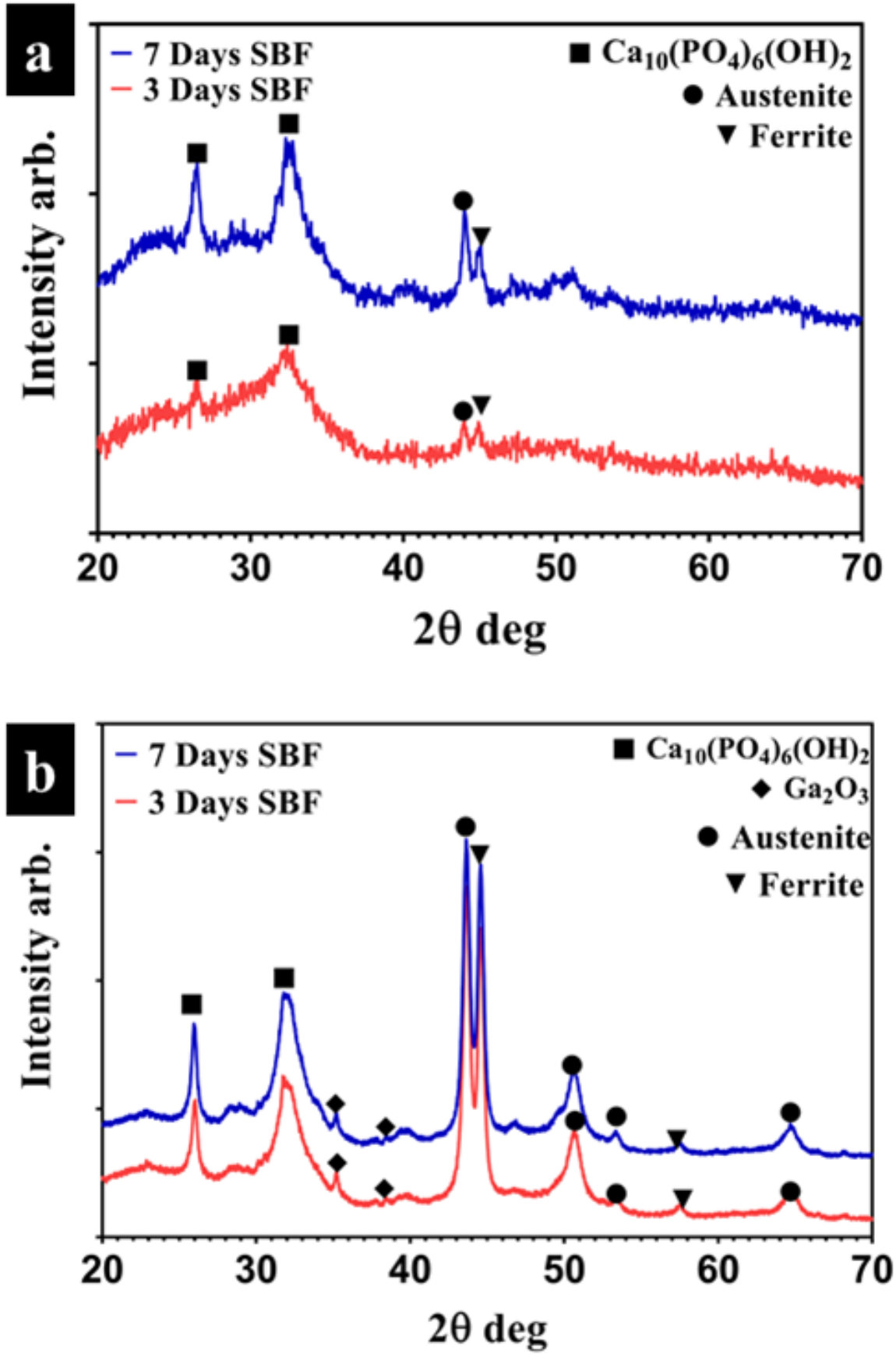

Figure 7.15: *XRD spectra after 3 and 7 days of soaking in SBF of (a) Ga_2O_3 doped Bioglass and (b) co-sprayed Ga_2O_3 and 45S5 hybrid coating.*

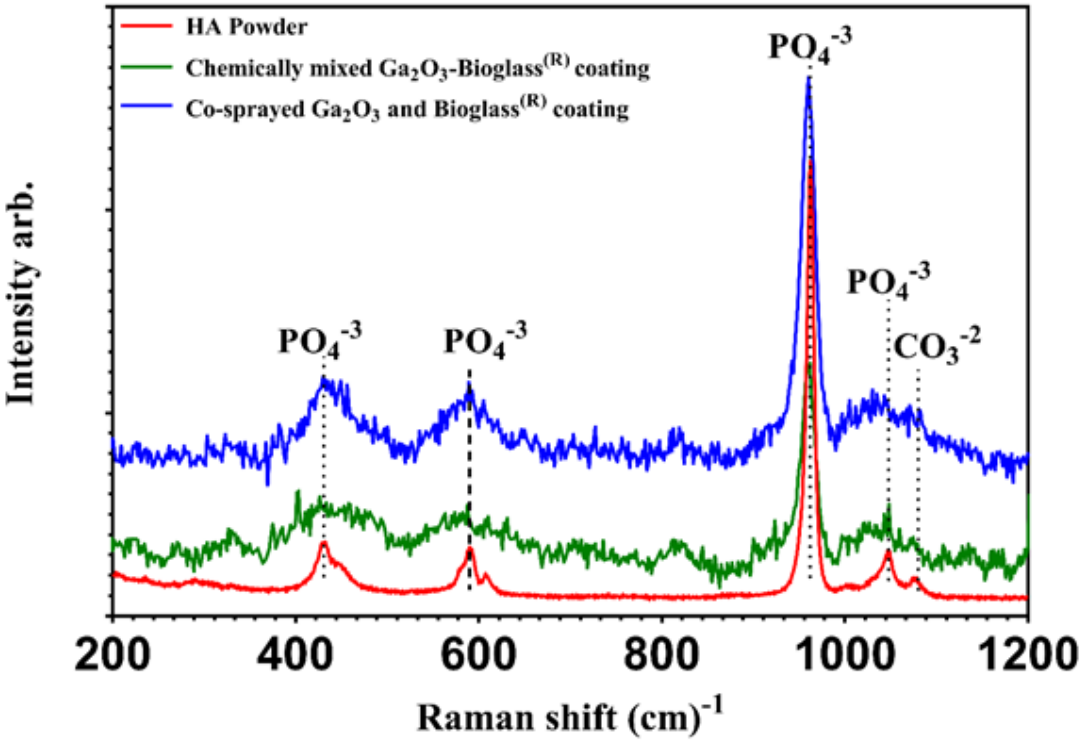

Figure 7.16: *Raman spectra of the Ga_2O_3 doped Bioglass® and co-sprayed Ga_2O_3 and Bioglass® coatings after 7 days of immersion in SBF; additionally Raman spectrum of Synthetic HA powder is also presented here.*

7.4.3 EDX line Scan along with the Cross-Section and Area Analysis on the Top Surfaces

For the Ga_2O_3 doped Bioglass® coating, the coating integrity was not good enough to cut sample for the EDX line analysis along the cross-section of the coating after SBF test. Figure 7.17 represents the EDX line scan along the cross-section of co-sprayed Ga_2O_3 and 45S5 coating after 3 and 7 days of SBF test. In Figure 7.17 b, Si content was 12.50 wt % at the interface between coating and substrate and 19 wt % at the top of the coating.

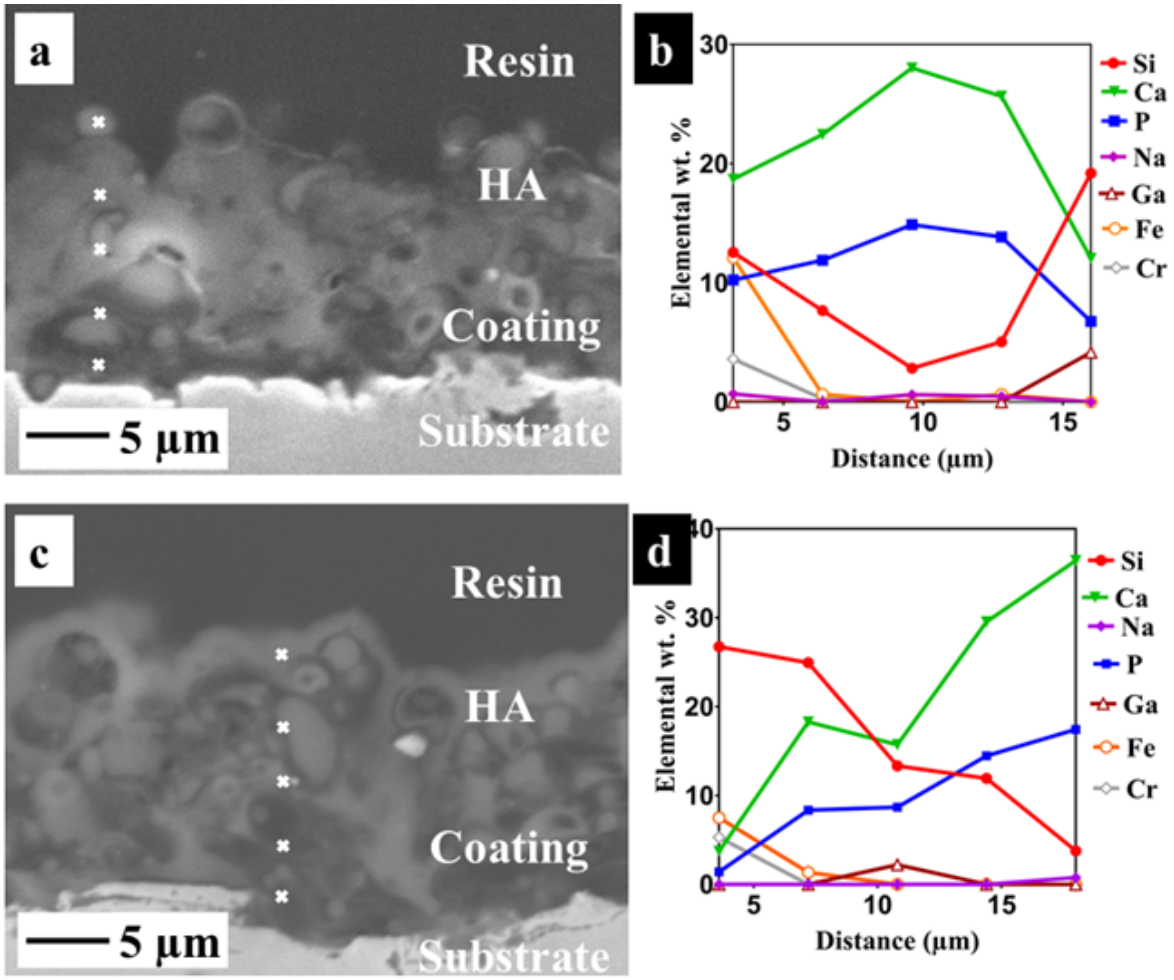

Figure 7.17: *BSE, SEM images of the cross- section of the co-sprayed Ga_2O_3 and Bioglass® coating (a) after 3 days and (b) after 7 days of immersion in SBF, (c), (d) are the respective EDX analysis. (distance is from substrate-coating interface towards coating top surface).*

Na wt % was 0.7 at the coating- substrate interface and 0 wt % at the top of the coating due to HA precipitation on the surface. Ca content was 18.7 wt % at the interface and 12.0 wt % at the top of the coating. P was observed to be 10.20 wt % at the interface and approximately 7.0 wt % at the top coating. Ga wt % was observed to be approximately 4 at the top of the coating after 3 days of immersion in SBF, however, no Ga was observed to be present at other point at this line. 12.10 wt % of Fe and 3.6 wt % of Cr were observed near the substrate. The EDX line scan of the coating after immersing in SBF for 7 days is shown in Figure 7.17 d. Near the substrate, Si content was 26 wt % and then started decreasing till the top of the coating where it decreased approximately to 3.7 wt %. No Na was observed in the coating. P was observed to be

1.4 wt % at the coating-substrate interface and then started increasing along the cross-section, and at the top it was observed to be 17 wt %. Content of Ca was observed to be 3.70 wt % at the coating-substrate interface and then started increasing till the top of the coating where it was noticed to be 36 wt % Ga was observed only in the middle of the EDX line scan which was 2.20 wt %. 7.50 wt % of Fe and 5.30 wt % Cr was observed at the coating- substrate interface.

Table 7.2 shows EDX area scan carried out at the top surface of the coatings after immersing in SBF for 3 and 7 days. In Ga_2O_3 doped Bioglass® coating, Si, Na and Ga wt % reduced to 9.0 ± 0.6, 1.8 ± 0.1 and 0.8 ± 0.2, whilst Ca and P content was increased to 30.7 ± 0.7 and 0.8 ± 0.2 after 7 days of immersion in SBF. For the co-sprayed Ga_2O_3 and 45S5 coating, Si, Na and Ga content reduced to 6.2 ± 0.8 wt %, 0.5 ± 0.0 wt % and 0 wt %. Whilst wt % of Ca and P increased to 25.2 ± 0.6 and 12.3 ± 0.3 wt % after 7 days of SBF test. This means that less glass coating was remained after SBF test for the co-sprayed glass coating in comparison to the Ga_2O_3 doped glass coating.

Table 7.3 shows the Ca/P ratio (atomic) for coatings after thermal spray and immersed in SBF for 3 and 7 days. Results suggested that this ratio was high (7.2 ± 0.6) for Ga_2O_3 doped Bioglass® coating than the co-sprayed Ga_2O_3 and 45S5 coating before SBF test. However, after immersing in SBF for 7 days Ca/P ratio was higher (1.6 ± 0.0 which is approximately equal to the Ca/P ratio of synthetic HA)) for the co-sprayed Ga_2O_3 and 45S5 coating than Ga_2O_3 doped Bioglass® coating, for which it was 1.4 ± 0.1.

Table 7.2: *EDX area scan at the top surface of the coatings after immersion in SBF for 3 and 7 days.*

Elements	Ga_2O_3 Incorporated Bioactive Glass Coating		Ga_2O_3 and Bioglass® Hybrid Coating	
	After 3 Days of SBF Immersion	After 7 Days of SBF Immersion	After 3 Days of SBF Immersion	After 7 Days of SBF Immersion
Si	22.7 ± 0.9	9.0 ± 0.6	10.2 ± 0.7	6.2 ± 0.8
Na	9.2 ± 4.2	1.8 ± 0.1	0.3 ± 0.1	0.5 ± 0.0
Ca	17.4 ± 1.0	30.7 ± 0.7	22.7 ± 0.6	25.2 ± 0.6
P	5.3 ± 2.5	14.2 ± 0.3	11.3 ± 0.1	12.3 ± 0.3
Ga	1.2 ± 0.2	0.8 ± 0.2	0.2 ± 0.1	0.0

Table 7.3: *Ca/P ratio (atomic %) of the as sprayed and soaking in SBF after 3 and 7 days.*

Coatings	Ca/P Ratio Soaking For 0 Days in SBF	Ca/P Ratio Soaking For 3 Days in SBF	Ca/P Ratio Soaking For 7 Days in SBF
Ga_2O_3 Incorporated Bioactive Glass Coating	7.2 ± 0.6	1.2 ± 0.1	1.4 ± 0.1
Ga_2O_3 and 45S5 Hybrid Coating	5.2 ± 0.5	1.5 ± 0.0	1.6 ± 0.0

7.5 In-vitro Cytotoxicity Tests of the Co-Sprayed Ga_2O_3 - Bioglass® Coating

The Ga_2O_3 doped Bioglass® coating integrity was not good enough to maintain adhesion to the substrate to cut sample for cytotoxicity tests, so no cell test was performed using this coating. Cytotoxicity of the co-sprayed Ga_2O_3 and 45S5 coating was tested using MG63 cells, and the results are summarised in Figure 7.18. As can be seen that the control produced relatively increased cellular response than the coated samples, which is an indication of a relative abundance of the cells present on the surface after incubation for 12 hours and 3 days; however, the relative intensity of the coating was very low in comparison to that produced by the control after 3 days of incubation. For each time points (for the repeat too, not shown here), the significant statistical differences were present as P value was less than 0.05. According to ISO 10993-5:2009 this coating was cytotoxic [298].

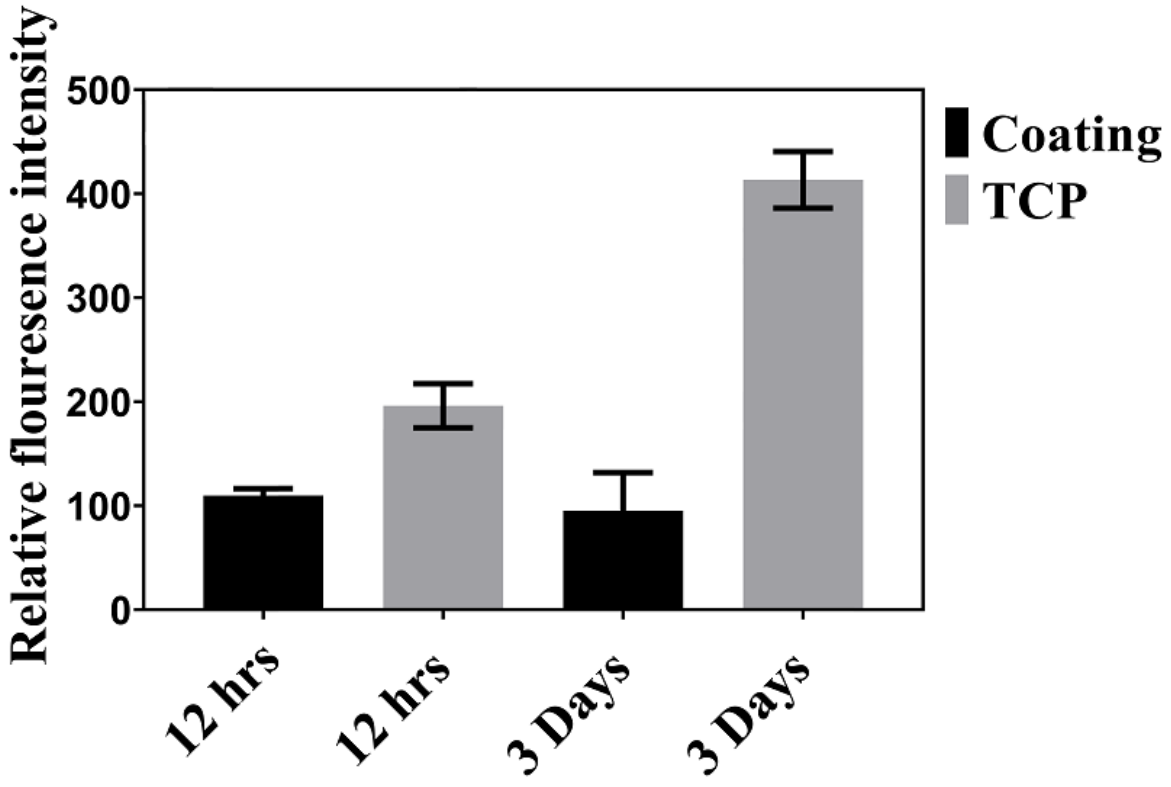

Figure 7.18: *Alamar blue assay results of the co-sprayed Ga_2O_3 and 45S5 coating after 12 hrs and 3 days of incubation with MG63 cells.*

7.6 Discussion

7.6.1 Coating Characterisation

The surface of the Ga_2O_3 doped Bioglass® coating is shown in Figure 7.5, and it can be seen that the surface of the coating had globules, well-molten splats and glass droplets. Similar morphology was obtained with Bioglass® while depositing at 75 kW (Fig 7.5 c, f). It means that 50 kW flame had enough heat energy for this glass to produce a surface morphology similar to the 45S5 coating deposited at 75 kW coating. This could be due to the addition of Ga_2O_3 to the glass, as it has been suggested that if Ga enters the glass network as a network modifier, glass transition temperature (and melting point) of the glass should decrease [299].

Figure 7.6 shows the cross-section of the Ga_2O_3 doped Bioglass® coating, and as it can be seen that the coating was not a uniform coating as the crack can be seen along the cross-section of the coating (Figure 7.6 b). This could be due to the residual stresses in the coating, which are caused by property mismatch or deposition process [300].

For the co-sprayed coating, produced by depositing Ga_2O_3 suspension and 45S5 suspension at 50 kW flame power, a uniform coating was obtained as the whole surface of the substrate was fully covered with a coating (Figure 7.9). Also, no visible crack was noticed along the cross-section of the coating (Figure 7.10). The surface of the coating had re-solidified glass with no flat splat. It means that the glass particles did not spent enough time in the flame to get fully molten or decelerated before reaching the substrate, which could be the reason of the low thickness (16 ± 3 μm) of this coating. This thickness is lower than that obtained by depositing Bioglass® at 50 kW flame power with the obtained thickness of 25 ± 1 μm (4.3.1). this could be due to the hybrid nozzle (shroud) attachment, as it was investigated by Suneil et al. that the attachment of the shroud results in a lower average particle velocity with a maximum difference of 100 m/s without and with a shroud attachment [300].

EDX analysis along the cross-section of the coatings (Figure 7.11) showed that the

variations in the composition of both coatings are approximately similar except for the content of Ga. As can be seen in Figure 7.11 b, the wt % of Ga is approximately uniformly distributed along the cross-section of the Ga_2O_3 doped Bioglass® coating. While for the co-sprayed coating, Ga was observed only at two points (Figure 7.11 d), in the middle of the coating (0.9 wt %) and near the top of the coating (7.8 wt %). The non-uniform distribution of Ga in the co-sprayed coating could be due to the low flowrate (25 ml/min) of Ga_2O_3 suspension in comparison to the Bioglass® suspension flow rate which was 50 ml/min. So, the coating was mainly composed of Bioglass with non-uniform distribution of Ga_2O_3.

The XRD spectrum (Figure 7.13 a) of the Ga_2O_3 doped Bioglass® coating was amorphous, no crystalline peak was observed. Similarly for the co-sprayed coating spectrum (Figure 7.13 b), crystalline peak associated with Ga_2O_3 was observed. This was due to the fact that Ga_2O_3 was not mixed with the glass before making the glass, but was co-sprayed with it and Ga retained its crystalline nature in thermal spraying.

In the Raman spectra of both coatings (Figure 7.13), the peak associated with 860 cm^{-1} was assigned due to the vibration of non-bridging oxygen (Figure 7.4) was no more identified in coating spectra. This could be due to the increase concentration of bridging oxygen (BO) in the glass network [153] as a result of thermal spray. The EDX analysis of the coatings could support the high concentration of BO, as the amount of Si in the coatings had been increased than the starting powder (Table 7.1). Moreover, in the spectrum of co-sprayed Ga_2O_3 and Bioglass® coating, no peak was identified for Ga_2O_3. This could be due to the random selection of the points on the top surface of the coating for Raman analysis. Since Ga was not uniformly distributed in coating, so it might be missing at the analysis point.

7.6.2 Coatings SBF Tests

The present results showed that the Ga_2O_3 doped Bioglass® was bioactive as apatite formation on the surface of the coating took place after immersing in SBF after 3 days (Figure 7.14 a, b). It has been investigated that adding 1 and 1.6 mol % Ga_2O_3 to

glass composition does not affect the apatite forming ability of the bioactive glass; moreover, this addition makes the glass durable in SBF which causes reduction in ion release [152].

The co-sprayed coating composed of Ga_2O_3 and 45S5 was bioactive too, as the coating showed apatite formation after 3 days of immersion (Figure 7.12 c, d). The Ga_2O_3 suspension had only 1 wt % solid loading [152]. However, this co-sprayed coating was chemically stable in SBF in comparison to 45S5 coating deposited at 50 kW (Chapter 4 section 4.4.3). As the 50 kW coating of 45S5 showed a reduction in thickness form 25 μm to 6 μm after immersing in SBF for 7 days [291], however, the present coating did not showed any noticeable reduction in thickness. This could be due to the presence of Ga_2O_3 in coating [152].

Moreover, after 7 days of immersion in SBF, EDX area scan (Table 7.3) showed that the Ga wt % was reduced to 0. However, it can be seen that there were still Ga in the coating, as observed by the EDX line scan along the cross-section of the coating (Figure 7.14 d). This could be due the precipitated HA layer on the surface of the coating, which did not let EDX to detect Ga while doing area scan at the top of the coating. Also, it could be due to the leaching out of the Ga in the solution from the top layer of the coating surface.

7.6.3 Cytotoxicity Tests

After 3 days of incubation of MG-63 cells with the co-sprayed Ga_2O_3 and Bioglass® (Figure 7.18) the relative intensity was very low compared to the control, which showed that this coating was cytotoxic. This could be attributed to the leaching of Ga^{3+} ion from the coating, which is known to possess antineoplastic and antiproliferative properties [301]. Antineoplastic property of gallium is due its ability to bind iron-transport protein i.e. transferrin (Tf), lactoferrin and ferritin, which enables it to accumulate in proliferating tissue (mostly tumours) where large amounts of Tf receptors (TfR) are released [302]. Ga^{3+} ion enters in Tf complexes via TfR by cells which leads to iron deprivation and ultimately prevent cell division may leading to apoptosis. This

could explain why cell viability was reduced when cultured with this coating.

7.7 Summary

According to the presented results and above discussion following conclusion can be drawn

- Ga_2O_3 1.2 wt % incorporated bioactive glass was prepared but could not be successfully deposited via SHVOF thermal spray at flame power of 75 kW, and a non-homogeneous coating was produced at flame power of 50 kW.
- Ga_2O_3 doped Bioglass® coating was bioactive as the coating revealed HA deposition after immersion in SBF.
- Co-sprayed coating of Ga_2O_3 and 45S5 was deposited at 50 kW flame power using a hybrid nozzle; however, the coating was thin which could be due to the decelerating affect of the particles in the presence of the shroud (Hybrid nozzle attachment).
- This co-sprayed coating was bioactive as HA was precipitated on the surface of the coating after immersion in SBF. Moreover, this coating was chemically stable in SBF as the thickness of the coating did not changed.
- Co-sprayed Ga_2O_3 and 45S5 coating was cytotoxic towards MG63 osteoblast like cells, as a pronounced (based on ISO 10993-5:2009) difference in cells viability (relative intensity) was observed in comparison to the control.

Chapter 8

Conclusion

The body of this work was focused on (i). investigating deposition of different materials namely Bioglass®, 13-93 and ICIE16 bioactive glasses, PBG, chemically mixed Ga_2O_3-Bioglass® and Ga_2O_3 and 45S5 hybrid coatings deposition via SHVOF thermal spraying for biomedical applications; (ii) optimisation of the process parameters to deposit a coating suitable for physiological fluid; (iii) studying the dissolution of bioactive coatings in SBF and cytotoxicity towards MG63 cells; (iv) investigation of ion release and mass degradation of PBG. The general conclusions of the research work are summarised as below.

Bioglass® (45S5) was successfully coated at flame powers of 50 and 75 kW on to stainless steel substrate. These flame powers were optimised while depositing 45S5. Four runs were performed to deposit 45S5, i.e. 25 kW, 50 kW, 75 kW and 90 kW. No deposition was achieved at flame power of 90 kW, thick coatings (25 ± 1 μm) at flame powers of 50 and 75 kW and thin coating (< 10 μm) was obtained at 25 kW flame power. Coatings deposited at 50 and 75 kW flame powers had flattened splats, round spheres on the surface of the coatings. The surface of the coating deposited at 75 kW flame power had globules and due to which the surface of this coating was rougher than the 50 kW coating. This was due to the melting of all the material because of high heat transfer from the flame to the particles in the combustion chamber, and then depositing as agglomerates at the surface of the coating. Heat transfer at 90 kW might be very

high that evaporated all of the material in the suspension, and consequently, no deposition was obtained at this flame power. The lower flame power of 25 kW had not enough energy to melt and accelerate the particles. When the non-molten particles and agglomerates with low velocity collide onto the substrate, bounced back, and impaired the deposition.

SBF studies showed that 25 kW coating was not bioactive, as no HA deposition was observed on the surface of the coating after even 7 days of immersion in SBF. Also, this coating was not stable in SBF as increased wt % of Fe and Cr were observed from the substrate after 3 and 7 days of immersion in SBF. 50 and 75 kW coatings of 45S5 revealed HA formation on the surface of the coatings after 3 days of immersion in SBF; however, 50 kW coating showed more dissolution in SBF (as its thickness reduced from 25 μm to 6 μm) than 75 kW coating (before SBF test thickness was 25 μm and after SBF test 23 μm). This could be due to the more porous microstructure of the 50 kW coating.

ICIE16 and 13-93 bioactive glass coatings were successfully deposited at the flame powers of 50 and 75 kW. At 50 kW, with both compositions porous ($\sim$ 6 %), thick ($\sim$ 68 μm), less hard (242 HV) and less rough (2 μm) coatings were obtained. Whilst at the flame power of 75 kW, thinner, denser, and harder ($\sim$ 4 % porosity, 300 HV, and 60 μm thick) coatings were obtained with both formulations. However, 13-93 coating obtained at 75 kW was rougher (Ra = 6.5 $\pm$ 0.6 μm) than that of the 75 kW coating of ICIE16, which was 3.7 $\pm$ 0.6 μm rough.

Each of the glass used in this work has a different network connectivity (NC). For ICIE16 the NC is 2.13 and which is closer to the NC of 45S5 (2.11), while for 13-93 it is 2.58. For ICIE16 coatings (50 and 75 kW), HA precipitated on the surfaces of the coatings after 3 days of immersion in SBF. Following the NC, 13-93 coatings were expected to show delayed apatite precipitation, which was observed for 13-93 coating deposited at 75 kW flame power after 7 days of immersion in SBF. However, its 50 kW coating showed HA precipitation after

3 days of immersion in SBF. Ca/P atomic ratio for ICIE16 coatings was 1.71 ± 0.05 for the 50 kW coating and 1.55 ± 0.01 for the 75 kW coating after 7 days of immersion in SBF, whilst for 13-93 it was 1.24 ± 0.06 for the 50 kW coating, and for the 75 kW coating 2.05 ± 0.74. These results suggested that HA precipitated on the surface of ICIE16 coatings had a composition closer to synthetic HA. It means that ICIE16 coatings are more reactive towards SBF, whilst 13-93 coatings were comparatively stable.

Cell viability and proliferation tests using MG63 cells demonstrated that ICIE16 and 13-93 coatings were cytocompatible. After 3 days of incubation, significant differences ($P < 0.05$) were present between the control and any of the coating. The relative intensity was higher for the control in comparison to the coatings. However, after 7 days of incubation, no significant differences were present ($P > 0.05$) in any of the results. The rougher coating of 13-93 deposited at 75 kW flame power showed highest proliferation (more than the control), suggesting that the cell response was better towards this coating in comparison to other three coatings. This could be due to the high roughness of the surface and high Mg wt % present in the coating composition.

Cell tests were also performed by coating the surfaces of ICIE16 and 13-93 coatings with gold. No significant differences were present among the coatings and control after incubation for 7 days; however, 13-93 coating deposited at 75 kW showed high intensity in comparison to other coating (but similar to the control), suggesting that the rougher surface of this coating had a positive impact on the proliferation of the cells.

This research work then looked into PBG (P40) coatings produced at the flame power of 50 and 75 kW. Similar to the above bioactive coatings, thin (16.0 ± 3.4 μm) and rougher (3.6 ± 0.1 μm) coating was obtained at 75 kW flame power, whilst thicker (24.6 ± 2.3 μm) and less rough (R_a = 2.7 ± 0.1 μm) coating was obtained at 50 kW. Due to these differences, 75 kW coating showed less dissolution in PBS and milli-Q water and less ion release in milli-Q water.

Raman spectra of these coatings were different from that of the P-40 before thermal spray. Results suggested that before thermal spray P-40 had Q^1, and Q^2 species. However, after the thermal spray, the Raman spectra of the coatings proposed that the concentration of Q^2 species decreased whilst the concentration of Q^1 increased and Q^0 species formed. These changes in the structure of the glass resulted in a reduced degradation and ion release profiles in comparison to those reported for P-40 thin film and bulk glass.

Moreover, antimicrobial bioactive coatings were also explored by spraying chemically mixed Ga_2O_3-Bioglass® and a co-sprayed coating of Ga_2O_3 and Bioglass® suspension (via hybrid nozzle) deposited at flame power of 50 kW. With chemically mixed Ga_2O_3-Bioglass®, the coating obtained was not of good quality, as the substrate was not uniformly covered with the coatings. Also, this coating could be easily removed in the form of flakes with a finger. This could be due to the residual stresses in the coating that caused the poor adhesion of the coating with the substrate. However, the coating was bioactive as the samples revealed apatite formation after 3 days of immersion in SBF.

Co-sprayed uniform coating, deposited with Ga_2O_3 and 45S5 suspensions via a hybrid nozzle was obtained at 50 kW flame power. This coating also developed HA after 3 days of immersion in SBF, suggesting that the coating was bioactive. Moreover, the cell tests demonstrated this coating to be cytotoxic, as a pronounced (based on ISO 10993-5:2009) reduction in cells viability (relative intensity) was observed in comparison to the control.

SHVOF is a promising technique for the deposition of adherent bioactive coatings, bioactive with antimicrobial ions coatings and bioresorbable coatings which may find applications upon bone load bearing implants for their potential to bond with the bone and to release therapeutic ions at the implant site.

Chapter 9

Future Work

This study has shown that coatings for biomedical applications can be produced via SHVOF. However, further research can be carried out on these coatings to investigate the adhesive strength of these coatings with the substrate. Also, the adhesion strength could be done after SBF tests in case of bioactive coatings.

For Bioglass® 45S5 coatings and bioactive glasses (ICIE16 and 13-93), ion release study can be done. This could be a way to determine the amount of ions release from the coatings related to specific compositions and their microstructures. Moreover, in-vivo study of these coatings should be a way to compare and contrast to bone bonding and bone ingrowth simulation ability.

For P-40 coatings, since the Raman analysis showed structural changes post deposition, this structural analysis warrants further investigation, via NMR characterisation. Also, in-vitro cell tests can be done to determine cytoxicity of these coatings.

For the chemically mixed Ga_2O_3-Bioglass® glass, Optimisation of the parameters such as wt % of Ga_2O_3 to prepare a glass that would be suitable for coating purposes. Moreover, glass transition temperature and the reason of residual stresses in the coating should be investigated so that the reason for the unsuccessful coating could be known.

The co-sprayed Ga_2O_3 and Bioglass® coating, the wt % of Ga_2O_3 in the sus-

pension should be also optimised so that the coating would not release Ga^{3+} in a toxic concentration. Moreover, further study is required to do ion leaching and antibacterial tests of the existing coating.

References

[1] Samuel G Steinemann. "Titanium—the material of choice?" In: *Periodontology* 17.1 (1998), pp. 7–21.

[2] Antonella Sola et al. "Bioactive glass coatings: a review". In: *Surface engineering* 27.8 (2011), pp. 560–572.

[3] B Kasemo and J Gold. "Implant surfaces and interface processes". In: *Advances in dental research* 13.1 (1999), pp. 8–20.

[4] Erik Lenguerrand et al. "Description of the rates, trends and surgical burden associated with revision for prosthetic joint infection following primary and revision knee replacements in England and Wales: an analysis of the National Joint Registry for England, Wales, Northern Ireland and the Isle of Man". In: *BMJ open* 7.7 (2017), e014056.

[5] Hwa Sen Chua et al. "Mortality and implant survival with simultaneous and staged bilateral total knee arthroplasty experience from the Australian Orthopaedic Association National Joint Replacement Registry". In: *The Journal of arthroplasty* 33.10 (2018), pp. 3167–3173.

[6] Besim Ben-Nissan et al. "Synthesis and characterization of hydroxyapatite nanocoatings by sol-gel method for clinical applications". In: *Biological and Biomedical*

Coatings Handbook: Processing and Characterization, CRC Press, Boca Raton, FL USA (2011), pp. 37–79.

[7] ID Thompson and LL Hench. "Mechanical properties of bioactive glasses, glass-ceramics and composites". In: *Proceedings of the Institution of Mechanical Engineers, Part H: Journal of Engineering in Medicine* 212.2 (1998), pp. 127–136.

[8] T Kokubo and H Takadama. "Leading Opinion". In: *How useful is SBF in predicting in-vivo bone bioactivity, Biomaterial* 27 (2006), pp. 2907–2915.

[9] Qiang Fu et al. "In-vivo evaluation of 13-93 bioactive glass scaffolds with trabecular and oriented microstructures in a subcutaneous rat implantation model". In: *Journal of biomedical materials research Part A* 95.1 (2010), pp. 235–244.

[10] Mohamed N Rahaman et al. "Bioactive glass in tissue engineering". In: *Acta biomaterialia* 7.6 (2011), pp. 2355–2373.

[11] Eduardo K Moioli et al. "Matrices and scaffolds for drug delivery in dental, oral and craniofacial tissue engineering". In: *Advanced drug delivery reviews* 59.4-5 (2007), pp. 308–324.

[12] Amy Nommeots-Nomm et al. "Direct ink writing of highly bioactive glasses". In: *Journal of the European Ceramic Society* 38.3 (2018), pp. 837–844.

[13] Francesco Baino and Enrica Verné. "Glass-based coatings on biomedical implants: A state-of-the-art review". In: *Biomedical Glasses* 3.1 (2017), pp. 1–17.

[14] I Elgayar et al. "Structural analysis of bioactive glasses". In: *Journal of Non-Crystalline Solids* 351.2 (2005), pp. 173–183.

[15] Amy Nommeots-Nomm et al. “Highly degradable porous melt-derived bioactive glass foam scaffolds for bone regeneration”. In: *Acta biomaterialia* 57 (2017), pp. 449–461.

[16] Bryan W Stuart et al. “Insights into structural characterisation and thermal properties of compositionally equivalent vapour-condensed and melt-quenched glasses”. In: *Materials & Design* 111 (2016), pp. 174–184.

[17] I Ahmed et al. “Phosphate glasses for tissue engineering: Part 1. Processing and characterisation of a ternary-based P_2O_5–CaO–Na_2O glass system”. In: *Biomaterials* 25.3 (2004), pp. 491–499.

[18] Jonathan Pratten et al. “In vitro attachment of Staphylococcus epidermidis to surgical sutures with and without Ag-containing bioactive glass coating”. In: *Journal of biomaterials applications* 19.1 (2004), pp. 47–57.

[19] AM Mulligan et al. “The effect of increasing copper content in phosphate-based glasses on biofilms of Streptococcus sanguis”. In: *Biomaterials* 24.10 (2003), pp. 1797–1807.

[20] Ehsan Zeimaran et al. “Antibacterial properties of poly (octanediol citrate)/gallium-containing bioglass composite scaffolds”. In: *Journal of Materials Science: Materials in Medicine* 27.1 (2016), p. 18.

[21] Wei Dong et al. “Investigation on the antibacterial micro-porous titanium with silver nano-particles”. In: *Journal of nanoscience and nanotechnology* 13.10 (2013), pp. 6782–6786.

[22] Sabeel P Valappil et al. “Antimicrobial gallium-doped phosphate-based glasses”. In: *Advanced functional materials* 18.5 (2008), pp. 732–741.

[23] Lech Pawlowski. *The science and engineering of thermal spray coatings*. John Wiley & Sons, 2008.

[24] Nuria Espallargas. *Future development of thermal spray coatings: Types, designs, manufacture and applications*. Elsevier, 2015.

[25] Pierre Fauchais et al. "From powders to thermally sprayed coatings". In: *Journal of thermal spray technology* 19.1-2 (2010), pp. 56–80.

[26] Maria Oksa et al. "Optimization and characterization of high velocity oxy-fuel sprayed coatings: techniques, materials, and applications". In: *Coatings* 1.1 (2011), pp. 17–52.

[27] Giovanni Bolelli et al. "Comparison between suspension plasma sprayed and high velocity suspension flame sprayed bioactive coatings". In: *Surface and Coatings Technology* 280 (2015), pp. 232–249.

[28] N Stiegler et al. "High-velocity suspension flame sprayed (HVSFS) hydroxyapatite coatings for biomedical applications". In: *Journal of thermal spray technology* 21.2 (2012), pp. 275–287.

[29] Lech Pawlowski. "Finely grained nanometric and submicrometric coatings by thermal spraying: A review". In: *Surface and Coatings Technology* 202.18 (2008), pp. 4318–4328.

[30] C Renghini et al. "Plasma sprayed hydroxyapatite coatings from nanostructured granules". In: *Materials Science and Engineering: B* 152.1-3 (2008), pp. 86–90.

[31] Pierre Fauchais et al. "Engineering a new class of thermal spray nano-based microstructures from agglomerated nanostructured particles, suspensions and

solutions: an invited review". In: *Journal of Physics D: Applied Physics* 44.9 (2011), p. 093001.

[32] Andreas Killinger et al. "High-velocity suspension flame spraying (HVSFS), a new approach for spraying nanoparticles with hypersonic speed". In: *Surface and Coatings Technology* 201.5 (2006), pp. 1922–1929.

[33] Giovanni Bolelli et al. "Properties of high velocity suspension flame sprayed (HVSFS) TiO2 coatings". In: *Surface and Coatings Technology* 203.12 (2009), pp. 1722–1732.

[34] Filofteia-Laura Toma et al. "Nanostructured photocatalytic titania coatings formed by suspension plasma spraying". In: *Journal of thermal spray technology* 15.4 (2006), pp. 587–592.

[35] R Rampon et al. "Liquid plasma sprayed coatings of yttria-stabilized zirconia for SOFC electrolytes". In: *Journal of thermal spray technology* 15.4 (2006), pp. 682–688.

[36] R Moreno and E Bannier. "Feedstock suspensions and solutions". In: *Future Development of Thermal Spray Coatings*. Elsevier, 2015, pp. 51–80.

[37] Giovanni Bolelli et al. "Investigation of high-velocity suspension flame sprayed (HVSFS) glass coatings". In: *Materials Letters* 62.17-18 (2008), pp. 2772–2775.

[38] Andreas Killinger et al. "Review of new developments in suspension and solution precursor thermal spray processes". In: *Journal of Thermal Spray Technology* 20.4 (2011), pp. 677–695.

[39] GM Raghavendra et al. *Biomaterials: Design, Development and Biomedical Applications, Nanotechnology Applications for Tissue Engineering*. 2015.

[40] Greeshma Thrivikraman et al. “In vitro/in vivo assessment and mechanisms of toxicity of bioceramic materials and its wear particulates”. In: *RSC Advances* 4.25 (2014), pp. 12763–12781.

[41] Mara Vallet-Reg. “Evolution of bioceramics within the field of biomaterials”. In: *Comptes Rendus Chimie* 13.1-2 (2010), pp. 174–185.

[42] L Hengh. “Bioceramics: From Concepts to Clinics”. In: *J. Am. Ceram. Soc* 74.7 (1991), pp. 1487–1510.

[43] LL Hench. “A Forecast for the Future. Biomaterials”. In: *Biomaterials* 19.16 (1998), pp. 1419–1423.

[44] Rajiv Gandhi et al. “Predictive risk factors for stiff knees in total knee arthroplasty”. In: *The Journal of arthroplasty* 21.1 (2006), pp. 46–52.

[45] Christie YK Lung et al. “A Multi-Element-Doped Porous Bioactive Glass Coating for Implant Applications”. In: *Materials* 14.4 (2021), p. 961.

[46] Larry L Hench. “The story of Bioglass®”. In: *Journal of Materials Science: Materials in Medicine* 17.11 (2006), pp. 967–978.

[47] F Imran et al. “Bioactive glass: A material for the future”. In: *WJD* 3 (2012), pp. 199–201.

[48] PN De Aza et al. “Bioactive glasses and glass-ceramics”. In: *Boletin-Sociedad Espanola De Ceramica Y Vidrio* 46.2 (2007), p. 45.

[49] Larry L Hench. “Bioceramics: from concept to clinic”. In: *Journal of the american ceramic society* 74.7 (1991), pp. 1487–1510.

[50] Julian Jones and Alexis Clare. *Bio-glasses: an introduction*. John Wiley & Sons, 2012.

[51] Marc Bohner and Jacques Lemaitre. “Can bioactivity be tested in vitro with SBF solution?” In: *Biomaterials* 30.12 (2009), pp. 2175–2179.

[52] Md Towhidul Islam et al. “The effect of MgO/TiO2 on structural and crystallization behavior of near invert phosphate-based glasses”. In: *Journal of Biomedical Materials Research Part B: Applied Biomaterials* 108.3 (2020), pp. 674–686.

[53] Gurbinder Kaur. *Clinical applications of biomaterials: State-of-the-art progress, trends, and novel approaches*. Springer, 2017.

[54] Gurbinder Kaur et al. “Review and the state of the art: sol–gel and melt quenched bioactive glasses for tissue engineering”. In: *Journal of Biomedical Materials Research Part B: Applied Biomaterials* 104.6 (2016), pp. 1248–1275.

[55] Julian R Jones. “Sol-gel derived glasses for medicine”. In: *Bio-Glasses, John Wiley & Sons, Ltd* (2012), pp. 29–44.

[56] Zoe Y Wu et al. “Melt-derived bioactive glass scaffolds produced by a gel-cast foaming technique”. In: *Acta Biomaterialia* 7.4 (2011), pp. 1807–1816.

[57] R Hill. “An alternative view of the degradation of bioglass”. In: *Journal of Materials Science Letters* 15.13 (1996), pp. 1122–1125.

[58] MD O’donnell et al. “Effect of P2O5 content in two series of soda lime phosphosilicate glasses on structure and properties–Part I: NMR”. In: *Journal of Non-Crystalline Solids* 354.30 (2008), pp. 3554–3560.

[59] Brice Ilharreborde et al. “Bioactive glass as a bone substitute for spinal fusion in adolescent idiopathic scoliosis: a comparative study with iliac crest autograft”. In: *Journal of Pediatric Orthopaedics* 28.3 (2008), pp. 347–351.

[60] Larry L Hench and David Greenspan. “Interactions between bioactive glass and collagen: a review and new perspectives”. In: *J. Aust. Ceram. Soc* 49.2 (2013), pp. 1–40.

[61] Fayez Bahmad Jr and Saumil N Merchant. “Histopathology of ossicular grafts and implants in chronic otitis media”. In: *Annals of Otology, Rhinology & Laryngology* 116.3 (2007), pp. 181–191.

[62] Julian R Jones. “Reprint of: Review of bioactive glass: From Hench to hybrids”. In: *Acta biomaterialia* 23 (2015), S53–S82.

[63] Ette S Tadjoedin et al. “High concentrations of bioactive glass material (BioGran®) vs. autogenous bone for sinus floor elevation: Histomorphometrical observations on three split mouth clinical cases”. In: *Clinical oral implants research* 13.4 (2002), pp. 428–436.

[64] Qizhi Chen. “Bioglass®-derived glass-ceramic scaffolds for bone tissue engineering”. PhD thesis. Imperial College London, 2007.

[65] DG Gillam et al. “The effects of a novel Bioglass® dentifrice on dentine sensitivity: a scanning electron microscopy investigation”. In: *Journal of Oral Rehabilitation* 29.4 (2002), pp. 305–313.

[66] Bao Jun Tai et al. “Anti-gingivitis effect of a dentifrice containing bioactive glass (NovaMin®) particulate”. In: *Journal of clinical periodontology* 33.2 (2006), pp. 86–91.

[67] AR Pradeep and Anuj Sharma. “Comparison of clinical efficacy of a dentifrice containing calcium sodium phosphosilicate to a dentifrice containing potassium

nitrate and to a placebo on dentinal hypersensitivity: a randomized clinical trial". In: *Journal of periodontology* 81.8 (2010), pp. 1167–1173.

[68] M Vahid Golpayegani et al. "Remineralization effect of topical NovaMin versus sodium fluoride (1.1%) on caries-like lesions in permanent teeth". In: *Journal of dentistry (Tehran, Iran)* 9.1 (2012), p. 68.

[69] Md Towhidul Islam et al. "Bioactive calcium phosphate–based glasses and ceramics and their biomedical applications: a review". In: *Journal of tissue engineering* 8 (2017), p. 2041731417719170.

[70] Sonia Lopez-Esteban et al. "Bioactive glass coatings for orthopedic metallic implants". In: *Journal of the European Ceramic Society* 23.15 (2003), pp. 2921–2930.

[71] S Lopez-Esteban et al. "Interfaces in graded coatings on titanium-based implants". In: *Journal of Biomedical Materials Research Part A: An Official Journal of The Society for Biomaterials, The Japanese Society for Biomaterials, and The Australian Society for Biomaterials and the Korean Society for Biomaterials* 88.4 (2009), pp. 1010–1021.

[72] Jose M Gomez-Vega et al. "Novel bioactive functionally graded coatings on Ti6Al4V". In: *Advanced Materials* 12.12 (2000), pp. 894–898.

[73] Francesco Baino et al. "Design, selection and characterization of novel glasses and glass-ceramics for use in prosthetic applications". In: *Ceramics International* 42.1 (2016), pp. 1482–1491.

[74] SM Salman et al. “The role of strontium and potassium on crystallization and bioactivity of Na2O–CaO–P2O5–SiO2 glasses”. In: *Ceramics International* 38.1 (2012), pp. 55–63.

[75] M Tylkowski and DS Brauer. “Mixed alkali effects in Bioglass® 45S5”. In: *Journal of non-crystalline solids* 376 (2013), pp. 175–181.

[76] Mina Eilaghi et al. “Effect of partial substitution of K2O for Na2O on sintering, crystallization and mechanical properties of SiO2-CaO-K2O-Na2O-CaF2 glass-ceramics”. In: *Transactions of the Indian Ceramic Society* 75.1 (2016), pp. 1–6.

[77] Daniel Groh et al. “Bioactive glasses with improved processing. Part 1. Thermal properties, ion release and apatite formation”. In: *Acta biomaterialia* 10.10 (2014), pp. 4465–4473.

[78] Franziska Dohler et al. “Bioactive glasses with improved processing. Part 2. Viscosity and fibre drawing”. In: *Journal of Non-Crystalline Solids* 432 (2016), pp. 130–136.

[79] Delia S Brauer. “Bioactive glasses—structure and properties”. In: *Angewandte Chemie International Edition* 54.14 (2015), pp. 4160–4181.

[80] Qiang Fu et al. “Mechanical and in vitro performance of 13–93 bioactive glass scaffolds prepared by a polymer foam replication technique”. In: *Acta biomaterialia* 4.6 (2008), pp. 1854–1864.

[81] Qiang Fu et al. “Silicate, borosilicate, and borate bioactive glass scaffolds with controllable degradation rate for bone tissue engineering applications. I. Prepa-

ration and in vitro degradation". In: *Journal of biomedical materials research part A* 95.1 (2010), pp. 164–171.

[82] Barbara Pföss et al. "Structuring of bioactive glass surfaces at the micrometer scale by direct casting intended to influence cell response". In: *Biomedical glasses* 2.1 (2016).

[83] Wing-Hin Lee et al. "High protein adsorptive capacity of amino acid-functionalized hydroxyapatite". In: *Journal of Biomedical Materials Research Part A* 101.3 (2013), pp. 873–883.

[84] T Paatola et al. "Coating of bioactive glass (13-93) fibers with bioabsorbable polymer". In: *Key Engineering Materials* 192 (2001).

[85] Robert G Hill and Delia S Brauer. "Predicting the bioactivity of glasses using the network connectivity or split network models". In: *Journal of Non-Crystalline Solids* 357.24 (2011), pp. 3884–3887.

[86] SJ Watts et al. "Influence of magnesia on the structure and properties of bioactive glasses". In: *Journal of Non-Crystalline Solids* 356.9-10 (2010), pp. 517–524.

[87] Roger F Brown et al. "Growth and differentiation of osteoblastic cells on 13–93 bioactive glass fibers and scaffolds". In: *Acta Biomaterialia* 4.2 (2008), pp. 387–396.

[88] Sayed Mahmood Rabiee et al. "Effect of ion substitution on properties of bioactive glasses: A review". In: *Ceramics International* 41.6 (2015), pp. 7241–7251.

[89] J Ma et al. “Effect of magnesia on the degradability and bioactivity of sol–gel derived SiO2–CaO–MgO–P2O5 system glasses”. In: *Colloids and Surfaces B: Biointerfaces* 81.1 (2010), pp. 87–95.

[90] M Vallet-Regi et al. “Effect of magnesium content on the in vitro bioactivity of CaO-MgO-SiO 2-P 2 O 5 sol-gel glasses”. In: *Journal of Materials Chemistry* 9.2 (1999), pp. 515–518.

[91] A Balamurugan et al. “Sol gel derived SiO2-CaO-MgO-P2O5 bioglass system—Preparation and in vitro characterization”. In: *Journal of Biomedical Materials Research Part B: Applied Biomaterials: An Official Journal of The Society for Biomaterials, The Japanese Society for Biomaterials, and The Australian Society for Biomaterials and the Korean Society for Biomaterials* 83.2 (2007), pp. 546–553.

[92] Marc Bohner. “Resorbable biomaterials as bone graft substitutes”. In: *Materials Today* 13.1-2 (2010), pp. 24–30.

[93] JOHN F BURKE et al. “Application of materials in medicine and dentistry”. In: *Biomaterials Science*. Elsevier, 1996, pp. 283–388.

[94] LL Hench et al. “20500 Abo, FINLAND.” In: *Bioceramics: Proceedings of the 4th International Symposium on Ceramics in Medicine, London, UK, September 1991*. German Ceramic Society. 1991, p. 155.

[95] Larry L Hench. “Genetic design of bioactive glass”. In: *Journal of the European Ceramic Society* 29.7 (2009), pp. 1257–1265.

[96] D Scott Metsger et al. “Tricalcium phosphate ceramic–a resorbable bone implant: review and current status.” In: *Journal of the American Dental Association (1939)* 105.6 (1982), pp. 1035–1038.

[97] TSUTOMU MINAMF and John D Mackenzie. "Thermal expansion and chemical durability of phosphate glasses". In: *Journal of the American Ceramic Society* 60.5-6 (1977), pp. 232–235.

[98] K Franks et al. "Investigation of thermal parameters and crytallisation in a ternary CaO–Na2O–P2O5-based glass system". In: *Biomaterials* 22.5 (2001), pp. 497–501.

[99] Md Towhidul Islam et al. "Effect of magnesium content on bioactivity of near invert phosphate-based glasses". In: *International Journal of Applied Glass Science* 8.4 (2017), pp. 391–402.

[100] Jonathan C Knowles. "Phosphate based glasses for biomedical applications". In: *Journal of Materials Chemistry* 13.10 (2003), pp. 2395–2401.

[101] Ensanya A Abou Neel et al. "Structure and properties of strontium-doped phosphate-based glasses". In: *Journal of the Royal Society Interface* 6.34 (2009), pp. 435–446.

[102] Ifty Ahmed et al. "Cytocompatibility and effect of increasing MgO content in a range of quaternary invert phosphate-based glasses". In: *Journal of biomaterials applications* 24.6 (2010), pp. 555–575.

[103] Ensanya A Abou Neel et al. "Doping of a high calcium oxide metaphosphate glass with titanium dioxide". In: *Journal of Non-Crystalline Solids* 355.16-17 (2009), pp. 991–1000.

[104] Wei Li et al. "Preparation and characterization of vancomycin releasing PHBV coated 45S5 Bioglass®-based glass–ceramic scaffolds for bone tissue engineering". In: *Journal of the European Ceramic Society* 34.2 (2014), pp. 505–514.

[105] Jonathan Massera et al. “Thermal properties and surface reactivity in simulated body fluid of new strontium ion-containing phosphate glasses”. In: *Journal of Materials Science: Materials in Medicine* 24.6 (2013), pp. 1407–1416.

[106] DS Brauer et al. “Fluoride-containing bioactive glass-ceramics”. In: *Journal of Non-Crystalline Solids* 358.12-13 (2012), pp. 1438–1442.

[107] Azadeh Kiani et al. “Titanium-containing bioactive phosphate glasses”. In: *Philosophical Transactions of the Royal Society A: Mathematical, Physical and Engineering Sciences* 370.1963 (2012), pp. 1352–1375.

[108] Toshihiro Kasuga et al. “Phosphate glasses and glass-ceramics for biomedical applications”. In: *Phosphorus Research Bulletin* 26 (2012), pp. 8–15.

[109] EA Abou Neel et al. “Effect of iron on the surface, degradation and ion release properties of phosphate-based glass fibres”. In: *Acta biomaterialia* 1.5 (2005), pp. 553–563.

[110] Wing-Hin Lee et al. “Modulating protein adsorption onto hydroxyapatite particles using different amino acid treatments”. In: *Journal of The Royal Society Interface* 9.70 (2012), pp. 918–927.

[111] Anthony G Avent et al. “The dissolution of silver–sodium–calcium–phosphate glasses for the control of urinary tract infections”. In: *Journal of non-crystalline solids* 328.1-3 (2003), pp. 31–39.

[112] EAA Neela and I Ahmed. “Characterization of antibacterial copper releasing degradable phosphate glass fibers”. In: *Biomaterials* 26 (2005), pp. 2247–2254.

[113] Bryan W Stuart et al. "Gallium incorporation into phosphate based glasses: Bulk and thin film properties". In: *Journal of the mechanical behavior of biomedical materials* 82 (2018), pp. 371–382.

[114] Daniela Carta et al. "Sol–gel synthesis and structural characterisation of P 2 O 5–B 2 O 3–Na 2 O glasses for biomedical applications". In: *Journal of materials chemistry* 19.1 (2009), pp. 150–158.

[115] Ifty Ahmed et al. "Developing unique geometries of phosphate-based glasses and their prospective biomedical applications". In: *Johnson Matthey Technology Review* (2018).

[116] Uwe Hoppe et al. "Variation in PO bonding in phosphate glasses-a neutron diffraction study". In: *Zeitschrift für Naturforschung A* 55.3-4 (2000), pp. 369–380.

[117] Ensanya A Abou Neel et al. "Bioactive functional materials: a perspective on phosphate-based glasses". In: *Journal of Materials Chemistry* 19.6 (2009), pp. 690–701.

[118] LY Zhang et al. "Statistical approach to modeling relationships of composition–structure–property I: Alkaline earth phosphate glasses". In: *Journal of Alloys and Compounds* 734 (2018), pp. 163–171.

[119] Nilay J Lakhkar et al. "Titanium phosphate glass microspheres for bone tissue engineering". In: *Acta biomaterialia* 8.11 (2012), pp. 4181–4190.

[120] Huasheng Gao et al. "Dissolution mechanism and release kinetics of phosphate controlled release glasses in aqueous medium". In: *Journal of controlled release* 96.1 (2004), pp. 29–36.

[121] Xiaoling Liu et al. “Magnesium coated bioresorbable phosphate glass fibres: investigation of the interface between fibre and polyester matrices”. In: *BioMed research international* 2013 (2013).

[122] BC Bunker et al. “Phosphate glass dissolution in aqueous solutions”. In: *Journal of Non-Crystalline Solids* 64.3 (1984), pp. 291–316.

[123] Gaurav Lalwani et al. “Tungsten disulfide nanotubes reinforced biodegradable polymers for bone tissue engineering”. In: *Acta biomaterialia* 9.9 (2013), pp. 8365–8373.

[124] Nusrat Sharmin et al. “Effect of boron addition on the thermal, degradation, and cytocompatibility properties of phosphate-based glasses”. In: *BioMed research international* 2013 (2013).

[125] Papia Haque et al. “Degradation properties and microstructural analysis of 40P2O5–24MgO–16CaO–16Na2O–4Fe2O3 phosphate glass fibres”. In: *Journal of Non-Crystalline Solids* 375 (2013), pp. 99–109.

[126] S Cozien-Cazuc et al. “Effects of aqueous aging on the mechanical properties of P 40 Na 20 Ca 16 Mg 24 phosphate glass fibres”. In: *Journal of materials science* 43.14 (2008), pp. 4834–4839.

[127] AJ Parsons et al. “Properties of sodium-based ternary phosphate glasses produced from readily available phosphate salts”. In: *Journal of non-crystalline solids* 352.50-51 (2006), pp. 5309–5317.

[128] Motohiro Uo et al. “Properties and cytotoxicity of water soluble Na2O–CaO–P2O5 glasses”. In: *Biomaterials* 19.24 (1998), pp. 2277–2284.

[129] Bryan W Stuart et al. "Degradation and characterization of resorbable phosphate-based glass thin-film coatings applied by radio-frequency magnetron sputtering". In: *ACS applied materials & interfaces* 7.49 (2015), pp. 27362–27372.

[130] Carla Renata Arciola et al. "Biofilm formation in Staphylococcus implant infections. A review of molecular mechanisms and implications for biofilm-resistant materials". In: *Biomaterials* 33.26 (2012), pp. 5967–5982.

[131] U Lorenz et al. "In vivo detection of Staphylococcus aureus in biofilm on vascular prostheses using non-invasive biophotonic imaging". In: *European Journal of Vascular and Endovascular Surgery* 41.1 (2011), pp. 68–75.

[132] Holger Rohde et al. "Polysaccharide intercellular adhesin or protein factors in biofilm accumulation of Staphylococcus epidermidis and Staphylococcus aureus isolated from prosthetic hip and knee joint infections". In: *Biomaterials* 28.9 (2007), pp. 1711–1720.

[133] Mohamed N Rahaman et al. "Emerging developments in the use of bioactive glasses for treating infected prosthetic joints". In: *Materials Science and Engineering: C* 41 (2014), pp. 224–231.

[134] Anthony G Gristina. "Biomaterial-centered infection: microbial adhesion versus tissue integration". In: *Science* 237.4822 (1987), pp. 1588–1595.

[135] JM Schierholz and J Beuth. "Implant infections: a haven for opportunistic bacteria". In: *Journal of Hospital Infection* 49.2 (2001), pp. 87–93.

[136] Michael C Hudson et al. "Staphylococcus aureus adhesion to bone matrix and bone-associated biomaterials". In: *FEMS microbiology letters* 173.2 (1999), pp. 279–284.

[137] Davide Campoccia et al. “The significance of infection related to orthopedic devices and issues of antibiotic resistance”. In: *Biomaterials* 27.11 (2006), pp. 2331–2339.

[138] Carla Renata Arciola et al. “Etiology of implant orthopedic infections: a survey on 1027 clinical isolates”. In: *The International journal of artificial organs* 28.11 (2005), pp. 1091–1100.

[139] Daniela Baldoni et al. “In vitro activity of gallium maltolate against Staphylococci in logarithmic, stationary, and biofilm growth phases: comparison of conventional and calorimetric susceptibility testing methods”. In: *Antimicrobial agents and chemotherapy* 54.1 (2010), pp. 157–163.

[140] V Mortazavi et al. “Antibacterial effects of sol-gel-derived bioactive glass nanoparticle on aerobic bacteria”. In: *Journal of Biomedical Materials Research Part A: An Official Journal of The Society for Biomaterials, The Japanese Society for Biomaterials, and The Australian Society for Biomaterials and the Korean Society for Biomaterials* 94.1 (2010), pp. 160–168.

[141] Eveliina Munukka et al. “Bactericidal effects of bioactive glasses on clinically important aerobic bacteria”. In: *Journal of Materials Science: Materials in Medicine* 19.1 (2008), pp. 27–32.

[142] Zong-Ping Xie et al. “In vivo study effect of particulate Bioglass® in the prevention of infection in open fracture fixation”. In: *Journal of Biomedical Materials Research Part B: Applied Biomaterials* 90.1 (2009), pp. 195–201.

[143] Gianni Pertici et al. “Composite polymer-coated mineral grafts for bone regeneration: material characterisation and model study”. In: *Annals of Oral & Maxillofacial Surgery* 2.1 (2014).

[144] Sheng Hu et al. “Study on antibacterial effect of 45S5 Bioglass®”. In: *Journal of Materials Science: Materials in Medicine* 20.1 (2009), pp. 281–286.

[145] Maria Bellantone et al. “Broad-spectrum bactericidal activity of Ag2O-doped bioactive glass”. In: *Antimicrobial agents and chemotherapy* 46.6 (2002), pp. 1940–1945.

[146] Patricia Stoor et al. “Antibacterial effects of a bioactive glass paste on oral microorganisms”. In: *Acta Odontologica Scandinavica* 56.3 (1998), pp. 161–165.

[147] Gurbinder Kaur et al. “A review of bioactive glasses: their structure, properties, fabrication and apatite formation”. In: *Journal of Biomedical Materials Research Part A: An Official Journal of The Society for Biomaterials, The Japanese Society for Biomaterials, and The Australian Society for Biomaterials and the Korean Society for Biomaterials* 102.1 (2014), pp. 254–274.

[148] Sabeel P Valappil et al. “Controlled delivery of antimicrobial gallium ions from phosphate-based glasses”. In: *Acta biomaterialia* 5.4 (2009), pp. 1198–1210.

[149] AW Wren et al. “Gallium containing glass polyalkenoate anti-cancerous bone cements: glass characterization and physical properties”. In: *Journal of Materials Science: Materials in Medicine* 23.8 (2012), pp. 1823–1833.

[150] Timothy J Keenan et al. “Relating ion release and pH to in vitro cell viability for gallium-inclusive bioactive glasses”. In: *Journal of materials science* 51.2 (2016), pp. 1107–1120.

[151] Lawrence R Bernstein. "Mechanisms of therapeutic activity for gallium". In: *Pharmacological reviews* 50.4 (1998), pp. 665–682.

[152] Mirco Franchini et al. "Gallium-containing phospho-silicate glasses: Synthesis and in vitro bioactivity". In: *Materials Science and Engineering: C* 32.6 (2012), pp. 1401–1406.

[153] AW Wren et al. "Characterisation of Ga 2 O 3–Na 2 O–CaO–ZnO–SiO 2 bioactive glasses". In: *Journal of materials science* 48.11 (2013), pp. 3999–4007.

[154] Chaoyuan Wang et al. "Bone growth is enhanced by novel bioceramic coatings on Ti alloy implants". In: *Journal of Biomedical Materials Research Part A: An Official Journal of The Society for Biomaterials, The Japanese Society for Biomaterials, and The Australian Society for Biomaterials and the Korean Society for Biomaterials* 90.2 (2009), pp. 419–428.

[155] Anders Palmquist et al. "Titanium oral implants: surface characteristics, interface biology and clinical outcome". In: *Journal of the Royal Society Interface* 7.suppl_5 (2010), S515–S527.

[156] Rüdiger Junker et al. "Effects of implant surface coatings and composition on bone integration: a systematic review". In: *Clinical oral implants research* 20 (2009), pp. 185–206.

[157] Sam Zhang. *Hydroxyapatite coatings for biomedical applications*. Taylor & Francis, 2013.

[158] Yunzhi Yang et al. "A review on calcium phosphate coatings produced using a sputtering process—an alternative to plasma spraying". In: *Biomaterials* 26.3 (2005), pp. 327–337.

[159] GP Dinda et al. “Pulsed laser deposition of hydroxyapatite thin films on Ti–6Al–4V: Effect of heat treatment on structure and properties”. In: *Acta biomaterialia* 5.5 (2009), pp. 1821–1830.

[160] Wojciech Suchanek and Masahiro Yoshimura. “Processing and properties of hydroxyapatite-based biomaterials for use as hard tissue replacement implants”. In: *Journal of Materials Research* 13.1 (1998), pp. 94–117.

[161] Livia E Sima et al. “Differentiation of mesenchymal stem cells onto highly adherent radio frequency-sputtered carbonated hydroxylapatite thin films”. In: *Journal of Biomedical Materials Research Part A* 95.4 (2010), pp. 1203–1214.

[162] A Dudek. “Investigations of microstructure and properties in bioceramic coatings used in medicine”. In: *Archives of Metallurgy and Materials* 56 (2011), pp. 135–140.

[163] Vladimir Fedorovich Pichugin et al. “The preparation of calcium phosphate coatings on titanium and nickel–titanium by rf-magnetron-sputtered deposition: composition, structure and micromechanical properties”. In: *Surface and Coatings Technology* 202.16 (2008), pp. 3913–3920.

[164] Ning Cao et al. “Plasma-sprayed hydroxyapatite coating on carbon/carbon composite scaffolds for bone tissue engineering and related tests in vivo”. In: *Journal of Biomedical Materials Research Part A: An Official Journal of The Society for Biomaterials, The Japanese Society for Biomaterials, and The Australian Society for Biomaterials and the Korean Society for Biomaterials* 92.3 (2010), pp. 1019–1027.

[165] Qian Tang et al. “Production and characterization of HA and SiHA coatings”. In: *Journal of Materials Science: Materials in Medicine* 21.1 (2010), pp. 173–181.

[166] Adele Carradó. “Structural, microstructural, and residual stress investigations of plasma-sprayed hydroxyapatite on Ti-6Al-4 V”. In: *ACS applied materials & interfaces* 2.2 (2010), pp. 561–565.

[167] N Patel et al. “In vivo assessment of hydroxyapatite and silicate-substituted hydroxyapatite granules using an ovine defect model”. In: *Journal of materials science: materials in medicine* 16.5 (2005), pp. 429–440.

[168] Marianne Toft Vestermark. “Strontium in the bone-implant interface”. In: *Dan Med Bull* 58.5 (2011), B4286.

[169] Weichang Xue et al. “Preparation and cell–materials interactions of plasma sprayed strontium-containing hydroxyapatite coating”. In: *Surface and Coatings technology* 201.8 (2007), pp. 4685–4693.

[170] C Capuccini et al. “Strontium-substituted hydroxyapatite coatings synthesized by pulsed-laser deposition: in vitro osteoblast and osteoclast response”. In: *Acta Biomaterialia* 4.6 (2008), pp. 1885–1893.

[171] JV Rau et al. “Properties of pulsed laser deposited fluorinated hydroxyapatite films on titanium”. In: *Materials Research Bulletin* 45.9 (2010), pp. 1304–1310.

[172] Qing Ling Feng et al. “Antibacterial effects of Ag-HAp thin films on alumina substrates”. In: *Thin Solid Films* 335.1-2 (1998), pp. 214–219.

[173] Yikai Chen et al. “Silver release from silver-containing hydroxyapatite coatings”. In: *Surface and coatings technology* 205.7 (2010), pp. 1892–1896.

[174] Takafumi Shimazaki et al. “In vivo antibacterial and silver-releasing properties of novel thermal sprayed silver-containing hydroxyapatite coating”. In: *Journal of Biomedical Materials Research Part B: Applied Biomaterials: An Official Journal of The Society for Biomaterials, The Japanese Society for Biomaterials, and The Australian Society for Biomaterials and the Korean Society for Biomaterials* 92.2 (2010), pp. 386–389.

[175] Bill GX Zhang et al. “Bioactive coatings for orthopaedic implants—recent trends in development of implant coatings”. In: *International Journal of Molecular Sciences* 15.7 (2014), pp. 11878–11921.

[176] Guy Daculsi et al. “Current state of the art of biphasic calcium phosphate bioceramics”. In: *Journal of Materials Science: Materials in Medicine* 14.3 (2003), pp. 195–200.

[177] Terrill F Saxon et al. “Dyadic interaction profiles in infancy and preschool intelligence”. In: *Journal of School Psychology* 38.1 (2000), pp. 9–25.

[178] Andrea Cattini. “Coatings of bioactive glasses and hydroxyapatite and their properties”. PhD thesis. Limoges, 2013.

[179] Chiara Vitale-Brovarone et al. “Bioactive glass-derived trabecular coating: a smart solution for enhancing osteointegration of prosthetic elements”. In: *Journal of Materials Science: Materials in Medicine* 23.10 (2012), pp. 2369–2380.

[180] Antoni P Tomsia et al. “Biomimetic bonelike composites and novel bioactive glass coatings”. In: *Advanced Engineering Materials* 7.11 (2005), pp. 999–1004.

[181] N Oliver Joy-anne et al. “Bioactive glass coatings on metallic implants for biomedical applications”. In: *Bioactive materials* 4 (2019), pp. 261–270.

[182] Chak Yin Tang et al. “Nanomechanical properties evaluation of bioactive glass coatings on titanium alloy substrate”. In: *Journal of Optoelectronics and Advanced Materials* 8.3 (2006), p. 1194.

[183] JM Gomez-Vega et al. “Glass-based coatings for titanium implant alloys”. In: *Journal of Biomedical Materials Research: An Official Journal of The Society for Biomaterials, The Japanese Society for Biomaterials, and The Australian Society for Biomaterials and the Korean Society for Biomaterials* 46.4 (1999), pp. 549–559.

[184] SMA Shibli et al. “Incorporation of nano zinc oxide for improvement of electroless nickel plating”. In: *Applied Surface Science* 253.3 (2006), pp. 1644–1648.

[185] Jorge Luis Enciso Manrique. “PROCESSING AND CHARACTERISATION OF BIOGLASS® COATING ON Ti6Al4V SUBTRATES”. In: *Supl. Rev. Latinoam. Metal. Mater. S* 1.1 (2009), pp. 77–90.

[186] A Balamurugan et al. “Electrochemical and structural evaluation of functionally graded bioglass-apatite composites electrophoretically deposited onto Ti6Al4V alloy”. In: *Electrochimica Acta* 54.4 (2009), pp. 1192–1198.

[187] F Lusquiños et al. “Main characteristics of calcium phosphate coatings obtained by laser cladding”. In: *Applied Surface Science* 247.1-4 (2005), pp. 486–492.

[188] DG Wang et al. “In situ synthesis of hydroxyapatite coating by laser cladding”. In: *Colloids and Surfaces B: biointerfaces* 66.2 (2008), pp. 155–162.

[189] R Comesaña et al. “Laser cladding of bioactive glass coatings”. In: *Acta biomaterialia* 6.3 (2010), pp. 953–961.

[190] Bryan W Stuart et al. “Mechanical, structural and dissolution properties of heat treated thin-film phosphate based glasses”. In: *Applied Surface Science* 416 (2017), pp. 605–617.

[191] Bryan Stuart et al. “Preferential sputtering in phosphate glass systems for the processing of bioactive coatings”. In: *Thin Solid Films* 589 (2015), pp. 534–542.

[192] Devis Bellucci et al. “High velocity suspension flame sprayed (HVSFS) potassium-based bioactive glass coatings with and without TiO2 bond coat”. In: *Surface and Coatings Technology* 206.19-20 (2012), pp. 3857–3868.

[193] John Henao et al. “Bio-active glass coatings manufactured by thermal spray: A status report”. In: *Journal of Materials Research and Technology* 8.5 (2019), pp. 4965–4984.

[194] Muhammad Rizki Hifdzia Fahmi et al. “Struktur dan karakteristik oksidasi temperatur tinggi lapisan SS430-AL pada substrat baja karbon dengan teknik Flame Spraying”. B.S. thesis. Fakultas Sains Dan Teknologi Universitas Islam Negeri Syarif Hidayatullah ...

[195] Sulzer Metco. “An introduction to thermal spray”. In: *Retrieved from* (2013).

[196] Herbert Herman et al. “Thermal spray: current status and future trends”. In: *MRS bulletin* 25.7 (2000), pp. 17–25.

[197] Pierre Fauchais. “Current status and future directions of thermal spray coatings and techniques”. In: *Future Development of Thermal Spray Coatings*. Elsevier, 2015, pp. 17–49.

[198] Andrew Siao Ming Ang et al. “Thermal spray maps: material genomics of processing technologies”. In: *Journal of thermal spray technology* 22.7 (2013), pp. 1170–1183.

[199] Masahiro Fukumoto et al. “Preparation and evaluation of ordinary attritor milled Ti-Al powders and corresponding thermal sprayed coatings”. In: *Materials transactions* 47.7 (2006), pp. 1717–1722.

[200] Andreas Wank. “Basics of thermal spray technology i processes”. In: *GTV Verschleiss-Schutz GmbH* ().

[201] P Fauchais et al. “Advanced Plasma Spray Applications”. In: *Adv. Plasma Spray Appl., InTech* (2012), pp. 149–188.

[202] Alok Vats et al. “Influence of deposition parameters on Tribological Performance of HVOF Coating: A review”. In: *IOP Conference Series: Materials Science and Engineering*. Vol. 1017. 1. IOP Publishing. 2021, p. 012015.

[203] JW Murray et al. “Suspension high velocity oxy-fuel (SHVOF)-sprayed alumina coatings: microstructure, nanoindentation and wear”. In: *Journal of Thermal Spray Technology* 25.8 (2016), pp. 1700–1710.

[204] YJ Su et al. “In situ characterization of small-particle plasma sprayed powders”. In: *Journal of thermal spray technology* 11.1 (2002), pp. 52–61.

[205] Pierre Fauchais and M Vardelle. “Sensors in spray processes”. In: *Journal of thermal spray technology* 19.4 (2010), pp. 668–694.

[206] Lech Pawlowski. “Suspension and solution thermal spray coatings”. In: *Surface and Coatings Technology* 203.19 (2009), pp. 2807–2829.

[207] Pierre Fauchais and Ghislain Montavon. "Latest developments in suspension and liquid precursor thermal spraying". In: *Journal of Thermal Spray Technology* 19.1-2 (2010), pp. 226–239.

[208] A Killinger et al. "What do we know, what are the current limitations of suspension HVOF spraying?" In: *Journal of Thermal Spray Technology* 24.7 (2015), pp. 1130–1142.

[209] R Gadow et al. "Manufacturing technologies for nanocomposite ceramic structural materials and coatings". In: *Materials Science and Engineering: B* 148.1-3 (2008), pp. 58–64.

[210] Stefan Romeis et al. "Top-down processing of submicron 45S5 Bioglass® for enhanced in vitro bioactivity and biocompatibility". In: *Procedia engineering* 102 (2015), pp. 534–541.

[211] Aleksandar Z Fišteš et al. "The effect of processing parameters on energy consumption of ball mill refiner for chocolate". In: *Hemijska industrija* 67.5 (2013), pp. 747–751.

[212] Cury Suryanarayana. "Mechanical alloying and milling". In: *Progress in materials science* 46.1-2 (2001), pp. 1–184.

[213] S Alamolhoda et al. "Role of intensive milling in mechano-thermal processing of TiAl/Al2O3 nano-composite". In: *Advanced powder technology* 23.3 (2012), pp. 343–348.

[214] FL Zhang et al. "Parameters optimization in the planetary ball milling of nanostructured tungsten carbide/cobalt powder". In: *International Journal of Refractory Metals and Hard Materials* 26.4 (2008), pp. 329–333.

[215] E Cañas et al. “Bioactive glass suspensions preparation for suspension plasma spraying”. In: *Journal of the European Ceramic Society* 36.16 (2016), pp. 4281–4290.

[216] L Sharifi et al. “High porous alumina bodies: production and properties via gel-casting technique”. In: *International Journal of Advanced Science and Technology* 65 (2014), pp. 59–70.

[217] Andrea Cattini et al. “Suspension plasma sprayed bioactive glass coatings: Effects of processing on microstructure, mechanical properties and in-vitro behaviour”. In: *Surface and Coatings Technology* 220 (2013), pp. 52–59.

[218] Giovanni Bolelli et al. “Processing and characterisation of high-velocity suspension flame sprayed (HVSFS) bioactive glass coatings”. In: (2010).

[219] Rodrigo Moreno. “The role of slip additives in tape-casting technology. I: Solvents and dispersants”. In: *American Ceramic Society Bulletin* 71.10 (1992), pp. 1521–1531.

[220] Robert J Hunter. *Zeta potential in colloid science: principles and applications*. Vol. 2. Academic press, 2013.

[221] AS Hedayat and John Stufken. “Compound orthogonal arrays”. In: *Technometrics* 41.1 (1999), pp. 57–61.

[222] Igor Zhitomirsky. “Cathodic electrodeposition of ceramic and organoceramic materials. Fundamental aspects”. In: *Advances in colloid and interface science* 97.1-3 (2002), pp. 279–317.

[223] Walid Haziz. *Processing and Properties of Porous Alumina Ceramics by Gel Casting*. 2015.

[224] William E Scott. *Principles of wet end chemistry*. Tappi Press, 1996.

[225] Jessica Vidales-Herrera and Israel López. "Nanomaterials in coatings: an industrial point of view". In: *Handbook of Nanomaterials for Manufacturing Applications*. Elsevier, 2020, pp. 51–77.

[226] Mats Larsson et al. "Suspension stability; why particle size, zeta potential and rheology are important". In: *Annual transactions of the Nordic rheology society* 20.2012 (2012), p. 6.

[227] Wen Shi et al. "Effects of magnesia particle addition on mechanical and bioactive properties of magnesia/titanium composite". In: *Materials Transactions* 43.12 (2002), pp. 3020–3024.

[228] JA Helsen et al. "Glasses and bioglasses: synthesis and coatings". In: *Journal of the European Ceramic Society* 17.2-3 (1997), pp. 147–152.

[229] Giovanni Bolelli et al. "Microstructure and in-vitro behaviour of a novel High Velocity Suspension Flame Sprayed (HVSFS) bioactive glass coating". In: *Surface and Coatings Technology* 205.4 (2010), pp. 1145–1149.

[230] O Rojas et al. "Influence of atmospheric plasma spraying parameters on porosity formation in coatings manufactured from 45S5 Bioglass® powder". In: *Journal of Thermal Spray Technology* 29.1 (2020), pp. 185–198.

[231] C Gabbi et al. "Bioactive glass coating: physicochemical aspects and biological findings". In: *Biomaterials* 16.7 (1995), pp. 515–520.

[232] JH Chern Lin et al. "Biocorrosion behavior of hydroxyapatite/bioactive glass plasma sprayed on Ti6A14V". In: *Materials Chemistry and Physics* 41.4 (1995), pp. 282–289.

[233] TM Lee et al. “Characteristics of plasma-sprayed bioactive glass coatings on Ti-6A1-4V alloy: an in vitro study”. In: *Surface and Coatings Technology* 79.1-3 (1996), pp. 170–177.

[234] E Verne et al. “Sintering and plasma spray deposition of bioactive glass-matrix composites for medical applications”. In: *Journal of the European Ceramic Society* 18.4 (1998), pp. 363–372.

[235] A Lopez-Sastre et al. “Coating titanium implants with bioglass and with hydroxyapatite”. In: *International orthopaedics* 22.6 (1998), pp. 380–383.

[236] Jan Schrooten et al. “Adhesion of new bioactive glass coating”. In: *Journal of Biomedical Materials Research: An Official Journal of The Society for Biomaterials, The Japanese Society for Biomaterials, and The Australian Society for Biomaterials* 44.3 (1999), pp. 243–252.

[237] JH Chern Lin et al. “Characterization of immersed hydroxyapatite-bioactive glass coatings in Hank’s solution”. In: *Materials chemistry and physics* 64.3 (2000), pp. 229–240.

[238] Edouard Jallot et al. “Dissolution kinetics, selective leaching, and interfacial reactions of a bioglass coating enriched in alumina”. In: *Journal of colloid and interface science* 233.1 (2001), pp. 83–90.

[239] Gultekin Goller. “The effect of bond coat on mechanical properties of plasma sprayed bioglass-titanium coatings”. In: *Ceramics international* 30.3 (2004), pp. 351–355.

[240] Verónica López Calvo et al. “45S5 bioactive glass coatings by atmospheric plasma spraying obtained from feedstocks prepared by different routes”. In: *Journal of Materials Science* 49.23 (2014), pp. 7933–7942.

[241] Lina Altomare et al. “Microstructure and in vitro behaviour of 45S5 bioglass coatings deposited by high velocity suspension flame spraying (HVSFS)”. In: *Journal of Materials Science: Materials in Medicine* 22.5 (2011), pp. 1303–1319.

[242] Chung-Cherng Lin et al. “Na2CaSi2O6–P2O5 based bioactive glasses. Part 1: Elasticity and structure”. In: *Journal of Non-Crystalline Solids* 351.40-42 (2005), pp. 3195–3203.

[243] Giovanni Bolelli et al. “Microstructural and in vitro characterisation of high-velocity suspension flame sprayed (HVSFS) bioactive glass coatings”. In: *Journal of the European Ceramic Society* 29.11 (2009), pp. 2249–2257.

[244] Giovanni Bolelli et al. “Deposition mechanisms in high velocity suspension spraying: case study for two bioactive materials”. In: *Surface and Coatings Technology* 210 (2012), pp. 28–45.

[245] C Suryanarayana and GE Korth. “Consolidation of nanocrystalline powders”. In: *Metals and Materials* 5.2 (1999), pp. 121–128.

[246] Sandra Cabanas-Polo and Aldo R Boccaccini. “Understanding bioactive glass powder suspensions for electrophoretic deposition of bioactive glass-polymer coatings”. In: *Journal of The Electrochemical Society* 162.11 (2015), p. D3077.

[247] S Chadha et al. “A high-fidelity simulation of the primary breakup within suspension high velocity oxy fuel thermal spray using a coupled volume of fluid

and discrete phase model." In: *International Journal of Multiphase Flow* 133 (2020), p. 103445.

[248] Mingwen Bai et al. "Microstructure and phase stability of suspension high velocity oxy-fuel sprayed yttria stabilised zirconia coatings from aqueous and ethanol based suspensions". In: *Journal of the European Ceramic Society* 38.4 (2018), pp. 1878–1887.

[249] FP Ottensmeyer. "Scattered electrons in microscopy and microanalysis". In: *Science* 215.4532 (1982), pp. 461–466.

[250] Jason Alexander Röhr. "Electron Transport in Solution Processed Antimony Sulphide Thin Films made from a Xanthate Precursor". In: (2014).

[251] Tamitake Itoh et al. "Surface-Enhanced Raman Scattering Spectroscopy: Electromagnetic Mechanism and Biomedical Applications". In: *Frontiers of Molecular Spectroscopy*. Elsevier, 2009, pp. 289–319.

[252] Md Wahadoszamen et al. "Laser Raman spectroscopy with different excitation sources and extension to surface enhanced Raman spectroscopy". In: *Journal of Spectroscopy* 2,015 (2015).

[253] TO PROVIDE SUPPORTING DOCUMENTATION. "Implants for surgery—In vitro evaluation for apatite-forming ability of implant materials". In: (2007).

[254] Alexander Hoppe et al. "In vitro reactivity of Cu doped 45S5 Bioglass® derived scaffolds for bone tissue engineering". In: *Journal of Materials Chemistry B* 1.41 (2013), pp. 5659–5674.

[255] Despina D Deligianni et al. “Effect of surface roughness of hydroxyapatite on human bone marrow cell adhesion, proliferation, differentiation and detachment strength”. In: *Biomaterials* 22.1 (2000), pp. 87–96.

[256] Devis Bellucci et al. “In situ Raman spectroscopy investigation of bioactive glass reactivity: Simulated body fluid solution vs TRIS-buffered solution”. In: *Materials characterization* 62.10 (2011), pp. 1021–1028.

[257] Ervino C Ziemath and Michel A Aegerter. “Raman and infrared investigations of glass and glass-ceramics with composition 2Na 2 O· 1CaO· 3SiO 2”. In: *Journal of materials research* 9.1 (1994), pp. 216–225.

[258] P González et al. “Raman spectroscopic study of bioactive silica based glasses”. In: *Journal of non-crystalline solids* 320.1-3 (2003), pp. 92–99.

[259] Anastasios Antonakos et al. “Micro-Raman and FTIR studies of synthetic and natural apatites”. In: *Biomaterials* 28.19 (2007), pp. 3043–3054.

[260] Deepak K Pattanayak. “Apatite wollastonite–poly methyl methacrylate bio-composites”. In: *Materials Science and Engineering: C* 29.5 (2009), pp. 1709–1714.

[261] G Penel et al. “MicroRaman spectral study of the PO 4 and CO 3 vibrational modes in synthetic and biological apatites”. In: *Calcified tissue international* 63.6 (1998), pp. 475–481.

[262] R Cuscó et al. “Differentiation between hydroxyapatite and β-tricalcium phosphate by means of μ-Raman spectroscopy”. In: *Journal of the European Ceramic Society* 18.9 (1998), pp. 1301–1305.

[263] Armelle Vardelle et al. “The 2016 thermal spray roadmap”. In: *Journal of thermal spray technology* 25.8 (2016), pp. 1376–1440.

[264] Mingwen Bai et al. “Suspension high velocity oxy-fuel spraying of a rutile TiO2 feedstock: Microstructure, phase evolution and photocatalytic behaviour”. In: *Ceramics International* 43.17 (2017), pp. 15288–15295.

[265] Jonas Gurauskis et al. “Self-supported ceramic substrates with directional porosity by mold freeze casting”. In: *Journal of the European Ceramic Society* 37.2 (2017), pp. 697–703.

[266] Ruud GC Beerkens. “Modeling the kinetics of volatilization from glass melts”. In: *Journal of the American Ceramic Society* 84.9 (2001), pp. 1952–1960.

[267] Matthew D O’Donnell. “Melt-derived bioactive glass”. In: *Bio-glasses. Chichester (UK): Wiley* (2012), pp. 13–28.

[268] JP Borrajo et al. “The role of the thickness and the substrate on the in vitro bioactivity of silica-based glass coatings”. In: *Materials Science and Engineering: C* 25.2 (2005), pp. 187–193.

[269] Mehdi Ebrahimi et al. “Biphasic calcium phosphates bioceramics (HA/TCP): Concept, physicochemical properties and the impact of standardization of study protocols in biomaterials research”. In: *Materials Science and Engineering: C* 71 (2017), pp. 1293–1312.

[270] Vikas Anand et al. “Evaluation of zinc and magnesium doped 45S5 mesoporous bioactive glass system for the growth of hydroxyl apatite layer”. In: *Journal of non-crystalline solids* 406 (2014), pp. 88–94.

[271] AMB Silva et al. “Structure of SiO2–MgO–Na2O glasses by FTIR, Raman and 29Si MAS NMR”. In: *Journal of Molecular Structure* 986.1-3 (2011), pp. 16–21.

[272] Andrea Cattini et al. “Microstructural design of functionally graded coatings composed of suspension plasma sprayed hydroxyapatite and bioactive glass”. In: *Journal of Biomedical Materials Research Part B: Applied Biomaterials* 102.3 (2014), pp. 551–560.

[273] George W Morey. “The constitution of glass”. In: *Journal of the American Ceramic Society* 17.1-12 (1934), pp. 315–328.

[274] Valentyna V Nosenko et al. “Nature of some features in Raman spectra of hydroxyapatite-containing materials”. In: *Journal of Raman Spectroscopy* 47.6 (2016), pp. 726–730.

[275] SN Kane et al. “PREFACE: International Conference on Recent Trends in Physics (ICRTP 2012)”. In: *Journal of Physics Conference Series*. Vol. 365. 1. 2012, p. 011001.

[276] Rodney W Trice and KT Faber. “Role of Lamellae Morphology on the Microstructural Development and Mechanical Properties of Small-Particle Plasma-Sprayed Alumina”. In: *Journal of the American Ceramic Society* 83.4 (2000), pp. 889–896.

[277] Z Pala et al. “Suspension high velocity oxy-fuel spraying of TiO2: A quantitative approach to phase composition”. In: *Journal of the European Ceramic Society* 37.2 (2017), pp. 801–810.

[278] Pavel Ctibor and Milan Hrabovsky. “Plasma sprayed TiO2: The influence of power of an electric supply on particle parameters in the flight and character

of sprayed coating". In: *Journal of the European Ceramic Society* 30.15 (2010), pp. 3131–3136.

[279] Yang Yu et al. "Contrasting in vitro apatite growth from bioactive glass surfaces with that of spontaneous precipitation". In: *Materials* 11.9 (2018), p. 1690.

[280] C Vitale Brovarone et al. "Macroporous bioactive glass-ceramic scaffolds for tissue engineering". In: *Journal of Materials Science: Materials in Medicine* 17.11 (2006), pp. 1069–1078.

[281] K Franks et al. "The effect of MgO on the solubility behavior and cell proliferation in a quaternary soluble phosphate based glass system". In: *Journal of Materials Science: Materials in Medicine* 13.6 (2002), pp. 549–556.

[282] A Saboori et al. "Synthesis, characterization and in vitro bioactivity of sol-gel-derived SiO2–CaO–P2O5–MgO bioglass". In: *Materials science and engineering: C* 29.1 (2009), pp. 335–340.

[283] Takeshi Yabutsuka et al. "Effect of doubled sandblasting process and basic simulated body fluid treatment on fabrication of bioactive stainless steels". In: *Materials* 11.8 (2018), p. 1334.

[284] Abdulrahman A Balhaddad et al. "Toward dental caries: Exploring nanoparticle-based platforms and calcium phosphate compounds for dental restorative materials". In: *Bioactive materials* 4 (2019), pp. 43–55.

[285] Paul W Brown and Roger I Martin. "An analysis of hydroxyapatite surface layer formation". In: *The journal of physical chemistry B* 103.10 (1999), pp. 1671–1675.

[286] Claus Moseke and U Gbureck. "Tetracalcium phosphate: Synthesis, properties and biomedical applications". In: *Acta Biomaterialia* 6.10 (2010), pp. 3815–3823.

[287] A Itälä et al. "Characterization of microrough bioactive glass surface: surface reactions and osteoblast responses in vitro". In: *Journal of Biomedical Materials Research: An Official Journal of The Society for Biomaterials, The Japanese Society for Biomaterials, and The Australian Society for Biomaterials and the Korean Society for Biomaterials* 62.3 (2002), pp. 404–411.

[288] Barbara D Boyan et al. "Role of material surfaces in regulating bone and cartilage cell response". In: *Biomaterials* 17.2 (1996), pp. 137–146.

[289] S Kaoua et al. "Preparation and characterization of phosphate glasses containing titanium and vanadium". In: *Journal of alloys and compounds* 429.1-2 (2007), pp. 276–279.

[290] Avadhesh Kumar Yadav and Prabhakar Singh. "A review of the structures of oxide glasses by Raman spectroscopy". In: *RSC advances* 5.83 (2015), pp. 67583–67609.

[291] S Bano et al. "Effect of processing on microstructure, mechanical properties and dissolution behaviour in SBF of Bioglass (45S5) coatings deposited by Suspension High Velocity Oxy Fuel (SHVOF) thermal spray". In: *Surface and Coatings Technology* 372 (2019), pp. 229–238.

[292] David M Sanders and Wolfgang K Haller. "Effect of Water Vapor on Sodium Vaporization from Two Silica-Based Glasses". In: *Journal of the American Ceramic Society* 60.3-4 (1977), pp. 138–141.

[293] Franck Pigeonneau et al. “Stability of vertical films of molten glass due to evaporation”. In: *Colloids and Surfaces A: Physicochemical and Engineering Aspects* 408 (2012), pp. 8–16.

[294] Azadeh Kiani et al. “Structural characterization and physical properties of P2O5–CaO–Na2O–TiO2 glasses by Fourier transform infrared, Raman and solid-state magic angle spinning nuclear magnetic resonance spectroscopies”. In: *Acta biomaterialia* 8.1 (2012), pp. 333–340.

[295] John R Van Wazer. “Phosphorus and its Compounds”. In: (1958).

[296] W Kiefer. “Recent advances in linear and nonlinear Raman spectroscopy I”. In: *Journal of Raman Spectroscopy: An International Journal for Original Work in all Aspects of Raman Spectroscopy, Including Higher Order Processes, and also Brillouin and Rayleigh Scattering* 38.12 (2007), pp. 1538–1553.

[297] Yanyan Zhao et al. “Raman spectroscopy of the transition of α-gallium oxyhydroxide to β-gallium oxide nanorods”. In: *Journal of Raman Spectroscopy: An International Journal for Original Work in all Aspects of Raman Spectroscopy, Including Higher Order Processes, and also Brillouin and Rayleigh Scattering* 39.10 (2008), pp. 1327–1331.

[298] BRITISH STANDARD and BSEN ISO. “Biological evaluation of medical devices—”. In: *Biol. Eval. Med. devices* (2003), pp. 10993–1.

[299] JOSEF C LAPP and JAMES E SHELBY. “Viscosity and thermal expansion of sodium and potassium galliosilicate glasses”. In: *Journal of the American Ceramic Society* 69.2 (1986), pp. 126–131.

[300] TA Owoseni et al. “Residual Stress Measurement of Suspension HVOF-Sprayed Alumina Coating via a Hole-Drilling Method”. In: *Journal of Thermal Spray Technology* 29.6 (2020), pp. 1339–1350.

[301] Christopher R Chitambar. “Medical applications and toxicities of gallium compounds”. In: *International journal of environmental research and public health* 7.5 (2010), pp. 2337–2361.

[302] Philippe Collery et al. “Gallium in cancer treatment”. In: *Critical reviews in oncology/hematology* 42.3 (2002), pp. 283–296.